NOTCH SIGNALING: MECHANISTIC AND FUNCTIONAL STUDIES IN INTESTINAL STEM CELLS AND COLORECTAL CANCER CELLS

A Dissertation

Presented to the Faculty of the Graduate School

of Cornell University

In Partial Fulfillment of the Requirements for the Degree of

Doctor of Philosophy

Specializing in Biomedical Engineering

by

Tara Srinivasan

May 2016

NOTCH SIGNALING: MECHANISTIC AND FUNCTIONAL STUDIES IN INTESTINAL STEM CELLS AND COLORECTAL CANCER CELLS

Tara Srinivasan, Ph. D.

Cornell University 2016

ABSTRACT:

The study of stem cell regulation in intestinal and colonic tissues is an area of significant focus within the scientific community, providing mechanistic insight into biological process and offering translational clinical potential. In this thesis we address the contribution of NOTCH signaling in maintaining the stem cell niche by modulating the mode of stem cell division and receptor-ligand interactions for cell-cell communication. Furthermore, we examine NOTCH-mediated spatiotemporal recovery of the intestinal stem cell (ISC) niche following single cell ablation. Finally, we demonstrate that elevated NOTCH signaling exists under conditions of physiological stress and in colon cancer initiating cells (CCICs), promoting tumorigenic potential of the intestinal epithelium. Overall, our research highlights the underlying complexities of NOTCH signaling as an essential pathway to maintain intestinal homeostasis and may inspire development of novel CRC therapeutic strategies.

Research efforts and findings during my graduate study have been consolidated into the following peer-reviewed publications, of which the four first co-author manuscripts are described in detail in this dissertation.

1. **Srinivasan, Tara**; Walters, Jewell; Bu, Pengcheng; Than, Elaine B.; Tung, Kuei-Ling; Chen, Kai-Yuan; Panarelli, Nicole; Milsom, Jeff; Augenlicht, Leonard; Lipkin, Steven M; Shen, Xiling. "NOTCH Signaling Regulates Asymmetric Division of Fast- and Slow-Cycling Colon Cancer Initiating Cells." *Cancer Research,* 2016. (*in press*)

2. **Srinivasan, Tara**; Than, Elaine B.; Bu, Pengcheng; Tung, Kuei-Ling; Chen, Kai-Yuan; Augenlicht, Leonard; Lipkin, Steven M.; Shen, Xiling. "NOTCH Signaling Regulates Fast- and Slow-Cycling Intestinal Stem Cells." *Scientific Reports,* 2016. (*in press*)

3. Chen, Kai-Yuan*; **Srinivasan, Tara*;** Choi, Jiahn*; Bu, Pengcheng; Tung, Kuei-Ling; Nishimura, Nozomi; Shen, Xiling. "Dynamic regulation of intestinal stem cell niche recovery in real-time." *Cell Systems*, 2015. *(in review)*

4. Murthy, Preetish KL*; **Srinivasan, Tara***; Bochter, Skye; Bu, Pengcheng; Cole, Susan; Shen, Xiling. "FRINGE-dependent modification of NOTCH Ligands in Intestinal Stem Cells." 2016. *(in preparation)*

5. Rothschild, Daniel; **Srinivasan, Tara**; Aponte-Santiago, Linette; Shen, Xiling; Irving, Allen. "The Ex Vivo Culture and Pattern Recognition Receptor Stimulation of Mouse Intestinal Organoids." *JoVE*, 2015. *(in press)*

6. Bu, Pengcheng*; Wang, Lihua*; Chen, Kai-Yuan; **Srinivasan, Tara**; Lakshminarasimha, Preetish; Tung, Kuei-Ling; Varanko, Anastasia; Ai, Yiwei; Lipkin, Steven; Shen, Xiling. "miR-34a and Numb synergize for asymmetric cell fate determination." *Cell Stem Cell*, 2016 Feb 4;18(2):189-202.

7. Crespo, Miguel; Tsai, Su-Yi; **Srinivasan, Tara**; Pipalia, Nina; Maxfield, Nina; Lipkin, Steven M; Evans, Todd; Chen, Shuibing. "Colonic Organoids Derived from Human Pluripotent Stem Cells for Modeling Colorectal Cancer and Drug Testing." *Nature Medicine*, 2015. *(in review)*

8. Wang, Lihua*; Bu, Pengcheng*; Ai, Yiwel; **Srinivasan, Tara**; Lipkin, Steven M; Shen, Xiling. "A Long Non-Coding RNA Targets MicroRNA miR-34a to Regulate Colon Cancer Stem Cell Asymmetric Division." *eLife*, 2016. *(in press)*

BIOGRAPHICAL SKETCH

Tara Srinivasan was born in 1989 in Secunderabad, India. At the age of one, Tara and her parents immigrated to the United States in Fremont, California. Her father was a mechanical engineer and from a young age, Tara was inspired to similarly pursue an interest in mathematics. Her mother, a homemaker, spent significant time during Tara's early years of education, fostering her academic advancement and cultivating a passion for learning and achievement. Tara attended public high school where she excelled in broad areas of study from liberal arts to technical disciplines, including science and mathematics. She graduated as valedictorian of her high school in 2007.

Tara attended the University of California, Berkeley for an undergraduate education. Her interest in both the fundamentals of engineering and life sciences led her to pursue a major in bioengineering with the eventual career prospect of devising novel therapeutics. As she began her undergraduate study, however, she discovered an increasing drive to understand the complexities of physiological and pathological systems. To this end, she pursued an additional major in molecular and cell biology to solidify her technical foundation. Ultimately, she graduated with Honors in May 2011, receiving a Bachelor's of Science degree in Bioengineering and a Bachelor's of Arts degree in Molecular and Cell Biology with an emphasis in Immunology.

Tara began working in a research laboratory in the Children's Hospital of Oakland Research Institute that focused on the pathogenesis of the sexually transmitted bacteria, *Chlamydia trachomatis* in 2007. Her advisor, Dr. Deborah Dean, provided her with the opportunity to investigate mechanisms of lateral gene transfer in C. *trachomatis* that assist in host immune evasion. Through this research, Tara learned a variety of molecular biology

techniques and she remained in the laboratory for four years, leading this investigation, which resulted in a first-author publication in 2011. She also received a fellowship from the American Society of Microbiology for this research and presented her findings at the annual ASM conference in New Orleans in 2011. Furthermore, she delivered an oral presentation at a national Chlamydia Basic Research Society conference in 2011 as the only undergraduate investigator. Upon completion of this project, Tara expanded her research expertise at the Buck Institute for Research on Aging in Dr. Bradford Gibson's laboratory. She worked closely with Dr. Jason Held, a principal scientist, who was an invaluable asset in her career development, sharing both his wealth of knowledge, and experience with many laboratory assays. Tara attributes much of her graduate research success to the foundation established under Dr. Held's guidance. Here, the research involved quantitating cysteine oxidation status in redox-sensitive p53 using OxMRM (Oxidation Multiple Reaction Monitoring) Mass Spectrometry technology developed by Dr. Held. Additionally, she examined dynamic temporal regulation of redox signaling to investigate its role in cancer signaling cascades, specifically in breast and colon cancer. Her contributions resulted in a peer-reviewed research article in the *International Journal of Proteomics*.

In August of 2012, Tara began her graduate doctoral study in biomedical engineering at Cornell University. Initially inspired to synthesize novel drug delivery systems, Tara discovered a greater passion for mechanistic studies of cancer biology. Eventually, she joined Dr. Xiling Shen's laboratory and through an existing collaboration, she was co-mentored by Dr. Steven Lipkin at Weill Cornell Medical College (WCMC) for the remainder of her graduate study. Her proposed doctoral work was supported by the prestigious graduate research fellowship from the National Science Foundation. After four years, Tara successfully defended her dissertation in May of 2016.

With love always to my parents

and to James (Jimmy) Rothschild

ACKNOWLEDGMENTS

I owe my principal advisor, Dr. Xiling Shen, significant gratitude and respect for his contribution in supporting my graduate career. Although I did not begin my study in Dr. Shen's laboratory, he graciously recognized and supported my knowledge and expertise, welcoming me into his research group. I have learned to be a more critical scientist, a better technical writer, and a better orator under his guidance. Any achievements made throughout the scientific process and the successful completion of this graduate dissertation was made possible only because of Dr. Shen's mentorship. I do not have the words to express my sincerest appreciation for providing me with an environment in which I was able to learn and thrive.

Importantly, I am deeply thankful for the guidance provided by my co-advisor, Dr. Steven Lipkin of Weill Cornell Medical College. Dr. Lipkin has been an invaluable asset in teaching me to think critically about designing experiments as well as articulating downstream results. He has also been extremely supportive of my appointment in his laboratory, which has given me the opportunity to learn and expand my technical knowledge and skillset in a highly collaborative clinical research environment.

I would also like to thank my committee members, Dr. Julius Lucks and Dr. Robert Weiss, for their constructive comments and guidance towards successfully completing my doctoral study. Additionally, I am grateful for the graduate research fellowship provided by the National Science Foundation that has been critical in supporting my research.

I extend my deepest heartfelt thanks to my dear colleagues and friends – Dr. Elaine Than of Dr. Lipkin's laboratory and Daniel Rothschild, a graduate student Dr. Irving Allen's laboratory at Virginia Polytechnic Institute (Virginia Tech). Both individuals have provided me with immense support and encouragement throughout my graduate career and I am forever

grateful. Furthermore, I am sincerely thankful to James (Jimmy) Rothschild whose support and confidence in me continues to be a source of strength and inspiration for my future. Finally, I am deeply thankful to my family who have given me every opportunity to succeed from a young age – I am especially indebted to my mother who embodies unconditional love with an enduring belief in my potential to achieve my dreams. Words will never be enough to acknowledge how instrumental she has been in my career thus far.

TABLE OF CONTENTS

LIST OF FIGURES

CHAPTER 1

CHAPTER 2

CHAPTER 4

CHAPTER 5

APPENDIX

LIST OF ABBREVIATIONS

ISC	Intestinal Stem Cell
TA	Transit Amplifying
LGR5	Leucine-rich repeat-containing G protein-coupled Receptor 5
ASCL2	Achaete-Schute Complex Homolog 2
OLFM4	Olfactomedin-4
BMI1	Polycomb Ring Finger Oncogene
HOPX	Homeodomain-Only Protein X
TERT	Telomerase Reverse Tanscriptase
LRIG-1	Leucine-rich Repeats and Immunoglobulin-like Domains 1
APC	Adenomatosis Polyposis Coli
POFUT-1	Protein O-Fucosyltransferase 1
DLL	Delta-like Ligand
EGF	Epidermal Growth Factor
BMP	Bone Morphogenetic Protein
CCIC	Colon Cancer Initiating Cell
FAP	Familial Adenomatous Polyopsis
HNPCC	Hereditary Nonpolyopsis Colon Cancer

CHAPTER 1

INTRODUCTION

Preface

The research investigations discussed in the subsequent chapters examine compelling phenomena such as asymmetric division, stem cell patterning, mechanisms of cell-cell signaling, and differential gene expression in intestinal and colonic tissues. Importantly, we employ the use of mouse model systems to study physiological states and the process of recovery following acute injury in the gastrointestinal tract. Furthermore, we extend our findings in clinical research of human colorectal cancer to develop insight into mechanisms regulating tumorigenesis and chemoresistance. Accordingly, Chapter 1 provides an overview of fundamental biology related to these studies in order to understand our findings and their significance within context of the scientific community.

1. Intestinal and Colonic Epithelium

1.1. Anatomy

The absorptive and digestive components of the human gastrointestinal tract are composed of the small intestine and colon (large intestine or bowel) (Figure 1). The small intestine is approximately 6.0-7.1 meters in length and 2.5-3 centimeters in diameter in the adult body [1]. The structure of the small intestine is divided into three consecutive sections: duodenum, jejunum and ileum, each of which provides complementary functions to support digestion and absorption of nutrients and minerals. The duodenum is the first and shortest segment (20-30 cm long) and is responsible for neutralizing gastric chyme from the stomach and receiving pancreatic digestive enzymes and bile from the gall bladder to break down proteins and emulsify fat [1]. The jejunum is approximately 2.5 meters long and is lined with finger-like projections, called villi, which absorb digested products (sugars, amino acids, fatty acis) into the bloodstream. Next, the ileum absorbs bile salts, vitamin B12, and any remaining nutrients. This segment is ~3 meters long, connecting the small intestine to the colon at the ileocecal junction. The colon, which is approximately 1.5 meters in length, contains four sections: ascending, transverse, descending, and sigmoid segments[1]. The main function of the colon, unlike the small intestine, is to absorb water and any remaining vitamins and nutrients before indigestible matter is compacted as feces and moves to the rectum.

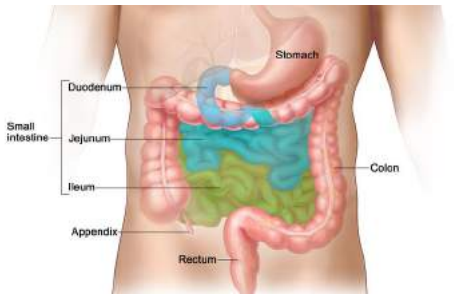

Figure 1. Anatomy of human small intestine and colon [1].

The single layer epithelium of the small intestine contains millions of crypt-villus units

while colonic epithelium contains only crypts (Figure 2). Villi are composed of post-mitotic cells on the surface, which are supported by internal blood and lymph vessels that transport absorbed nutrients. Each villus is attached at the base to self-renewing crypts of Lieberkuhn, epithelial invaginations with a rich source of proliferating cells to drive intestinal regeneration. The entire epithelial lining has a high turnover rate and is replaced approximately every five days in the human body [1, 2]. This efficient mechanism of intestinal homeostasis is achieved by intestinal stem cells (ISCs) situated at the crypt base, which are capable of self-renewal or differentiation and migration along the crypt-villus axis to comprise the specialized linages of the epithelium.

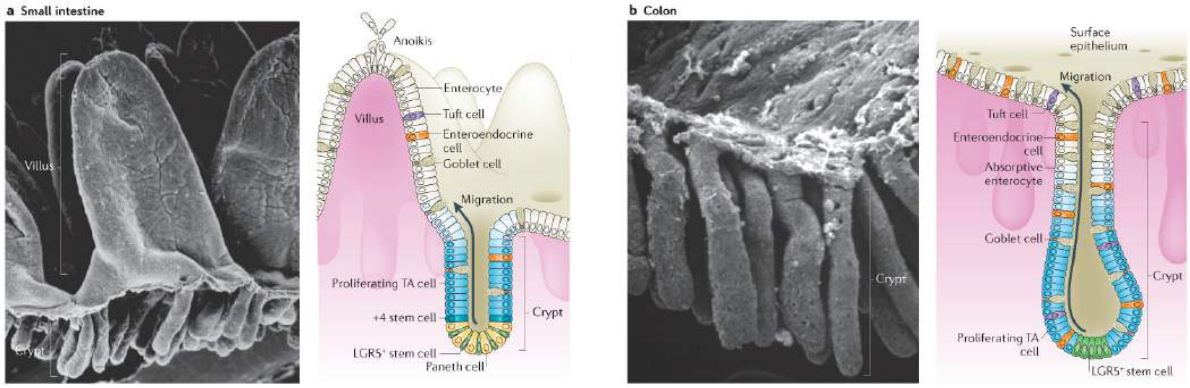

Figure 2. Epithelial regeneration in small intestine and colon [3].

1.2. Intestinal Stem Cells

Approximately 4-7 intestinal stem cells (ISCs) are located in the crypt base and maintain homeostasis by a series of complex signaling pathways arising from adjacent epithelial and stromal cells that dictates lineage specification [3]. Multipotent LGR5-expressing (Leu-rich repeat-containing G protein-coupled receptor 5-expressing) crypt base columnar (CBC) stem cells are interspersed at the crypt base and can undergo self-renewal or give rise to transit-amplifying (TA) daughter cells. These progenitor cells rapidly divide (~3-4 cell divisions) to produce the mature short-lived terminally differentiated progeny that populate the intestinal epithelium. These specialized cell types include microfold cells (M cells), Paneth cells,

absorptive enterocytes, and secretory lineages such as enteroendocrine cells, goblet cells, and tuft cells [4-6]. With the exception of Paneth cells that are retained in the crypt base, the upward migration of TA cells progressively commits these progenitors towards terminally differentiated cell fates [3]. ISCs migrate upwards into the TA zone followed by the differentiated cell zone at the surface of villi (small intestine) or crypts (colon) where cells eventually undergo apoptosis and are shed into the lumen.

The most prominent marker of CBCs is LGR5, a receptor for the WNT pathway agonist family of R-SPONDINs. Members of the R-SPONDIN family are responsible for enhancing WNT signaling within the stem cell zone. Using an inducible LGR5-EGFP allele crossed to a ROSA26-LacZ reporter, Barker and colleagues identified approximately 10-15 LGR5-GFP+ cells per crypt, which divided every 24 hours and were intermingled with Paneth cells in crypt bottoms [4]. Using Tamoxifen inducible lineage tracing, LGR5+ ISCs were capable of clonally generating the various epithelial lineages within five days. From isolated LGR5-GFP+ ISCs, gene expression analysis identified other ISC markers, including ASCL2, OLFM4, and Musashi-1 (Figure 3). ASCL2 (Achaete-scute complex homolog 2) is a transcription factor that robustly marks CBCs in both the intestine and colon [7]. Olfactomedin-4 (OLFM4), an anti-apoptotic secreted glycoprotein, is a robust marker of murine stem cells restricted to the small intestine and is directly regulated by NOTCH signaling [8, 9]. MUSASHI-1, an oncogenic RNA binding protein, and CD133 (also known as PROMININ-1), a transmembrane glycoprotein, were initially proposed as CBC markers. However, several studies have indicated that MUSASHI-1 and CD133 expression is not limited to the stem cell zone; rather progenitors in the lower TA compartment have high expression of both genes [10-12]. SPARC related modulator calcium binding 2 (SMOC2) has also been confirmed as a marker with CBC specificity [11]. Finally, CBCs have elevated expression of transmembrane ephrin type-B receptor 2 (EPHB2), a member

of the receptor tyrosine kinase family. Previous studies have demonstrated that EPHB2 expression decreases gradually along the crypt villus axis. In murine small intestinal stem cells and human colonic stem cells, CBCs are identified by $EPHB2^{high}$ expression [13, 14].

Through lineage tracing and transplantation experiments, there is also evidence for the existence of a quiescent population with a label retaining stem cell identity situated at the +4 position from the crypt base [15]. This second intestinal stem cell (ISC) population expresses different markers that include BMI1, HOPX, TERT, and LRIG-1 (Figure 3) [16-19]. BMI1, a proto-oncogene polycomb repressor complex, is a 326 amino acid protein with a cysteine rich RING finger binding domain. This domain is responsible for zinc complexing and downstream ubiquitination. BMI1 was first proposed as a marker for slow-cycling stem cells by lineage tracing in the proximal small intestine [19]. These studies in mice carrying a Tamoxifen-inducible BMI1reporter showed that BMI1 stem cells were located at the +4 position at the base of intestinal crypts and were capable of self-renewal, proliferation, and differentiation into all of the mature lineages of the epithelium. This model of crypt regeneration resembled that of LGR5+ stem cell-mediated activity both in kinetics and morphology. Interestingly, when BMI1+ ISCs conditionally labeled with Rosa26 expressed diphtheria toxin for selective ablation, crypts failed to self-renew and were eventually depleted. In fact, there is evidence that LGR5+ ISCs are critical for routinely maintaining homeostasis and crypt self-renewal while BMI+ ISCs are involved in repair following injury [15].

Homeodomain-only protein (HOPX) is a homeobox protein that lacks specific amino acid residues essential for DNA binding. Previous work using a HOPX-LacZ reporter demonstrated that HOPX was expressed by +4 cells that were long lived (label retaining) throughout both the intestine and colon [16]. Telomerase reverse transcriptase (TERT) is the catalytic domain of the telomerase enzyme. In combination with telomerase RNA component,

TERT is responsible for the addition of repetitive DNA nucleotide sequences at the end of telomeres on chromosomes. TERT is up-regulated in stem-cells to promote self-renewal without limiting the number of cell divisions imposed by shortened telomeres [20]. Using lineage tracing in mouse models, studies showed that TERT+ cells were label retaining stem cells, resistant to radiation injury, and comprised a distinct pool of stem cells compared to LGR5+ ISCs [17, 20]. Finally, Leucine-rich repeats and immunoglobulin-like domains 1 (LRIG-1) is a transmembrane protein that inhibits ERBB, a member of the tyrosine kinase family. Using a Tamoxifen inducible LRIG-1 reporter in lineage tracing studies showed that a subset, approximately 20% of LRIG-1+ ISCs, possessed a label retaining identity. Microarray analysis of LGR5+ ISCs demonstrated a proliferation and stemness signature while LRIG-1+ ISCs showed down-regulation of the corresponding cell cycle genes.

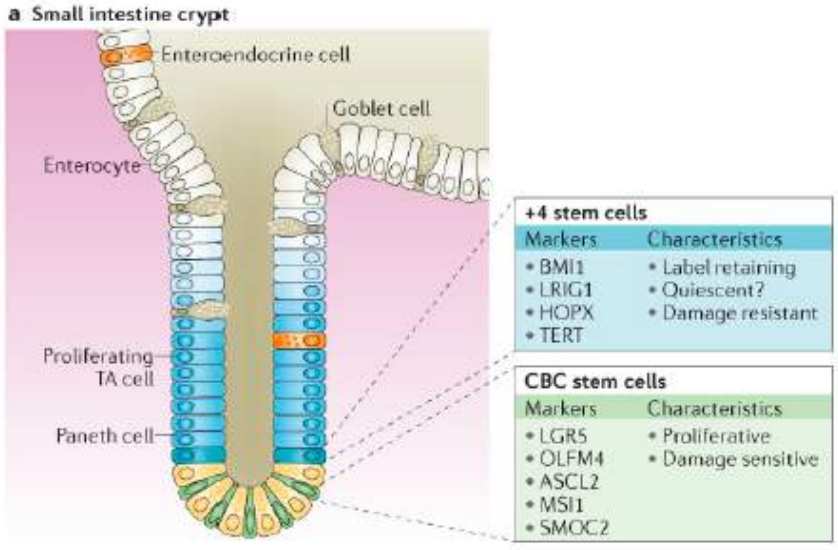

Figure 3. Intestinal Stem Cell Markers [3].

Previously, it has been shown that LGR5+ stem cells can trans-differentiate into +4 cells expressing HOPX [16]. Reciprocally, +4 ISCs can trans-differentiate into LGR5+ CBC daughter cells as a compensatory mechanism following experimental ablation of LGR5-expressing cells using diphtheria toxin [16, 21]. This suggests that interconversion between actively proliferating

LGR5+ and quiescent BMI1+ ISCs is a mechanism of homeostasis and repair in the intestine, highlighting plasticity of the intestinal crypt stem cell lineages. Additional evidence of plasticity was proposed by Winton et al. [2] who expressed chromatin marker histone 2B-YFP throughout the small intestine to study label retention. It was observed that non-Paneth label retaining cells were viable for up to three weeks, and expressed CBC, +4 ISC, and Paneth cell markers. Further examination revealed that this second type of quiescent label retaining cell is a Paneth cell- and enteroendocrine-precursor that exists in a non-dividing state for several weeks before terminal differentiation. Due to the complexity of stem cell plasticity, several studies have shown broad overlapping expression of +4 markers in LGR5+ ISCs [11] using RNA *in situ* hybridization. Therefore, more detailed analysis of CBC and +4 stem cell populations is required to resolve their specific identities.

1.3. Transit Amplifying Cells

LGR5+ ISCs divide every 24 hours and these daughter cells migrate upwards into the TA zone that is comprised of short-lived progenitors. TA cells only require about 12 hours for each of their four to five cells divisions before moving into the differentiated compartment [11]. Proliferation and migration are prominent in the TA zone, and notably, proliferation eventually terminates at the crypt-villus boundary. Accordingly, villi contain only post-mitotic cells. The specification of the various differentiated lineages that populate the intestinal and colonic epithelium originates at the +5 position in the TA zone of crypts. WNT signaling mediated by R-SPONDINs is essential to maintain the TA proliferative capacity [22, 23]. Notably, NOTCH signaling promotes differentiation into absorptive enterocytes through suppression of NOTCH pathway transcription factor, atonal homolog 1 (ATOH1). In contrast, NOTCH inhibition, which elevates ATOH1, favors secretory lineage differentiation [3].

1.4. Differentiated Epithelial Cells

The terminally differentiated lineages of the intestinal epithelium include absorptive enterocytes, mucus-secreting Goblet cells, anti-microbial secreting Paneth cells, chemosensing Tuft cells, hormone-secreting enteroendocrine cells, and microfold (M)-cells [3] (Figure 4).

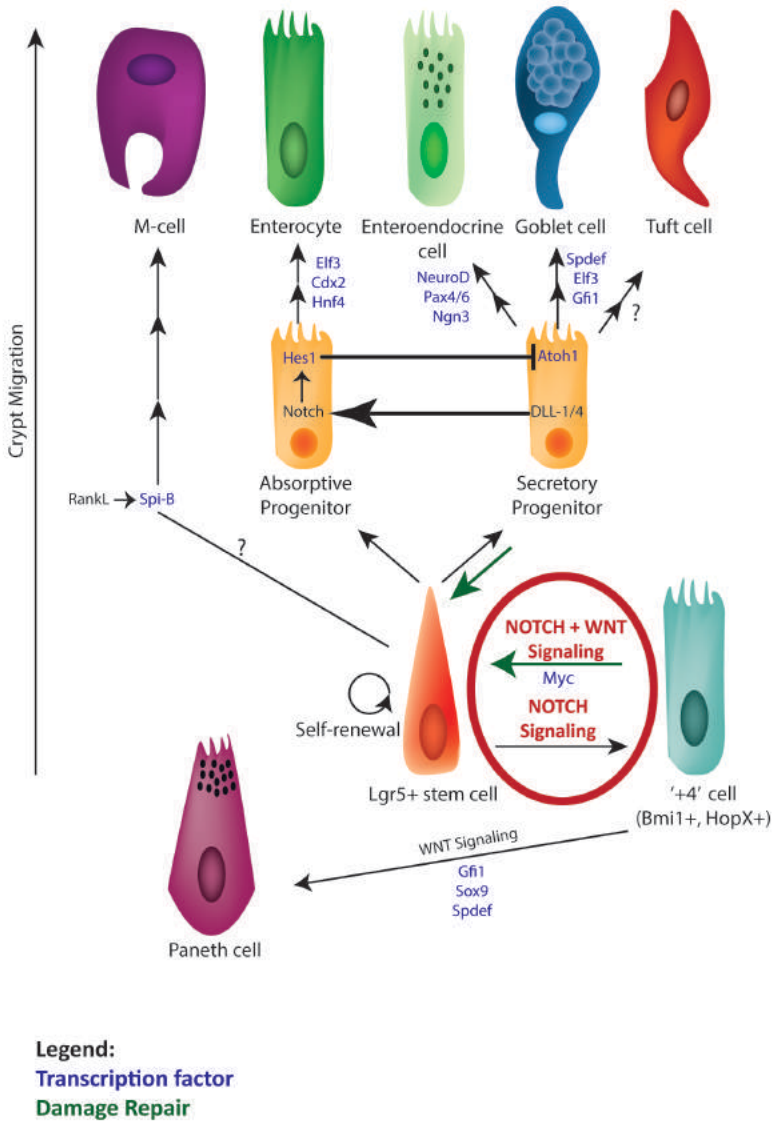

Figure 4. Lineage Specification in Intestinal Epithelium.

Enterocytes are the primary cell type found in villi and are responsible for nutrient absorption into the bloodstream. Goblet cells secrete protective mucus lining along the intestinal tract. NOTCH signaling inhibition leads to Goblet cell hyperplasia, indicating this lineage is the primary secretory type, specified by SPDEF transcription factor activity [24]. Paneth cells,

unlike the other mature lineages, are found only in the small intestine, are retained at the crypt base and provide critical niche signaling to CBC cells. Furthermore, this granular cell type produces various anti-microbial peptides that regulate gut microbiota. Paneth cell specification is promoted by SOX9 transcription factor binding in the WNT signaling pathway [2]. Fibroblast growth factors have also been shown to be important in Paneth cell formation. Unlike the other epithelial cell types, which survive for up to one week, Paneth cells persist up to two months. Tuft cells only constitute 0.4% of the adult epithelium and their precise function remains unknown. This lineage derives from DLL+ precursors, but is independent of ATOH1, SOX9 and NEUROG3 transcription factor specification [25, 26]. Enteroendocrine cells are classified by the types of specific hormones produced are specified by the NEUROG3 transcription factor. Collectively, this lineage comprises 1% of the epithelium and regulates intestinal function. M-cells coat the surface of gut-associated lymphoid tissues (called Peyer's patches), serving as the intersection of the intestinal lumen and underlying immune system. M-cells transport luminal antigens to lymphoid tissue and this lineage specification involves SPI-B transcription factor and RANKL cytokine activity [3, 25].

2. Signaling Pathways

Although the precise microenvironmental and signaling cues that dictate LGR5+ stem cell renewal vs. differentiation are not fully understood, WNT and NOTCH signaling are known to be important pathways associated with stem cell self-renewal (Figure 5) [6, 8, 27-29].

2.1. Wnt Signaling

WNT Signaling is critical in adult intestinal tissues, regulating the stem cell zone and committed progenitors in the TA compartment. The primary branch of WNT signaling, called the "canonical" pathway, which critically depends on β-CATENIN as a transcription factor. In the absence of WNT ligand, cytosolic β-CATENIN is ubiquitinated for degradation by binding

to a destruction complex that includes AXIN, adenomatosis polyposis coli (APC), glycogen synthase kinase (GSK3), and casein kinase 1α (CK1α). WNT signaling is activated by the presence of WNT ligand, which binds a seven-transmembrane receptor, called FRIZZLED, and a co-receptor, called low-density lipoprotein receptor-related protein (LRP) [30]. The ligand-receptor association induces phosphorylation of DISHEVELED, an adaptor protein, which inhibits GSK3 and causes accumulation of cytosolic β-catenin. Subsequently, β-catenin translocates to the nucleus and associates with DNA-binding proteins from the LEF/TCF family to activate expression of specific WNT effector genes. In intestinal tissue, R-SPONDINs are a family of secreted agonists that enhance WNT activity by binding to their corresponding receptor (LGR4/5/6). Next, RSPONDINs associate and remove zinc and ring finger 43 (Znfr3) transmembrane ubiquitin ligase from the membrane, leading to increased and stabilized FRIZZLED and enhanced WNT effector gene expression [30].

Studies conducted both *in vitro* and *in vivo* demonstrated that WNT signaling is essential for ISC proliferation and pluripotency. Accordingly, ISCs accumulate nuclear β-CATENIN, and CBC markers LGR5, ASCL2, and EPHB2 are direct WNT targets, indicating active WNT signaling. ISC proliferation is facilitated by TCF target gene c-MYC expression, which suppresses cell cycle inhibitor p21 [23]. Genetic knockdown or deletion of WNT effectors TCF and β-CATENIN result in complete intestinal crypt loss. Furthermore, ectopic expression of WNT antagonist DKK1 causes extensive crypt architecture collapse. Excessive WNT signaling through RSPONDIN induction causes ISC hyperplasia [3, 31]. Additionally, mutations in the tumor suppressor protein, APC, result in constant activation of the WNT pathway and its downstream targets, such as c-MYC, causing uncontrolled proliferation and adenomatous transformation of the intestinal epithelium [32].

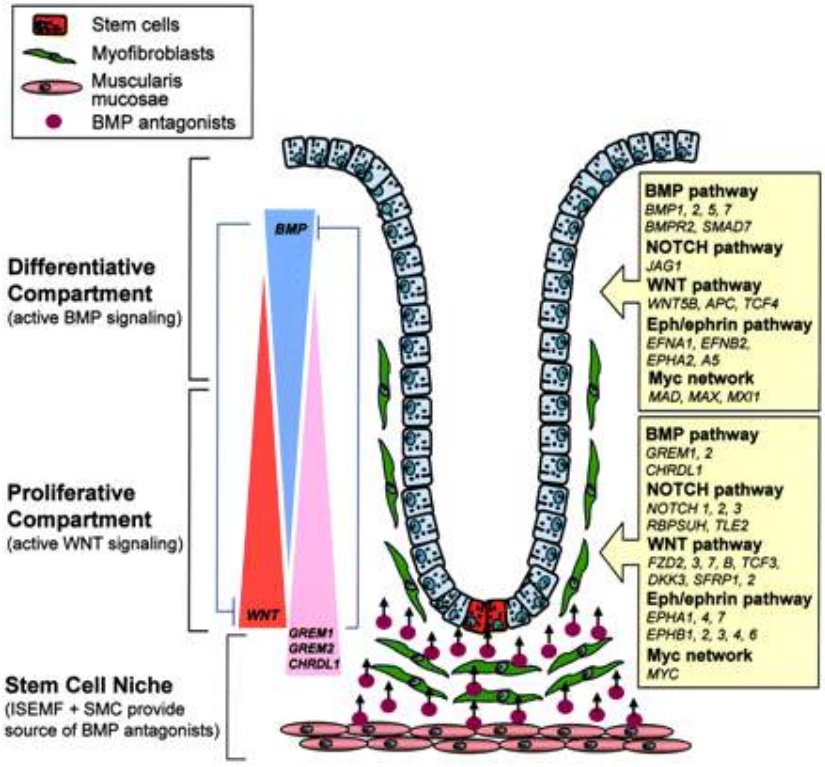

Figure 5. Intestinal Crypt Signaling Pathways.[33]

2.2. Notch Signaling

In mammals, the NOTCH family consists of four receptors (NOTCH1-4) and Delta/Serrate/Lag (DSL) ligands classified into DELTA-like (DLL1, DLL3, DLL4), and SERRATE-like (JAGGED1 and JAGGED2) groups. NOTCH receptors are transmembrane proteins that have an extracellular ligand binding domain, containing Epidermal Growth Factor (EGF)-like repeats and an intracellular transactivation domain [34]. DSL ligands also contain EGF-like repeats while JAGGED1 and JAGGED2 contain cysteine-rich domains. NOTCH signaling is activated by DSL ligand (on the signal-sending cells) binding to NOTCH receptors on adjacent cells (signal receiving cells) (Figure 6). Receptor-ligand association causes a disintegrin and metalloprotease (ADAM) enzyme to induce extracellular proteolysis of the NOTCH receptor juxtamembrane site. Subsequently, a γ-secretase complex cleaves the NOTCH receptor transmembrane portion, releasing the NOTCH intracellular domain (NICD) into the

cytoplasm, which then translocates into the nucleus. NICD associates with the DNA-binding transcription factor CSL (CBF-1/RBP-Jκ,Su(H),Lag-1) and causes downstream expression of NOTCH target genes Hairy and Enhancer of Split 1 and 5 (HES1 and HES5) [35].

In addition to the canonical NOTCH transactivation described earlier, NOTCH DSL ligands can result in *cis*-inhibition on the signal-sending cell. The precise mechanism of *cis*-inhibition is unclear, although there is evidence that a high threshold effect of DSL ligand inhibits NOTCH signaling in the same cell. *Cis* interaction results in endocytosis and degradation of both receptor and corresponding ligands [34, 35]. This contributes to a feedback mechanism in cells such that once sufficient levels of DSL ligands are expressed on the signal-sending cell *cis*-inhibition prevents over-activation of NOTCH signaling.

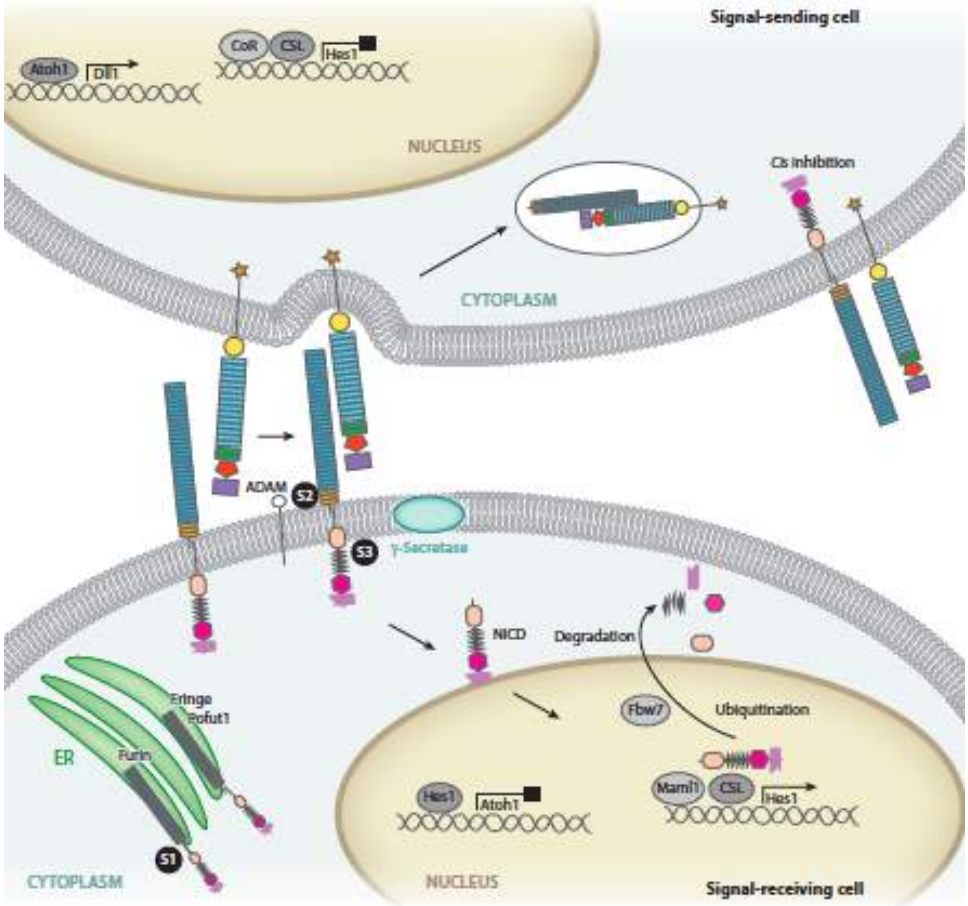

Figure 6. Notch Signaling Pathway [34].

The proliferative zone of crypts containing stem cells and progenitors also expresses essential Notch pathway components, such as receptors NOTCH-1 and NOTCH-2, ligands DLL-1, DLL-4, and JAG-1, and downstream effector genes HES1 and HES5 [24, 29, 36]. Furthermore, the simultaneous genetic knockout of NOTCH-1 and NOTCH-2 receptors results in terminal differentiation of crypt progenitor cells into post-mitotic Goblet cells [29]. It has also been established that differential NOTCH activity as a result of lateral inhibition in neighboring progenitor cells specifies absorptive or secretory lineages [27, 37]. Finally, NOTCH signaling elevates the transcriptional expression of BMI1, which contributes to ISC self renewal [38].

2.3. BMP Signaling

Bone morphogenetic protein (BMP) signaling is part of the TGF-β superfamily, which plays a role in regulating cell proliferation, differentiation and apoptosis in intestinal crypts.

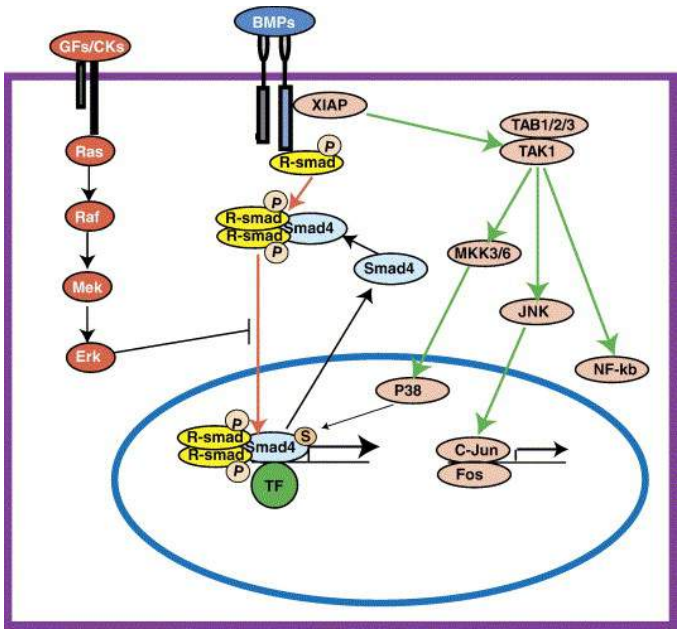

Figure 7. BMP Signaling Pathway [39].

BMP signal transduction involves BMP receptor type I (BMP2 and BMP4 in the small intestine) phosphorylation of SMAD1/5/8 proteins. SMAD4/8 form a heterotrimeric complex that translocates to the nucleus to bind with other transcription factors and activate target gene

expression (Figure 7). Specifically, BMP signaling inhibits ISC self-renewal and proliferation by antagonism of the WNT signaling pathway [39]. Moreover, genetic disruption of BMP receptors in the adult mouse intestine resulted in impaired terminal differentiation of the secretory cell lineage. In contrast, WNT signaling and absorptive cell differentiation were not affected by BMP silencing. Several studies have shown a primary role for BMP signaling in regulating the epithelial architecture of the crypt-villus axis [40].

2.4. HEDGEHOG Signaling

HEDGEHOG signaling plays a negative feedback role in the maintenance of homeostasis in the intestinal epithelium. In both mice and humans, three types of HEDGEHOG proteins exist: Indian HEDGEHOG, Desert HEDGEHOG, and Sonic HEDGEHOG. To activate signaling, DISPATCHED releases the N-terminal fragment of HEDGEHOG from the membrane, which subsequently binds PATCHED, a transmembrane receptor. This binding relieves the inhibition on another transmembrane receptor protein, SMOOTHENED [41]. Active SMOOTHENED then causes cytoplasmic glioblastoma transcription factors (GLI 1/2/3) translocate to the nucleus and activate target gene expression (Figure 8) [41].

Previous reports have shown that Indian HEDGEHOG (IHH) is the main type of HEDGEHOG expressed in the small intestine and colon, although low levels of Sonic HEDGEHOG (SHH) have been detected in colonic crypts. Mesenchymal cells, including smooth muscle cells, and myofibroblast-like cells are the main HEDGEHOG responsive cells. Studies in HEDGEHOG reporter mice demonstrated that signaling is exclusively paracrine from the mesemchyme to the epithelium [41]. Indeed genetic disruption of HEDGEHOG signaling showed that HEDGEHOG is required to maintain smooth muscle cells and myofibroblast-like cells. Within the adult, IHH is expressed by differentiated cells in both the small intestine and colon. IHH also is a negative regulator of intestinal stem cell proliferation at the base of crypts,

as well as the size of the crypt compartment [3, 41]. Loss of IHH causes an increase in mesenchymal and macrophage cells, showing a response similar to wound healing. Therefore, HEDGEHOG signaling is likely critical in triggering a wound healing response upon crypt damage [3].

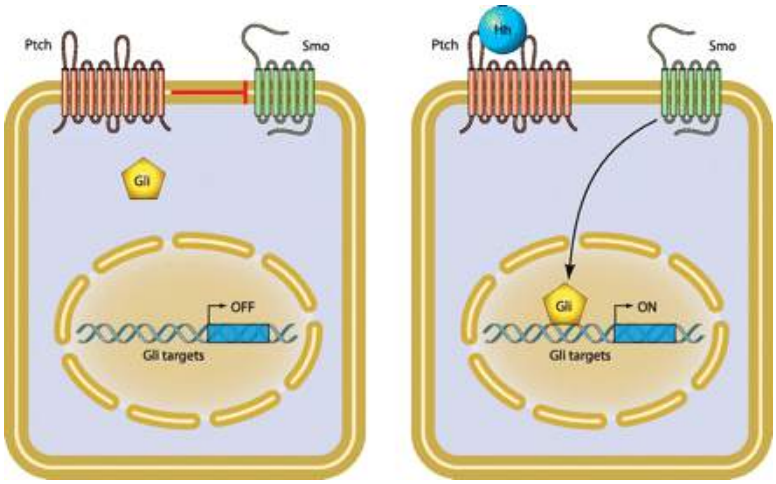

Figure 8. Hedgehog Signaling Pathway [41].

3. Stem Cell Niche

The intestinal stem cell niche is composed of adjacent Paneth cells and subepithelial myofibroblasts that support the crypt base. This microenvironment provides ISCs with essential signaling cues, including Paneth-derived DLLs, epidermal growth factor (EGF), WNT3, and WNT2b. In the colon, Paneth cells are substituted by a subpopulation of CD117+ goblet cells that provide DLLs and EGF ligands. DLL1+DLL4+ Paneth cells interact with NOTCH1/2 on LGR5+ CBCs, suppressing ATOH1 and preventing early differentiation into secretory epithelial cells. Furthermore, genetic deletion of Paneth cells results in loss of LGR5+ CBCs and failure to regenerate crypts *in vitro* and *in vivo* [42]. Additionally, Paneth cells carrying mutant WNT3 are unable to generate intestinal 3D organoid 'mini-guts.' When ATOH1 expression was silenced *in vivo*, Paneth cells were eliminated but ISC self-renewal was unaffected. In contrast, ATOH1 depletion could not support *in vitro* growth of intestinal organoids [43]. Taken together, these

finding suggest that Paneth cells are a critical factor in niche signaling *in vitro*, but physiologically there is redundancy to support ISC self-renewal *in vivo*. Notably, NOTCH ligands on Paneth cells are essential *in vivo*, while other Paneth-derived niche factors are not unique. For example, WNT and EGF factors are redundantly generated by the subepithelial mesemchyme [30]. Within the niche, WNT signaling is highly regulated to prevent excessive proliferation and WNT signaling is diminished along the crypt-villus axis. In the base of crypts, WNT signaling is negatively regulated by both BMP and HEDGEHOG signaling. In the colon, stroma-derived GREMLIN1/2 and CHORDIN-LIKE1 act as BMP antagonists to suppress pro-differentiation signals in the stem cell zone. At the +4 position, WNT signaling is antagonized by Frizzled-related proteins. The upward migration of progenitors at the +5 position into differentiated cells involves coordinated signaling from both BMP and HEDGEHOG pathways to promote differentiation [3, 30, 43].

4. Patterning in the Crypt

Paneth cells and LGR5+ CBCs are found in a close alternating 'soccer-ball' pattern at the base of intestinal crypts, indicating that direct association is necessary to maintain ISC homeostasis. On average in adult intestinal tissue, crypts consistently possess 15 LGR5+ CBCs and 10 Paneth cells [4, 44]. Studies that involve lineage tracing indicated that ISCs primarily divide symmetrically every 24 hours and daughter cells subsequently compete to occupy the limited niche space in between Paneth cells. Thus, ISCs are in constant competition without any one daughter developing a clonal advantage for approximately three months at which time crypts become monoclonal (Figure 9). This process, termed, "neutral drift" suggests that, on average, every crypt is derived from a single ISCs that existed approximately three months earlier [6, 44]. Additionally, this process dictates that the number of ISCs per crypt critically depends on the available surface area unoccupied by Paneth cells.

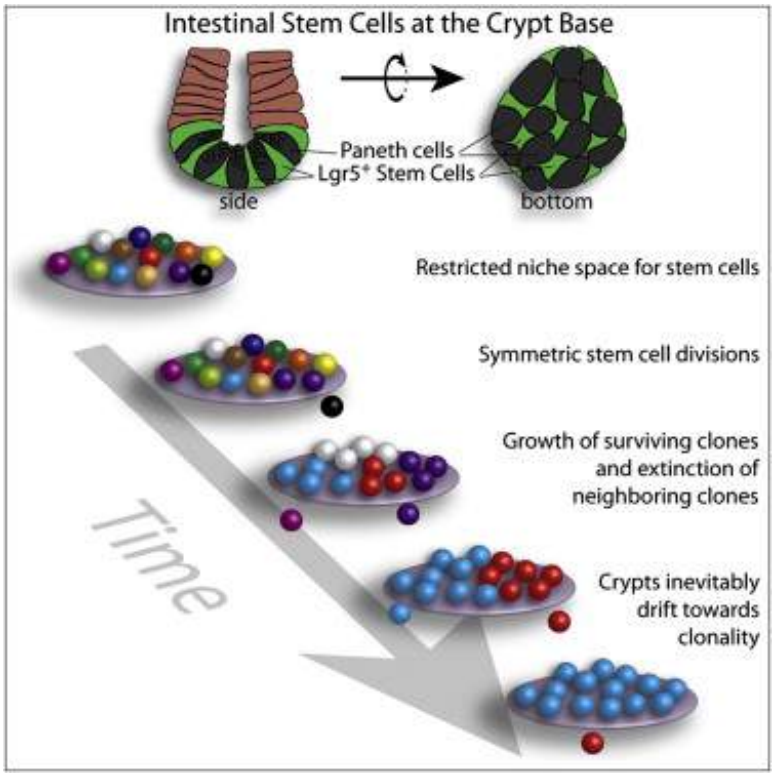

Figure 9. Neutral Drift in Intestinal Crypts [6]

Since Paneth cells are critical mediators of ISCs, the mechanisms governing Paneth cell numbers are highly regulated to maintain homeostasis. This is accomplished by active WNT signaling with negative feedback. Specifically, high WNT signaling promote Paneth cell fate in the absence of NOTCH effectors. As WNT signaling promotes proliferation of both Paneth cells and ISCs, a negative feedback loop mediated by WNT target genes RNF43 and ZNRF3 exists to prevent over-expansion of crypts [24, 45]. Both RNF43 and ZNRF3 act as transmembrance ligases that recruit FRIZZLED away from the plasma membrane and suppress WNT signaling. Therefore, the size of the crypt niche is regulated by negative-feedback inhibitors. Paneth cells, unlike other differentiated epithelial cells, migrate towards the base of crypts due to the repulsion of EPHB receptors and EPHRINB ligands. In particular, Paneth cells express WNT target gene EPHB3 while differentiated cells express increasing levels of EPHRINB1 along the crypt-villus axis [46]. The repulsion of this surface receptor-ligand interaction forces the Paneth cell to home

downwards in contrast to other proliferating TA cells. Indeed, genetic deletion of EPHB3 in mice demonstrates a failure off Paneth cells to migrate efficiently downwards to the crypt base [46]. Therefore, patterning of Paneth cells and ISCs at the crypt base is critical to regulate intestinal homeostasis.

5. Modes of Intestinal Stem Cell Renewal

Intestinal stem cells are capable of exquisite regulation over their mode of cell division to ensure long-term homeostasis. As described earlier, LGR5+ ISCs predominantly divide symmetrically in a 'neutral drift' process to produce daughters that are either both stem cells or both progenitor cells [44]. Symmetric division is the primary model to populate the stem cell zone rapidly during development and to repopulate the pool of stem cells in the event of tissue injury. Importantly, ISCs are also capable of asymmetric division, generating a stem cell daughter and a progenitor daughter that will differentiate (Figure 10). Neutral drift does not exclude the possibility of asymmetric division, which maintains the number of stem cells long term and can be activated under stress conditions, such as inflammation. Both the rate and mode of ISC division are highly regulated in adult tissues to provide flexibility of cell composition in response to physiological perturbation and to prevent excessive proliferation [47].

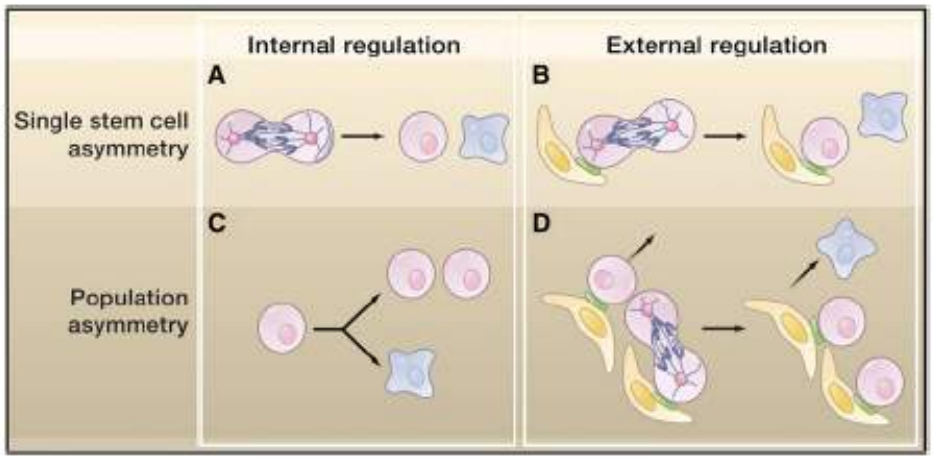

Figure 10. Mechanisms of Stem Cell Renewal at single cell or population level [48].

The integration of computational modeling and experimental studies demonstrate that crypt morphogenesis is dynamically controlled. Specifically, symmetric divisions are first used to expand the number of stem cells at the base of crypts. Subsequently, ISCs then display a transition to asymmetric divisions, which is used to create the progenitor and differentiated lineages of the epithelium [49]. Here we note that the temporal hierarchy is key in developing mature crypts and in maintaining crypt turnover in adult tissues.

An added layer of complexity derives from the relative contribution of extrinsic factors and niche signals compared to intrinsic, cell-autonomous regulation in governing ISC division. Asymmetric division can occur at the single cell level through niche-dependent and niche-independent processes [50]. In externally regulated ISC asymmetric division, one daughter cell is maintained in the stem cell compartment for self-renewal while the its counterpart is committed to differentiation following displacement from the stem cell niche. Previous research suggests that this mechanism is a critical reserve when ISCs are displaced from the niche, ensuring that the total pool of ISCs in the crypt base remains relatively constant. In contrast, intrinsic asymmetry arises from segregation of specific polarity proteins and cell fate determinants during cell division, ensuring both a stem cell fate and a differentiated fate to each of the daughters, respectively [47]. In addition, population asymmetry is also a mechanism that is used to balance proliferation and differentiation in intestinal tissues subjected to neutral drift dynamics [51]. In particular, niche-dependent asymmetric division at the population level involves displacement of ISCs from the stem cell compartment and simultaneous proliferation of neighboring ISCs. This strategy has been recognized as a robust mechanism to restore homeostasis in response to tissue damage. Finally, balancing autonomously regulated proliferation and loss of stem cells within crypts represents intrinsic population asymmetry [51]. Overall, the anatomical size and range of the ISC niche impose constraints on the mode of stem cell renewal and division, governing

stochastic cell fates for long-term tissue maintenance [48]. In the rapidly cycling intestinal tissue, understanding stem cell regulation is critical to provide insight into various gastrointestinal pathologies and cancer.

6. Fringe Family Modifications

In addition to transcriptional regulation within the intestinal niche, post-translational modifications are being discovered as mediators of signal transduction pathways. In particular, the extracellular domains of both NOTCH receptors and DSL ligands are highly glycosylated. Notably, POFUT-1, an O-fucosyltransferase is and endoplasmic reticulum (ER)-derived enzyme that fucosylates EGF repeats on NOTCH receptors. This glycosylation is essential for functional NOTCH signaling as POFUT-1 acts as a chaperone protein, promoting folding of NOTCH EGF domains [52]. Additionally, FRINGE proteins are responsible for the addition of N-acetylglucosamine (GlcNAc) to O-fucose on hydroxyl groups of Serine or Threonine residues on conserved EGF-like repeats on NOTCH receptors and DSL ligands. EGF-like repeats are defined as conserved motifs containing six cysteine residues forming three disulfide bonds with the binding site of O-fucose embedded in this region (Figure 11). Although NOTCH molecules contain multiple EGF repeats modified by O-fucose, FRINGE proteins only selectively modify specific EGFs with a preference for glutamic acid and proline amino acids in specific positions relative to the binding site on Serine or Threonine residues. It is important to note that the precise function of this type of glycosylation is not fully understood; however, evidence suggests that this modification may increase receptor-ligand binding affinity [53].

FRINGE was first studied in *drosophila* during developmental patterning of the wing and mammalian homologs have been since identified. The Fringe family of protein enzymes consists of three members: Lunatic Fringe, Manic Fringe, and Radical Fringe. Fringe proteins have been identified to play a role in the NOTCH signaling pathway during developmental processes. In

adult tissues, Lunatic Fringe (L-FRINGE) is a single pass type II membrane protein that is capable of translocation to the golgi apparatus membrane. L-FRINGE acts as a glycosyltransferase, playing a critical role during developmental segmentation and in elongating O-linked fucose domains on NOTCH receptors and ligands [54]. L-FRINGE knockout mice experienced increased perinatal death due to rib malformation while adult knockout mice displayed multiple phenotypic defects. Additonally, Manic FRINGE (M-FRINGE) plays a role in developmental segmentation and Radical FRINGE (R-FRINGE) is important during the development process, creating limb buds. However, R-FRINGE genetic deletion did not result in any obvious developmental limb defect, suggesting signaling redundancy [53]. Although NOTCH signaling has been studied extensively, the precise role of L-, M-, and R-FRINGE in NOTCH modulation in adult intestinal tissues has not been fully elucidated.

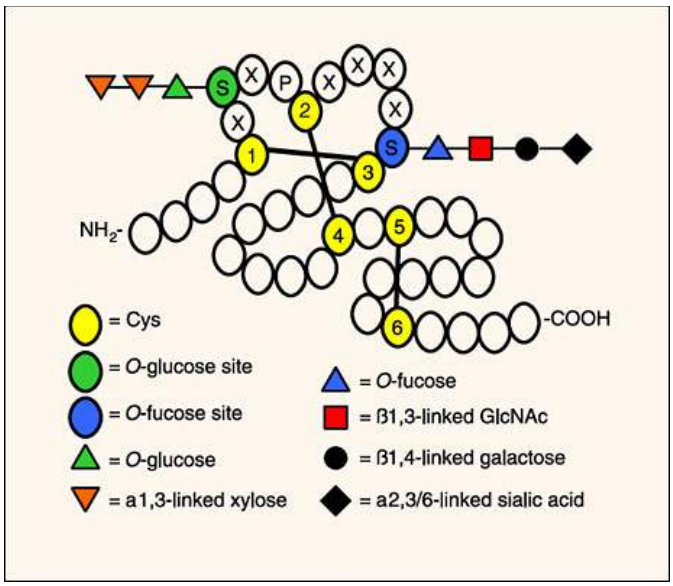

Figure 11. EGF-like repeat with Fringe modification (red) indicated [55].

Previous research indicates that both NOTCH receptors and DSL ligands may be modified by FRINGE. L-FRINGE has been shown to have the highest catalytic activity of the other FRINGE members [53, 54]. Indeed, murine DLL3 has been shown to be glycosylated by L-FRINGE *in vitro* [56]. Analysis of NOTCH extracellular domains showed that O-fucose

glycans could exist as a disaccharide, a trisaccharide, or a tetrasaccharide due to FRINGE activity. However, only the mature O-fucose tetrasaccharide (composed of *O*-fucose modified with a ß1,3-linked GlcNAc and elongated with a galactose and sialic acid to make Sia-α2,3/6-Gal-ß1,4-GlcNAc-ß1, 3-Fuc-α1-*O*-Ser/Thr), was necessary for the FRINGE effect (Figure 11) [54]. In comparing DSL ligands, FRINGE activity was found to modify O-fucose that inhibits NOTCH signaling from JAGGED ligands but enhances signaling from DLL ligands [54]. There is also evidence that FRINGE may be secreted out of cells to glycosylate receptors on neighboring cells [57]. Subsequent reports indicate that secreted FRINGE does not increase NOTCH signaling *in vitro* [58], indicating that further studies are required to resolve FRINGE activity in intestinal crypts.

7. Gastrointestinal Cancers

Gastrointestinal cancers refer to neoplasms that occur in the gastrointestinal (GI) tract and accessory organs, which include the esophagus, stomach, small intestine, colon, rectum, anus, pancreas, liver, and gall bladder. Collectively, GI cancers account for more cases compared to any other organ system and are the most lethal cancers worldwide. The etiology underlying GI related cancers are varied, including genetic predisposition, diet, inflammation, and environmental factors [59]. Consequently, research efforts are focused on identifying new molecular targets and next-generation therapies to improve patient outcome and survival [60]. The remainder of Chapter 1 will focus on cancer arising in the lower GI tract, including the small intestine and colon as an extension of the biology we described earlier in these tissues.

7.1. Cancer in the Small Intestine

Cancers of the small intestine are relatively rare, affecting 1 in 100,000 people worldwide and representing 0.4% of cancer cases in the United States. Only 2% of gastrointestinal cancers occur in the small intestine compared to approximately 60% in the colon [59]. As described

earlier, the muscosa of the small intestine is renewed every 5-7 days, containing a variety of epithelial cell types, neuroendocrine cells, immune cells and mesenchymal cells. Consequently, cancers originating from these different cell types are classified into the following groups: carcinoid tumors, adenomas, adenocarcinomas, lymphomas, and mesenchymal tumors. Carcinoid tumors are derived from serotonin-secreting neuroendocrine cells, called Kulchitsky cells [61]. These tumors are multi-focal and are most commonly found in the ileum of the small intestine. Inactivation and deletion in specific chromosome (18p, 18q, 11q, 16q, and 9p) leading to critical changes in oncogenes and tumor suppressor genes are associated with carcinoid tumors [61]. Overall, neuroendocrine tumors account for 40% of small intestine cancers.

Adenomas and adenocarcinomas refer to cancers arising in glandular tissue, such as the mucosal surface of the small intestine that contains secretions from underlying exocrine glands [62]. Adenomatous polyps are benign, non-invasive tumors that can later develop into malignant adenocarincomas, invading the basement membrane of tissue and spreading to other organs. Adenocarcinoma occurs most frequently in the duodenum and proximal jejunum of the small intestine and pathogenesis involves mutations in various tumor suppressor genes and oncogenes, including APC, KRAS, p53, and E-CADHERIN [59]. In approximately 15% of adenocarcinomas of the small intestine, microsatellite instability has been detected, indicating DNA mismatch repair deficiency. Overall, adenocarcinoma accounts for approximately 40% of cancer cases in the small intestine [62].

Neoplams may also occur in the following immune cells: B cells, T cells and Natural Killer cells of the enteric system, giving rise to non-Hodgkin lymphomas [59]. Further subclassification of lymphoproliferative tumors include mucosa-associated lymphoid tissue (MALT) lymphoma, diffuse large B cell lymphoma, enteropathy T-cell associated lymphoma (EALT), and immunoproliferative small intestinal disease (IPSID). Among these enteric

neoplasms, B cell lymphoma is the most common; transformation and tumorigenesis involve dysrgulation of key signaling pathways, chromosomal translocation, and immune cell interaction with the mucosa [63].

Finally, the most common of small intestinal cancers originate in mesemchymal cells, which are called gastrointestinal stromal tumors (GIST) [64]. Transformation occurs in the interstitial cells of Cajal, which are located between the longtitudinal and circular muscular layers of the small intestine and regulate GI motility. Cajal cells have been shown to have mutations in the proto-oncogene, CD117, a surface KIT tyrosine kinase receptor. Furthermore, gain of function in CD117 of Cajal cells are associated with over 90% of GIST tumors [64].

7.2. Colorectal Cancer (CRC)

Colorectal Cancer (CRC) is the third most commonly diagnosed cancer in both men and women worldwide, comprising approximately 9.7% of all cancer cases. There are 1.5 million new CRC cases annually and as a leading cause of cancer-related mortality, CRC accounts for over 600,000 deaths each year [65, 66]. In approximately 33% of CRC tumors, the primary tumor occurs in the rectum while remaining tumor sites are most commonly found in the sigmoid colon. Early detection of CRC through routine colonoscopy coupled with surgical intervention has an approximately 90% cure rate. However, the high incidence of mortality associated with advanced CRC is usually due to secondary metastasis to the liver. A variety of factors influence individual patient prognosis, including gender, age, diet, GI inflammation, bowel obstruction, tumor location, symptomatic display, and potential of surgical resection to remove the majority of cancerous tissues [66]. Additionally, tumor features are significant in prognostic value and depend on the degree of submucosal invasion, tumor differentiation, architecture, and ploidy. During surgical resection of the primary tumor, the presence of lymph node invasion is the most important criteria to define patient prognosis and long-term outcome. Severe lymph node

infiltration at the time of diagnosis indicates a highly aggressive and advanced stage of CRC, limiting the efficacy of current therapies [60]. Consequently, research efforts are focused on identifying prognostic markers to identify patients that will derive greatest treatment benefit from surgery alone, chemotherapy, combinatorial therapy, or experimental therapy. Finally, there is an unmet need to fully elucidate the pathogenesis of CRC [67], which involves a variety of genetic, epigenetic, and environmental factors that affect the best treatment option for long-term benefit.

7.3. CRC Etiology: Hereditary vs. Sporadic

CRC exhibits a high degree of patient heterogeneity, but may be broadly grouped into two distinct classes: a less common, heritable subtype and a more frequent, "sporadic" subtype [66, 67]. Approximately 10-12% of CRC cases are inherited and associated with family history and genetic predisposition. Hereditary forms of CRC may be further subdivided into three broad groups: Familial Adenomatous Polyopsis (FAP), Hereditary Nonpolyopsis Colorectal Cancer (HNPCC), and a general inherited form of CRC that is distinct from FAP and HNPCC. FAP patients have germline mutations in the tumor suppressor APC and consequently, a 100% lifetime risk of developing CRC [68]. The FAP phenotype is distinct wherein the colon contains numerous adenomatous polyps, requiring resection of whole fragments of affected tissue, called a colectomy. FAP has three forms, which range in clinical severity: FAP, attenuated FAP and MYH-associated polyposis. Traditional FAP is the most severe cases in which APC is rendered nonfunctional. Attenuated FAP involves germline mutations in APC, which only slightly impair its tumor suppressor activity [68]. Finally, MYH-associated polyposis is an autosomal recessive form of FAP and involves mutations in the DNA repair enzyme MUTYH.

HNPCC, also known as Lynch Syndrome, is characterized by mutations in DNA mismatch repair genes that include MLH1, MSH2, MSH6, PMS1 and PMS2 [69]. There is an approximately 80% lifetime risk of developing CRC due to HNPCC. Like FAP, treatment

options usually involve surgical resection of affected tissue in combination with chemotherapy. The heritable subtype involves patients with a family history of CRC but who have germline mutations distinct from FAP and HNPCC [60]. Mutations in the EGF, RAS, PI3K/AKT pathways are commonly found in these patients. In contrast to these heritable forms, sporadic CRC is most common among patients and accounts for 80-85% of CRC cases. Spontaneous CRC involves somatic mutations in APC to develop sporadic adenomatous polyposis (SAP). While mutations in APC occur early in this cancer, secondary genetic, epigenetic and environmental factors cause alterations to propagate CRC development [67].

7.4. Colorectal Cancer Stages

Although colorectal cancer (CRC) displays a high degree of heterogeneity in molecular and functional assays, histopathological features are used to classify CRC into broad categories: Stages 0-IV (Figure 12). Stage 0 is defined as very early stage CRC in which the mucosal lining of the colon contains a high grade of dysplasia, called polyps, which are subsequently removed through polypectomy during a routine colonscopy to prevent cancer progression [66]. In Stage I CRC, polyps proliferate and develop into tumors that invade the mucosal layer of the colon. At this early stage, tumor and non-tumor tissues are usually well defined, making surgical resection of tumors a favorable option for treatment. Patient survival following surgery is greater than 90% at this stage [60]. Next, Stage II CRC involves invasion into the submucosal layer of the colon without spreading to neighboring lymph nodes. In particular, Stage II is subclassfied into IIA, IIB, and IIC depending on the extent of invasion into the submucosal layer, muscular layer, or beyond the colon wall, respectively. The most effective intervention at this stage again involves surgical resection of tumors and the survival rate is more than 80% [66].

Stage III CRC is defined by the spread of cancer throughout the wall of the colon in addition to the neighboring lymph nodes. Subclassification of this stage includes Stage IIIA,

IIIB, and IIIC, which depend on the extent of cancerous tissue in the inner, middle or outer layer of the colonic wall, respectively [70]. Due to the presence of cancer in the lymph nodes, surgical intervention must be supplemented with chemotherapy for effective treatment. The survival rate at this stage is between 30-60% [66]. Finally, the last stage of CRC, Stage IV, is characterized by metastasis of cancer to other organs, such as the liver, ovary, and intestines. A combinatorial therapeutic approach is required at this stage, which includes surgical resection of affected tissues, radiation, and chemotherapy. Despite the extensive therapeutic efforts, survival at this stage is only 3% [70].

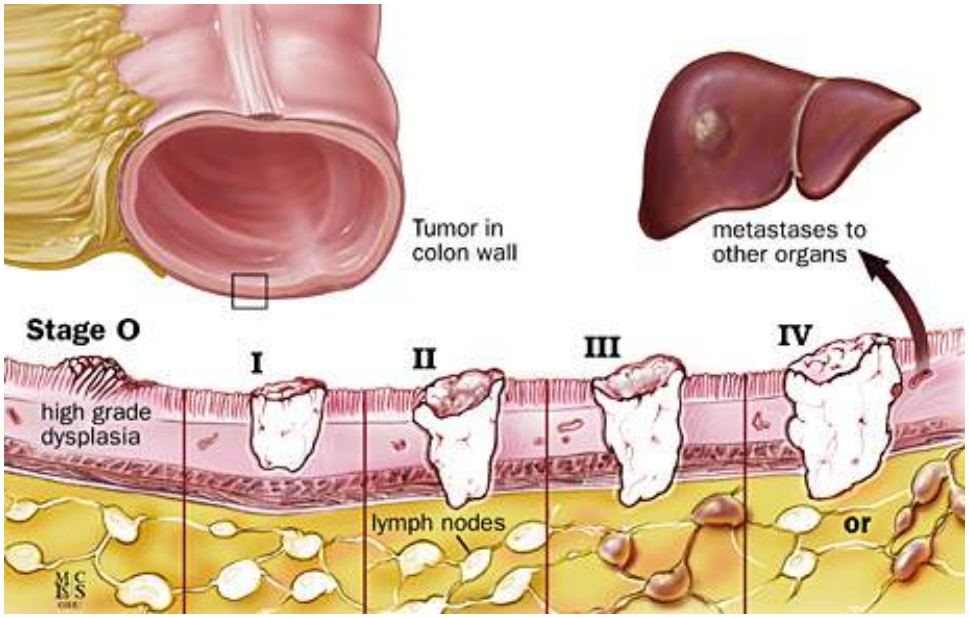

Figure 12. Stages 0-IV of Colorectal Cancer [70].

7.5. CRC Metastasis

The development of CRC-related metastasis is an intricate and highly selective process, depending on the characteristics of cancer initiating cells and the individual host environment. Metastatic disease is achieved by extravasation and detachment of cancer cells from the primary tumor, which spread through the bloodstream or lymph system to local and distant sites, generating secondary tumors. While colorectal cancers arise from the accumulation of genetic

and epigenetic alterations in the primary neoplasm, metastatic disease is shown to rely critically on the interaction between tumor cells and the microenvironment [71, 72].

Interestingly, the process of metastasis is relatively inefficient, but is extremely clinically significant in determining patient prognosis. Six models of CRC metastasis have been proposed, including the linear progression model, transient compartment model, fusion model, gene transfer model, early oncogenesis model, and genetic predisposition model [71]. In the linear progression hypothesis, a subset of cells from the primary neoplasm acquires full metastatic potential due to the accumulation of somatic mutations. Next, the transient compartment model suggests that all cells within the primary neoplasm have metastatic potential, but only some cells will be the source of secondary tumors due to epigenetic or positional restrictions [72]. The fusion model defines a metastatic cell as a hybrid between a detached, circulating tumor cell and a lymphoid cell [71]. Additionally, the gene transfer model suggests that the primary tumor contains cells that have metastatic potential due to the accumulation of genetic mutations. However, instead of specific cancer cells colonizing a secondary site, genetic material from these cells is released into the bloodstream and acquired by stem cells at the secondary site. These stem cells subsequently become metastatic and develop tumors. In contrast, the early oncogenesis model predicts that an early somatic mutation in the original neoplasm defines a pro-metastatic gene signature, and even the sites of potential metastasis [73]. Finally, in the genetic predisposition model, germline polymorphisms influence the metastatic potential of a primary neoplasm [71]. It is important to note that each hypothesis explains metastatic potential but has theoretical limitations, suggesting that a combination of these models contribute to CRC metastatic disease.

Clinical research studies have indicated that primary colorectal neoplasms preferentially develop metastatic tumors in specific organs, including the liver and the lungs [72]. Initiation of

metastasis begins with a gene expression signature that is related to cell motility, extracellular matrix degradation, angiogenesis and immune suppression. Next, genes associated with metastatic progression and virulence become dysregulated to form secondary tumors at specific sites [74]. The homing of CRC cells to the liver occurs via portal and systemic circulation. Liver-specific chemokine receptor-ligand interactions, such as CCR6-CCL20 and CXCR2-CXCL1, are in part, responsible for development of metatstatic disease in the liver [73]. Overall, approximately 10-20% of patients present with liver metastasis at the time of CRC detection, called synchronous metastasis. In contrast, approximately 20-50% of CRC cases with no metastatic tumors at the time of primary tumor resection will eventually develop liver metastasis within 5 years [74]. Liver metastasis begins with the formation of discrete nodules, which eventually grow and can replace much of the existing hepatic tissue. Due to the complexity and lack of control over hepatic metastases, treatment options are extremely limited. When the degree of metastasis replaces over 80% of liver tissue, causing physical obstruction, the patient will eventually develop terminal liver failure [74].

Additionally, CRC may also spread through systemic circulation to the lungs or via the lymphatic system to lymph nodes. Approximately 10-25% of CRC cases will metastasize to the lungs (inclusive of colonizing other tissues) [72]. Metastatic sites on the lung are usually discrete nodules that are capable of being treated with current therapies. In general, lung metastasis is not life-threatening and may even be asymptomatic in most cases [72, 74]. Overall, CRC metastasis is a complex phenomenon, involving a variety of factors. Due to the clinical significance in patient prognosis, many research efforts are dedicated to identifying targets for novel therapies.

7.6. CRC Tumorigenesis and Pathogenesis

A variety of key signaling pathways, as described earlier in Section 1.3, are dysregulated in CRC and contribute to tumorigenesis (Figure 13). Such pathways include WNT, NOTCH

signaling, TGF-β, and HEDGEHOG signaling. In addition, alterations occur in RAS, EGFR, PI(3)K/AKT signaling cascades that drive the progression of normal colonic epithelial cells into CRC [66]. WNT signaling is most notably disrupted through APC mutations in hereditary and sporadic CRC. Inactivation of APC leads to constitutive expression of WNT target genes. In addition, mutations have been found in β-CATENIN, preventing its degradation and leading to overexpression of WNT targets [30].

Murine studies of CRC have demonstrated that NOTCH signaling activity is high during tumorigenesis, but is attenuated during tumor progression in late stage CRC [75]. Indeed, suppression of NOTCH signaling achieved through γ-secretase inhibition induces differentiation of adenoma cells into goblet cells and targeted JAG-1 deletion decreases intestinal tumor volumes in $APC^{Min/+}$ mice [24, 76]. Additionally, evidence for the oncogenic potential of NOTCH signaling in human CRC exists due to the high expression of downstream effector genes in adenomas and early stage tumors compared to late stage adenocarcinomas [75, 77]. Studies of CRC tumors have indicated there is elevated expression of NOTCH ligands, suggesting activation of NOTCH is critical in tumorigenesis. In addition, research shows NOTCH activation is required for downstream RAS-mediated transformation of the colonic epithelium.

TGF-β signaling disruption has been implicated in CRC due to changes in key target genes involved in cell cycle checkpoints (p21, p27, p15) that lead to tumorigenesis. TGF-β signaling involves downstream transcription factors SMAD2 and SMAD4, which are mutated in up to 25% of CRC cases [78]. Many components of the TGF-β signaling cascade may be altered, promoting tumor growth; consequently, there is ongoing research to identify new molecular targets in this pathway for novel therapies.

HEDGEHOG signaling may be dysregulated, leading to overexpression of downstream target genes involved in cell proliferation. Research studies have shown high expression of

HEDGEHOG components: SHH, PATCHED, and SMOOTHENED in both adenomas and adenocarimomas found in the colon [79]. *In vitro* analysis of primary murine colonic epithelial cells shows that SHH promotes progression of CRC. Overall, excessive HEDGEHOG activity is associated with transformation and tumorigenesis [66, 79].

The RAS family is composed of monomeric guanine nucleotide-binding proteins (G proteins) that modulate signal transduction pathways involved cell cycle checkpoints and proliferation. RAS proteins activate kinases which phosphorylate key transcription factors that are implicated in various cancers, including MYC, RSK, MAPK, and FOS [80]. In approximately 20% of cancer cases, mutations in RAS genes leading to excessive signaling have been detected. Of the RAS proteins (HRAS, NRAS, KRAS4A, KRAS4B), over 40% of colorectal cancer contain KRAS mutations. Active mutant KRAS is conformationally stable and is constitutively active regardless of extracellular growth factors, such as EGF. Consequently, anti-EGFR chemotherapies are particularly ineffective in patients with mutant KRAS [80].

EGFR (epidermal growth factor) signaling is implicated in CRC tumorigenesis and progression. EGFR belongs to the HER (human EGF receptor) family, which consists of HER1, HER2, HER3, and HER4 and the following ligands: EGF, heregulin, amphiregulin, TGF-α, and heparin-binding EGF [65]. EGFR mediates target genes that regulate cell proliferation, angiogenesis, invasion and migration. Consequently, EGFR overexpression has been detected in over 90% of metastatic CRC and is associated with chemoresistance. Current therapies involve small molecule inhibitors and monoclonal EGFR antibodies to suppress tumor-associated angiogenesis and induce apoptosis in CRC [60].

The PI(3)K (phosphatidylinositol-3'-kinase) family contains twelve members that are activated by a variety of growth factors, integrins, hormones, vitamins and the MAPK pathway [81]. Downstream effector gene expression regulates tumorigensis, metabolism, migration, and

survival in many cancers, including CRC. Additionally, AKT signaling is dysregulated, affecting cell cycle inhibitors and apoptosis, leading to increased survival of tumor cells. Constitutive activation of PI(3)K/AKT signaling in CRC, as a result of accumulated mutations, is also associated with chemoresistance [65]. Therefore, research efforts are focused on isolating specific components within this cascade for novel therapeutic development.

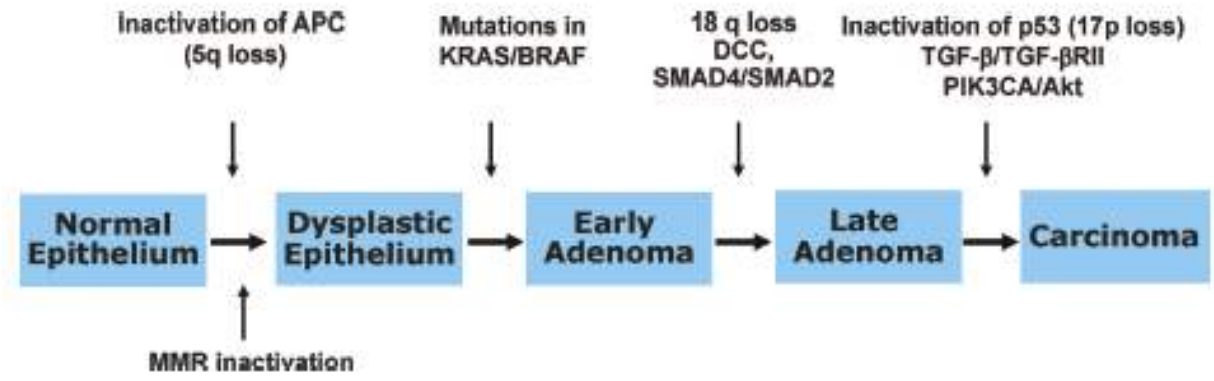

Figure 13. CRC Pathogenesis [66].

8. Colon Cancer Initiating Cells

8.1. Background

The identification of leukemic stem cells led to the characterization of cancer stem cells that exist in solid breast, brain and colorectal tumors. Such cancer stem cells represent a small subpopuluation (~1%) of heterogeneous tumors, possess stem cell-like features, and can initiate tumor growth [66]. Importantly, studies in solid CRC tumors indicate that genetic aberrations in this subfraction, called colon cancer initiating cells (CCICs) or colon cancer stem cells (CCSCs), are critical in tumorigenesis, metastasis, and CRC recurrence. Like their intestinal stem cell (ISC) counterparts, patient-derived CCICs are capable of symmetric self-renewal and asymmetric division in order to drive growth and differentiation within a tumor [82].

CCIC express surface markers, including CD44, CD133, CD166, and ALDH1 as well as

the intestinal stem cell markers: LGR5, EPHB2, and BMI1 [83, 84]. Serial passage studies of CCICs isolated from patients indicated that CD133+ CRC cells could generate heterogeneous tumors in immune-deficient mouse xenograft models and could be propagated *in vitro* in long term culture [85]. Interestingly, xenograft tumors derived from CCIC were able to recapitulate the histological, pathological and hierarchical features of the primary tumor unlike those derived from common immortalized CRC cell lines. In contrast, CRC-derived cells with a non-CCIC phenotype were unable to generate xenograft tumors and could not be sustained under laboratory conditions in culture [85].

8.2. Significance

CCIC contribute to cellular diversity and intra-tumoral heterogeneity in CRC, affecting chemoresistance and metastatic potential. Critical pathways in ISC homeostasis, such as WNT, NOTCH, TGF-B, and HEDHGEHOG signaling are elevated in CCICs, suggesting a role in chemoresistance. Previous reports showed that CCICs also have elevated DNA repair activity and anti-apoptotic mechanisms through gene expression analyses [84]. Indeed, CCIC not only have chemoresistant properties, but cytotoxic therapies enrich their relative number in CRC tumors. Consequently, the development of novel CRC therapeutic strategies relies on identifying targets to selectively inhibit CCIC growth and survival. Moreover it was shown that an intestinal stem cell (ISC) proliferative gene signature in CCIC was correlated with poor prognosis and CRC recurrence [13]. In contrast, a crypt differentiation gene signature in the primary tumor was associated with better patient outcome and survival. Interestingly, this ISC-like population in poorly differentiated CRC tumors does not express EPHB2; silencing of this WNT signaling molecule may contribute to loss of tumor architecture and enhanced invasive potential [13]. Furthermore, sequence analyses of LGR5, ALDH1, and CD44 in CRC patients indicated that polymorphisms in these genes may predict relapse following treatment with common

chemotherapy agent 5-flourouracil (5-FU) [86].

Specific CCIC markers have been reported to correlate with CRC metastasis. In particular, CCIC expressing a CD44 variant (CD44v6) are elevated in metastatic tissues compared to the primary tumor [87]. Unlike CD44v6- CCICs, CD44v6+ CCICs formed aggressive and large mestastatic lesions and are more dependent on PI(3)K signaling. Indeed, cancer-associated fibroblasts secrete cytokines, including hepatocyte growth factor, stromal-derived growth factor 1a, and osteopontin, which increase CD44v6 expression and downstream metastasis [87]. Targeted therapies against CD44v6 or PI(3)K inhibition reduced the frequency of CRC metastasis. Additionally, CD26 expression was shown to be associated with the epithelial-mesenchymal transition (EMT) phenotype in CCICs and metastasis [88]. Taken together, these findings suggest that specific CCIC populations may predict individual patient outcome, prognosis, and treatment response.

8.3. Regulation

Similar to normal ISCs, which rely on the crypt niche and stroma to provide signaling cues, CCICs rely on the hypoxic tumor microenvironment to stimulate key pathways, including WNT, BMP, and NOTCH. In particular, cancer-associated myofibroblasts secrete HGF to activate WNT signaling and maintain the CCIC phenotype. Constitutive WNT activation through mutations in the tumor suppressor APC or the effector β-CATENIN lead to excessive proliferation and enhanced tumorigenic potential of CCICs [82]. Additionally, mutations in SMAD4, suppressing BMP signaling have been identified in CCIC [89], promoting self-renewal and tumor growth.

The role of Notch signaling in normal ISC renewal and in CRC formation suggests that Notch signaling is an important regulator of CCICs [90]. Previous studies have indicated that cancer-associated endothelial cells secrete soluble JAGGED-1 to stimulate NOTCH signaling,

promoting CRC progression, chemoresistance, and metastasis. Indeed, we have previously shown that CCIC self-renewal and tumor formation critically rely on NOTCH activation and regulation [91, 92]. Furthermore, tumor-generated hypoxia maintains the CCIC phenotype through HIF-1a, BMI1 and NOTCH1 [93]. Due to the heterogeneity that exists among CCICs, however, the precise regulatory role of NOTCH signaling remains to be fully clarified.

A variety of other signaling pathways have been reported to be dysregulated in CCICs, suggesting that a combinatorial therapy based on theses targets may be promising. Specifically, HEDGEHOG signaling is excessively activated in CCIC, promoting self-renewal and CRC progression [94]. Additionally, loss of the tumor suppressor p53 activity enriches CCIC proliferative capacity and is correlated with late stage poorly differentiated CRC tumors. NF-κB and reactive oxygen species (ROS) production are elevated in CCICs and adenomas, suggesting a critical role in tumorigenesis [95]. CCICs have also been reported to overexpress inhibitor of DNA binding (ID) proteins (helix-loop-helix transcriptional regulators), which promote tumor growth and drug tolerance. The role of ID proteins was further confirmed in specific knockdown studies of ID1 and ID3, which suppressed CCIC self-renewal, decreased tumor formation, increased chemosensitivity to Oxaliplatin, and increased DNA damage to promote apoptosis [96]. Overall, CCICs represent a highly tumorigenic population characterized by aberrations in key stem cell and cancer signaling pathways.

8.4. miRNA Regulation and Asymmetric Division

Micro-RNAs (miRNAs) are endogenous, short, non-coding RNA fragments that typically bind to the 3’ untranslated region (UTR) of specific mRNA transcripts. This binding inhibits translation into downstream polypeptides and miRNA-bound RNA is subsequently degraded [97]. As a critical post-transcriptional regulator, miRNAs are frequently dysregulated in a variety of cancers. In the context of CRC, miRNAs have been shown to regulate the mode of CCIC

division and differentiation capacity through modulation of NOTCH and WNT signaling. CCICs may divide symmetrically to generate two CCIC daughters or asymmetrically to generate one CCIC and one differentiated daughter. Asymmetric division, which occurs at a frequency of approximately 20% in CCICs, contribute to cellular diversity within a tumor [92]. In particular, recent studies have identified that miR-34a inhibits NOTCH signaling, generating a NOTCH1 bimodal distribution, which dictates self-renewal or differentiation. Moreover, miR-34a creates differential NOTCH distribution and leads to CCIC fate asymmetry [92]. Using a fluorescent NOTCH reporter, previous investigations have demonstrated that miR-34a-regulated asymmetric division generates a $NOTCH^{high}$ daughter that expresses CCIC markers and a $NOTCH^{low}$ daughter, which expresses differentiation markers [98]. Interestingly, late stage CRC patients demonstrate a lack of miR-34a activity, leading to symmetric divisions to generate poorly differentiated tumors. Although rare under normal physiological conditions, asymmetric division may be activated in CCIC to promote carcinogenesis.

Previous studies have also shown that CCIC symmetric division is regulated by miR-146a, which targets cell fate determinant NUMB to stabilize β-CATENIN and promotes WNT signaling. Additionally, WNT activity upregulates the transcription factor SNAIL and miR-146a, creating a feedback loop. Overall, miR-146a promotes tumor growth and drug resistance to the chemotherapy agent cetuximab [99]. In addition, suppression of miR-200c is correlated with increased CCIC proliferation and metastasis [100]. MiRNAs are originally synthesized as long RNA precursors, which are then cleaved by a DICER complex into their mature form. Interestingly, DICER knockdown increases the relative proliferative capacity, EMT transition, and metastatic potential of CCICs [101]. Further research is required to elucidate other miRNAs, their upstream regulation, and their downstream targets that regulate CCIC behavior.

8.5. Targeted Therapies

Targeted therapies in CRC that focus specifically on CCICs are currently being explored in clinical research. Selective elimination of CCICs relies on biomarkers or essential signaling pathways. In particular, BMI1 inhibitors have been shown to decrease tumor volume and CCIC self-renewal capacity long-term [102]. Neutralizing anti-IL-4 antibody therapy promotes apoptosis in CCIC to shrink CRC tumors [103]. Additionally, small molecule antagonists of WNT signaling through COX-2 inhibition or anti-HGF monoclonal antibody therapy is associated with CCIC differentiation and apoptosis [66]. Finally, NOTCH signaling within CCIC may be selectively targeted through γ-secretase inhibition or antibodies against NOTCH ligands DLL-1 to prevent CCIC self-renewal [91].

It is important to note that CCICs from the same tumor are often treated as a homogenous population. However, different CCIC markers (CD26, CD44, CD133, CD166) correlate with various subtypes, each population differing in tumor initiation, long term self-renewal and metastatic potential [84]. Given the established plasticity that exists within CCIC, a more careful characterization to identify specific subpopulations is required. Additionally, similar to the interconversion process of slow and fast cycling ISCs, CCICs may be able to subvert this mechanism to provide CRCs with a growth and survival strategy, promoting self-renewal, tumorigenicity, and chemoresistance [82]. Chemotherapies that focus on targeting fast-proliferating cells and shrinking tumor volume may inadvertently enrich the slow-cycling CCIC population, giving rise to recurrence and chemoresistance. Therefore, the development of effective therapies in CRC must account for CCIC heterogeneity, targeting specific subfractions for elimination.

9. CRC Therapeutic Approaches

Current therapies for CRC include surgical intervention, radiation, chemotherapy and specific targeted therapies. The specific single or combinatorial approach employed in each case

depends on CRC stage, genetic factors, and individual patient factors.

9.1. Direct Intervention

Surgical resection of solid CRC tumors may be used as an independent approach during Stage 0 and Stage I cases with a low rate of recurrence in patients who have sporadic CRC [104]. Stage II CRC patients often require surgery in combination with chemotherapy or immunotherapy depending on the aggressiveness of cancer spread. Stage III CRC patients specifically require adjuvant therapy to improve prognosis and long-term outcome. Stage IV CRC patients often require a strict combinatorial approach [105], including surgical resection, chemotherapy, and targeted therapies.

Radiation therapy involves the use of high-energy particles, such as X-Rays, to eliminate cancer cells and consequently, shrink or ablate CRC tumors. Radiation may be used in a variety of cases and in combination with chemotherapy, called chemoradiation. The size and location of some CRC tumors may be difficult to remove with surgery immediately; consequently, radiation may be first used to decrease tumor volume and facilitate surgical resection [106]. Alternatively, radiation may be performed after surgery to ensure that remaining cancer cells are ablated, decreasing the chance of recurrence. Radiation is also an effective option of treatment for patients who are not healthy enough to withstand surgical excision of tumors. Finally, in cases of CRC metastasis where cancer has spread to multiple organs, radiation may be used to decrease tumors and associated symptoms, though with limited efficacy [106].

9.2. Chemotherapy

Chemotherapy to effectively treat CRC at different stages broadly includes 5-fluorouracil (5-FU), Oxaliplatin and Irinotecan formulations. 5-FU is the most commonly used CRC drug belonging to the flouropyrimidine class of compounds [60]. It is frequently administered in combination with folinic acid (Leucovorin), which serves as an adjuvant to improve patient

response and survival [107]. Due to variation in genetic background, affecing pharmacokinetics, membrane transport and metabolism of 5-FU, chemoresistance among CRC patients has been detected. Additionally, the platinum derivative, Oxaliplatin, is frequently used in CRC therapy, especially to treat late stage cancer. Oxaliplatin forms crosslinks in the DNA of tumor cells, suppressing DNA synthesis and subsequent cell proliferation [107]. Finally, Irintotecan is a cytotoxic topoisomerase II inhibitor, leading to suppression of DNA replication and transcription. Combinatorial drug formulations involving 5-fluorouracil/Leucovorin/Oxaliplatin (FOLFOX) or 5-fluorouracil/Leucovorin/Irinotecan (FOLFIRI) are the most effective chemotherapy regimens to treat advanced CRC and metastatic disease [107]. Research efforts are focused on genomic analyses of CRC patients to identify biomarkers of chemoresistance in order to predict whether patients will benefit from FOLFOX, FOLFIRI or an alternative chemotherapy regimen [108].

Importantly, adjuvant therapies also use tumor-associated antigens stimulate an immune response in CRC to provide significant patient benefit when used in combination with 5-FU, Oxaliplatin, or Leucovorin chemotherapy to treat Stage III CRC [105]. However, only a subset of Stage II CRC patients derives therapeutic benefit from adjuvant treatment based on specific molecular and high-risk histopathologic features [60]. Therefore, ongoing clinical research suggests that alternative therapies based on targeted delivery or nutritional supplements may be used in conjunction with chemotherapy and surgery for improving individual patient outcome.

9.3. Additional Therapies

9.3.1. Receptor Based Targeted Therapy

The development of colon cancer-specific therapeutics is based on targeted monoclonal antibody formulations [109]. Many classes of monoclonal antibodies target tumor-specific pathways, such as proliferation, invasion, and angiogenesis. A notable receptor-based therapy is

Panitumumab, a monoclonal antibody directed against EGFR, which increases patient prognosis by up to two years in advanced CRC when used in combination with conventional chemotherapy. Additional colon cancer cell targets include galectin-1 and galectin-3, a class of surface expressed lectins [109]. Finally, drug delivery vehicles, such as liposomes, nanoparticles, or polymeric carriers are employed in conjunction with CRC cell-specific targeting to improve the local release of drug formulations within the colon to selectively induce apoptosis in tumors.

9.3.2. Gene Therapy

Ongoing preclinical and clinical trial data indicate that gene therapy is a novel treatment approach that may be combined with existing methods to improve patient outcome and survival. However, further research is required to optimize gene delivery, targeting efficiency and anti-cancer potency. Various types of gene therapy strategies are being explored that modulate immune cell response or mutant gene expression to reduce CRC tumor incidence and volume. Specifically, immunogene therapies involve immune stimulation to generate a cell- or antibody-mediated response against tumor cells [110]. Additionally, since HLA class I surface makers are suppressed in over 60% of CRC cases, gene transfer to upregulate HLA expression generates a systemic anti-tumor response in clinical trials [60]. Next, cytokine gene therapy involving elevated IL-2 expression has been shown to increase CRC tumorigenicity to generate a T-cell response, inducing tumor-specific cytotoxicity with limited side effects [110]. Various expression vectors, such as cationic lipid constructs, adenoviral or retroviral gene transfer systems have been successfully used to elevate IL-2 expression with varied anti-tumor efficacy, suggesting that a combinational approach may be required.

Many CRC cells express the cell surface carcino-embyonic antigen (CEA) [111]. Therefore, a variety of viral vectors, derived from recombinant vaccinia or canary pox viruses, that contain human CEA are promising approaches to generate an anti-tumor response [110].

Gene therapies are also being developed on the basis of mutant gene correction in CRC. Specifically, gene correction in tumor suppressor genes, such as p53, or oncogenes, such as KRAS, delivered via adenoviral vectors induce a tumor-specific apoptotic response in preclinical animal models of CRC [110]. Finally, in cases of hereditary CRC, gene therapy is a promising option to address mutations in DNA mismatch repair genes in combination with demethylating agents to restore function [60].

9.3.3. Nutritional Supplements

Advancements in dietary and nutritional supplements have been shown to prevent CRC progression and reduce CRC mortality. Specifically, calcium and vitamin D consumption have been reported to be protective against some degree of CRC. Patients who regularly consume a high level of dietary calcium may reduce the incidence of polyps and carcinogenesis [60]. Additionally, curcumin, the main ingredient in the turmeric spice, was shown to prevent and slow the progression of CRC in rat models. Guar-gum tablets of curcumin have been developed for colon-specific delivery as a potential CRC treatment in patients [112]. Quercetin, an anti-oxidant commonly found in onions, reduced the number and size of colon polyps when administered to patients who had both sporadic or FAP CRC [112]. Finally, omega-3 fatty acids and fish oil supplements may reduce the risk of developing CRC [60].

10. Computational Insights in CRC

High-throughput analyses in systems biology are powerful tools to identify heterogeneity among cancers of the same tissue type and enable the discovery of novel biomarkers that may be useful in cancer prevention, screening, surveillance, and chemoresistance [113]. In the context of CRC, genomics, transcriptomics, proteomics, and metabolomics have each provided a unique dimensional understanding and simultaneous insight into critical processes, such as tumorigenesis, pathogenesis, and metastasis.

10.1. Genomics

Genomics involves the study of the complete nucleotide sequences, including coding and non-coding regions, in the chromosomes of cells that comprise CRC tumors. Whole genome sequencing of CRC revealed that a variety of mutations existed with high frequency, termed "gene mountains," while others were more sporadic, called "gene hills." Interestingly, this analysis indicated that the majority of mutations driving tumor development and cancer propagation were relatively infrequent gene hill members [114]. Moreover, the heterogeneity among different CRC tumors suggested that analysis on the basis of a small set of genes was insufficient for prognostic or therapeutic predictions. Subsequent computational analysis involving multiple CRC genomes compared sequences according to four classifications: nucleotide similarity, known protein-protein interaction, functional annotation, and signaling pathways. This integrated approach demonstrated that while cancer-driving genetic mutations were infrequent and heterogeneous among CRC tumors, they converged and occurred in shared molecular pathways [113]. Genomic aberrations in CRC commonly include point mutations in WNT, NOTCH, TGF-β, EGFR, RAS, and PI(3)K/AKT pathways as well as DNA mismatch repair networks [115]. Taken together, using a genomics-based approach, key signaling pathways were identified as cancer drivers rather than single genes.

10.2. Transcriptomics

Global gene expression analysis, called transcriptomics, allows for the simultaneous comparison evaluation of thousands of gene transcripts in order to provide information on the physiological status of tissues. In CRC, "gene signatures" are being developed in order to predict prognosis, drug response, metastasis, and relapse. Expression profiling, based on microarray data, is commonly used to study CRC at different stages of progression, including dysplasia to adenoma, adenocarcinoma, and metastasis [113]. From this approach, research investigations in

patient CRC specimens have identified a set of 50 differentially expressed genes in adenoma vs. adenocarcinoma and in CRC vs. normal tissue. Clinical CRC expression data has also confirmed the 'intermediate' histopathological stage of adenomas in the normal tissue-carcinoma spectrum, demonstrating modest changes in gene expression. Furthermore, using supervised computational clustering analysis, a specific set of genes was shown to correlate and potentially predict 5-year survival in late stage CRC patients [116].

Microarray analysis of CRC specimens from patient biopsies prior to surgery has the ability to inform precise tumor classification, prognosis, and treatment prediction. In particular, patients found to posses a specific 23-gene signature indicative of CRC recurrence were candidates for receiving adjuvant chemotherapy to improve their individual survival rate [116]. Beyond screening using traditional mutations in KRAS and p53 as well as 18q chromosomal loss, global gene expression provides significantly more sensitivity and accuracy [113]. However, due to CRC intra-tumoral heterogeneity, multiple patient biopsies must be analyzed for a more complete physiological understanding. Overall, differentially expressed genes have been identified among CRC adenoma, adenocarcinoma and metastasis, which included cell cycle control, survival, DNA damage repair, immune evasion, and cytoskeletal remodeling genes [113, 116]. These data reflect inherent changes in the primary biological processes dominating each CRC stages and are informative in developing targeted therapies.

10.3. Proteomics

In studying CRC, proteomics involves analysis of the complete protein profile expressed by cancer cells, including peptide post-translational modifications, mapping and quantification. Liquid chromatography and mass spectrometry (LC-MS) approaches are commonly integrated with protein informatics to generate robust datasets [114]. Proteomics-based studies are used to non-invasively analyze patient sera in order to identify novel biomarkers for screening CRC in

different stages. Current screening relies on CEA expression, which only has a sensitivity rate of 30-40% in detection of early stage CRC [113]. However, by comparing sera from over 100 CRC patients, proteomics have advanced CRC detection based on several proteins from the immune complement system: C3a-des-arg (an isoform of C3a anaphylatoxin), α1-antitrypsin and transferrin. In addition, collapsin response mediator protein-2 (CRMP-2) was identified as a suitable CRC biomarker, which increased the sensitivity rate to approximately 77.5% when used in conjunction with CEA [113]. Overall, further studies that utilize a proteomics approach will be valuable in addressing CRC heterogeneity, increasing the robustness of newly identified biomarkers for screening and prognosis.

10.4. Metabolomics

Metabolomics involves a sensitive, global analysis of the metabolic profile of CRC tissues. This approach relies on identifying metabolites, which are small molecules that participate in anabolic, catabolic, absorptive, transport, and detoxifying processes and contribute to growth and tissue maintenance [113]. Clinical metabolite profiling of surgically resected CRC tissues are informative in understanding how global metabolic pathways may behave at different stages. Previous research has identified approximately 80 metabolites related to the TCA cycle or amino acid purine synthesis that may distinguish CRC from normal tissue [113]. Importantly, CRC tissues have a discriminatory panel of metabolites related to glucose uptake and lactate conversion, suggesting that these cancer cells rely more on glycolysis for respiration compared to normal tissue, which utilizes TCA cycle-dependent oxidative phosphorylation. These findings suggest that a more in-depth analysis of tumor metabolism is useful in identifying new targets to effectively inhibit cancer growth and progression [113]. Overall, this cost-effective, non-invasive, high-throughput analysis enables a comparative understanding of many CRC patient tissues. Upon integration with different "-omics" approaches, metabolite profiling is a power tool

to correlate changes in gene structure, expression, and protein modifications in order to generate complex pathway maps for CRC with diagnostic and prognostic significance.

11. Summary

The study of stem cell regulation in intestinal and colonic tissues is an area of significant focus within the scientific community, providing mechanistic insight into biological process and offering translational clinical potential. The remaining chapters will address the contribution of NOTCH signaling in maintaining the stem cell niche by modulating the mode of stem cell division and receptor-ligand interactions for cell-cell communication. Furthermore, we examine NOTCH-mediated spatiotemporal recovery of the ISC niche following single cell ablation. Finally, we demonstrate that elevated NOTCH signaling exists under conditions of physiological stress and in CCICs, promoting tumorigenic potential of the intestinal epithelium. Overall, our research highlights the underlying complexities of NOTCH signaling as an essential pathway to maintain intestinal homeostasis and may inspire development of novel CRC therapeutic strategies.

REFERENCES

1. Costanzo, L.S., *Physiology*. 2nd ed. 2002, Philadelphia: Saunders. xi, 451 p.
2. Clevers, H., *The intestinal crypt, a prototype stem cell compartment.* Cell, 2013. **154**(2): p. 274-84.
3. Barker, N., *Adult intestinal stem cells: critical drivers of epithelial homeostasis and regeneration.* Nat Rev Mol Cell Biol, 2014. **15**(1): p. 19-33.
4. Barker, N., et al., *Identification of stem cells in small intestine and colon by marker gene Lgr5.* Nature, 2007. **449**(7165): p. 1003-7.
5. de Lau, W., et al., *Peyer's patch M cells derived from Lgr5(+) stem cells require SpiB and are induced by RankL in cultured "miniguts".* Mol Cell Biol, 2012. **32**(18): p. 3639-47.
6. Snippert, H.J., et al., *Intestinal crypt homeostasis results from neutral competition between symmetrically dividing Lgr5 stem cells.* Cell, 2010. **143**(1): p. 134-44.
7. van der Flier, L.G., et al., *Transcription factor achaete scute-like 2 controls intestinal stem cell fate.* Cell, 2009. **136**(5): p. 903-12.
8. VanDussen, K.L., et al., *Notch signaling modulates proliferation and differentiation of intestinal crypt base columnar stem cells.* Development, 2012. **139**(3): p. 488-97.
9. van der Flier, L.G., et al., *OLFM4 is a robust marker for stem cells in human intestine and marks a subset of colorectal cancer cells.* Gastroenterology, 2009. **137**(1): p. 15-7.

10. Itzkovitz, S., et al., *Single-molecule transcript counting of stem-cell markers in the mouse intestine.* Nat Cell Biol, 2012. **14**(1): p. 106-14.
11. Munoz, J., et al., *The Lgr5 intestinal stem cell signature: robust expression of proposed quiescent '+4' cell markers.* EMBO J, 2012. **31**(14): p. 3079-91.
12. Snippert, H.J., et al., *Prominin-1/CD133 marks stem cells and early progenitors in mouse small intestine.* Gastroenterology, 2009. **136**(7): p. 2187-2194 e1.
13. Merlos-Suarez, A., et al., *The intestinal stem cell signature identifies colorectal cancer stem cells and predicts disease relapse.* Cell Stem Cell, 2011. **8**(5): p. 511-24.
14. Jung, P., et al., *Isolation and in vitro expansion of human colonic stem cells.* Nat Med, 2011. **17**(10): p. 1225-7.
15. Yan, K.S., et al., *The intestinal stem cell markers Bmi1 and Lgr5 identify two functionally distinct populations.* Proc Natl Acad Sci U S A, 2012. **109**(2): p. 466-71.
16. Takeda, N., et al., *Interconversion between intestinal stem cell populations in distinct niches.* Science, 2011. **334**(6061): p. 1420-4.
17. Montgomery, R.K., et al., *Mouse telomerase reverse transcriptase (mTert) expression marks slowly cycling intestinal stem cells.* Proc Natl Acad Sci U S A, 2011. **108**(1): p. 179-84.
18. Powell, A.E., et al., *The pan-ErbB negative regulator Lrig1 is an intestinal stem cell marker that functions as a tumor suppressor.* Cell, 2012. **149**(1): p. 146-58.
19. Sangiorgi, E. and M.R. Capecchi, *Bmi1 is expressed in vivo in intestinal stem cells.* Nat Genet, 2008. **40**(7): p. 915-20.
20. Breault, D.T., et al., *Generation of mTert-GFP mice as a model to identify and study tissue progenitor cells.* Proc Natl Acad Sci U S A, 2008. **105**(30): p. 10420-5.
21. Tian, H., et al., *A reserve stem cell population in small intestine renders Lgr5-positive cells dispensable.* Nature, 2011. **478**(7368): p. 255-9.
22. de Lau, W., et al., *Lgr5 homologues associate with Wnt receptors and mediate R-spondin signalling.* Nature, 2011. **476**(7360): p. 293-7.
23. Carmon, K.S., et al., *LGR5 interacts and cointernalizes with Wnt receptors to modulate Wnt/beta-catenin signaling.* Mol Cell Biol, 2012. **32**(11): p. 2054-64.
24. van Es, J.H., et al., *Notch/gamma-secretase inhibition turns proliferative cells in intestinal crypts and adenomas into goblet cells.* Nature, 2005. **435**(7044): p. 959-63.
25. Gerbe, F., C. Legraverend, and P. Jay, *The intestinal epithelium tuft cells: specification and function.* Cell Mol Life Sci, 2012. **69**(17): p. 2907-17.
26. Gerbe, F., et al., *Distinct ATOH1 and Neurog3 requirements define tuft cells as a new secretory cell type in the intestinal epithelium.* J Cell Biol, 2011. **192**(5): p. 767-80.
27. Fre, S., et al., *Notch signals control the fate of immature progenitor cells in the intestine.* Nature, 2005. **435**(7044): p. 964-8.
28. Pellegrinet, L., et al., *Dll1- and dll4-mediated notch signaling are required for homeostasis of intestinal stem cells.* Gastroenterology, 2011. **140**(4): p. 1230-1240 e1-7.
29. Riccio, O., et al., *Loss of intestinal crypt progenitor cells owing to inactivation of both Notch1 and Notch2 is accompanied by derepression of CDK inhibitors p27Kip1 and p57Kip2.* EMBO Rep, 2008. **9**(4): p. 377-83.
30. Clevers, H. and R. Nusse, *Wnt/beta-catenin signaling and disease.* Cell, 2012. **149**(6): p. 1192-205.
31. Carmon, K.S., et al., *R-spondins function as ligands of the orphan receptors LGR4 and LGR5 to regulate Wnt/beta-catenin signaling.* Proc Natl Acad Sci U S A, 2011. **108**(28): p. 11452-7.

32. Haegebarth, A. and H. Clevers, *Wnt signaling, lgr5, and stem cells in the intestine and skin.* Am J Pathol, 2009. **174**(3): p. 715-21.
33. Kosinski, C., et al., *Gene expression patterns of human colon tops and basal crypts and BMP antagonists as intestinal stem cell niche factors.* Proc Natl Acad Sci U S A, 2007. **104**(39): p. 15418-23.
34. Noah, T.K. and N.F. Shroyer, *Notch in the intestine: regulation of homeostasis and pathogenesis.* Annu Rev Physiol, 2013. **75**: p. 263-88.
35. Borggrefe, T. and F. Oswald, *The Notch signaling pathway: transcriptional regulation at Notch target genes.* Cell Mol Life Sci, 2009. **66**(10): p. 1631-46.
36. Schroder, N. and A. Gossler, *Expression of Notch pathway components in fetal and adult mouse small intestine.* Gene Expr Patterns, 2002. **2**(3-4): p. 247-50.
37. Stanger, B.Z., et al., *Direct regulation of intestinal fate by Notch.* Proc Natl Acad Sci U S A, 2005. **102**(35): p. 12443-8.
38. Lopez-Arribillaga, E., et al., *Bmi1 regulates murine intestinal stem cell proliferation and self-renewal downstream of Notch.* Development, 2015. **142**(1): p. 41-50.
39. Zhang, J. and L. Li, *BMP signaling and stem cell regulation.* Dev Biol, 2005. **284**(1): p. 1-11.
40. Auclair, B.A., et al., *Bone morphogenetic protein signaling is essential for terminal differentiation of the intestinal secretory cell lineage.* Gastroenterology, 2007. **133**(3): p. 887-96.
41. Buller, N.V., et al., *Hedgehog signaling and maintenance of homeostasis in the intestinal epithelium.* Physiology (Bethesda), 2012. **27**(3): p. 148-55.
42. Sato, T., et al., *Single Lgr5 stem cells build crypt-villus structures in vitro without a mesenchymal niche.* Nature, 2009. **459**(7244): p. 262-5.
43. Krausova, M. and V. Korinek, *Wnt signaling in adult intestinal stem cells and cancer.* Cell Signal, 2014. **26**(3): p. 570-9.
44. Lopez-Garcia, C., et al., *Intestinal stem cell replacement follows a pattern of neutral drift.* Science, 2010. **330**(6005): p. 822-5.
45. Koo, B.K., et al., *Controlled gene expression in primary Lgr5 organoid cultures.* Nat Methods, 2012. **9**(1): p. 81-3.
46. Batlle, E., et al., *Beta-catenin and TCF mediate cell positioning in the intestinal epithelium by controlling the expression of EphB/ephrinB.* Cell, 2002. **111**(2): p. 251-63.
47. Simons, B.D. and H. Clevers, *Stem cell self-renewal in intestinal crypt.* Exp Cell Res, 2011. **317**(19): p. 2719-24.
48. Simons, B.D. and H. Clevers, *Strategies for homeostatic stem cell self-renewal in adult tissues.* Cell, 2011. **145**(6): p. 851-62.
49. Itzkovitz, S., et al., *Optimality in the development of intestinal crypts.* Cell, 2012. **148**(3): p. 608-19.
50. Voog, J. and D.L. Jones, *Stem cells and the niche: a dynamic duo.* Cell Stem Cell, 2010. **6**(2): p. 103-15.
51. Watt, F.M. and B.L. Hogan, *Out of Eden: stem cells and their niches.* Science, 2000. **287**(5457): p. 1427-30.
52. Okajima, T. and K.D. Irvine, *Regulation of notch signaling by o-linked fucose.* Cell, 2002. **111**(6): p. 893-904.
53. Moloney, D.J., et al., *Fringe is a glycosyltransferase that modifies Notch.* Nature, 2000. **406**(6794): p. 369-75.

54. Chen, J., D.J. Moloney, and P. Stanley, *Fringe modulation of Jagged1-induced Notch signaling requires the action of beta 4galactosyltransferase-1.* Proc Natl Acad Sci U S A, 2001. **98**(24): p. 13716-21.
55. Harris, R.J. and M.W. Spellman, *O-linked fucose and other post-translational modifications unique to EGF modules.* Glycobiology, 1993. **3**(3): p. 219-24.
56. Serth, K., et al., *O-fucosylation of DLL3 is required for its function during somitogenesis.* PLoS One, 2015. **10**(4): p. e0123776.
57. Johnston, S.H., et al., *A family of mammalian Fringe genes implicated in boundary determination and the Notch pathway.* Development, 1997. **124**(11): p. 2245-54.
58. Hicks, C., et al., *Fringe differentially modulates Jagged1 and Delta1 signalling through Notch1 and Notch2.* Nat Cell Biol, 2000. **2**(8): p. 515-20.
59. Schottenfeld, D., J.L. Beebe-Dimmer, and F.D. Vigneau, *The epidemiology and pathogenesis of neoplasia in the small intestine.* Ann Epidemiol, 2009. **19**(1): p. 58-69.
60. Gulbake, A., et al., *Insight to drug delivery aspects for colorectal cancer.* World J Gastroenterol, 2016. **22**(2): p. 582-99.
61. Kytola, S., et al., *Comparative genomic hybridization identifies loss of 18q22-qter as an early and specific event in tumorigenesis of midgut carcinoids.* Am J Pathol, 2001. **158**(5): p. 1803-8.
62. Severson, R.K., et al., *Increasing incidence of adenocarcinomas and carcinoid tumors of the small intestine in adults.* Cancer Epidemiol Biomarkers Prev, 1996. **5**(2): p. 81-4.
63. Kuppers, R., *Mechanisms of B-cell lymphoma pathogenesis.* Nat Rev Cancer, 2005. **5**(4): p. 251-62.
64. Katz, S.C. and R.P. DeMatteo, *Gastrointestinal stromal tumors and leiomyosarcomas.* J Surg Oncol, 2008. **97**(4): p. 350-9.
65. McLeod, H.L. and G.I. Murray, *Tumour markers of prognosis in colorectal cancer.* Br J Cancer, 1999. **79**(2): p. 191-203.
66. Saif, M.W. and E. Chu, *Biology of colorectal cancer.* Cancer J, 2010. **16**(3): p. 196-201.
67. Stigliano, V., et al., *Early-onset colorectal cancer: a sporadic or inherited disease?* World J Gastroenterol, 2014. **20**(35): p. 12420-30.
68. Patel, S.G. and D.J. Ahnen, *Familial colon cancer syndromes: an update of a rapidly evolving field.* Curr Gastroenterol Rep, 2012. **14**(5): p. 428-38.
69. Peltomaki, P., *Role of DNA mismatch repair defects in the pathogenesis of human cancer.* J Clin Oncol, 2003. **21**(6): p. 1174-9.
70. Kumar, V. and S.L. Robbins, *Robbins basic pathology*. 8th ed. 2007, Philadelphia, PA: Saunders/Elsevier. xiv, 946 p.
71. Hunter, K.W., N.P. Crawford, and J. Alsarraj, *Mechanisms of metastasis.* Breast Cancer Res, 2008. **10 Suppl 1**: p. S2.
72. Fakih, M.G., *Metastatic colorectal cancer: current state and future directions.* J Clin Oncol, 2015. **33**(16): p. 1809-24.
73. Yamasaki, M., et al., *The gene expression profile represents the molecular nature of liver metastasis in colorectal cancer.* Int J Oncol, 2007. **30**(1): p. 129-38.
74. Beauchemin, N. and J. Huot, *Metastasis of colorectal cancer*, in *Cancer metastasis - biology and treatment,*. 2010, Springer,: Dordrecht ; New York. p. 1 online resource.
75. Fre, S., et al., *Notch and Wnt signals cooperatively control cell proliferation and tumorigenesis in the intestine.* Proc Natl Acad Sci U S A, 2009. **106**(15): p. 6309-14.
76. Rodilla, V., et al., *Jagged1 is the pathological link between Wnt and Notch pathways in colorectal cancer.* Proc Natl Acad Sci U S A, 2009. **106**(15): p. 6315-20.

77. Reedijk, M., et al., *Activation of Notch signaling in human colon adenocarcinoma.* Int J Oncol, 2008. **33**(6): p. 1223-9.
78. Massague, J., S.W. Blain, and R.S. Lo, *TGFbeta signaling in growth control, cancer, and heritable disorders.* Cell, 2000. **103**(2): p. 295-309.
79. Monzo, M., et al., *Sonic hedgehog mRNA expression by real-time quantitative PCR in normal and tumor tissues from colorectal cancer patients.* Cancer Lett, 2006. **233**(1): p. 117-23.
80. Siddiqui, A.D. and B. Piperdi, *KRAS mutation in colon cancer: a marker of resistance to EGFR-I therapy.* Ann Surg Oncol, 2010. **17**(4): p. 1168-76.
81. Fearon, E.R. and B. Vogelstein, *A genetic model for colorectal tumorigenesis.* Cell, 1990. **61**(5): p. 759-67.
82. Clevers, H., *The cancer stem cell: premises, promises and challenges.* Nat Med, 2011. **17**(3): p. 313-9.
83. Ricci-Vitiani, L., et al., *Identification and expansion of human colon-cancer-initiating cells.* Nature, 2007. **445**(7123): p. 111-5.
84. Dalerba, P., et al., *Phenotypic characterization of human colorectal cancer stem cells.* Proc Natl Acad Sci U S A, 2007. **104**(24): p. 10158-63.
85. O'Brien, C.A., et al., *A human colon cancer cell capable of initiating tumour growth in immunodeficient mice.* Nature, 2007. **445**(7123): p. 106-10.
86. Gerger, A., et al., *Common cancer stem cell gene variants predict colon cancer recurrence.* Clin Cancer Res, 2011. **17**(21): p. 6934-43.
87. Todaro, M., et al., *CD44v6 is a marker of constitutive and reprogrammed cancer stem cells driving colon cancer metastasis.* Cell Stem Cell, 2014. **14**(3): p. 342-56.
88. Pang, R., et al., *A subpopulation of CD26+ cancer stem cells with metastatic capacity in human colorectal cancer.* Cell Stem Cell, 2010. **6**(6): p. 603-15.
89. Joudeh, J., et al., *Novel antineoplastics targeting genetic changes in colorectal cancer.* Adv Exp Med Biol, 2013. **779**: p. 1-34.
90. Qiao, L. and B.C. Wong, *Role of Notch signaling in colorectal cancer.* Carcinogenesis, 2009. **30**(12): p. 1979-86.
91. Sikandar, S.S., et al., *NOTCH signaling is required for formation and self-renewal of tumor-initiating cells and for repression of secretory cell differentiation in colon cancer.* Cancer Res, 2010. **70**(4): p. 1469-78.
92. Bu, P., et al., *A microRNA miR-34a-regulated bimodal switch targets Notch in colon cancer stem cells.* Cell Stem Cell, 2013. **12**(5): p. 602-15.
93. Yeung, T.M., S.C. Gandhi, and W.F. Bodmer, *Hypoxia and lineage specification of cell line-derived colorectal cancer stem cells.* Proc Natl Acad Sci U S A, 2011. **108**(11): p. 4382-7.
94. Varnat, F., et al., *Human colon cancer epithelial cells harbour active HEDGEHOG-GLI signalling that is essential for tumour growth, recurrence, metastasis and stem cell survival and expansion.* EMBO Mol Med, 2009. **1**(6-7): p. 338-51.
95. Myant, K.B., et al., *ROS production and NF-kappaB activation triggered by RAC1 facilitate WNT-driven intestinal stem cell proliferation and colorectal cancer initiation.* Cell Stem Cell, 2013. **12**(6): p. 761-73.
96. O'Brien, C.A., et al., *ID1 and ID3 regulate the self-renewal capacity of human colon cancer-initiating cells through p21.* Cancer Cell, 2012. **21**(6): p. 777-92.
97. Pauli, A., J.L. Rinn, and A.F. Schier, *Non-coding RNAs as regulators of embryogenesis.* Nat Rev Genet, 2011. **12**(2): p. 136-49.

98. Bu, P., et al., *Asymmetric division: a marker for cancer stem cells in early stage tumors?* Oncotarget, 2013. **4**(7): p. 950-1.
99. Hwang, W.L., et al., *MicroRNA-146a directs the symmetric division of Snail-dominant colorectal cancer stem cells.* Nat Cell Biol, 2014. **16**(3): p. 268-80.
100. Lu, Y.X., et al., *Regulation of colorectal carcinoma stemness, growth, and metastasis by an miR-200c-Sox2-negative feedback loop mechanism.* Clin Cancer Res, 2014. **20**(10): p. 2631-42.
101. Iliou, M.S., et al., *Impaired DICER1 function promotes stemness and metastasis in colon cancer.* Oncogene, 2014. **33**(30): p. 4003-15.
102. Kreso, A., et al., *Self-renewal as a therapeutic target in human colorectal cancer.* Nat Med, 2014. **20**(1): p. 29-36.
103. Todaro, M., et al., *Colon cancer stem cells dictate tumor growth and resist cell death by production of interleukin-4.* Cell Stem Cell, 2007. **1**(4): p. 389-402.
104. Ahmed, S., et al., *Advances in the management of colorectal cancer: from biology to treatment.* Int J Colorectal Dis, 2014. **29**(9): p. 1031-42.
105. Wasserberg, N., *Interval to surgery after neoadjuvant treatment for colorectal cancer.* World J Gastroenterol, 2014. **20**(15): p. 4256-62.
106. Wilhelmsen, M., et al., *Determinants of recurrence after intended curative resection for colorectal cancer.* Scand J Gastroenterol, 2014. **49**(12): p. 1399-408.
107. Chourasia, M.K. and S.K. Jain, *Pharmaceutical approaches to colon targeted drug delivery systems.* J Pharm Pharm Sci, 2003. **6**(1): p. 33-66.
108. Chan, S.K., et al., *Meta-analysis of colorectal cancer gene expression profiling studies identifies consistently reported candidate biomarkers.* Cancer Epidemiol Biomarkers Prev, 2008. **17**(3): p. 543-52.
109. Patel, M., T. Shah, and A. Amin, *Therapeutic opportunities in colon-specific drug-delivery systems.* Crit Rev Ther Drug Carrier Syst, 2007. **24**(2): p. 147-202.
110. Palmer, D.H., M.J. Chen, and D.J. Kerr, *Gene therapy for colorectal cancer.* Br Med Bull, 2002. **64**: p. 201-25.
111. Shah, R., et al., *Biomarkers for early detection of colorectal cancer and polyps: systematic review.* Cancer Epidemiol Biomarkers Prev, 2014. **23**(9): p. 1712-28.
112. Cruz-Correa, M., et al., *Combination treatment with curcumin and quercetin of adenomas in familial adenomatous polyposis.* Clin Gastroenterol Hepatol, 2006. **4**(8): p. 1035-8.
113. Nambiar, P.R., R.R. Gupta, and V. Misra, *An "Omics" based survey of human colon cancer.* Mutat Res, 2010. **693**(1-2): p. 3-18.
114. Schweiger, M.R., et al., *Genomics and epigenomics of colorectal cancer.* Wiley Interdiscip Rev Syst Biol Med, 2013. **5**(2): p. 205-19.
115. Hong, Y., et al., *A 'metastasis-prone' signature for early-stage mismatch-repair proficient sporadic colorectal cancer patients and its implications for possible therapeutics.* Clin Exp Metastasis, 2010. **27**(2): p. 83-90.
116. Bertucci, F., et al., *Gene expression profiling of colon cancer by DNA microarrays and correlation with histoclinical parameters.* Oncogene, 2004. **23**(7): p. 1377-91.

CHAPTER 2

NOTCH signaling regulates asymmetric division of fast- and slow-cycling colon cancer initiating cells and intestinal stem cells

Contributors:

(Srinivasan, Tara; Walters, Jewell; Bu, Pengcheng; Than, Elaine B.; Tung, Kuei-Ling; Chen, Kai-Yuan; Panarelli, Nicole; Milsom, Jeff; Augenlict, Leonard; Shen, Xiling; Lipkin, Steven M.)

PREFACE

Colorectal cancer cells with stem-like properties, referred to as colon cancer initiating cells (CCICs), have high tumorigenic potential. While CCICs can differentiate to promote cellular heterogeneity, it remains unclear whether CCICs within a tumor contain distinct subpopulations. Here we describe the co-existence of fast- and slow-cycling CCICs, which can undergo asymmetric division to generate each other, highlighting CCIC plasticity and inter-convertibility. Fast-cycling CCICs express markers such as LGR5 and CD133, and depend on MYC for their proliferation, whereas slow-cycling CCICs express markers such as BMI1 and hTERT, and are independent of MYC. NOTCH signaling promotes asymmetric division, and regulates the balance between these two populations. Furthermore, NOTCH signaling plays a similar role in the mouse intestine, and can activate asymmetric division when the tissue is under stress. Overall, these data provide insights into CCIC heterogeneity and plasticity, demonstrating a direct interconversion mechanism between slow- and fast-cycling CCICs.

INTRODUCTION

Colorectal cancer (CRC) is the second leading cause of cancer death. One important insight in recent years is the recognition that CRCs exhibit a high level of intratumoral cellular heterogeneity. Even genetically identical CRC cells from the same tumor typically demonstrate significant variability with regard to proliferation, invasive potential and chemoresistance [1-4]. This has also led to an appreciation that CRC cellular diversity can be hierarchically organized, with growth driven by a subset of cells with stem-like properties, referred to as colon cancer initiating cells (CCICs) or stem cells (CCSCs) [5-8]. Consistent with a role for CCIC in tumor progression, a ‘‘stemness’’ signature has been shown to predict CRC relapse [8, 9]. CCICs have been associated with markers including CD133, LGR5, BMI1, CD44, ALDH1, etc [1, 8, 10, 11]. LGR5, a co-receptor for the WNT ligand RSPO1, is also a marker for fast-cycling intestinal and

colon stem cells [12-15], although LGR5 expression is not strongly associated with CRC prognosis [16]. High expression of BMI1 is associated with poor survival and CRC recurrence [17-20], and targeted anti-BMI1 therapy inhibits tumor xenograft growth and self-renewal [1].

CCIC can divide symmetrically to generate two CCIC daughters or asymmetrically to generate one CCIC daughter and one more differentiated daughter [10, 21, 22]. Disruption of asymmetric division can alter the balance between self-renewal and differentiation in CCIC and impact tumor growth. Similar behavior has also been reported in other types of cancer stem cells [23-25]. Differential NOTCH activity can lead to asymmetric CCIC division [21]. In mice, studies of CRC have demonstrated the NOTCH signaling activity is high during tumorigenesis [26]. Suppression of NOTCH signaling induces differentiation of adenoma cells into goblet cells and targeted JAG-1 deletion decreases intestinal tumor volumes in $APC^{Min/+}$ mice [27, 28]. Evidence for the oncogenic potential of NOTCH signaling in human CRC exists due to the high expression of downstream effector genes in adenomas and early stage tumors compared to late stage adenocarcinomas, suggesting NOTCH activation is important for tumorigenesis [26, 29]. Furthermore, NOTCH also promotes CRC chemoresistance [30] and metastasis [31, 32].

Here, we demonstrate co-existence of fast- and slow-cycling CCIC populations in the same tumors. Fast-cycling CCICs express LGR5, CD133, CD44, etc, while slow-cycling CCICs express BMI1, hTERT, HOPX, etc. The two populations can directly interconvert via asymmetric division, which simultaneously generates a fast-cycling daughter cell and a slow-cycling daughter cell. Fast-cycling CCICs depend on MYC for proliferation, but slow-cycling CCICs are less dependent on MYC. NOTCH signaling promotes such asymmetric division and regulates the balance between the two CCIC populations. In mouse intestinal crypts, NOTCH signaling also regulates the balance between proliferative and quiescent stem cells, and activates asymmetric division when the tissue is under stress. Maintaining both fast- and slow-cycling

stem cells may provide a growth and survival strategy for neoplastic tissue.

RESULTS

Asymmetric BMI1+/LGR5+ cell pairs in CRC

Histopathological review of stage I through IV primary CRC tumors recurrently identified a distinctive paired cell morphology: a cell with a long, slender nucleus is situated adjacent to another cell with a smaller, rounded nucleus (Fig. 1a). To understand this paired cell morphology more precisely, we used immunofluorescence (IF) microscopy to study patient normal colon and CRC specimens. IF revealed the co-localization of a larger BMI1+ cell with a slender nucleus adjacent to a smaller, rounder LGR5+ cell. Multiple BMI1+/LGR5+ pairs could often be detected in the same magnification field in CRC specimens of more advanced stages (Fig. 1b). We next examined whether BMI1+/LGR5+ cell pairs could directly result from asymmetric cell division, using α-TUBULIN staining for mitotic spindle labeling and Ki67 staining as a proliferation marker (Fig. 1c). In multiple BMI1+/LGR5+ pairs present in primary CRC tissue, α-TUBULIN staining is consistent with the telophase (final phase of mitosis) configuration of microtubules – the midbody at the division plane during cytokiensis and asters at the poles. Furthermore, Ki67 expression was also detected, confirming that these asymmetric pairs were dividing. Quantitative analysis revealed that the frequency of dividing BMI1+/LGR5+ cell pairs increases in neoplastic tissue compared to normal colon tissue (Fig. 1c; $p = 0.001$; Student t-test). Overall, these data suggest that BMI1+/LGR5+ pairs could result from asymmetric cell division and are associated with CRC.

To understand the lineage relationship between BMI1+ and LGR5+ cells in asymmetric pairs, we derived and characterized CCIC lines from CRC patients as previously described [5, 33] and performed a two-cell assay [21]. We plated CCICs at low density and monitored single cells ~36 hours through one cycle of cell division followed by single IF and co-IF of cell pairs

(Supplementary Fig. 1A) for different markers including BMI1, LGR5, NOTCH1 and others. Co-IF for LGR5 and BMI1 confirmed that CCICs can divide into asymmetric BMI1+/LGR5+ daughter cell pairs; additionally, we observed a notable difference in the longest nuclear diameters of the BMI1+ CCIC and its LGR5+ counterpart (Supplementary Fig. 1B). The presence of these BMI1+/LGR5+ asymmetric cell pairs in CCIC is consistent with what we had observed in primary CRCs. In approximately 5% of newly divided pairs, we identified asymmetric division producing daughter cell pairs that exhibit the specific cellular and nuclear morphology with a crescent-shaped CCIC enveloping another CCIC (Supplementary Fig. 1C). Using co-IF for PARD3A (a polarity cell fate marker for asymmetric division) and LGR5 expression, we then confirmed a similar 4.5% frequency of asymmetric cell division in CCICs (Supplementary Fig. 1D). In contrast, HCT116 cells, a CRC line that does not have CCIC, showed no evidence of asymmetric division as determined by specific nuclear morphology and PARD3A/LGR5 expression (Supplementary Fig. 1D).

Next, we characterized asymmetric CCIC daughter cell pairs based on the expression of stem cell markers and various signaling pathway components (Fig. 2a, 2b; Supplementary Fig. 1E, 1F, 1G). These studies revealed that the BMI1+ CCIC also expressed high levels of NOTCH1 receptor (NOTCH1), HES5 (a downstream marker of active NOTCH signaling), hTERT, and the TGF-β pathway markers nuclear phospho-SMAD1/5 [34, 35]. In asymmetric cell pairs, the partnered LGR5+ daughter also expressed the WNT marker nuclear β-CATENIN, NOTCH ligand DLL4, and the stem cell markers CD44, ALDH1, and CD133 [7, 35-37]. Several intestinal stem cell markers [12] were also found to specifically label asymmetric CCIC pairs in which BMI1+ daughters are hTERT+ and HOPX+ while LGR5+ daughters are OLFM4+ and ASCL2+ (Supplementary Fig. 1F, 1G). Using the pair cell assay, the WNT activity status of BMI1+(NOTCH1+)/LGR5+ cell pairs was evaluated by infecting CCICs with a lentiviral TCF-

GFP reporter construct and treatment with WNT3A ligand, which revealed that the LGR5+ CCIC daughter displays active WNT signaling (Supplementary Fig. 1H). Furthermore, based on FACS analysis, TCF-GFP reporter and CD133 expression overlapped primarily with the LGR5+/BMI1- CCIC population (Supplementary Fig. 1I).

We then used time-lapse microscopy to investigate which type of CCIC (BMI1+ or LGR5+) gives rise to the BMI1+/LGR5+ pair. Because BMI1 is an intracellular protein, NOTCH1 was used as a surrogate membrane marker for BMI1, based on our finding that BMI1+ CCIC is NOTCH1+ and LGR5+ CCIC is NOTCH1-. We performed time-lapse imaging of NOTCH1/LGR5 double sorted cells over the course of 48 hours followed by fixation and IF (Fig. 2c). A round, NOTCH1-/LGR5+ CCIC produced an elongated, BMI1+ daughter cell. Reciprocally, a crescent-shaped, NOTCH1+/LGR5- CCIC generated a rounder daughter cell, which further divided into two smaller, rounder LGR5+ daughter cells. Therefore, both LGR5+ and BMI1+ CCICs are capable of generating asymmetric BMI1+/LGR5+ pairs through division.

BMI1 and LGR5 CCICs are capable of both symmetric and asymmetric divisions (Fig. 2d). For asymmetric division, PARD3A polarizes to the side of the BMI1 daughter compartment during cytokinesis, as confirmed by α-TUBULIN staining of midbody at the division plane, supporting intrinsic asymmetric division of CCICs to generate BMI1+ and LGR5+ daughters (Supplementary Fig. 1J). The three-dimensional morphology of cell fate asymmetry was analyzed using confocal imaging and z-stack acquisition, revealing that BMI1+(PARD3A+) CCIC physically envelops the smaller LGR5+(NUMB+) CCIC daughter cell in 3 dimensions (Supplementary Movie 1).

LGR5+ daughter is faster-cycling than BMI1+ daughter, dependent on MYC

We evaluated the proliferative capacity of the LGR5+ daughter cell vs. the BMI1+ daughter cell in asymmetric pairs by performing BrdU incorporation in the pair-cell assay. Single

cells were plated and allowed to divide once in proliferative medium for 24 hours (1st division) before treatment of BrdU for 3 hours to label the cells entering the 2nd division [24]. Co-IF showed that the smaller, rounder LGR5+ daughter is positive for BrdU (Fig. 2e). Quantitative analysis in BMI1+/LGR5+ asymmetric pairs showed that BrdU incorporation occurred most frequently in LGR5+ daughters ($p = 0.004$, one-way ANOVA) (Fig. 2e), consistent with faster-cycling LGR5+ CCIC vs. slower-cycling BMI1+ CCIC.

Because LGR5+ daughters have higher WNT signaling levels than BMI1+ daughters (Fig. 2a; Supplementary Fig. 1H, 1I), and WNT upregulates MYC, a transcription factor known to promote proliferation and growth [38], we examined the potential role of MYC in promoting differential proliferative capacity between LGR5+ and BMI1+ daughters by establishing a knockdown model using MYC-siRNA transfection. Efficient MYC knockdown was validated by Western blot analysis (Supplementary Fig. 2A). We then validated that MYC knockdown does not interfere with Notch signaling. NICD expression (Supplementary Fig. 2A) and RT-PCR for NOTCH effectors Hes1 and Hes5 (Supplementary Fig. 2B) showed that CCIC with MYC knockdown maintained the same level of NOTCH signaling activity compared to control (scrambled siRNA-transfected CCICs). Furthermore, we observed decreased expression of MYC target genes: Cyclin D2 and Ornithine Decarboxylase (ODC), and increased expression of p21 in MYC-siRNA treated CCICs, consistent with the anti-proliferative effect of MYC knockdown (Supplementary Fig. 2B). While overall CCIC proliferation was suppressed with MYC knockdown, co-IF for BMI1 and LGR5 expression in α-TUBULIN showed that division of LGR5+ cells was disproportionally affected (Fig. 2f). MYC siRNA knockdown also switched BrdU incorporation from the LGR5+ daughter cell to the BMI1+ daughter in asymmetric CCIC pairs (Fig. 2g). Furthermore, quantitative analysis of asymmetric BMI1+/LGR5+ pairs showed that, while overall BrdU incorporation is significantly reduced by MYC knockdown, BrdU

incorporation occurred most frequently in BMI1+ daughters ($p = 0.005$, one-way ANOVA) (Fig. 2g). This reversal of relative proliferation potential between BMI1+ and LGR5+ daughter CCICs suggests that LGR5+ CCIC proliferation is more dependent on MYC. We then analyzed how MYC knockdown affects the timing of division in BMI1+ vs. LGR5+ CCIC populations following BrdU incorporation, which showed that the absolute number of proliferating LGR5+ CCIC decreased substantially ($p = .002$, Student t-test) while the number of dividing BMI1+ CCICs was consistent with the control (Supplementary Fig. 2C). FACS analysis confirmed that MYC-siRNA resulted in a smaller population of Ki67+ dividing CCICs compared to the control, and this gated population showed a greater percentage of BMI1+ vs. LGR5+ CCICs (Fig. 2h). Overall, these experiments are consistent with asymmetric proliferation potential between LGR5+ and BMI1+ CCICs being dependent on MYC.

BMI1+ and LGR5+ CCICs interconvert in xenograft tumors

To study the properties of symmetric vs. asymmetric CCIC pairs (Supplementary Fig. 3A), we isolated a gated population (8.3%) of CCICs with distinctly larger forward scattering, which were presumably doublets (Fig. 3a). Cell viability assay for 7-AAD expression confirmed that the population consisted of live cells (Supplementary Fig. 3B). Again, using NOTCH1 as an extracellular surrogate marker for BMI1 specifically for the doublets, FACS analysis of the gated population detected a NOTCH1+/LGR5+ doublet population and NOTCH1+/LGR5- and NOTCH1-/LGR5+ doublet populations. A subset of each double-sorted CCIC population was further analyzed for intracellular BMI1 expression, validating the correlation of NOTCH1 and BMI1 in CCIC pairs (Supplementary Fig. 3C). RT-PCR analysis within each double-sorted NOTCH1/LGR5 population was also used to confirm BMI1 and LGR5 expression (Supplementary Fig. 3D). Next, IF microscopy of plated NOTCH1+/LGR5+ CCIC pairs was performed first without BMI1 or LGR5 primary antibody to validate the absence of signal from

bound FACS antibody (Supplementary Fig. 3E). Co-IF for BMI1 and LGR5 on the double-sorted NOTCH1+/LGR5+ population demonstrated that these pairs are consistently BMI1+/LGR5+ (Fig. 3b). We then assayed the frequency of BMI1+/LGR5+ asymmetric division in each NOTCH1/LGR5 double-sorted CCIC population (Fig. 3b). Quantitative analysis showed that enrichment for NOTCH1 and LGR5 in the double positive fraction increased the BMI1+/LGR5+ cell pairs to approximately 80% vs. 4% in the unsorted (control) population ($p = 0.009$; one-way ANOVA). Furthermore, NOTCH1+/LGR5- and NOTCH1-/LGR5+ single positive populations showed corresponding increases in BMI1/BMI1 and LGR5/LGR5 symmetric pairs, respectively, compared to the control.

Equal numbers of sorted CCIC doublets - double positive (NOTCH1+/LGR5+), single positive (NOTCH1-/LGR5+ or NOTCH1+/LGR5-), double negative (NOTCH1-/LGR5-) - or unsorted CCICs (a doublet counts as 2 CCICs) were plated in Matrigel and assayed for clonogenicity after two weeks (Supplementary Fig. 3F). The double- or single-positive doublet populations yielded colonies that grew significantly faster compared to the unsorted population and the double negative doublet population ($p = 0.001$; one-way ANOVA). Next, 1000 NOTCH1+/LGR5+, NOTCH1-/LGR5+, NOTCH1+/LGR5-, or NOTCH1-/LGR5- doublets or an equal number of unsorted CCICs (a doublet counts as 2 CCICs) were subcutaneously injected to form xenograft tumors in mice (Supplementary Fig. 3G). Consistent with clonogenicity results, the double- or single-positive doublet populations showed greater tumor incidence and tumor volume compared to the double-negative and unsorted cohorts ($p = 0.0005$ and $p = 0.0004$, respectively; one-way ANOVA) (Fig. 3c).

Furthermore, co-IF of xenograft tumor sections and FACS analysis of dissociated tumors revealed that the tumors derived from double- or single-positive (NOTCH1+/LGR5+, NOTCH1-/LGR5+, NOTCH1+/LGR5-) doublets contained both BMI1+ and LGR5+ subfractions with

similar ratios (Fig. 3d). Testing another primary CCIC line (CCIC-2) through the same FACS and xenograft assays was consistent with our previous results, demonstrating the existence of asymmetric BMI1+/LGR5+ cell pairs and the ability to interconvert between BMI1+ and LGR5+ populations (Supplementary Fig. 3H-3L). Taken together, these *in vivo* data suggest that BMI1+ CCICs and LGR5+ CCICs co-exist, are somewhat balanced within a tumor, and can generate each other potentially through asymmetric division.

NOTCH signaling regulates CCIC BMI1+/LGR5+ asymmetric division

NOTCH levels are higher in the slow-cycling (BMI1+) daughter than in the fast-cycling (LGR5+) daughter, raising the possibility that NOTCH signaling may play a role in regulating asymmetric BMI1+/LGR5+ division. We first studied the effect of NOTCH suppression on BMI1+/LGR5+ asymmetric division in xenograft tumors. Briefly, 1 x 10^6 unsorted CCICs were injected s.c. into NOD/SCID mice to form tumors; after 5 weeks, tumors were directly injected with DMSO or NOTCH inhibitor DAPT over 72 hours before being harvested and assayed. The short treatment duration was chosen to evaluate short-term effects on cell division and to avoid potential senescence, apoptosis, or complete depletion/conversion of cell fates often associated with long-term treatments. Western blot analysis validated NICD suppression and RT-PCR data showed decreased expression of NOTCH downstream targets Hes1 and Hes5 upon DAPT treatment (Supplementary Fig. 3M). Co-IF for BMI1, LGR5, and α-TUBULIN as well as Ki67 staining confirmed the existence of asymmetric BMI1+/LGR5+ cell division in tumor sections. DAPT treatment reduced the frequency of BMI1+/LGR5+ dividing pairs to 0.6% compared to 5.2% in DMSO-treated tumors ($p = 0.003$; Student t-test) (Fig. 3e). FACS analysis of dissociated xenograft tumors showed that DAPT treatment also reduced the ratio of BMI1+ vs. LGR5+ CCIC populations ($p =0.0002$; Student t-test) within 72 hours (Fig. 3f).

We further studied the role of NOTCH on CCIC asymmetric division *in vitro* (Fig. 4a).

Performing the pair-cell assay, CCICs were treated with DMSO or increasing concentrations of DAPT. Co-IF of DMSO-treated CCICs showed the presence of asymmetric BMI1+(NOTCH1+)/LGR5+ cell pairs. Next, RT-PCR for Hes1 and Hes5 confirmed DAPT suppression of NOTCH activity. We observed that increasing concentrations of DAPT reduced CCIC BMI1+/LGR5+ cell pairs compared to the control ($p = 0.01$; Student t-test). Additionally, asymmetric division as determined by nuclear morphology and BMI1/LGR5 expression was not detected in HCT116 or RKO cells under any condition (Supplementary Fig. 4A). In order to validate that NOTCH modulation affects the mode of cell division, we performed NOTCH1, LGR5, and α-TUBULIN co-staining of CCIC pairs just before cell division completion in DMSO- and DAPT-treated cells (Supplementary Fig. 4B, 4C). We observed asymmetric distribution of NOTCH1 and LGR5 in the control group compared to symmetric expression of both markers with DAPT treatment, suggesting that NOTCH signaling regulates asymmetric division to generate BMI1/LGR5 CCIC pairs. FACS analysis following a short, 24-hour DAPT treatment also showed that NOTCH suppression decreased the BMI1+/LGR5+ double positive population containing the asymmetric pairs and reduced the ratio of BMI1+ vs. LGR5+ CCIC populations (Supplementary Fig. 4D).

During many examples of NOTCH driven asymmetric division, NUMB localizes to one side of the dividing cell and causes degradation of membrane-bound NOTCH receptors and NICD [39, 40], which creates differential NOTCH signaling levels in daughter cells [41]. We tested the effect of NUMB knockdown on asymmetric BMI1+/LGR5+ CCIC pairs (Fig. 4b). CCICs were infected with lentivirus allowing stable expression of NUMB shRNA or scrambled shRNAs (control). Consistent with NUMB knockdown, IF microscopy showed diminished NUMB expression, western blotting showed reduced NUMB protein levels (Supplementary Fig. 4E), and qPCR analysis of NOTCH signaling targets showed an increase in Hes1 and Hes5

expression. Targeted knockdown of NUMB increased the number of asymmetric BMI1+/LGR5+ cell pairs from 5% (control) to 9.5% ($p = 0.008$; Student t-test). Thus, NUMB is not required for CCIC asymmetric division producing BMI1+ and LGR5+ daughter pairs, while higher NOTCH activity promotes BMI1+/LGR5+ daughter pairs.

We also used a mutant NUMB (NUMB-SYM), which suppresses NOTCH signaling but does not partition differentially among daughters [42]. Lentiviral expression of NUMB-SYM and subsequent pair cell assay analysis using IF for NUMB localization validated the overexpression of NUMB segregation in both symmetric and asymmetric division of NUMB-SYM expressing CCICs compared to the control group (Fig. 4c). Western blotting confirmed an increase of NUMB protein (Supplementary Fig. 4F) and RT-PCR analysis of Hes1 and Hes5 validated decreased expression from the NUMB-SYM expressing CCICs vs. empty vector-transduced (control) CCICs. Similar to NOTCH inhibition, NUMB-SYM led to a decrease in the number of BMI1+/LGR5+ cell pairs from approximately 4.5% (control) to 2% ($p = 0.0022$; Student t-test). The suppression of asymmetric division by NUMB-SYM is consistent with NOTCH activity levels promoting this type of asymmetric division.

Next, we established a knockdown model for NOTCH ligand JAG-1. CCICs were infected with JAG-1 shRNA or with scrambled shRNA (control) lentiviral particles prior to performing the pair cell assay (Fig. 4d). IF, Western blot (Supplementary Fig. 4G), and gene expression analysis for NOTCH effectors Hes1 and Hes5 validated the knockdown efficiency for JAG-1. JAG-1 shRNA caused a notable decrease of asymmetric BMI1+/LGR5+ daughter cell pairs to less than 1% ($p = 0.0028$; Student t-test) compared to the control group (~5%).

Finally, we overexpressed the NOTCH intracellular domain (NICD), which is known to translocate to the nucleus to activate expression of NOTCH effector genes in CCICs, and evaluated the impact of increased NOTCH signaling (Fig. 4e). Following NICD-OE, co-IF of

BMI1/LGR5+ CCIC pairs showed differential NOTCH1 expression levels in which the BMI1+ daughter is NOTCH1-high compared to the LGR5+ (NOTCH1-low) daughter. CCICs that incorporated the NICD-OE construct showed corresponding increases in NICD as well as HES1 and HES5 through Western blotting (Supplementary Fig. 4H) and RT-PCR analyses. NICD overexpression increased asymmetric BMI1+/LGR5+ cell pairs to approximately 10% compared to 4.5% in the empty vector-transduced (control) group ($p = 0.0029$; Student t-test). BMI1 expression was elevated in NICD-CCICs (Supplementary Fig. 4I), consistent with previous reports showing BMI1 as a downstream target of NOTCH in T cells [43] and murine intestinal cells [44]. NOTCH1, LGR5, and α-TUBULIN co-staining of NICD-OE CCIC pairs showed that differential asymmetric distribution of NOTCH1 preceded the end of cell division (Supplementary Fig. 4J). Overall, together with NUMB and NUMB-SYM experiments, these data are consistent with a mechanistic role for NOTCH signaling to drive generation of BMI1+/LGR5+ CCIC asymmetric daughter cell pairs.

NOTCH signaling balances BMI1+ and LGR5+ populations in intestinal organoids

We then investigated whether the above mechanism is unique to CCICs, or a parallel mechanism exists in normal stem cells. In the intestine [12], fast-cycling $LGR5_{\text{-expressing}}$ (Leucine-rich repeat-containing G protein-coupled receptor 5-expressing) crypt base columnar (CBC) stem cells are the primary driver of crypt regeneration. LGR5+ CBCs can self-renew, or produce transit-amplifying (TA) daughter cells that rapidly divide and terminally differentiate into various lineages that populate the intestinal epithelium [12, 45-47]. There is also evidence for another more quiescent stem cell population [48], which have been associated with markers including BMI1, HOPX, TERT and LRIG-1 [49-53]. Single-molecule transcript analyses suggest that the presence of LGR5 and BMI1 mRNAs is more prevalent than that indicated by antibody staining and they potentially overlap in a subset of cells, raising the possibility that post-

translational mechanisms may amplify the difference in protein levels and these two populations may be more plastic than previously thought [54, 55].

Mouse intestinal stem cells (ISCs) were first propagated as organoids in order to quantify the relative ratio of BMI1+ and LGR5+ ISC under conditions with different NOTCH signaling levels [56]. When NOTCH signaling was inhibited with the γ-secretase inhibitor DAPT for 48 hours and visualized by co-IF, the ratio of BMI1+/LGR5+ cells decreased vs. DMSO-treated controls ($p = 0.0001$; Student t-test) (Fig. 5a, 5b). Western analysis for NICD confirmed inhibition of NOTCH activity due to DAPT treatment (Supplementary Fig. 5A).

POFUT-1 (Protein *O*-fucosyltransferase 1) is an enzyme responsible for the addition of fucose by O-linkage on EGF domains of NOTCH receptors and is required for functional NOTCH signaling [57]. To validate the results from chemical inhibition of NOTCH signaling, ISCs derived from mice expressing a LGR5-EGFP-creER/POFUT-1$^{flox/flox}$ genotype were treated *in vitro* with 4-hydroxy-Tamoxifen for approximately 48 hours to induce POFUT-1 knockout/NOTCH inhibition and visualized by IF (Fig. 5a). Similar to DAPT treatment, the BMI1+/LGR5+ cell ratio decreased vs. DMSO-treated controls ($p = 0.0001$; Student t-test) (Fig. 5b). Western analysis showed POFUT-1 and NICD were not detectable using this model of NOTCH suppression (Supplementary Fig. 5B).

Next, we examined the effect of stimulation of the NOTCH pathway via soluble JAG-1 embedded in Matrigel [49, 58]. JAG-1 stimulation of NOTCH in ISCs generated from LGR5-EGFP mice significantly increased the ratio of BMI1+/LGR5+ ISCs vs. DMSO-treated controls ($p = 0.0001$; Student t-test) (Fig. 5a, 5b). As expected, JAG-1 treatment also increased NICD levels (Supplementary Fig. 5C). Taken together, these findings show that NOTCH signaling increases the ratio of BMI1+/LGR5+ ISCs, whereas NOTCH inhibition reduces this ratio.

NOTCH signaling balances BMI1+ and LGR5+ populations *in vivo*

To confirm organoid studies, we used LGR5-EGFP mice treated with DMSO. Intestinal sections were harvested and analyzed by IF for LGR5 (detected by GFP antibody) and BMI1 expression. BMI1+ cells largely localized to nuclei in the +4 position and LGR5+ cells were found interspersed at the crypt base (Fig. 5c). As previously reported, antibody staining of LGR5-GFP and BMI1 is more specific than single-molecule RNA FISH, suggesting that post-translational mechanisms may amplify the difference in protein levels [55]. LGR5-EGFP mice were treated with DAPT by i.p injections to inhibit NOTCH signaling. Quantification over multiple crypts showed a marked reduction in the ratio of BMI1+/LGR5+ ISCs compared to the DMSO-treated control group ($p = 0.0001$; one-way ANOVA) (Fig. 5c, 5d). NOTCH signaling was also inhibited using LGR5-EGFP-creER/POFUT-1$^{flox/flox}$ mice that were administered daily Tamoxifen i.p injections to induce POFUT-1$^{-/-}$ (knockout) phenotype. Similar to DAPT treatment, the ratio of BMI1+/LGR5+ ISCs was significantly reduced in the POFUT-1$^{-/-}$ vs. DMSO-treated control group ($p = 0.0001$; one-way ANOVA (Fig. 5c, 5d). Protein expression analysis confirmed POFUT-1 was not detected in POFUT-1$^{-/-}$ tissue. Similarly, western blotting for NICD expression from harvested intestinal tissue validated NOTCH suppression by DAPT and POFUT-1$^{-/-}$ (Fig. 5d). Finally, we crossed a Rosa26-YFP-NICD mouse strain [59] with an LGR5-EGFP-CreERT2 strain to generate an LGR5-EGFP-CreERT2 x Rosa26-YFP-NICD mouse strain as a model for NOTCH stimulation via NICD expression in ISC following Tamoxifen induction. Co-IF based on LGR5 and BMI1 expression showed elevated BMI1 staining in cells located around the +4 position while LGR5 expression was similar to the DMSO-treated control group (Fig. 5c). The ratio of the number of ISCs expressing BMI1 relative to LGR5 showed a significant increase compared to the control ($p = 0.0001$; one-way ANOVA (Fig. 5d). Western blot analysis confirmed NICD overexpression from harvested intestinal tissue (Fig. 5d). Overall, our observation of BMI1+ cells *in vitro* and *in vivo* is consistent with a role

for NOTCH signaling to drive production of BMI1+ ISC (Supplementary Fig. 5D, 5E).

Asymmetric BMI1+/LGR5+ division of ISC organoid cells

To assess a potential role for NOTCH signaling to regulate LGR5+ and BMI1+ (HOPX+) normal stem cell populations, we first examined *in vitro* organoid cultures of single ISCs derived from mice carrying an EGFP knock-in driven by the LGR5 promoter (LGR5-EGFP). Murine crypts were isolated, dissociated into single cells, embedded in Matrigel overlaid with growth media, and observed 16 hours post-plating to visualize the mitotic outcome of single stem cells by IF. Using α-TUBULIN staining, we observed single ISCs producing BMI1+/LGR5+, LGR5+/LGR5+, and BMI1+/BMI1+ daughter pairs in the final stages of cell division (Fig. 6a). In order to confirm antibody specificity, ISCs were treated with a microtubule-depolymerizing agent (Colchicine) for 4 hours following the pair cell assay, which showed an absence of α-TUBULIN expression in Ki67+ dividing pairs (Supplementary Fig. 6A). Next, we tested additional microtubule markers, including β-TUBULIN (Supplementary Fig. 6B) and γ-TUBULIN (Supplementary Fig. 6C) in pair cell assays, which consistently showed the generation of BMI1+/LGR5+ asymmetric ISC daughters. We also found asymmetric distribution of LGR5 and the cell fate marker PARD3A in ISC daughter pairs prior to completion of cell division using mitotic spindle labeling (Supplementary Fig. 6D).

Single ISCs were analyzed further using the pair cell assay for conditions that modulate NOTCH signaling (Fig. 6b). RT-PCR analysis of Hes1 and Hes5 validated NOTCH signaling upon treatment with DAPT or JAG-1, respectively (Supplementary Fig. 6E). Consistent with CCIC behavior, the frequency of BMI1+/LGR5+ cell pairs was reduced upon NOTCH inhibition and increased upon NOTCH stimulation in the DMSO-treated control ($p = 0.002$; one-way ANOVA). To understand whether this process can be influenced by stress to the system, we treated organoids with TNF-α, a pro-inflammatory cytokine linked to chronic colitis and

carcinogenesis [60, 61] and increased apoptosis of organoid cells [62]. TNF-α was administered at a low dosage of 10ng/ml to LGR5-EGFP ISCs over 72 hours. We found that TNF-α up-regulated NICD by Western blot analysis, as well as expression of Hes1 and Hes5 by RT-PCR (Supplementary Fig. 6F). TNF-α treated ISCs showed a marked increase to 4.3% BMI1+/LGR5+ divisions ($p = 0.003$, one-way ANOVA) (Fig. 6c). When DAPT was added to the culture medium during the last 48 hours of TNF-α treatment, there were corresponding decreases in NICD, Hes1 and Hes5 levels (Supplementary Fig. 6F) and notably, BMI1+/LGR5+ asymmetric division reduced to 0.1% ($p = 0.002$, one-way ANOVA) (Fig. 6c). FACS analysis was then used to quantify the BMI1+ vs. LGR5+ ISC population balance in TNF-α, and TNF-α+DAPT treatment groups (Fig. 6d). Consistent with our earlier findings, the BMI1+/LGR5+ double positive population containing BMI1+/LGR+ pairs increased with TNF-α treatment and decreased with TNF-α+DAPT treatment. The ratio of BMI1+/LGR5+ ISCs increased with TNF-α treatment and decreased with TNF-α+DAPT treatment. These data suggest that normal ISCs are capable of NOTCH-dependent asymmetric BMI1+/LGR5+ division, which can be triggered by stress.

Asymmetric BMI1+/LGR5+ division *in vivo*

We then examined LGR5-EGFP intestinal tissue to study ISC division using α-TUBULIN and Ki67 expression. We detected only LGR5+/LGR5+ and BMI1+/BMI1+ symmetric division (Supplementary Fig. 7A). This suggests that asymmetric BMI1+/LGR5+ division does not happen or is very rare in intestinal crypts *in vivo*, unlike in organoids, where stem cells are encouraged to proliferate by growth factors such as WNT, R-SPONDIN, and NOGGIN. To examine the effect of stress on ISC division, LGR5-EGFP mice were treated with 3% dextran sodium sulfate (DSS) in the drinking water for 5 days followed by a 5-day recovery period with plain water [61]. DSS causes chronic inflammation that increases intestinal cell

apoptosis. Consistent with TNF-α treatment in organoids, we detected asymmetric BMI1+/LGR5+ daughters in α-TUBULIN+/γ-TUBULIN+/Ki67+ dividing pairs (Fig. 6e). DSS treatment increased BMI1+/LGR5+ asymmetric division frequency to 3.9% ($p = 0.002$; one-way ANOVA) (Fig. 6f). When DSS-treated mice were injected with DAPT during the last 3 days of the plain water diet, the number of asymmetric BMI1+/LGR5+ cell pairs reduced to 0.2% ($p = 0.004$; one-way ANOVA) (Fig. 6f). DSS treatment increased NOTCH signaling levels, while the addition of DAPT reduced NOTCH signaling levels, in terms of NICD, Hes1, and Hes5 expression (Supplementary Fig. 7B). DSS and DSS+DAPT intestinal tissues were then harvested and analyzed by FACS to quantify BMI1+ vs. LGR5+ population balance (Fig. 6g). Again, the double-positive population containing BMI1+/LGR5+ pairs increased with DSS treatment and decreased with DSS+DAPT treatment. The ratio of BMI1+/LGR5+ ISCs increased with DSS treatment and decreased with DSS+DAPT treatment. Therefore, these data suggest that stress can trigger asymmetric BMI1+/LGR5+ division in the intestine, potentially to increase conversion between BMI1+ and LGR5+ cells.

MYC promotes LGR5+ proliferation in organoids

Pair cell assays using LGR5-EGFP ISCs followed by BrdU labeling confirmed that the LGR5+ daughter is faster-cycling than the BMI1+ daughter (Supplementary Fig. 8A). MYC-siRNA transfection was then performed to understand how MYC affects the proliferation potential of fast- vs. slow-cycling ISCs. Western blot analysis validated MYC knockdown conditions (Supplementary Fig. 8B). MYC knockdown reduced BrdU label expression in LGR5+ daughter cells in BMI1+/LGR5+ pairs relative to the control (Supplementary Fig. 8A) ($p = 0.002$, one-way ANOVA). Subsequently, FACS analysis was used to understand the balance of BMI1+ vs. LGR5+ ISCs with MYC knockdown (Supplementary Fig. 8C). MYC-siRNA increased the ratio of BMI1+/LGR5+ ISCs relative to the control, consistent with LGR5+

proliferation being more dependent on MYC. Taken together, our data supports a greater dependence on MYC for fast-cycling (LGR5+) cells compared to slow-cycling (BMI1+) cells.

DISCUSSION

CCICs from the same tumor are often treated as a homogenous population. Here we demonstrate that fast- and slow-cycling subfractions can co-exist and CCICs can asymmetrically divide to generate both types, adding more nuances to our understanding of CCIC. Specifically, we show that the NOTCH and MYC are important mechanisms to regulate the balance between the two populations. NOTCH-dependent asymmetric division may help to ensure CCIC diversity by maintaining both slow-cycling, MYC-independent BMI1+ CCICs and fast-cycling, MYC-dependent LGR5+ CCICs, which may provide CRC with a growth and survival strategy to promote self-renewal, tumorigenicity, and chemoresistance.

In mouse intestine, LGR5+ CBCs are fast-cycling and thought to divide symmetrically [46, 63], while BMI1+/HOPX+ cells are largely quiescent. However, single-molecule RNA FISH suggests that the mRNA levels of these markers are not as clearly cut, raising the possibility of plasticity [54, 55]. Targeted ablation of LGR5+ ISCs in transgenic mice with diphtheria toxin revealed that intestinal crypt homeostasis could be rescued by rare, normally quiescent ISCs [53]. Remarkably, the two populations can be replenished when each is depleted [49]. Our data suggest potential roles for the NOTCH pathway and MYC to regulate the balance between fast- and slow-cycling populations, and asymmetric division can potentially be activated under stress/tissue repair conditions to aid direct interconversion. This mechanism is likely silent and insignificant during normal tissue homeostasis, but becomes activated in CCICs.

METHODS

Antibodies.

Primary Antibody	**Supplier**	**Catalog Number**	**Dilution***

Anti-ALDH1A	Santa Cruz	Sc-398578	1:100 (IF)
anti-APC	Abcam	ab40778	1:1000 (WB)
Anti-ASCL2	Millipore	MAB4418	1:50 (IF)
Anti-α-TUBULIN	Abcam	Ab6160	1:500 (IF)
Anti-β-TUBULIN	Sigma Aldrich	**T8328**	1:100 (IF)
Anti-γ-TUBULIN	Abcam	Ab11316	1:100 (IF)
anti-β-ACTIN	Abcam	ab6276	1:4000 (WB)
anti-β-CATENIN	Santa Cruz Biotechnology	sc-59737	1:50 (IF)
Anti-BMI1 (for CCIC specificity)	Rockland	600-101-392	1:100 (IF)
Anti-BMI1 (for IF murine specificity)	Cell Signaling	5856	1:50 (IF)
Anti-BMI1 (for FACS murine specificity)	Abcam	Ab14389	1:100 (FACS)
BMI1-PE	BD Biosciences	562528	1:100 (FACS)
BMI1-Cy5	BD Biosciences	562650	1:100 (FACS)
anti-BrdU	Sigma Aldrich	Ab6326	1:100 (IF)
anti-CD44	Cell Signaling	3570	1:200 (IF)
Anti-CD133	Millipore	MABE4399	1:100 (IF)
anti-DLL4	Abcam	ab7280	1:100 (IF)
anti-GFP	Abcam	ab5450	1:100 (IF)
anti-HES5	Santa Cruz Biotechnology	sc-25395	1:100 (IF)
anti-HOPX	Santa Cruz	sc-25146	1:50 (IF)
Anti-hTERT	Millipore	MABD55	1:100 (IF)
anti-JAGGED1	Santa Cruz Biotechnology	sc-6011	1:100 (IF)
Anti-Ki67	Abcam	ab15580	1:200 (IF)
anti-LGR5	Abcam	ab75732	1:50 (IF); 1:100 (FACS)
anti-MYC	Santa Cruz Biotechnology	sc-40	1:1000 (WB)
anti-NICD	Cell Signaling	2421	1:1000 (WB)
anti-NOTCH1	Abcam	Ab44986	1:50 (IF)

NOTCH1-PE	BD Biosciences	536421	1:100 (FACS)
anti-NUMB	Cell Signaling	2756	1:100 (IF)
Anti-OLFM2	Antibodies-online	ABIN1999012	1:100 (IF)
anti-PARD3A	Santa Cruz	sc-79577	1:100 (IF)
anti-POFUT1	Abcam	ab154051	1:2000 (WB)
anti-pSMAD1/5	Cell Signaling	9516	1:100 (IF)

*Application: IF: (Immunofluorescence); WB: (Western Blotting)

The corresponding Alexa Fluor® -488 or Alexa Fluor® -555 conjugated secondary antibodies were purchased from Life Technologies. Alexa Fluor® 647 secondary antibody (anti-rat: A-21472; anti-mouse: A-21463; anti-rabbit: A-21443) was purchased from Life Technologies.

CCIC Culture.

CCIC lines were generated as previously described [1]. Exome sequencing data was collected for these lines and mutations were subsequently analyzed [2]. Cell suspensions were cultured in ultra low-attachment flasks in serum free DMEM:F12 medium (Invitrogen) supplemented with minimal nonessential amino acids (Thermo Fisher), sodium pyruvate (Thermo Fisher), N2 supplement (Invitrogen), B27 supplement (Invitrogen), 4 μg/ml heparin (Sigma), antibiotic-antimycotic (Invitrogen), 20 ng/ml basic fibroblast growth factor (R&D Systems) and 40 ng/ml epidermal growth factor (R&D Systems) at 37°C and 5% CO_2. In order to passage CCICs, cell suspension was gently centrifuged, suspended in 1X Trypsin-EDTA (Invitrogen) for 5 minutes at 37°C, and mechanically dissociated into single cells before final resuspension in growth culture medium.

CCIC Studies

For DAPT treatment, cells were resuspended at the appropriate density in serum free medium DAPT (EMD Biosciences) or DMSO (Sigma) and incubated for 48 hours. Lentiviral constructs containing NUMB-shRNA (Cat. no: SHCLND-NM_003744), JAG-1 shRNA (Cat. no. SHCLND-NM_000214), or scrambled shRNA (control) (Cat. no. SHC016) along with

lentiviral packaging particles (**SHP001)** were ordered from Sigma Aldrich. NICD gene sequence and approximately 300 base pairs of flanking sequence was amplified from human genomic DNA and cloned into the lentiviral vector pSMPUW-Puro Lentivirus Expression Vector (Cell Biolab Cat. no VPK-212) and used in conjunction with packaging plasmids from Clontech to generate NICD-OE (NICD overexpression). As a control, an empty vector was purchased from Addgene (Plasmid #17408) along with lentiviral packaging plasmids (Addgene Plasmid #8454 and #8455). In order to create the NUMB-SYM construct, a pEF-BOS expression vector containing NUMB was obtained from Weimin Zhong's laboratory [3] and this sequence was recloned into a GFP lentiviral vector (Clontech). A lentiviral WNT reporter (TCF-EGFP) construct containing 7xTcf-eGFP//SV40-PuroR was purchased from Addgene (Plasmid #24305) and used with viral packaging plasmids from Clontech. Subsequently, empty vector, NUMB-shRNA, JAG-1 shRNA, NICD-OE, NUMB-SYM, or TCF-EGFP -expressing lentivirus was generated when HEK293T cells were co-transfected with the viral vectors and associated packaging plasmids. After 48 hours, the supernatant (NUMB-shRNA, JAG-1 shRNA, NICD-OE, NUMB-SYM) was collected and used to infect CCICs with puromycin selection in accordance with a previously described method [4]. For the WNT reporter assay, CCICs were treated with WNT3A ligand (R&D; 5036-WN-010) for 24 hours followed by viral transduction of TCF-EGFP and puromycin selection. Single CCICs were also transfected with MYC-siRNA (Santa Cruz Biotech cat. no: sc-29226) or scrambled siRNA (Santa Cruz Biotech cat. no: sc-37007) according to the manufacturer's instructions followed by FACS analysis to assess BMI1 and LGR5 expression in Ki67+ dividing CCIC population.

BrdU Incorporation Assay

BrdU Incorporation Assay was performed as previously described [4]. Briefly, single CCICs or MYC-siRNA transfected CCICs were plated and grown in culture medium containing DMEM + 10% FBS for 16 hours. Following this division, cells were treated for 3 hours with

10mM BrdU (Sigma), fixed in cold 70% ethanol, followed by incubation for 1 hour in 2M HCl. Next, cells were washed with PBS and incubated for 2 minutes with 100mM $Na_2B_4O_7$. The protocol below for co-immunofluorescence was then followed beginning with blocking in 10% normal goat serum for 1 hour. BrdU labeling was quantified in BMI1+/LGR5+ asymmetric pairs for incorporation into LGR5+, BMI1+ or both LGR5+ and BMI1+ CCICs.

Immunofluorescence of CCICs

CCICs were fixed approximately 16 hours post-plating with 4% paraformaldehyde at room temperature for 20 min, then rinsed three times with PBS. Following fixation, cells were permeabilized with 0.2% Triton X-100 and incubated in a blocking solution (5% BSA or normal serum (goat, rabbit or horse) and 0.1% Triton-X in PBS) for 1 hour. For single or co-immunofluorescence staining, primary antibodies diluted in blocking solution were added overnight at 4°C overnight. To ensure specificity, a no primary antibody control staining was performed. The slides were then washed in PBS and incubated with the appropriate secondary antibody for 1 hour at room temperature and counterstained/mounted with Vectashield containing DAPI (Vector Laboratories). Images were acquired on an inverted fluorescence microscope (Nikon Eclipse E800, Morrell Instruments) controlled by SPOT Basic imaging software (Spot Imaging Solutions/Morrell Instruments). At least n=100 cells from three independent BMI/LGR5 co-staining experiments were analyzed to observe and record types of mitotic division: symmetric (LGR5/LGR5 or BMI1/BMI1) or asymmetric: (BMI1/LGR5). Data was presented as fraction (%) ‘asymmetric vs. symmetric cell divisions’ with means ± SEM and the significance was tested with Student t-test. Asymmetric daughter nuclei were further analyzed using SPOT software to compare mean diameters.

The CCICs co-stained for NUMB and PARD3A were analyzed by confocal microscopy for 3D rotational reconstruction using DRAQ-5 dye (Cell Signaling) to label DNA content. In brief, confocal microscopy was performed at room temperature on the Zeiss LSM 510 laser

scanning confocal microscope using a plan Apo 63× 1.40 oil objective. Images were collected and analyzed with confocal software (LSM 510 Meta; Zeiss) and Photoshop (Adobe).

Microscopy of human colonic tumor tissue

Frozen sections of normal human colonic tissue or tissue from various stages of colon cancer (Normal colon, n = 20, n=5 per CRC stage) embedded in O.C.T were obtained. Sections were stained with Hematoxylin and Eosin (H&E) according to standard methods. For immunofluorescence, sections were allowed to warm to room temperature, fixed in 4% PFA for 15 minutes and subsequently followed the above protocol for CCIC immunofluorescence. Sections were analyzed for α-TUBULIN, Ki67, and LGR5 and BMI1 co-expression. The fraction of dividing BMI1+/LGR5+/α-TUBULIN+ asymmetric pairs was quantified in α-TUBULIN+ dividing pairs per 500 crypts. The data represent the mean ± S.E.M from 1500 crypts/specimen.

Quantitative RT-PCR and Protein Analysis

A Qiagen RNeasy Plus kit was used to extract total RNA followed by reverse transcription to cDNA using ABI Taqman Reverse Transcription kit (Applied Biosystems). ABI Taqman Master mix and ABI Prism HT7900 were used to run quantitative real-time PCR. Taqman primers (ABI) purchased from Life Technologies were used for BMI1 (Product ID: Hs00995536_m1), LGR5 (Product ID: Hs00969422_m1), HES1 (Product ID: Hs00172878_m1), HES5 (Product ID: Hs01387463_g1), Cyclin D2 (CCND2) (Product ID: Hs00153380_m1), p21 (CDKN1A) (Product ID: Hs00355782_m1), ODC1 (Product ID: Hs01547697_g1), and GAPDH (control) (Product ID: Hs02758991_g1). The data represents the average result of three independent experiments normalized to GAPDH with error bars designating S.E.M. Protein isolation from CCICs, ISCs, and harvested mouse intestinal tissue as well as methods for Western Blotting were performed as previously described [5]. β-actin was used as a control for normalization.

Clonogenicity and Xenograft Tumor Assays.

Flow cytometry was first used to analyze CCICs according to side scattering and forward scattering to isolate a 'doublet' population. 7-AAD dye (Molecular Probes, A-1310) was used to label CCICs just prior to FACS to assay viability in the doublet population. Flow cytometry was then used to sort CCICs from this gated doublet population into four subpopulations: LGR5+/NOTCH1+, LGR5+/NOTCH1-, LGR5-/NOTCH1+, and LGR5-/NOTCH1-. This was achieved by incubating CCICs with a NOTCH1-PE conjugated antibody and an LGR5 primary antibody that was then labeled with FITC. A subset of each of the four populations was harvested and analyzed for BMI1 and LGR5 expression by RT-PCR as described above. A subset of each of the four populations was also isolated, incubated with BMI1-CY5.5 conjugated antibody, and analyzed for BMI1 expression by FACS. A subset of LGR5+/NOTCH1- and LGR5-/NOTCH1+ CCIC populations were also plated in chamber slides for time lapse microscopy over 48 hours to observe the generation of asymmetric pairs that were fixed at 48 hours and analyzed by IF as described earlier. A subset of LGR5+/NOTCH1+ CCICs were plated in chamber slides, fixed and visualized by immunofluorescence for BMI1 and LGR5 according to the above protocol. To validate that IF results were not the result of bound FACS antibody, LGR5+/NOTCH1+ CCICs were also plated, fixed and incubated directly with Alexa-488 or -555 secondary antibodies. For clonogenicity assays, sorted cells (LGR5+/NOTCH1+, LGR5+/NOTCH1-, LGR5-/NOTCH1+, and LGR5-/NOTCH1-) or unsorted CCICs (control) were embedded in Matrigel (BD Biosciences) and seeded in 24-well plates. Cells were cultured in CCIC growth medium and observed over 14 days to assess clonogenicity based on the number of colonies formed. In order to characterize *in vivo* tumor potential, CCICs representing five populations (LGR5+/NOTCH1+, LGR5+/NOTCH1-, LGR5-/NOTCH1+, and LGR5-/NOTCH1, or unsorted cells (control)) were subcutaneously injected into 8 week old NOD/SCID mice into the upper left back, upper right back, mid back, lower left back and lower right back,

respectively, of each mouse. Injections contained 1000 CCICs suspended in 200ul of 1:1 culture medium: Matrigel mixture. Tumor incidence was analyzed after 7 weeks by visual inspection. Following euthanasia, tumors were harvested and measured using a caliper, and the associated volume was calculated according to the formula: $\frac{1}{2}(LxW^2)$ where L and W represent the length and width of the tumor, respectively. The data is represented as the mean ± S.E.M. derived from 5 mice per treatment group. Xenograft tumors from one animal were subsequently embedded in O.C.T, frozen, cryo-sectioned, and stained with Hematoxylin and Eosin (H&E) or analyzed by co-IF for BMI1, LGR5, α-TUBULIN and Ki67 expression. Each xenograft tumor from each of the remaining four animals was separately minced into small fragments, resuspended in PBS, and centrifuged to remove debris in the supernatant. Tumor fragments were then suspended in Accumax/EDTA solution (Millipore) and incubated at room temperature for 30 minutes while shaking. After incubation, fragments were further mechanically disrupted by pipetting and centrifuged to collect a cell pellet. The supernatant was discarded and each pellet was resuspended in 2 mls PBS and passed through a 70um filter to collect single cells and doublets. After cell counting, the suspension was incubated with 7-AAD dye to assess viability, a BMI1-CY5 conjugated antibody, and an LGR5 primary antibody that was subsequently with FITC. FACS was conducted using a Beckman Coulter flow cytometer with a 130um filter to allow analysis of single and doublet CCICs. FlowJo software was used to analyze data and to gate populations according to 7-AAD viability, and forward and side scattering. Cutoff thresholds were provided by using unstained dissociated xenograft tumor cells as a negative control.

An additional xenograft experiment was performed by injecting 1 x 10^6 unsorted CCICs subcutaneously into 8 week old NOD/SCID mice (n = 6) to propagate tumors over four weeks. Subsequently, tumors were directly injected over 3 days with DMSO (n = 3 mice) or DAPT (n = 3 mice) delivered at a dose of 200 mg/kg every 12 hours [6]. Tumors were then harvested,

dissociated and subjected to FACS, Western blotting and RT-PCR analysis.

Animal experiments for Mouse Intestinal Stem Cell Studies.

LGR5-EGFP and LGR5-EGFP-creER/POFUT-1$^{flox/flox}$ mice on a mixed 129/C57BL/6 background were a generous gift from Dr. Leonard Augenlicht's laboratory. Mice were genotyped to confirm allelic identity using PCR analysis with LGR5 common forward primer: 5'- CTGCTCTCTGCTCCCAGTCT-3', LGR5 WT reverse primer: 5'-ATACCCCATCCCTTTTGAGC-3', LGR5 mutant reverse primer: 5'-GAACTTCAGGGTCAGCTTGC -3', POFUT-1 forward primer: 5'-GGGTCACCTTCATGTACAAGTGAGTG-3' and POFUT-1 reverse primer: 5'-ACCCACAGGCTGTGCAGTCTTTG-3'. The thermocyling profile used for PCR amplification is described as follows: for LGR5-EGFP: 94°C (3 min)/[94°C (30 sec), 66°C (30 sec), 72°C (30 sec)] for 35 cycles/72°C (2 min) and for POFUT-1: 94°C (2 min)/[94°C (30 sec), 58°C (30 sec), 72°C (90 sec)] for 34 cycles/72°C (5 min). Daily intraperitoneal (i.p) injections of Tamoxifen (Sigma) at a dose of 75 mg/kg dissolved in sterile corn oil were used for 5 consecutive days to induce Cre enzyme activity in 8 week old POFUT-1$^{flox/flox}$ mice [6]. The DAPT treatment regimen for LGR5-EGFP/POFUT-1$^{+/+}$ mice was 200 mg/kg every 12 hours for 3 days delivered by i.p injection [6]. As a control, mice were treated with DMSO (Sigma) at the corresponding time points. For DSS treatment, 8 week old LGR5-EGFP mice were administered 3% Dextran Sodium Sulfate (DSS) (36,000–50,000 kDa; MP Biomedicals) in the drinking water for 5 days, followed by plain water for 5 days. During the last three days of the plain water diet, mice were injected i.p. with DMSO or DAPT according to the regimen described earlier. All experiments were performed in accordance with the ethical and care guidelines established by the Research Animal Resource Center of Weill Cornell Medical College followed the protocol (2009-0029).

Intestinal Crypt isolation and Organoid Culture.

Small intestines and colons were harvested and opened longitudinally immediately after

sacrificing 8-week-old untreated LGR5-EGFP and LGR5-EGFP-creER/POFUT-1$^{flox/flox}$ mice for establishing organoid culture. Villi were removed gently using a glass coverslip. Murine tissue was washed with cold phosphate-buffered saline (PBS), cut into 5.0 mm fragments and again washed with cold PBS. Tissue fragments were incubated in 2.0mM EDTA in PBS on ice for 30 minutes followed by replacement of the EDTA medium with cold PBS. To release the villous fraction, a 10mL pipette was used to vigorously resuspend the tissue several times and the supernatant was discarded. The remaining tissue was then suspended in cold PBS and mechanically agitated several times to release crypts into the supernatant. Crypt fractions were collected and centrifuged at 6,000 RPM for 5 minutes to determine which fractions were most enriched by microscopic examination. The appropriate fractions were combined, diluted in cold PBS, and centrifuged to yield a crypt-containing pellet. The pellet was then diluted in Advanced DMEM/F12 (Invitrogen) containing Glutamax (Invitrogen), passed through 70um filter and centrifuged again to purify crypts for organoid culture or single cell dissociation. In order to achieve single cell dissociation from crypts, purified crypt pellets were incubated at 37°C in SMEM (Invitrogen) that contained 0.8 KU/ml DNase (Sigma), 10 uM ROCK pathway inhibitor Y-27632 (Sigma), and 1 mg/mL Trypsin-EDTA (Invitrogen) for 30 minutes. Single cells were then passed though a 40um filter.

Crypts or single cell derivatives were embedded in 50ul Matrigel (BD Biosciences) seeded on pre-warmed 24-well plates at a concentration of 1000 cells or crypts/mL. Following Matrigel polymerization, complete intestinal stem cell (ISC) media was added to each well. The formulation for ISC media is as follows: Advanced DMEM/F12 (Invitrogen) supplemented with Glutamax (Invitrogen), 10mM HEPES (Invitogen), N2 (Invitrogen), B27 without vitamin A (Invitrogen), and 1 uM *N*-acetylcysteine (Sigma). To ensure bioactivity of growth factors, a separate solution ISC media containing 50ng/mL EGF (Invitrogen), 100ng/mL Noggin

(Peprotech), and 10% R-SPONDIN1 conditioned media (generated in house) was freshly prepared each passage. Growth factors were added every 2 days with full media replacement every 4 days. Passage occurred once per week at a ratio of 1:4 by removing organoids from Matrigel with cold PBS, mechanically disrupted using a fire-polished glass pipette and resuspended in fresh Matrigel.

Immunofluorescence of Murine Crypts or *in vitro* organoids

Intestinal tissues of LGR5-EGFP mice and LGR5-EGFP-creER/POFUT-1$^{flox/flox}$ mice treated *in vivo* as described earlier (n=3 per condition) were harvested, snap frozen in O.C.T, and cryo-sectioned. Frozen intestinal tissue corresponding to NICD overexpression (OE) was a generous gift from Xiling Shen's laboratory. Briefly, LGR5-EGFP-CreERT2 x Rosa26-YFP-NICD knock-in mouse strain was treated daily with 75 mg/kg Tamoxifen for 8 consecutive days to induce Cre enzyme activity and NICD-OE phenotype. All murine frozen tissue specimens were fixed with 4% PFA for co-immunofluorescence using BMI1 and LGR5 (detected by GFP) expression according to the protocol described above. DAPI (Invitrogen) was used as a counterstain for IF on the inverted fluorescent microscope. Murine frozen tissue sections were also used for staining with Hematoxylin and Eosin according to standard protocol. LGR5 and BMI1 expression was quantified within individual crypts using n=100 crypts/mouse.

Intestinal organoids embedded in Matrigel that were treated under stated conditions were either fixed with 4% PFA for 15 minutes at room temperature for co-immunofluorescence according to the established protocol or harvested for protein analysis via Western Blotting using methods previously described [5]. Visualization of organoids was performed using BMI1 and LGR5 (detected by GFP) expression and ToPro-3 as a nuclear counterstain on a Zeiss LSM 510 laser scanning confocal microscope using an Apo 40× 1.40 oil objective. The experiment was performed in triplicate and LGR5 and BMI1 expression was quantified within individual organoids using n=100 organoids/replicate.

In a 16-hour pair cell assay, single LGR5-EGFP ISCs were treated with one of the following: DMSO, 10uM DAPT (EMD Millipore) for 48 hours [1], or 1uM JAG-1 (AnaSpec) for 48 hours [7]. ISCs were then fixed and stained for BMI1, LGR5 and TUBULIN expression to observe dividing pairs. In order to determine TUBULIN antibody specificity following a 16 hour pair cell assay, single ISCs were treated with 10μM colchicine (Santa Cruz: cat # 64-86-8) for 4 hours prior to fixation [8]. In a separate pair cell assay, single LGR5-EGFP ISCs were treated with 10ng/ml TNF-a (R&D) dissolved in culture medium for 72 hours. TNF-a–treated ISCs were simultaneously treated with DMSO or DAPT during the last 48 hours as described above. Subsequently, ISCs were subjected to FACS analysis for BMI1 and LGR5 expression.

Single LGR5-EGFP ISCs were also transfected with MYC-siRNA (Santa Cruz Biotech cat. no: sc-29227) or scrambled siRNA (Santa Cruz Biotech cat. no: 37007) according to the manufacturer's instructions. Subsequently, FACS analysis was performed for BMI1 and LGR5 expression. Additionally, following a 16 hour pair cell assay LGR5-EGFP ISCs transfected with MYC-siRNA or scrambled siRNA were pulsed with 10mM BrdU (Sigma) for three hours, fixed in cold 70% ethanol, followed by incubation for 1 hour in 2M HCl. Next, cells were washed with PBS and incubated for 2 minutes with 100mM $Na_2B_4O_7$. The protocol for co-IF was then followed beginning with blocking in 10% normal goat serum for 1 hour. BrdU labeling was quantified in BMI1+/LGR5+ asymmetric pairs for incorporation into LGR5+, BMI1+ or both LGR5+ and BMI1+ ISCs.

Figure 1. CRC tumors contain BMI1+/LGR5+ cell pairs.

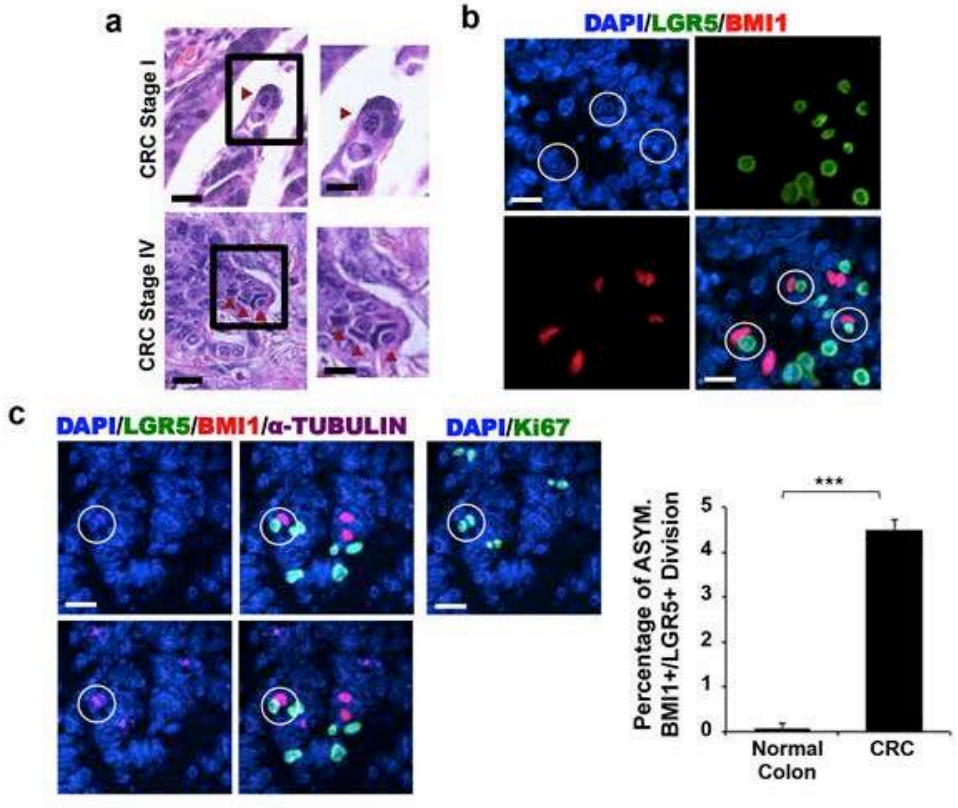

(**a**) Representative H&E images of human tumor tissue derived from Colorectal Cancer (CRC) Stage I (top row) and Stage IV (bottom row) at low (left) and high (right) magnifications, showing the presence of cell pairs with asymmetric morphology (a cell with a long, slender nucleus adjacent to another cell with a rounded nucleus). Scale bar represents 50 μm and 25 μm at low and high magnifications, respectively. (**b**) Representative co-IF staining of human colonic tumor section derived from CRC stage IV showing the presence of BMI1+(red)/LGR5 (green) asymmetric CCIC pairs. DAPI (blue) labels nuclei and scale bar represents 25μm. (**c**) Left: Representative co-IF of human CRC tumor specimen showing LGR5 (green), BMI1 (red), and α-TUBULIN (purple) expression. Also shown is Ki67 staining (green). DAPI (blue) labels nuclei and scale bar represents 25 μm. Right: Quantitative analysis of the frequency of dividing (α-TUBULIN+) BMI1+/LGR5+ asymmetric cell pairs in normal colon vs. CRC tumor tissue based on co-IF. The data represents the mean ± S.E.M (***, p = 0.001; Student t-test).

Figure 2. Characterization of asymmetric BMI1+/LGR5+ CCIC daughter pairs.

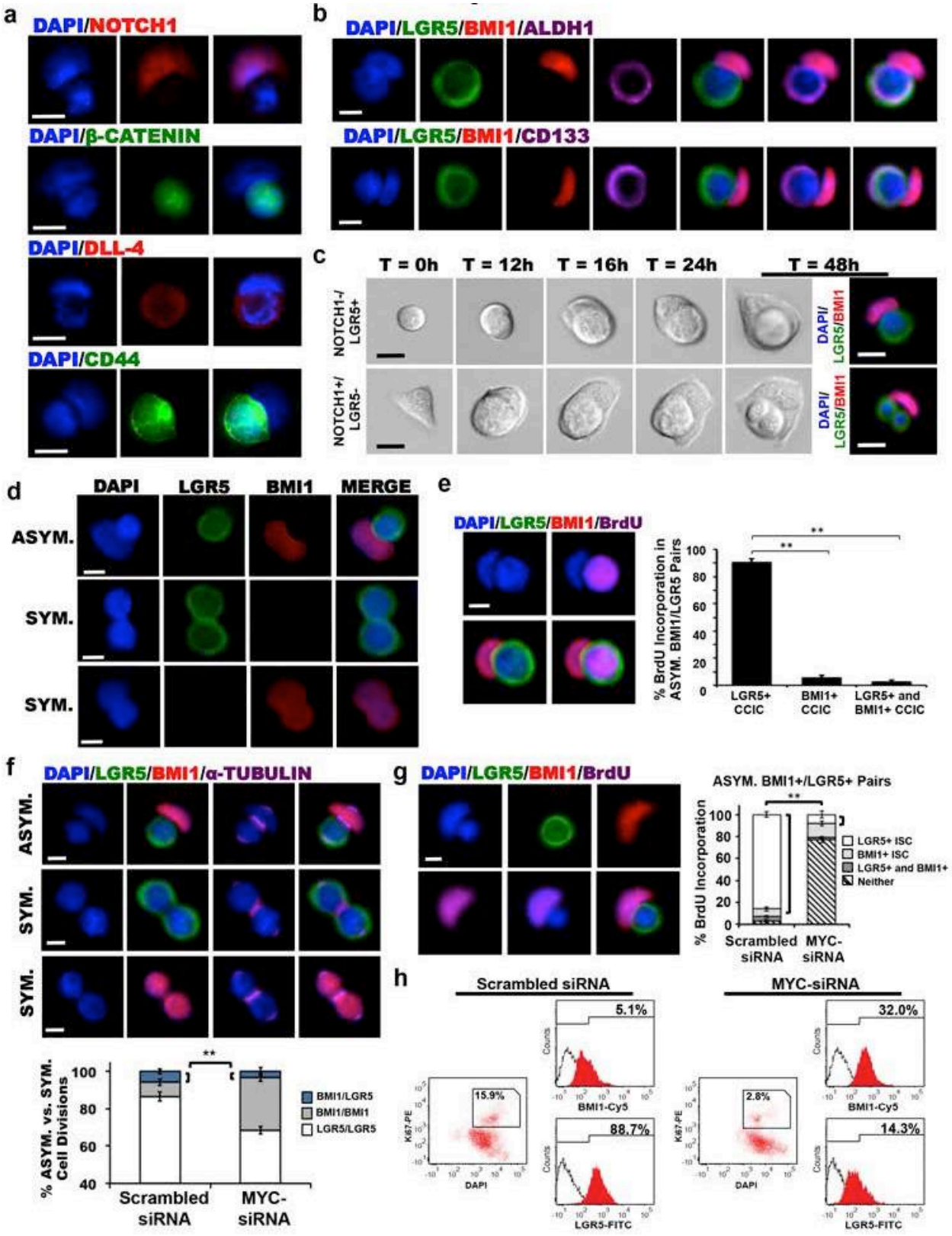

(Also see Supplementary Fig. 1, Fig. 2)

(a) IF images demonstrating asymmetric partitioning of various cell markers; BMI1+ CCIC (NOTCH1+); LGR5+ CCIC (β-Catenin+, DLL4+, CD44+). DAPI (blue) labels nuclei; scale bar represents 10μm. **(b)** Co-IF images of BMI1+ (red)/LGR5+ (green) CCIC daughter pairs showing asymmetric expression of ALDH1 (purple) and CD133 (purple). DAPI (blue) labels nuclei and scale bar represents 10μm. **(c)** Representative time-lapse series of single NOTCH1-/LGR5+ CCIC (top panel) and NOTCH1+/LGR5- CCIC (bottom panel) undergoing asymmetric division over 48 hours. Shown also is co-IF for each asymmetric CCIC daughter pair after fixation at 48 hours, indicating LGR5 (green) and BMI1 (red) expression. DAPI labels nuclei and scale bar represents 10μm in bright field and IF images. **(d)** Co-IF based on BMI1 (red) and LGR5 (green) staining showing segregation of stem cell markers in asymmetric and symmetric CCIC daughter pairs. DAPI (blue) labels nuclei; scale bar represents 10μm. (**e**) BrdU incorporation assay following the division of a single CCIC to generate a BMI1+/LGR5+ daughter pair. Left: Representative co-IF image based on LGR5 (green), BMI1 (red), and BrdU (purple) staining. DAPI (blue) labels nuclei; scale bar represents 10μm. Right: Quantitative analysis in asymmetric BMI1+/LGR5+ pairs with percentage of BrdU incorporation present in the LGR5+ CCIC, BMI1+ CCIC or both LGR5+ and BMI1+ CCIC daughters indicated (**, $p = 0.004$, one-way ANOVA). **(f)** Single CCIC were transfected with scrambled siRNA (Sc. siRNA) or MYC-siRNA. Top: Representative co-IF images of CCIC daughter pairs undergoing BMI1+/LGR5+ asymmetric, LGR5+ symmetric, or BMI1+ symmetric division. IF staining: LGR5 (green), BMI1 (red) and α-TUBULIN (purple). DAPI (blue) labels nuclei and scale bar represents 10μm. Bottom: Percentage of CCIC undergoing BMI1+/LGR5+ asymmetric (blue), BMI1+/BMI1+ symmetric (grey), or LGR5+/LGR5+ symmetric (white) cell division determined by co-IF for LGR5, BMI1, and α-TUBULIN expression. The data represents mean ± S.E.M from three independent experiments with n = 100/replicate (**, $p = 0.0033$, one-way ANOVA). **(g)**

BrdU incorporation assay following the division of a single CCIC transfected with MYC-siRNA to generate a BMI1+/LGR5+ daughter pair. Left: Representative co-IF image based on LGR5 (green), BMI1 (red), and BrdU (purple) staining. DAPI (blue) labels nuclei; scale bar represents 10μm. Right: Quantitative analysis in asymmetric BMI1+/LGR5+ pairs with percentage of BrdU incorporation present in LGR5+ CCIC, BMI1+ CCIC, both LGR5+ and BMI1+ CCICs, or neither indicated (**, $p = 0.005$, one-way ANOVA). **(h)** FACS analysis of CCIC transfected with scrambled siRNA (left) or MYC-siRNA (right) showing the expression of LGR5 and BMI1 within the gated Ki67+ dividing population.

Figure 3. Xenograft tumors from CCIC pairs.

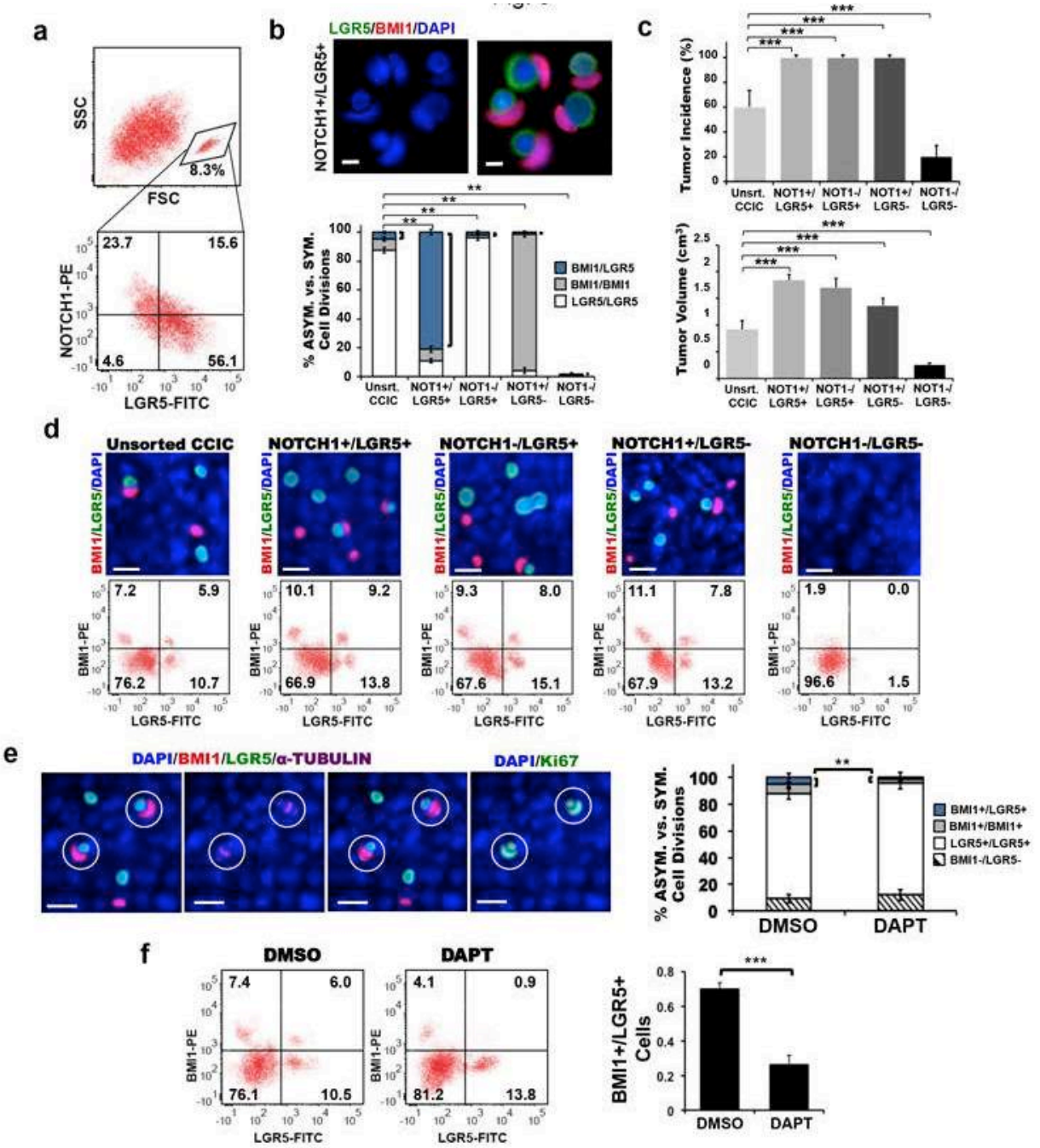

(Also see Supplementary Fig. 3)

(a) FACS plots showing a gated population (~8.3%) of CCIC with larger forward scattering (presumably doublets) and the expression of NOTCH1 and LGR5 within the gated population. The cutoff thresholds are provided by the negative controls with isotype-matched IgG followed

by FITC or PE conjugated secondary antibodies. **(b)** Top: Representative co-IF image of NOTCH1+/LGR5+ CCIC fraction, showing enrichment of BMI1+(red)/LGR5+(green) asymmetric daughter cell pairs. DAPI (blue) labels nuclei; scale bar represents 10μm. Bottom: Fraction of BMI1+/LGR5+ asymmetric (blue), BMI1+/BMI1+ symmetric (grey) and LGR5+/LGR5+ symmetric (white) cell divisions in unsorted (control), NOTCH1+/LGR5+, NOTCH1-/LGR5+, NOTCH1+/LGR5-, and NOTCH1-/LGR5- CCIC populations. The data represents mean ± S.E.M. from three independent experiments with n = 100 (**, p = 0.009; one-way ANOVA)**.** Unsorted: 'Unsrt'; NOTCH1: 'NOT1". **(c)** Unsorted (control), NOTCH1+/LGR5+, NOTCH1-/LGR5+, NOTCH1+/LGR5-, and NOTCH1-/LGR5- CCIC populations were each injected subcutaneously into distinct anatomical locations of each NOD/SCID mouse (n = 5) to develop xenograft tumors that were assayed after 7 weeks. Shown is quantification of tumor incidence (top panel) and tumor volume (bottom panel) derived from each CCIC population injected. The data represents mean ± S.E.M. of n = 5 mice. (left: ***, p =0.0005; right: ***, p=0.0004; one-way ANOVA). Unsorted: 'Unsrt'; NOTCH1: 'NOT1". (**d**) Top: Co-IF showing BMI1(red) and LGR5 (green) expression in xenograft tumors from (c). DAPI (blue) labels nuclei and scale bar represents 25μm. Bottom: FACS analysis showing BMI1 and LGR5 expression in dissociated xenograft tumors from (c). **(e)** $1x10^6$ unsorted CCICs were injected subcutaneously (s.c.) into NOD/SCID mice (n = 6) to develop xenograft tumors over 5 weeks. Subsequently, tumors were directly injected with either DMSO (n = 3) or DAPT (n = 3) over 72 hours, then harvested and assayed. Left: Representative co-IF of xenograft tumor showing BMI1+(red)/LGR5+(green) asymmetric pairs with α-TUBULIN (purple) expression. Also shown is Ki67 staining (green). DAPI (blue) labels nuclei and scale bar represents 25 μm. Right: Frequency of BMI1+/LGR5+ asymmetric (blue), BMI1+/BMI1+ symmetric (grey), or LGR5+/LGR5+ symmetric (white) cell division from xenograft tumors determined by co-IF for

LGR5, BMI1, and α-TUBULIN expression. The data represent mean ± S.E.M of n = 500 TUBULIN+ dividing pairs/mouse (**, p = 0.003, Student t-test). **(f)** Shown are representative FACS plots for BMI1 and LGR5 expression (left) and the ratio of BMI1+/LGR5+ cells determined by FACS (right) from xenograft assay developed in (e). The data represents mean ± S.E.M. of n = 3 mice/condition. (***, p =0.0002; Student t-test).

Figure 4. NOTCH signaling promotes BMI1+/LGR5+ daughter pairs.

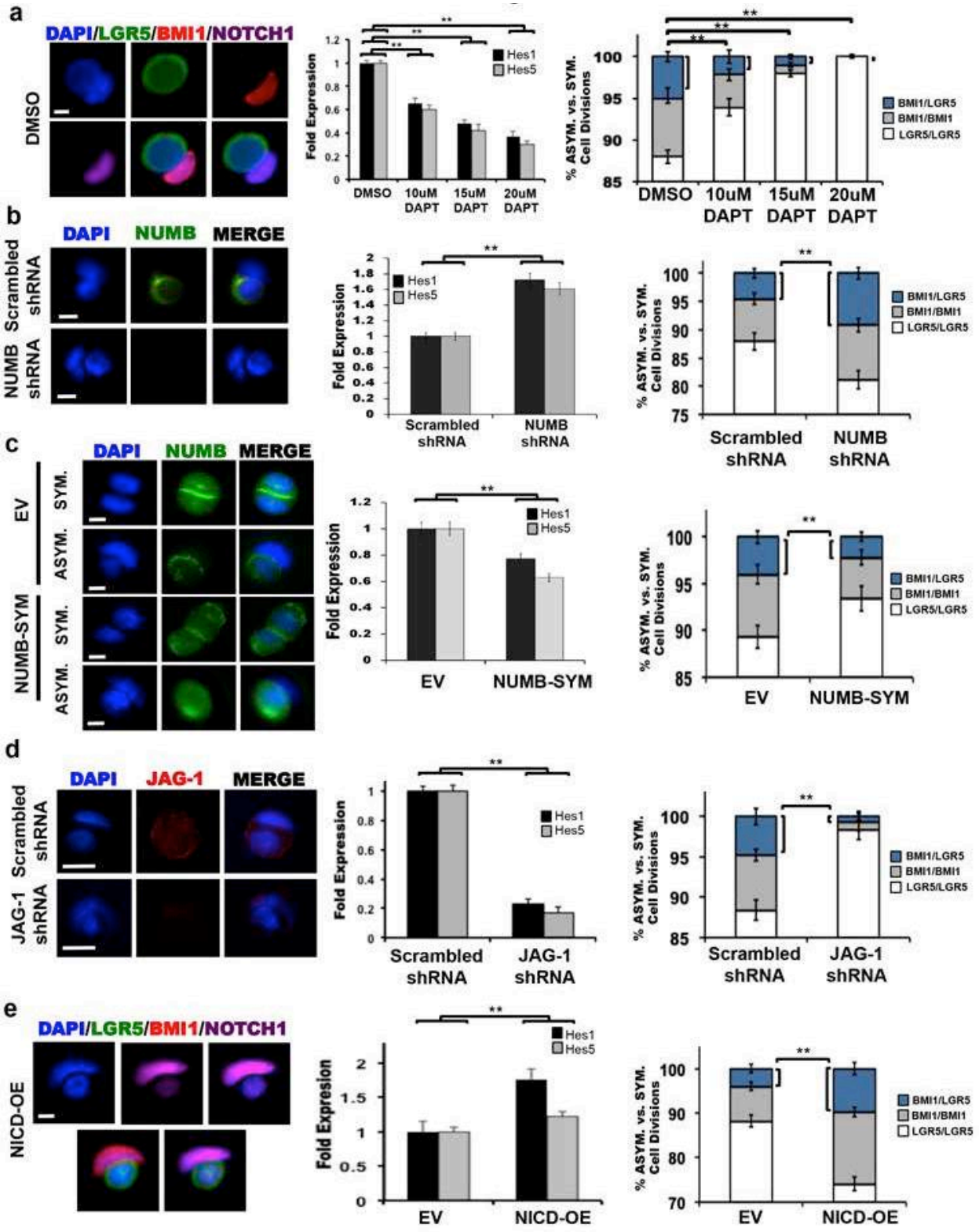

(Also see Supplementary Fig. 4)

(a) NOTCH signaling inhibition decreases BMI1+/LGR5+ CCIC pairs. In a pair-cell assay, single CCICs were treated with DMSO (control) vs. increasing concentrations of DAPT (γ-secretase inhibitor). Left: Representative co-IF image from DMSO condition of a BMI1+(red)/LGR5+(green) pair, indicating asymmetric NOTCH1 (purple) expression. DAPI labels nuclei and scale bar represents 10μm. Middle: RT-qPCR measurements of NOTCH signaling effector genes Hes1 and Hes5 expression with increasing concentrations of DAPT (performed in triplicate and presented mean ± S.E.M.). Right: Fraction of BMI1+/LGR5+ asymmetric (blue), BMI1+/BMI1+ symmetric (grey) and LGR5+/LGR5+ symmetric (white) cell divisions for each treatment condition (**, p = 0.01; one-way ANOVA for statistical significance). (**b**) Knockdown of NUMB increased NOTCH signaling activity and frequency of asymmetric BMI1+/LGR5+ pairs. Left: Representative IF images showing NUMB (green) staining of CCIC daughter pairs infected with scrambled shRNA (control) or NUMB-shRNA. DAPI (blue) labels nuclei and scale bar represents 10μm. Middle: RT-qPCR showing that Hes1 and Hes5 expression was increased by NUMB knockdown (performed in triplicate and presented mean ± S.E.M.). Right: Pair-cell assay of single CCICs infected with scrambled shRNA (control) versus NUMB-shRNA indicates that the frequency of asymmetric BMI1+/LGR5+ division (blue) increased upon knockdown of NUMB (**, p = 0.008; Student t-test for statistical significance). (**c**) Symmetric NUMB ('NUMB-SYM') mutant decreased NOTCH signaling and frequency of asymmetric BMI1+/LGR5+ pairs. Left: Representative IF staining of CCIC infected with NUMB-SYM. Top panel indicates normal segregation of NUMB (green) in empty vector (EV)-transduced CCIC (control); bottom panel shows that overexpression of NUMB-SYM has no effect on asymmetric daughter cell pair morphology or the partitioning of NUMB. DAPI (blue) labels nuclei and scale bar represents 10μm. Middle: NUMB-SYM decreased Hes1 and Hes5 expression measured by RT-qPCR (performed in triplicate and presented mean ±

S.E.M.). Right: Fraction of asymmetric BMI1+/LGR5+ cell divisions (blue) decreased in NUMB-SYM expressing CCICs relative to control (**, p = 0.0022; Student t-test for statistical significance). (**d**) Knockdown of JAG-1 decreased NOTCH signaling and frequency of asymmetric BMI1+/LGR5+ pairs. Left: Representative IF images showing JAG-1 (red) staining of CCIC daughter pairs infected with scrambled shRNA (control) or JAG-1 shRNA. DAPI (blue) labels nuclei and scale bar represents 10μm. Middle: JAG-1 knockdown decreased Hes1 and Hes5 expression measured by RT-qPCR (performed in triplicate and presented mean ± S.E.M.). Right: JAG-1 shRNA reduced the frequency of asymmetric BMI1+/LGR5+ division (blue) in CCICs relative to control (**, p = 0.0028; Student t-test for statistical significance). (**e**) Ectopic NICD expression increased NOTCH signaling and frequency of asymmetric BMI1+/LGR5+ pairs. CCICs were infected with an ectopic NICD expression (NICD-OE) construct. Left: Representative co-IF image of NICD-OE BMI1+(red)/ LGR5+(green) CCIC pair, indicating differential asymmetric NOTCH1 (purple) expression. Middle: NICD-OE increased Hes1 and (slightly) Hes5 levels measured by RT-qPCR (performed in triplicate and presented mean ± S.E.M.). Right: NICD-OE increased the frequency of asymmetric BMI1+/LGR5+ pairs (blue) relative to empty vector (EV)-transduced (control) CCICs (**, p = 0.0019; Student t-test for statistical significance). In all '% ASYM vs. SYM Cell Divisions' bar graphs, the fraction (expressed as percent) of single CCICs undergoing BMI1+/LGR5+ asymmetric (blue), BMI1+/BMI1+ symmetric (grey), or LGR5+/LGR5+ symmetric (white) cell division was determined by specific nuclear morphology and co-IF for LGR5 and BMI1 expression (data not shown). Each graph represents mean ± S.E.M from three independent experiments with n = 100/replicate.

Figure 5. NOTCH regulates balance between LGR5+ and BMI1+ ISC populations.

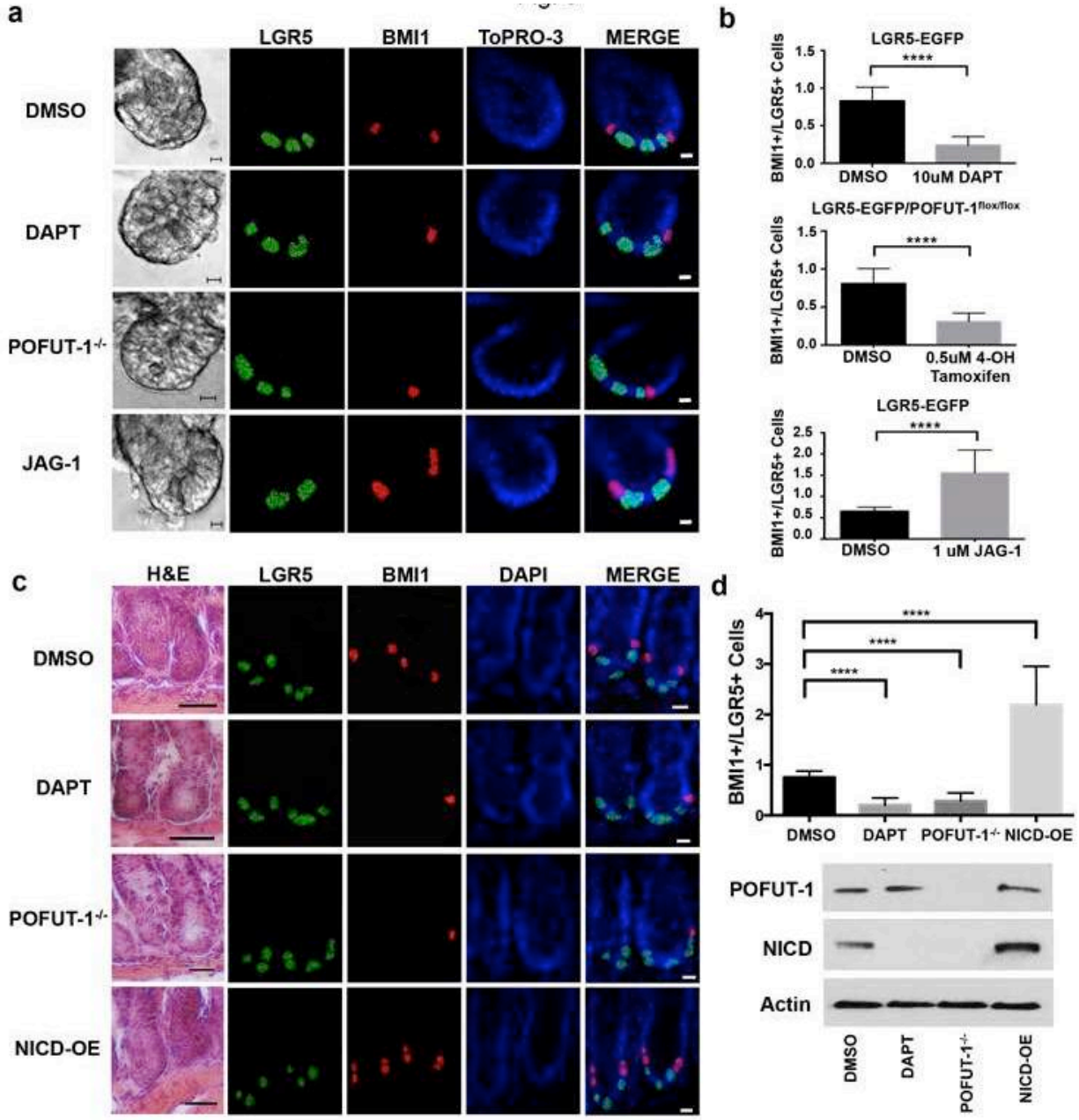

(Also see Supplementary Fig. 5)

(**a**) Representative bright field and IF images from mouse LGR5-EGFP or LGR5-EGFP-creER/POFUT-1$^{flox/flox}$ ISCs (propagated as organoids) after 48-hour treatment with DMSO (Control), 10uM DAPT, 0.5uM 4-OH-Tamoxifen to induce POFUT-1$^{-/-}$ phenotype, or 1uM JAG-1. Anti-GFP antibody (green) detects LGR5-GFP+ cells; BMI1 (red) and ToPRO-3 (blue) labels

nuclei. Scale bar represents 20μm. (**b**) Relative quantification of BMI1+ and LGR5+ cells for each experimental condition described in (a). The data represent independent experiments performed in triplicate shown as mean ± S.E.M of n=100 organoids /replicate (****, p=0.0001; Student t-test for statistical significance). (**c**) *In vivo* treatments were administered by i.p injections as follows: DMSO (on LGR5-EGFP mice as control); DAPT (on LGR5-EGFP mice every 12 hours for 3 days); Tamoxifen (on LGR5-EGFP-creER/POFUT-$1^{flox/flox}$ mice every 24 hours for 5 consecutive days) to induce POFUT-$1^{-/-}$ phenotype; or Tamoxifen (on LGR5-EGFP-CreERT2/Rosa26-YFP-NICD mice every 24 hours for 8 consecutive days) to induce the NICD overexpression phenotype. Shown are representative images of intestinal crypts including H&E staining and co-IF for each condition. Anti-GFP antibody (green) detects LGR5-GFP+ cells; BMI1 (red) and DAPI (blue) labels nuclei. Scale bar represents 200μm for H&E images and 20μm for IF images. (**d**) Top: Relative quantification of BMI1+ and LGR5+ cells from mice (n=3 per treatment group) for each condition described in (c). The data represent mean ± S.E.M of n=100 crypts per mouse (****, p=0.0001, one-way ANOVA for statistical significance). Bottom: Western Blot analysis for POFUT-1 and NICD expression from harvested intestinal tissue under each condition. Actin was used as a loading control.

Figure 6. NOTCH signaling promotes asymmetric BMI1+/LGR5+ ISC division.

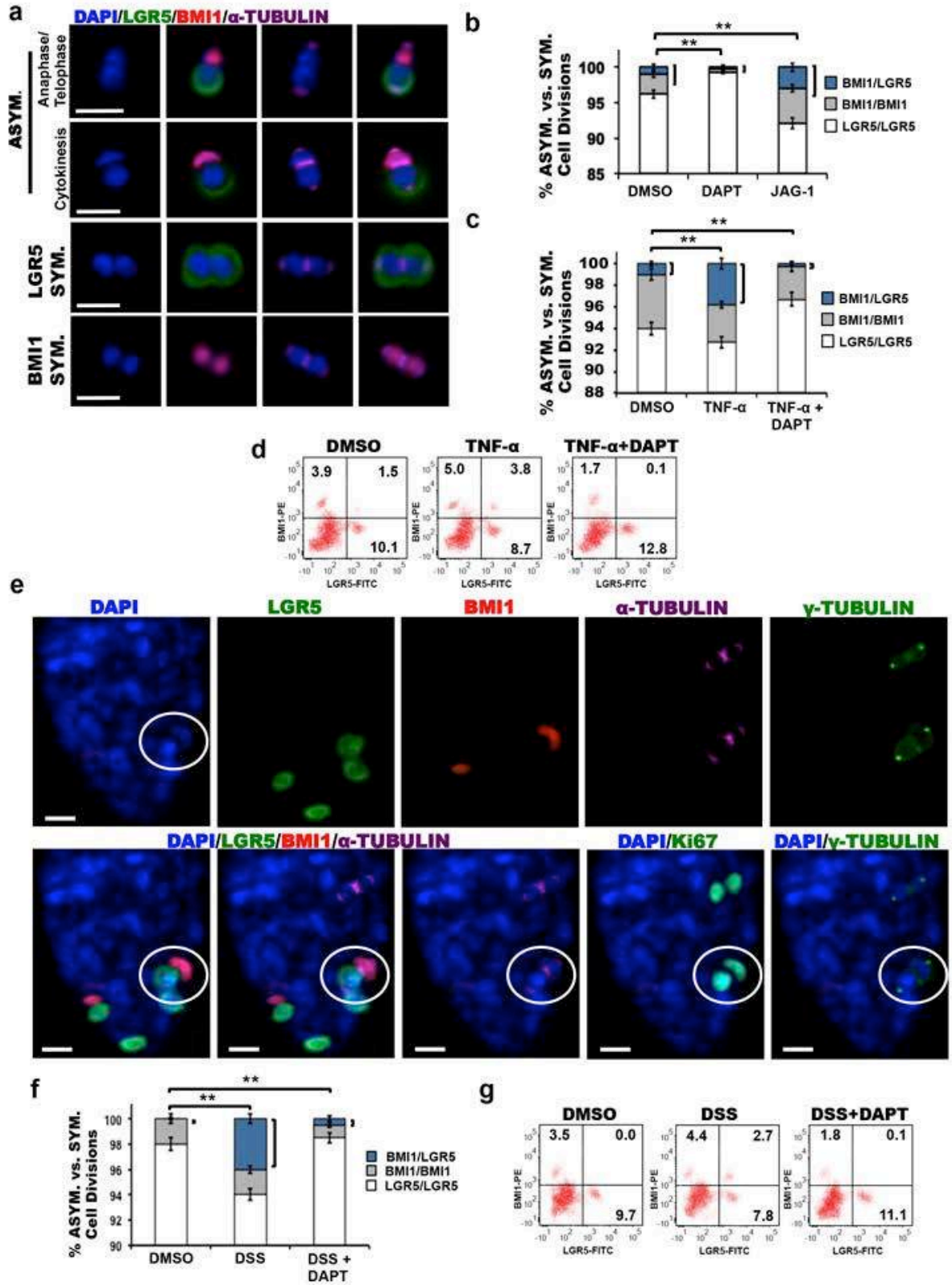

(Also see Supplementary Fig. 6, Fig. 7)

(**a**) Representative co-IF from pair cell assays showing a LGR5-EGFP ISC daughter pair just prior to completion of asymmetric (top) or LGR5+ symmetric (middle) or BMI1+ symmetric (bottom) cell division. IF staining: Anti-GFP antibody (green) detects LGR5, BMI1 (red), α-TUBULIN (purple), and DAPI (blue) labels nuclei. Scale bar represents 50μm. (**b**) Single LGR5-EGFP ISCs were treated with DMSO (control), 10uM DAPT or 1uM JAG-1 for 16h in a pair cell assay. Shown is percentage of single ISCs undergoing BMI1+/LGR5+ asymmetric (blue), BMI1+/BMI1+ symmetric (grey), or LGR5+/LGR5+ symmetric (white) cell division determined by co-IF for LGR5, BMI1, and α-TUBULIN expression. The frequency of BMI1+/LGR5+ asymmetric pairs decreased with NOTCH inhibition by DAPT (**, p = 0.002, one-way ANOVA) and increased with NOTCH stimulation by JAG-1 (**, p = 0.002, one-way ANOVA). The data represents mean ± S.E.M from three independent experiments with n = 100/replicate. **(c)** Single LGR5-EGFP ISCs were treated with DMSO in a pair cell assay. Additionally, LGR5-EGFP ISCs were treated with 10ng/ml TNF-α for 72 hours with simultaneous administration of DMSO or 10uM DAPT during the last 48 hours. Shown is percentage of single ISCs undergoing BMI1+/LGR5+ asymmetric (blue), BMI1+/BMI1+ symmetric (grey), or LGR5+/LGR5+ symmetric (white) cell division determined by co-IF for LGR5, BMI1, and α-TUBULIN expression. The data represents mean ± S.E.M from three independent experiments with n = 100/replicate (**, p = 0.003 (TNF-α), p = 0.002 (TNF-α+DAPT); one-way ANOVA). **(d)** FACS analysis showing BMI1 and LGR5 expression for each treatment condition following assay described in (c). **(e)** *In vivo* treatments (n = 3 mice/condition) were administered by i.p injections as follows: DMSO (on LGR5-EGFP mice as control). LGR5-EGFP mice were administered 3% DSS in the drinking water for 5 days, followed by plain water for 5 days. During the last three days of the plain water diet, mice were injected i.p. with DMSO or DAPT every 12 hours. Shown are representative co-IF images of intestinal crypts demonstrating BMI1+/LGR5+

asymmetric division. Anti-GFP antibody (green) detects LGR5-GFP+ cells; BMI1 (red), and α-TUBULIN (purple) expression. Also shown is Ki67 (green) and γ-TUBULIN (green) staining. DAPI (blue) labels nuclei and scale bar represents 20μm. **(f)** Quantitative analysis from mice (n=3 per treatment group) for each condition described in (e). Shown is the frequency of BMI1+/LGR5+ asymmetric (blue), BMI1+/BMI1+ symmetric (grey), or LGR5+/LGR5+ symmetric (white) cell division determined by co-IF for LGR5, BMI1, and α-TUBULIN expression. The data represent mean ± S.E.M of n = 500 TUBULIN+ dividing pairs/mouse (**, $p = 0.002$ (DSS), $p = 0.004$ (DSS+DAPT); one-way ANOVA). **(g)** FACS analysis showing BMI1 and LGR5 expression for each treatment condition following assay described in (e).

Supplementary Fig. 1. Characterization of BMI1+/LGR5+ CCIC asymmetric daughter cell pairs. Related to Fig. 2.

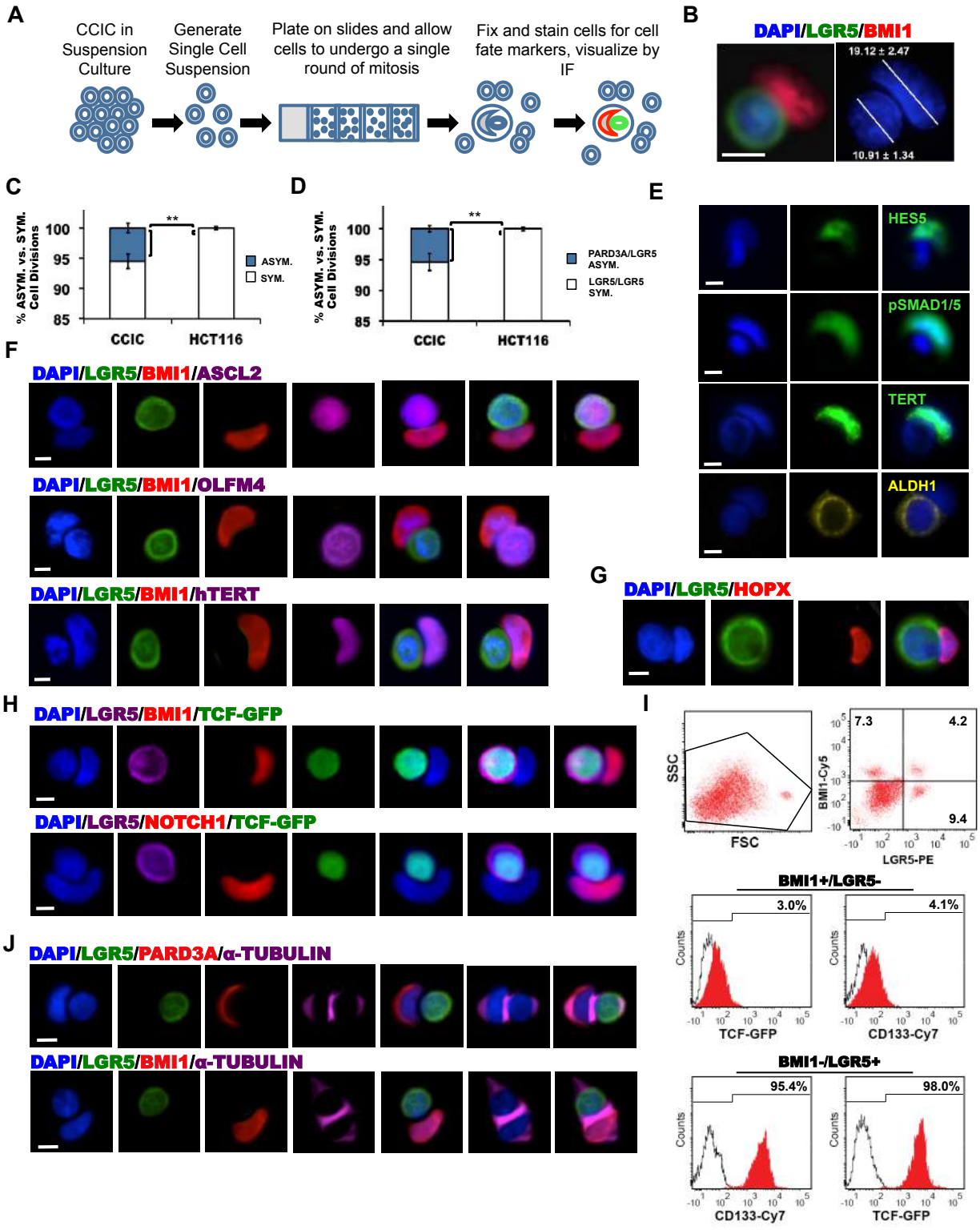

(A) Schematic representation of the pair-cell assay used to characterize asymmetric daughter cell pairs following mitosis. (B) Representative image of a BMI1+(red)/LGR5+(green) asymmetric nuclei pair stained with DAPI (blue) showing mean nuclear diameters (μm) ± S.E.M; scale bar represents 10μm. (C) Fraction of asymmetric (blue) vs. symmetric (white) cell divisions of single CCICs and HCT116 cells based on nuclear morphology. The data represents mean ± S.E.M from three independent experiments with n = 100 (**, p = 0.0029, Student t-test for statistical significance). (D) Fraction of cell divisions from single CCICs vs. HCT116 cells corresponding to asymmetric (blue) or symmetric (white) division based on nuclear morphology with co-IF for LGR5 and the asymmetric cell fate marker, PARD3A. No asymmetric division was detected in HCT116 cells (**, p = 0.0025, Student t-test for statistical significance). The data represents mean ± S.E.M from three independent experiments with n = 100/replicate. (E) IF images showing asymmetric partitioning of cell markers; BMI1+ CCIC daughter cell: (HES5+, pSMAD1/5+, hTERT+); LGR5+ CCIC daughter cell: (ALDH1+). DAPI (blue) labels nuclei and scale bar represents 10μm. (F) Co-IF images of BMI1+ (red)/LGR5+ (green) CCIC daughter pairs showing asymmetric expression of ASCL2, OLFM4, and hTERT (purple). DAPI (blue) labels nuclei and scale bar represents 10μm. (G) Representative co-IF based on LGR5 (green) and HOPX (red) staining in CCICs showing asymmetric distribution of stem cell markers in a daughter cell pair. DAPI (blue) labels nuclei and scale bar represents 10μm. (H) CCICs were transduced with TCF-GFP lentiviral construct and treated with WNT3A ligand to indicate WNT signaling status in a pair cell assay. Shown are representative co-IF series of a BMI1+ (red)/LGR5+ (purple) (top) or a NOTCH1+ (red)/LGR5+ (purple) (bottom) asymmetric CCIC daughter pair with active WNT signaling indicated by GFP (green) expression. DAPI (blue) labels nuclei and scale bar represents 10μm. (I) FACS plots of CCICs transduced with TCF-GFP lentiviral construct and treated with WNT3A ligand to indicate WNT signaling status. Shown is

forward scattering (FSC) vs. side scattering (SSC) analysis, indicating a gated population and the expression of BMI1 and LGR5 within this gated population (top). Also shown is the expression of TCF-GFP and CD133 within BMI1+/LGR5- (middle) and BMI1-/LGR5+ (bottom) subpopulations. (J) Top panel: Representative co-IF of CCIC daughter pair just prior to completion of cell division showing expression of LGR5 (green), asymmetric cell division marker PARD3A (red), and α-TUBULIN (purple). Bottom panel: Representative co-IF of CCIC daughter pair just prior to completion of cell division showing expression of LGR5 (green), BMI1 (red) and α-TUBULIN (purple). In both panels, DAPI (blue) labels nuclei and scale bar represents 10μm.

Supplementary Fig. 2. MYC knockdown in CCIC. Related to Fig. 2.

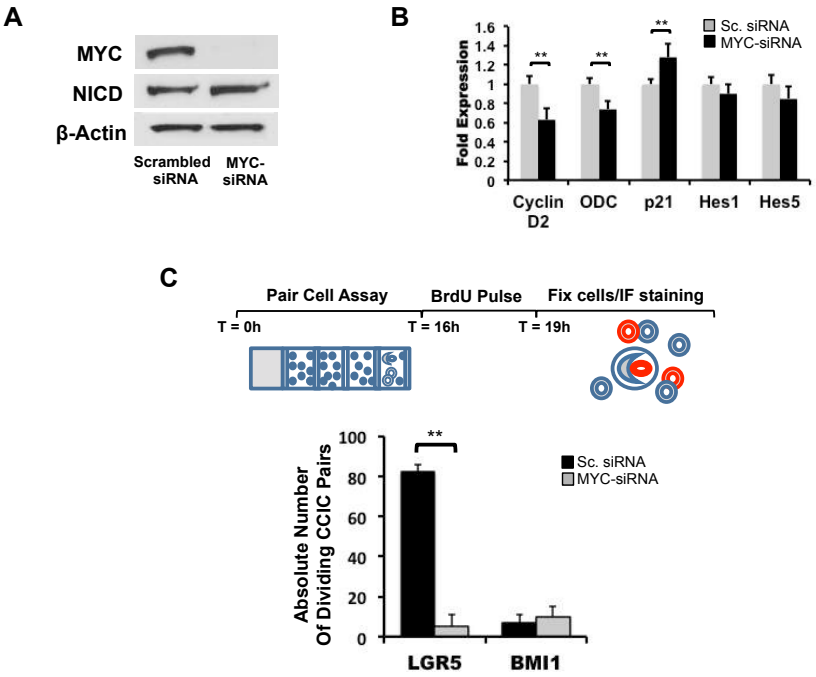

(A) CCIC were transfected with MYC-siRNA. Shown is Western blot data verifying MYC knockdown and similar NICD expression under DMSO (control) and MYC knockdown conditions. Actin was used as a loading control. (B) RT-PCR measurements of MYC target genes regulating cell cycle progression (Cyclin D2, Ornithine Decarboxylase (ODC), p21), as well as Hes1 and Hes5 expression in CCICs transfected with MYC-siRNA in a pair cell assay. The experiment was performed in triplicate and presented mean ± S.E.M. (**, p = 0.01; Student t-test). (C) CCIC were transfected with MYC-siRNA in a pair cell assay followed by BrdU incorporation. Top: Schematic representation of timeline showing 16-hour pair cell assay, followed by 3 hour BrdU labeling and immediate fixation and co-IF staining for BrdU, LGR5, and BMI1. Bottom: Quantitative analysis for the absolute number of LGR5+ and BMI1+ CCIC (transfected with scrambled siRNA or MYC-siRNA) observed dividing at T=19 hours. The experiment was performed in triplicate and presented mean ± S.E.M (**, p = .002, Student t-test).

Supplementary Fig. 3. Asymmetric NOTCH1+/LGR5+ CCIC pairs. Related to Fig. 3.

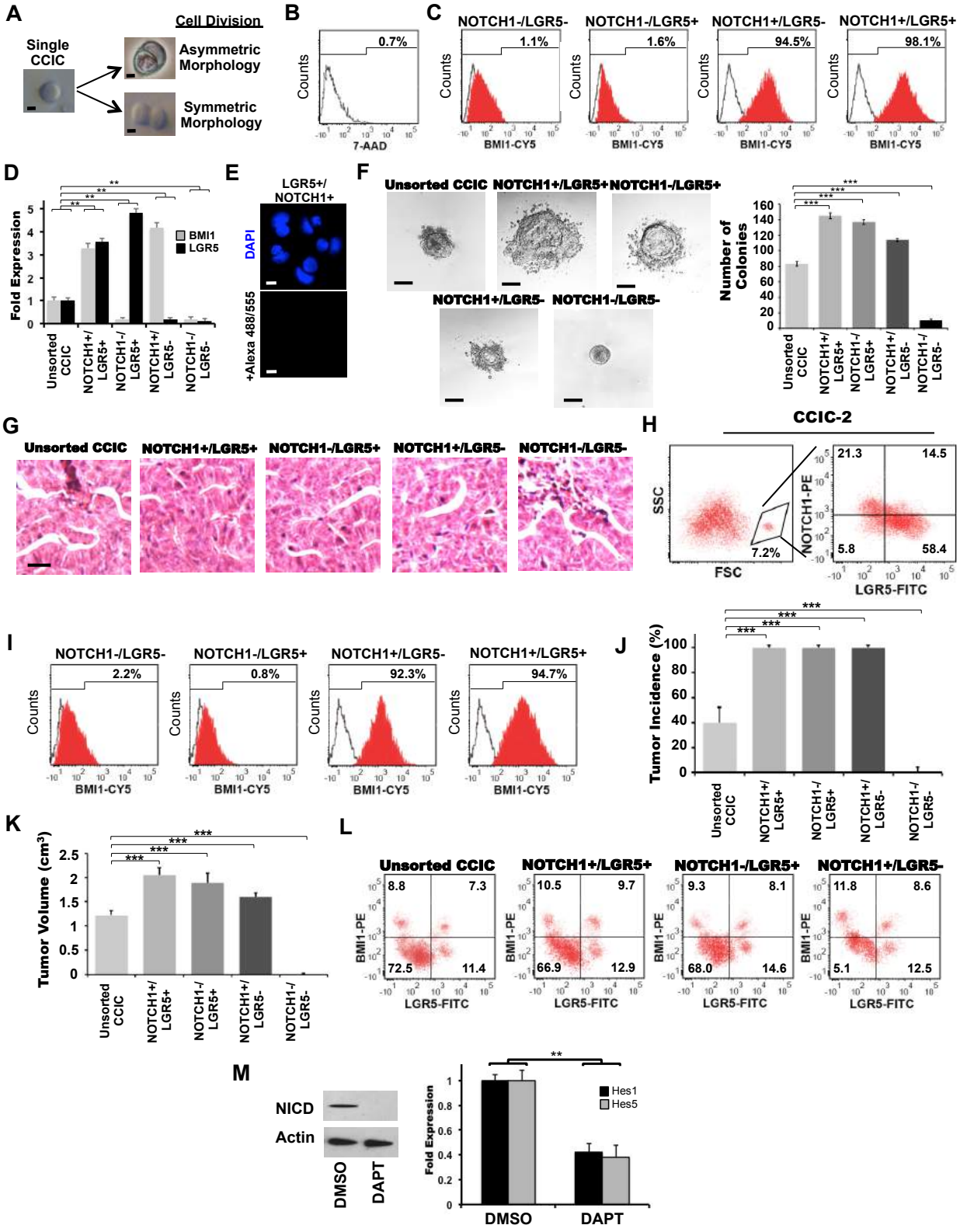

(A) Representative brightfield microscopy images illustrating the morphology associated with asymmetric and symmetric division in CCICs. Scale bar represents 10μm. (B) FACS data showing 7-AAD expression in the gated population of CCICs indicated in Fig. 3a. (C) FACS data showing intracellular BMI1 expression in a subset of each double sorted populations shown in Fig. 3a (NOTCH1-/LGR5-, NOTCH1-/LGR5+, NOTCH1+/LGR5-, NOTCH1+/LGR5+). (D) RT-PCR measurements of BMI1 and LGR5 gene expression in a subset of each NOTCH1/LGR5 double sorted populations shown in Fig. 3a. The experiment was performed in triplicate and presented mean ± S.E.M. (**, p = 0.01; Student t-test). (E) Representative co-IF using both Alexa-488 and Alexa-555 secondary antibody labeling of fixed NOTCH1+/LGR5+ CCICs without the addition of primary antibody. (F) In a clonogenicity assay, unsorted (control), NOTCH1+/LGR5+, NOTCH1-/LGR5+, NOTCH1+/LGR5-, and NOTCH1-/LGR5- CCIC populations were embedded in Matrigel and cultured for 14 days. Left: Representative bright field images of colonies derived from each CCIC population. Scale bar represents 50 μm. Right: Quantitative analysis of the number of colonies formed after 14 days. The data represents mean ± S.E.M from three independent experiments (***, p = 0.001; one-way ANOVA for statistical significance). (G) Unsorted (control), NOTCH1+/LGR5+, NOTCH1-/LGR5+, NOTCH1+/LGR5-, and NOTCH1-/LGR5- CCIC populations were each injected subcutaneously into distinct anatomical locations of each NOD/SCID mouse (n = 5) to develop xenograft tumors that were assayed after 7 weeks. Shown are representative H&E images of subcutaneous xenograft tumors derived from each CCIC population. Scale bar represents 200μm. (H) FACS plots from a separate CCIC line (CCIC-2) showing a gated population (~7.2%) of CCIC with larger forward scattering (presumably doublets) and the expression of NOTCH1 and LGR5 within the gated population. (I) FACS data showing intracellular BMI1 expression in a subset of each double sorted populations of CCIC-2 shown in Supplementary Fig. 2G (NOTCH1-/LGR5-,

NOTCH1-/LGR5+, NOTCH1+/LGR5-, NOTCH1+/LGR5+) (J) Unsorted (control), NOTCH1+/LGR5+, NOTCH1-/LGR5+, NOTCH1+/LGR5-, and NOTCH1-/LGR5- CCIC-2 populations were each injected subcutaneously into distinct anatomical locations of each NOD/SCID mouse (n = 5) to develop xenograft tumors that were assayed after 7 weeks. Shown is quantitative analysis of tumor incidence derived from each CCIC-2 population. The data represents mean ± S.E.M. of n = 5 mice. (***, p =0.001; one-way ANOVA for statistical significance). (K) Measurement of tumor volume derived from each CCIC-2 population injected in xenograft assay described in S2J. The data represents mean ± S.E.M. of n = 5 mice. (***, p =0.001; one-way ANOVA for statistical significance). (L) FACS analysis of dissociated tumors developed in xenograft assay (Supplementary Fig. 2J) from each CCIC-2 population showing LGR5 and BMI1 expression. (M) Western blot analysis for NICD (left) and RT-qPCR measurements (right) (performed in triplicate and presented mean ± S.E.M) for Hes1 and Hes5 expression from dissociated xenograft tumors described in Fig. 3e, Fig. 3f (**, p = .003; Student t-test).

Supplementary Fig. 4. Analysis of CCIC under NOTCH modulation. Related to Fig. 4.

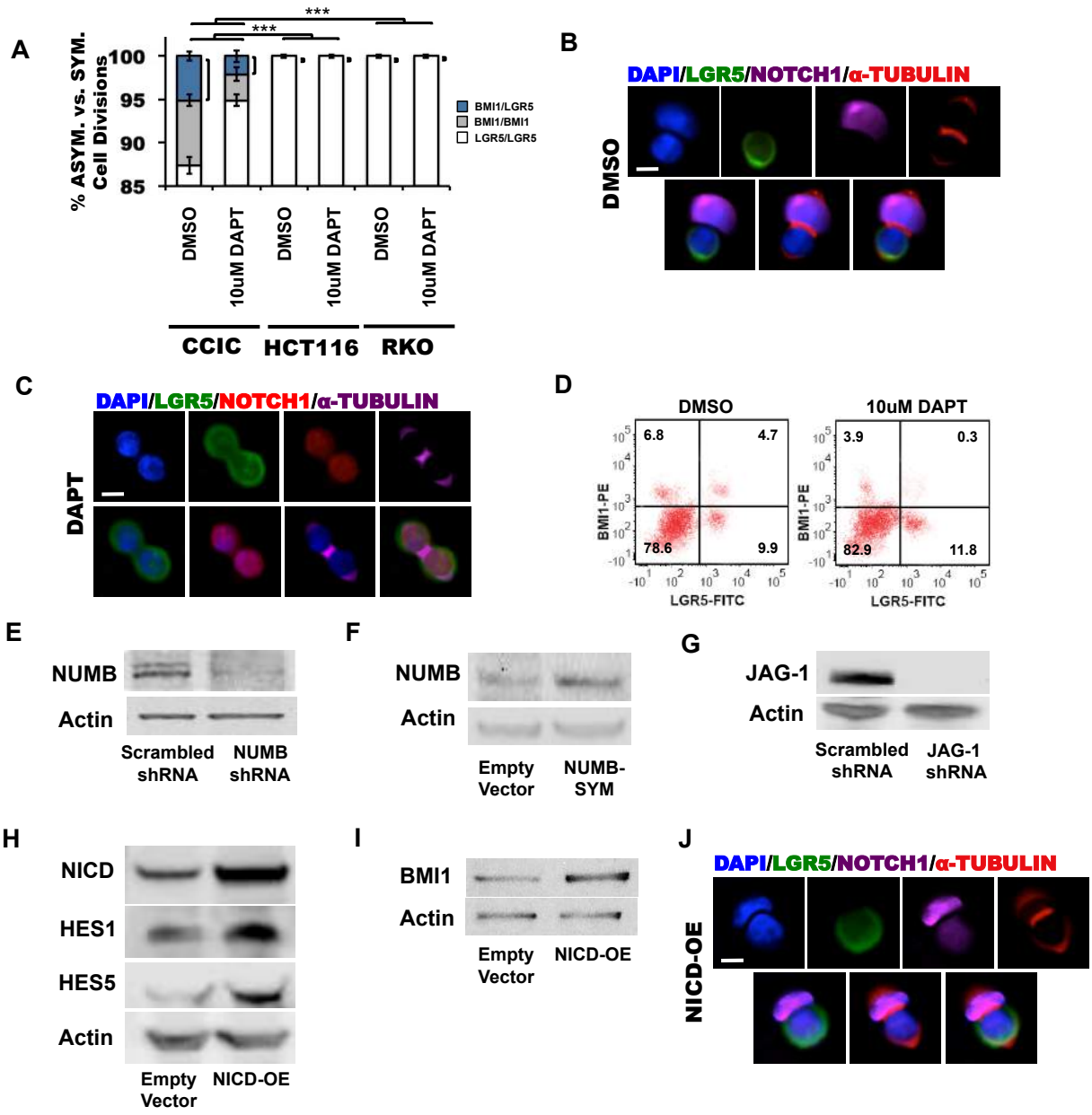

(A) In a pair-cell assay, single CCICs, HCT116 cells, and RKO cells were treated with DMSO (control) vs. DAPT (γ-secretase inhibitor). Shown is quantitative analysis for the percentage of BMI1+/LGR5+ asymmetric (blue), BMI1+/BMI1+ symmetric (grey), and LGR5+/LGR5+ symmetric (white) cell divisions detected for each condition (***, p = 0.001; one-way ANOVA for statistical significance). Each graph represents mean ± S.E.M from three independent

experiments with n = 100/replicate. (B) Corresponding co-IF images from the pair cell assay (Supplementary Fig. 4A) of CCICs treated with DMSO. Shown is a representative asymmetric CCIC daughter pair just prior to completion of cell division indicating LGR5 (green), NOTCH1 (purple) and α-TUBULIN (red) expression. DAPI (blue) labels nuclei and scale bar represents 10μm. (C) Corresponding co-IF images from the pair cell assay (Supplementary Fig. 4A) of CCICs treated with 10μM DAPT. Shown is a representative symmetric CCIC daughter pair just prior to completion of cell division indicating LGR5 (green), NOTCH1 (red) and α-TUBULIN (purple) expression. DAPI (blue) labels nuclei and scale bar represents 10μm. (D) FACS analysis indicating BMI1 and LGR5 expression following a pair-cell assay in which CCICs were treated with DMSO or DAPT. (E) Western blot verifying shRNA knockdown of NUMB in CCICs. Actin was used as a loading control. (F) Western blot verifying NUMB-SYM expression in CCIC with Actin as a loading control. (G) Western blot data showing JAG-1 knockdown in CCIC. Actin was used as the loading control. (H) Western blot data for NICD, HES1, HES5 and Actin (loading control) after CCICs were infected with an ectopic NICD (NICD-OE) construct. (I) Western blot data showing BMI1 expression in CCICs transduced with an empty vector (control) or infected with an ectopic NICD-OE construct. (J) Corresponding co-IF images from the pair cell assay (Fig. 4e) of CCICs infected with NICD-OE construct. Shown is a representative asymmetric CCIC daughter pair just prior to completion of cell division indicating LGR5 (green), NOTCH1 (purple) and α-TUBULIN (red) expression. DAPI (blue) labels nuclei and scale bar represents 10μm.

Supplementary Fig. 5. Analysis of murine ISC organoids and intestinal crypts under NOTCH modulation conditions. Related to Fig. 5.

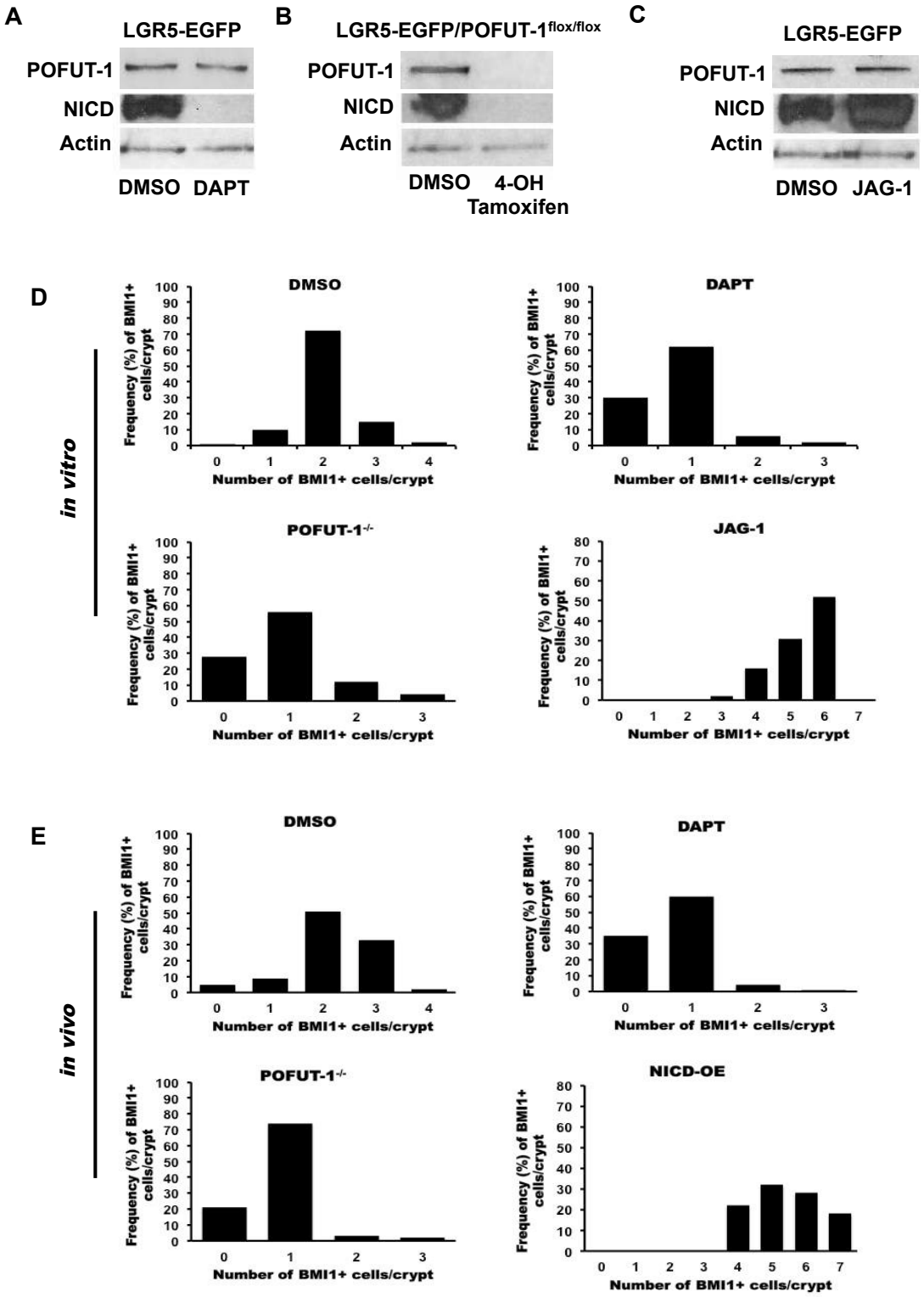

(A) Western blot data from LGR5-EGFP ISC organoids, demonstrating suppression of NICD by DAPT treatment. Actin was used as a loading control. (B) Western blot data from LGR5-EGFP-creER/POFUT-1$^{flox/flox}$ ISC organoids following 4-OH Tamoxifen induction of POFUT-1$^{-/-}$ phenotype, showing an absence of POFUT-1 and NICD. Actin was used as a loading control. (C) Western blot data from LGR5-EGFP ISC organoids after JAG-1 treatment indicating increased NICD expression. Actin was used as a loading control. (D) Frequency of BMI1+ cells/crypt from *in vitro* assays (Fig. 5a, Fig. 5b) from murine LGR5-EGFP ISC organoids treated with DMSO, DAPT or JAG-1, and LGR5-EGFP-creER/POFUT-1$^{flox/flox}$ ISC organoids following 4-OH Tamoxifen induction of POFUT-1$^{-/-}$ phenotype. The data represent n = 300 crypts/condition. (E) Frequency of BMI1+ cells/crypt from *in vivo* assays (Fig. 5c, Fig. 5d) from LGR5-EGFP mice treated with DMSO or DAPT, Tamoxifen-induced LGR5-EGFP-creER/POFUT-1$^{-/-}$ mice, and Tamoxifen-induced LGR5-EGFP-CreERT2/Rosa26-YFP-NICD mice. The data represent n = 300 crypts/condition.

Supplementary Fig. 6. Asymmetric division in ISC organoids. Related to Fig. 6.

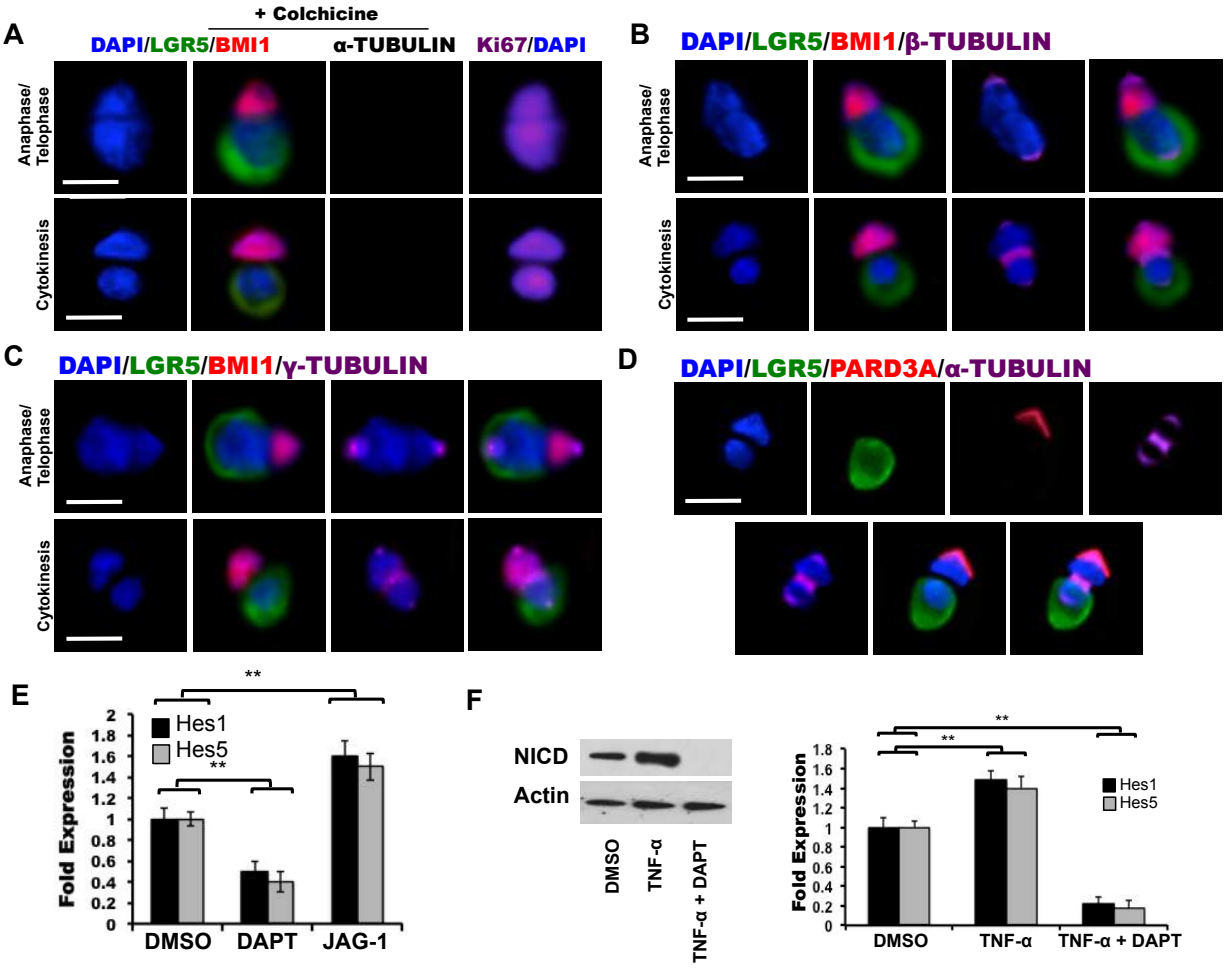

(A) Representative co-IF of a LGR5-EGFP ISC daughter pair during anaphase/telophase (top) and cytokinesis (bottom) following 4 hour treatment with microtubule depolymerization agent (Colchicine). IF staining: Anti-GFP detects LGR5 (green), BMI1 (red), Ki67 (purple). DAPI (blue) labels nuclei and scale bar represents 50μm. (B) Representative co-IF of a LGR5-EGFP ISC daughter pair during anaphase/telophase (top) and cytokinesis (bottom). IF staining: Anti-GFP detects LGR5 (green), BMI1 (red), and β-TUBULIN (purple). DAPI (blue) labels nuclei and scale bar represents 50μm. (C) Representative co-IF of a LGR5-EGFP ISC daughter pair during anaphase/telophase (top) and cytokinesis (bottom). IF staining: Anti-GFP detects LGR5 (green), BMI1 (red), and γ-TUBULIN (purple). DAPI (blue) labels nuclei and scale bar

represents 50μm. (D) Representative co-IF of a LGR5-EGFP ISC daughter pair just prior to completion of cell division. IF staining: Anti-GFP detects LGR5 (green), asymmetric cell fate marker PARD3A (red), and α-TUBULIN (purple). DAPI (blue) labels nuclei and scale bar represents 50μm. (E) Single LGR5-EGFP ISCs were treated with DMSO (control), 10uM DAPT or 1uM JAG-1 for 16h in a pair cell assay (Fig. 6b). Shown is RT-PCR data for expression of NOTCH effector genes Hes1 and Hes5 under each experimental condition (performed in triplicate and presented mean ± S.E.M.; $p = 0.01$; Student t-test for statistical significance). (F) Single LGR5-EGFP ISCs were treated with DMSO, 10ng/ml TNF-α, or both 10ng/ml TNF-α and 10uM DAPT (Fig. 6c). Shown is Western blot analysis for NICD expression (left) and RT-PCR data of NOTCH effector genes Hes1 and Hes5 (right) under each experimental condition (performed in triplicate and presented mean ± S.E.M.; $p = 0.01$; Student t-test for statistical significance).

Supplementary Fig. 7. Murine *in vivo* ISC division. Related to Fig. 6.

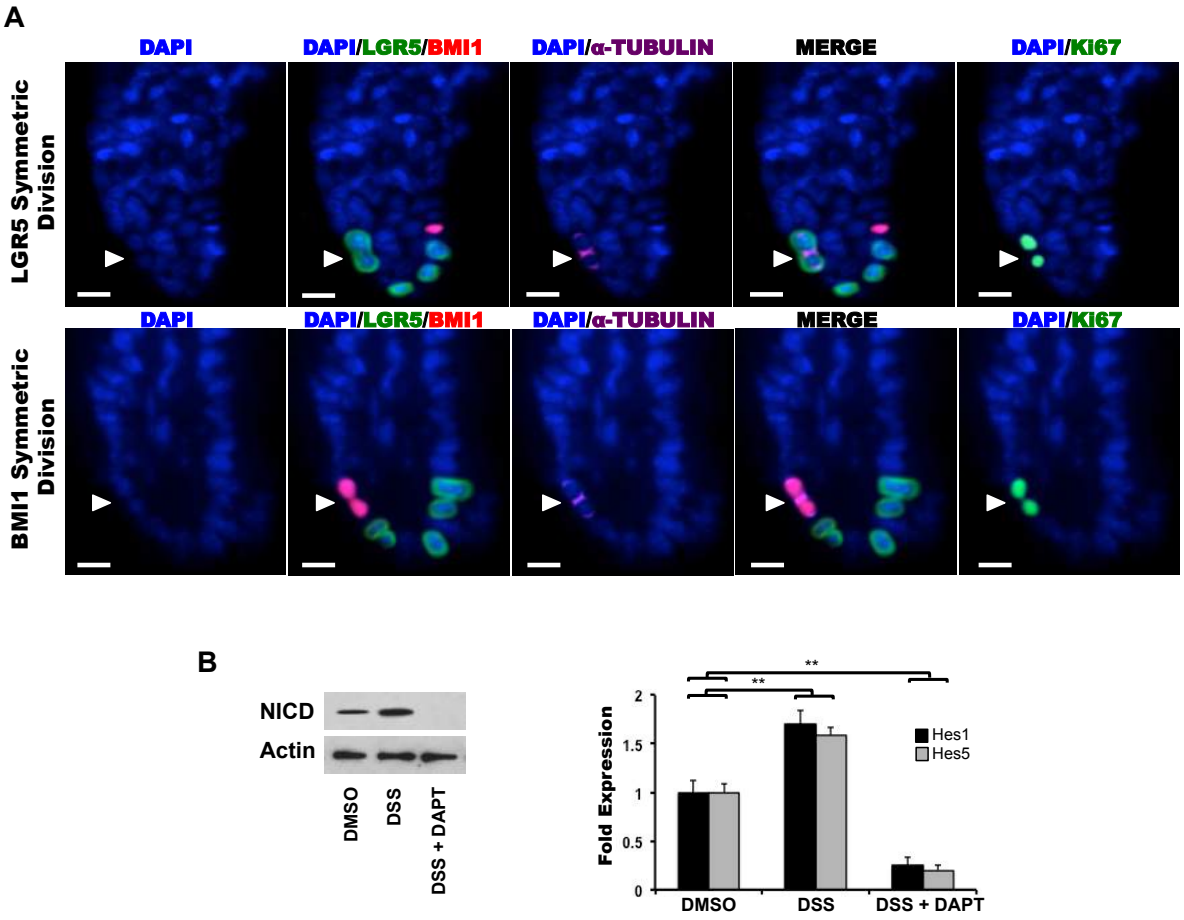

(A) LGR5-EGFP mice were administered DMSO by i.p injection. Shown are representative co-IF images of intestinal crypts demonstrating LGR5+ (top panel) or BMI1+ (bottom panel) symmetric division. Anti-GFP antibody (green) detects LGR5-GFP+ cells; BMI1 (red), α-TUBULIN (purple) and DAPI (blue) labels nuclei. Ki67 staining (green) is also included. Scale bar represents 20μm. (B) *In vivo* assays were performed as described in Fig. 6f. Shown is corresponding western blot analysis for NICD expression (left) and RT-PCR data of NOTCH effector genes Hes1 and Hes5 (right) under each experimental condition (performed in triplicate and presented mean ± S.E.M.; **, p = 0.01; Student t-test for statistical significance).

Supplementary Fig. 8. MYC knockdown in ISC organoids.

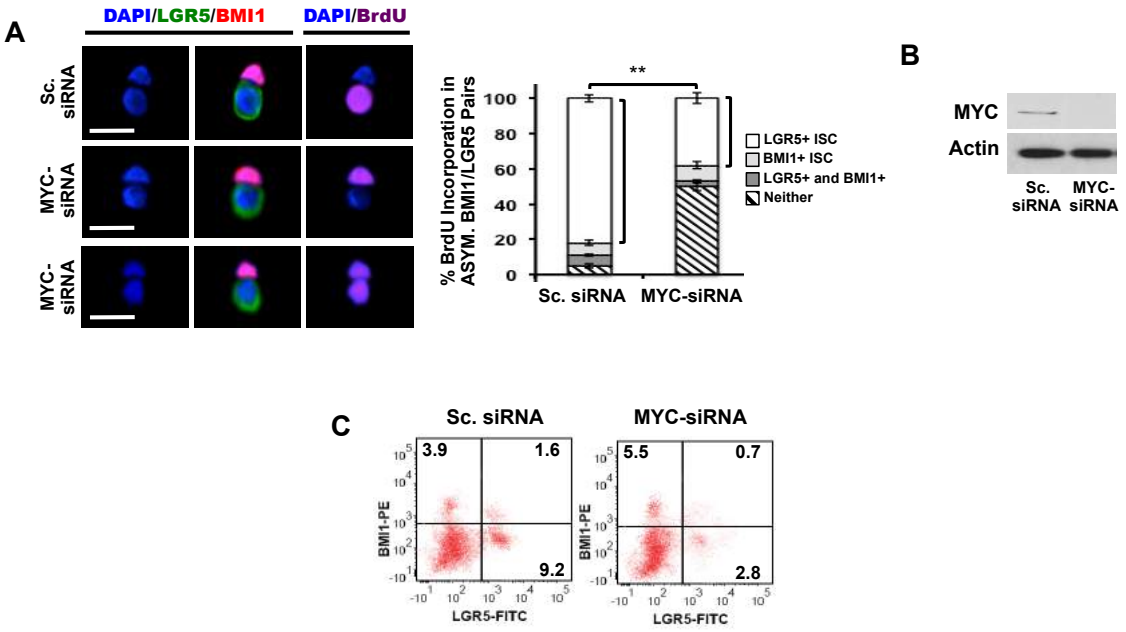

(A) BrdU incorporation assay following the division of single LGR5-EGFP ISCs transfected with scrambled siRNA or MYC-siRNA to generate a BMI1+/LGR5+ daughter pair. Left: Representative co-IF images showing BrdU incorporation in LGR5+, BMI1+, or both LGR5+ and BMI1+ ISC daughters. Staining: anti-GFP detects LGR5 (green), BMI1 (red), BrdU (purple). DAPI (blue) labels nuclei and scale bar represents 50μm. Right: Quantitative analysis in asymmetric BMI1+/LGR5+ pairs with percentage of BrdU incorporation present in LGR5+ ISC, BMI1+ ISC, both LGR5+ and BMI1+ ISCs, or neither indicated (**, p = 0.002, one-way ANOVA). (B) Single murine LGR5-EGFP ISCs were transfected with scrambled siRNA (Sc. siRNA) or MYC-siRNA. Shown is Western blot data for MYC expression under specified conditions. Actin was used as a loading control. (C) FACS analysis indicating BMI1 and LGR5 expression in LGR5-EGFP ISCs transfected with scrambled siRNA (Sc. siRNA) or MYC-siRNA.

REFENCES

1. Kreso, A., et al., *Self-renewal as a therapeutic target in human colorectal cancer*. Nat Med, 2014. **20**(1): p. 29-36.
2. Dick, J.E., *Stem cell concepts renew cancer research*. Blood, 2008. **112**(13): p. 4793-807.
3. Meacham, C.E. and S.J. Morrison, *Tumour heterogeneity and cancer cell plasticity*. Nature, 2013. **501**(7467): p. 328-37.
4. Nguyen, L.V., et al., *Cancer stem cells: an evolving concept*. Nat Rev Cancer, 2012. **12**(2): p. 133-43.
5. Sikandar, S.S., et al., *NOTCH signaling is required for formation and self-renewal of tumor-initiating cells and for repression of secretory cell differentiation in colon cancer*. Cancer Res, 2010. **70**(4): p. 1469-78.
6. Leng, Z., et al., *Kruppel-like factor 4 acts as an oncogene in colon cancer stem cell-enriched spheroid cells*. PLoS One, 2013. **8**(2): p. e56082.
7. Dalerba, P., et al., *Phenotypic characterization of human colorectal cancer stem cells*. Proc Natl Acad Sci U S A, 2007. **104**(24): p. 10158-63.
8. Merlos-Suarez, A., et al., *The intestinal stem cell signature identifies colorectal cancer stem cells and predicts disease relapse*. Cell Stem Cell, 2011. **8**(5): p. 511-24.
9. Giampieri, R., et al., *Cancer stem cell gene profile as predictor of relapse in high risk stage II and stage III, radically resected colon cancer patients*. PLoS One, 2013. **8**(9): p. e72843.
10. O'Brien, C.A., et al., *ID1 and ID3 Regulate the Self-Renewal Capacity of Human Colon Cancer-Initiating Cells through p21*. Cancer Cell, 2012. **21**(6): p. 777-92.
11. Zeuner, A., et al., *Colorectal Cancer Stem Cells: From the Crypt to the Clinic*. Cell Stem Cell, 2014. **15**(6): p. 692-705.
12. Barker, N., *Adult intestinal stem cells: critical drivers of epithelial homeostasis and regeneration*. Nat Rev Mol Cell Biol, 2014. **15**(1): p. 19-33.
13. Carmon, K.S., et al., *R-spondins function as ligands of the orphan receptors LGR4 and LGR5 to regulate Wnt/beta-catenin signaling*. Proc Natl Acad Sci U S A, 2011. **108**(28): p. 11452-7.
14. Carmon, K.S., et al., *LGR5 interacts and cointernalizes with Wnt receptors to modulate Wnt/beta-catenin signaling*. Mol Cell Biol, 2012. **32**(11): p. 2054-64.
15. Glinka, A., et al., *LGR4 and LGR5 are R-spondin receptors mediating Wnt/beta-catenin and Wnt/PCP signalling*. EMBO Rep, 2011. **12**(10): p. 1055-61.
16. Ziskin, J.L., et al., *In situ validation of an intestinal stem cell signature in colorectal cancer*. Gut, 2013. **62**(7): p. 1012-23.
17. Kim, J.H., et al., *The Bmi-1 oncoprotein is overexpressed in human colorectal cancer and correlates with the reduced p16INK4a/p14ARF proteins*. Cancer Lett, 2004. **203**(2): p. 217-24.
18. Li, D.W., et al., *Expression level of Bmi-1 oncoprotein is associated with progression and prognosis in colon cancer*. J Cancer Res Clin Oncol, 2010. **136**(7): p. 997-1006.
19. Du, J., et al., *Polycomb group protein Bmi1 expression in colon cancers predicts the survival*. Med Oncol, 2010. **27**(4): p. 1273-6.
20. Tateishi, K., et al., *Dysregulated expression of stem cell factor Bmi1 in precancerous lesions of the gastrointestinal tract*. Clin Cancer Res, 2006. **12**(23): p. 6960-6.

21. Bu, P., et al., *A microRNA miR-34a-regulated bimodal switch targets Notch in colon cancer stem cells*. Cell Stem Cell, 2013. **12**(5): p. 602-15.
22. Hwang, W.L., et al., *MicroRNA-146a directs the symmetric division of Snail-dominant colorectal cancer stem cells*. Nat Cell Biol, 2014. **16**(3): p. 268-280.
23. Cicalese, A., et al., *The tumor suppressor p53 regulates polarity of self-renewing divisions in mammary stem cells*. Cell, 2009. **138**(6): p. 1083-95.
24. Sugiarto, S., et al., *Asymmetry-defective oligodendrocyte progenitors are glioma precursors*. Cancer Cell, 2011. **20**(3): p. 328-40.
25. Lathia, J.D., et al., *Distribution of CD133 reveals glioma stem cells self-renew through symmetric and asymmetric cell divisions*. Cell Death Dis, 2011. **2**: p. e200.
26. Fre, S., et al., *Notch and Wnt signals cooperatively control cell proliferation and tumorigenesis in the intestine*. Proc Natl Acad Sci U S A, 2009. **106**(15): p. 6309-14.
27. van Es, J.H., et al., *Notch/gamma-secretase inhibition turns proliferative cells in intestinal crypts and adenomas into goblet cells*. Nature, 2005. **435**(7044): p. 959-63.
28. Rodilla, V., et al., *Jagged1 is the pathological link between Wnt and Notch pathways in colorectal cancer*. Proc Natl Acad Sci U S A, 2009. **106**(15): p. 6315-20.
29. Reedijk, M., et al., *Activation of Notch signaling in human colon adenocarcinoma*. Int J Oncol, 2008. **33**(6): p. 1223-9.
30. Meng, R.D., et al., *gamma-Secretase inhibitors abrogate oxaliplatin-induced activation of the Notch-1 signaling pathway in colon cancer cells resulting in enhanced chemosensitivity*. Cancer Res, 2009. **69**(2): p. 573-82.
31. Sonoshita, M., et al., *Suppression of colon cancer metastasis by Aes through inhibition of Notch signaling*. Cancer Cell, 2011. **19**(1): p. 125-37.
32. Chen, H.J., et al., *Chemokine 25-induced signaling suppresses colon cancer invasion and metastasis*. J Clin Invest, 2012. **122**(9): p. 3184-96.
33. Chen, H.J., et al., *Comprehensive models of human primary and metastatic colorectal tumors in immunodeficient and immunocompetent mice by chemokine targeting*. Nat Biotechnol, 2015. **33**(6): p. 656-60.
34. Gagliardi, G., K. Moroz, and C.F. Bellows, *Immunolocalization of DCAMKL-1, a putative intestinal stem cell marker, in normal colonic tissue*. Pathol Res Pract, 2012. **208**(8): p. 475-9.
35. Reynolds, A., et al., *Canonical Wnt signals combined with suppressed TGFbeta/BMP pathways promote renewal of the native human colonic epithelium*. Gut, 2014. **63**(4): p. 610-21.
36. Huang, E.H., et al., *Aldehyde dehydrogenase 1 is a marker for normal and malignant human colonic stem cells (SC) and tracks SC overpopulation during colon tumorigenesis*. Cancer Res, 2009. **69**(8): p. 3382-9.
37. Gracz, A.D., et al., *Brief report: CD24 and CD44 mark human intestinal epithelial cell populations with characteristics of active and facultative stem cells*. Stem Cells, 2013. **31**(9): p. 2024-30.
38. Espada, J., et al., *Wnt signalling and cancer stem cells*. Clin Transl Oncol, 2009. **11**(7): p. 411-27.
39. McGill, M.A. and C.J. McGlade, *Mammalian numb proteins promote Notch1 receptor ubiquitination and degradation of the Notch1 intracellular domain*. J Biol Chem, 2003. **278**(25): p. 23196-203.
40. Schweisguth, F., *Regulation of notch signaling activity*. Curr Biol, 2004. **14**(3): p. R129-38.

41. Neumuller, R.A. and J.A. Knoblich, *Dividing cellular asymmetry: asymmetric cell division and its implications for stem cells and cancer*. Genes Dev, 2009. **23**(23): p. 2675-99.
42. Zhong, W., et al., *Differential expression of mammalian Numb, Numblike and Notch1 suggests distinct roles during mouse cortical neurogenesis*. Development, 1997. **124**(10): p. 1887-97.
43. Schaller, M.A., et al., *Delta-like 4 differentially regulates murine CD4 T cell expansion via BMI1*. PLoS One, 2010. **5**(8): p. e12172.
44. Lopez-Arribillaga, E., et al., *Bmi1 regulates murine intestinal stem cell proliferation and self-renewal downstream of Notch*. Development, 2015. **142**(1): p. 41-50.
45. Barker, N., et al., *Identification of stem cells in small intestine and colon by marker gene Lgr5*. Nature, 2007. **449**(7165): p. 1003-7.
46. Snippert, H.J., et al., *Intestinal crypt homeostasis results from neutral competition between symmetrically dividing Lgr5 stem cells*. Cell, 2010. **143**(1): p. 134-44.
47. de Lau, W., et al., *Peyer's patch M cells derived from Lgr5(+) stem cells require SpiB and are induced by RankL in cultured "miniguts"*. Mol Cell Biol, 2012. **32**(18): p. 3639-47.
48. Yan, K.S., et al., *The intestinal stem cell markers Bmi1 and Lgr5 identify two functionally distinct populations*. Proc Natl Acad Sci U S A, 2012. **109**(2): p. 466-71.
49. Takeda, N., et al., *Interconversion between intestinal stem cell populations in distinct niches*. Science, 2011. **334**(6061): p. 1420-4.
50. Montgomery, R.K., et al., *Mouse telomerase reverse transcriptase (mTert) expression marks slowly cycling intestinal stem cells*. Proc Natl Acad Sci U S A, 2011. **108**(1): p. 179-84.
51. Powell, A.E., et al., *The pan-ErbB negative regulator Lrig1 is an intestinal stem cell marker that functions as a tumor suppressor*. Cell, 2012. **149**(1): p. 146-58.
52. Sangiorgi, E. and M.R. Capecchi, *Bmi1 is expressed in vivo in intestinal stem cells*. Nat Genet, 2008. **40**(7): p. 915-20.
53. Tian, H., et al., *A reserve stem cell population in small intestine renders Lgr5-positive cells dispensable*. Nature, 2011. **478**(7368): p. 255-9.
54. Munoz, J., et al., *The Lgr5 intestinal stem cell signature: robust expression of proposed quiescent '+4' cell markers*. EMBO J, 2012.
55. Itzkovitz, S., et al., *Single-molecule transcript counting of stem-cell markers in the mouse intestine*. Nat Cell Biol, 2012. **14**(1): p. 106-14.
56. Sato, T., et al., *Single Lgr5 stem cells build crypt-villus structures in vitro without a mesenchymal niche*. Nature, 2009. **459**(7244): p. 262-5.
57. Guilmeau, S., et al., *Intestinal deletion of Pofut1 in the mouse inactivates notch signaling and causes enterocolitis*. Gastroenterology, 2008. **135**(3): p. 849-60, 860 e1-6.
58. VanDussen, K.L., et al., *Notch signaling modulates proliferation and differentiation of intestinal crypt base columnar stem cells*. Development, 2012. **139**(3): p. 488-97.
59. Fre, S., et al., *Notch lineages and activity in intestinal stem cells determined by a new set of knock-in mice*. PLoS One, 2011. **6**(10): p. e25785.
60. Coussens, L.M. and Z. Werb, *Inflammation and cancer*. Nature, 2002. **420**(6917): p. 860-7.
61. Popivanova, B.K., et al., *Blocking TNF-alpha in mice reduces colorectal carcinogenesis associated with chronic colitis*. J Clin Invest, 2008. **118**(2): p. 560-70.

62. Grabinger, T., et al., *Ex vivo culture of intestinal crypt organoids as a model system for assessing cell death induction in intestinal epithelial cells and enteropathy*. Cell Death Dis, 2014. **5**: p. e1228.
63. Lopez-Garcia, C., et al., *Intestinal stem cell replacement follows a pattern of neutral drift*. Science, 2010. **330**(6005): p. 822-5.

CHAPTER 3

Dynamic regulation of intestinal stem cell niche recovery in real-time

Contributing Authors:

Kai-Yuan Chen[*]*, Jiahn Choi*[*]*, Tara Srinivasan*[*]*, Kuei-Ling Tung, Pengcheng Bu, Julio M. Belmonte, Sarah King, Anastasia Kristine Varanko, Mavee Witherspoon, Amit Lakhanpal, Sandy Nandagopal, Steven Lipkin, Michael Elowitz, James A. Glazier, Nozomi Nishimura, and Xiling Shen*

* These authors contributed equally to the study.

PREFACE

The stem cell niche provides the microenvironment for regulating stem cell self-renewal and tissue homeostasis. However, how the niche replaces lost cells and recovers from damage remains largely unknown. Here, we developed a systems biology approach combining *in vivo* laser ablation and chronic imaging, dynamic systems analysis, and agent-based multiscale modeling to study this spatiotemporal process in the intestinal epithelium, which is capable of rapid regeneration. We ablated individual stem or Paneth cells in the mouse intestinal crypt with high-precision photodisruption using a femtosecond laser, and monitored the *in vivo* dynamics of intestinal niche recovery in real-time, stabilized by surgically implanted 3D-printed scaffold. We observed that the niche recovers immediately after cell loss by rearranging stem/Paneth cell patterns rather than waiting for new cell division to fill the vacancy. Different from classic lateral inhibition in developmental patterning, intestinal stem cells employ a unique positive feedback mechanism via direct Notch1 binding, triggered by stem/non-stem cell communication, to sustain the niche. Inactivation of the positive feedback by CRISPR/Cas9 modification disrupts the niche pattern, limits self-renewal, and renders the niche incapable of recovery in organoids. Dynamical system analysis and multiscale stochastic modeling demonstrated that this regulation scheme enhances the stability and robustness of the Notch-mediated patterning when cell turnover rate is high. This study highlights the need of a systems approach that integrates *in vivo*, *in vitro*, and *in silico* models coupled with methods of precise perturbation and monitoring to comprehend spatiotemporal regulation, which often involves feedback and cell-cell communication.

INTRODUCTION

The stem cell niche provides a spatial environment to regulate stem cell self-renewal and differentiation[1]. Some mammalian tissues, especially regenerative ones, seem to rely on stem cell

niches rather than asymmetric division to control the number of proliferative stem cells. Remarkably, the niche often has the ability to recover from damaged cells and restore homeostasis. However, we know very little of this spatiotemporal process and its underlying control mechanism.

One prominent example is the stem cell niche at the base of the intestinal crypt. In the niche, self-renewing LGR5+ crypt base columnar (CBC) cells and lysozyme-secreting Paneth cells form a mosaic pattern[2,3]. As proliferative intestinal stem cells (ISCs), CBCs divide symmetrically, compete with each other in a neutral drift process, and regenerate the intestinal epithelium in 3 to 5 days[4,5]. Remarkably, the stem cell niche is capable of recovering from radiation or chemical damages[6,7].

RESULTS

In vivo imaging and laser ablation of crypt base

To understand how the niche spatiotemporally maintains homeostasis, we need to observe its actions *in vivo*. An abdominal window for intravital microscopy has been previously demonstrated[8,9]. The organ of interest was first glued to the coverslip on the window for imaging. Because adherence by glue often causes substantial inflammation, lethal intestinal obstruction, and detachment from the window due to intestinal peristalsis, we replaced the glue with a 3D printed, biocompatible scaffold insert, which was designed to stabilize the intestine and minimize its movement without blocking its motility functions (Fig. 1a). The scaffold was first sutured to the skin, and a portion of the small intestine was then positioned beneath the abdominal window (Fig. 1b). The mice live normally for months carrying the window and scaffold. Furthermore, replacing the glue with the scaffold allowed us to design an openable window, through which staining dye and small molecule inhibitors could be locally administered throughout the imaging period. Vasculature was labeled with an injection of FITC or Texas-red

dextran. These vessels were stable over weeks, enabling them to be used as a roadmap to image the same areas repeatedly (Supplementary Fig. S1a). Imaging LGR5-EGFP mice[2] showed the mosaic stem cell niche pattern at the crypt base, where LGR5+ CBCs fluoresce green while Paneth cells appear dark (Fig. 1c). This LGR5+ CBCs/Paneth cell pattern could sustain stably for one day (Supplementary Fig. S1b).

To understand how precisely the niche is regulated, we need to observe its response to loss of individual cells. This level of spatial specificity is difficult to achieve by current methods of radiation, chemical treatment, or genetic ablation, which either cause massive damage or wipe out entire lineages. We therefore designed and built a custom two-photon excited fluorescence (2PEF) microscope integrated with a low-repetition-rate, high-pulse-energy femtosecond (fs) laser, which is capable of penetrating the intestinal wall to reach the epithelium facing the lumen (Fig. 1d). In order to ablate a cell of choice, one or two 50-fs pulses is delivered from a Ti:Sapphire regenerative amplifier (800-nm wavelength, 1-kHz repetition rate) to the target while the surrounding region is being continuously monitored. Incident pulse energy is adjusted to provide an estimated 50-100 nJ at the focus. Because the damage is mediated by an electron-ion plasma formed by nonlinear optical absorption in a process called photodisruption, there is very little thermal energy deposited[10]. As a result, the damage is largely confined to the focal volume[11] (Supplementary Fig.S1c).

We redesigned the abdominal frame to install an openable window as aforementioned. This new capability enabled us to locally administer Hoechst dye through the window to stain cell nuclei, and then close the window for imaging and laser ablation. We first targeted an LGR5-EGFP+ CBC in the intestinal stem cell niche. The GFP signal of the targeted cell quickly dissipated, while GFP signals from neighboring CBCs remain unperturbed. The nucleus of the targeted cell disappeared between 10-30 minutes, while nuclei of the remaining cells appeared

intact up to 105 minutes after ablation (Fig. 1e). The similar dynamics is also shown when a Paneth cell was targeted (Supplementary Fig. S1d), while the untargeted crypt still remained stable CBC/Paneth pattern (Supplementary Fig. S1e).

Niche cells rearrange after ablation

We previously expected that the void created by ablation of a CBC would be later filled by division of a neighboring CBC, which takes 24~48 hours to complete[2]. This expectation arose from an assumption that the mosaic CBC/Panetch cell pattern is largely fixed based on a "footprint" provided by the underlying lamina propria. However, time-lapse images after ablation suggest that the niche is rather dynamic, with adjacent CBCs expanding and surrounding cells rearranging within an hour (Fig. 1e). In contrast, niches in neighboring crypts without laser ablation remain unperturbed, confirming that the dynamic rearrangement was in response to the loss of the ablated CBC (Supplementary Fig. S1f).

A more systematic ablation/imaging study found that cells in proximity consistently rearrange to fill the void after ablation of a single CBC or Paneth cell, and the mosaic CBC/Paneth cell configuration is somewhat restored after an hour or two. With further adjustments, the niche appears normal a day later, although the pattern does not look identical to the one before ablation. (Fig. 1e, Supplementary Fig. 1g). Remarkably, the niche also reshuffles rather quickly to restore the spatial configuration even when multiple CBCs or Paneth cells are ablated (Fig. 1f). A day later, the niche again appears normal but different from the one before ablation, suggesting that its configuration does not rely on a fixed "footprint" –rather—it probably depends on local cell-cell contact and communication.

Notch signaling in the niche

Paneth cells provide niche factors including epidermal growth factor (EGF), Wnt ligands (WNT3A), Notch ligands, and bone morphogenetic protein (BMP) inhibitor Noggin to support

CBC stem cell self-renewal, while pericryptal stromal cells underneath the niche also supply additional Wnt ligands (WNT2B)[12]. Regulation of the niche is certainly a concerted effort involving many such signal pathways. For proof-of-principle, we first focused on the role of Notch signaling, a juxtacrine signaling pathway linked to developmental patterning[13,14]. Notch signaling is mediated through direct cell-to-cell contact of membrane-bound Notch ligands on one cell and trans-membrane Notch receptors on adjacent cells. The extracellular domain of Notch receptors binds Notch ligands, which activates receptor cleavage that releases the Notch receptor intracellular domain (NICD) to translocate to the nucleus. NICD interacts with the DNA-binding protein RBPJk to activate expression of genes, such as the HES family transcription factors.

Notch signaling is essential for intestinal stem cell self-renewal and crypt homeostasis [15,16]. Among Notch receptors, inhibition of both Notch1 and Notch2 completely depletes proliferative stem/progenitor cells[17]. Inhibition of Notch1 alone is sufficient to cause a defective intestinal phenotype, while inhibition of Notch2 alone causes no significant phenotype[18]. Notch3 and Notch4 are not expressed in the intestinal epithelium[19]. Among Notch ligands, DLL1 and DLL4 are essential and function redundantly, and inactivation of both causes loss of stem and progenitor cells; in contrast, JAG1 is not essential[20].

To examine the effect of Notch inhibition on the niche in real-time, DBZ, a γ-secretase inhibitor that prevents Notch receptor cleavage, was locally injected into the submucosal layer of the target intestinal region through the openable window prior to imaging. DBZ steadily degraded GFP signals in CBCs and blurred the pattern until GFP signals were hardly detectable in the same niche (confirmed by intact vasculature) 24 hours later (Supplementary Fig. S1h, S1i). Therefore, Notch signaling is important for CBC self-renewal.

Notch lateral inhibition and positive feedback

In the niche, Paneth cells express lysozyme and CD24[3] (Fig. 2a). Using an established protocol[3], we isolated LGR5-EGFP+ CBCs and CD24+ Paneth cells from mouse intestinal organoid culture (Supplementary Fig. S2a). Immunofluorescence (IF) confirmed that the sorted CD24+ Paneth cells express lysozyme (Supplementary Fig. S2b). Notch receptors (Notch1, Notch2) and signaling effectors (Hes1, Hes5) are enriched in CBCs, while Notch ligands (Dll1, Dll4, Jag1) and the secretory lineage regulator, Atoh1[21], are enriched in Paneth cells (Fig. 2b). Inhibition of Notch receptor cleavage by the γ-secretase inhibitor DAPT significantly up-regulated ligand expression, indicating that activated Notch signaling suppresses ligand expression (Fig. 2c, d). This is consistent with classic lateral inhibition (LI), where ligands on a 'sender' cell (in this case, Paneth cell) activate receptors on a 'receiving' cell (in this case, CBC), which in turn, suppresses ligand expression in the receiver cell[22]. This intercellular feedback scheme causes bifurcation between adjacent cells, resulting in two opposite Notch signaling states (Fig. 2e).

Additionally, Notch activation by recombinant JAG1[23] or EDTA[24] significantly increased receptor (Notch1/2) expression, while DAPT significantly reduced receptor expression (Fig. 2c, d). This suggests the existence of a positive feedback loop, where activated Notch receptors up-regulate their own expression (Fig. 2e). To validate that positive feedback acts via NICD, the cleaved and activated intracellular domain from the Notch1 receptor, we crossed a LGR5-EGFP strain with a Rosa26-YFP-NICD strain[19] to generate a Tamoxifen-inducible LGR5-EGFP-CreERT2 x Rosa26-YFP-NICD (NICD-OE) mouse strain. In derived organoids, Tamoxifen-induced NICD expression up-regulated Notch receptor expression, while DAPT suppressed receptor and up-regulated Notch ligand expression (Supplementary Fig. S2c, S2d). Therefore, NICD activates expression of Notch receptors, forming a positive autoregulation.

NICD directly activates Notch1 transcription

Although both Notch1 and Notch2 form positive autoregulation, Notch1 has a stronger response than Notch2 (Fig. 2d and Supplementary Fig. S2c). This is consistent with previous reports showing that Notch1 and Notch2 are somewhat functionally redundant, but Notch1 is more critical to stem cell self-renewal and crypt homeostasis while Notch2 is dispensable[25]. To delineate how Notch1 and Notch2 are correlated with CBC functions in the niche, we performed lineage tracing using Tamoxifen-inducible Notch1^{CreER} x ROSA26^{tdTomato} and Notch2^{CreER} x ROSA26^{tdTomato} transgenic mouse reporter strains[19,26]. After induction, labeled Notch1+ cells showed a similar pattern that largely overlaps with CBCs in the niche (Fig. 2f). From Day 1 to Day 3, marked progeny of Notch1+ cells expanded out of the niche and overtook the trans-amplifying (TA) progenitor compartments; by Day 30, the marked clones of the original Notch1+ cells replaced the entire epithelium (Fig. 2g, Supplementary Fig. S2e). In contrast, labeled Notch2+ cells and their clones were much fewer and more sporadic (Supplementary Fig. S2e). These lineage tracing experiments confirmed that Notch1 are more active in CBCs and more critical to crypt regeneration than Notch2, which is consistent with previous findings[19,20,25,26].

We analyzed the LICR ChIP-Seq dataset of mouse small intestinal cells from ENCODE using the UCSC genome browser[27] to investigate regulation of Notch1 and Notch2 transcription. The 2nd intron region of the Notch1 gene is highly enriched with enhancer Histone marks H3K4me1 and H3K27ac[28-30], while no such regions were found in the Notch2 sequence (Supplementary Fig. S3a). Computational analysis of this region with MotifMap[31] predicted a putative binding motif for RBPJk, the DNA-binding protein that forms an effector complex with NICD to activate Notch signaling. A unique 8 base pair sequence (TTCCCACG, Chr2: 26,349,981-26,349,988) was identified (Fig. 3a). ChIP-PCR shows that NICD binds to this sequence in CBCs, and the binding was enhanced by JAG1 activation of receptors and

suppressed by DAPT inhibition of receptor cleavage (Fig. 3b). Similarly, ChIP-PCR analysis of Tamoxifen-induced NICD-OE intestinal cells (from NICD-OE mice) also showed elevated NICD binding compared to uninduced control (Supplementary Fig. S3b). Therefore, the NICD/RBPJk complex interacts with this sequence motif.

We next designed CRISPR-Cas9 vectors targeting the NICD binding sequence (Supplementary Fig. S3c). CRISPR/Cas9 vectors with specific guide RNAs (gRNAs) were transfected into single LGR5-EGFP CBCs, which were subsequently propagated as organoids. Sequencing results indicate the presence of indels in the target NICD binding region formed through Non-Homologous End Joining (NHEJ) (Supplementary Fig. S3d). The mutated binding motif significantly reduced NICD binding compared to the empty vector (EV) control in CBCs sorted from organoids treated with DMSO (control), JAG1, or DAPT, according to ChIP-qPCR (Supplementary Fig. S3e). The mutations also significantly decreased Notch1 transcript levels measured by RT-qPCR (Supplementary Fig. S3f) and NICD levels measured by Western blot (Supplementary Fig. S3g). Expression levels of Notch signaling components (Notch1, Notch2, Hes1, Hes5) and LGR5 all decreased by the mutated binding motif in the CRISPR/Cas9-targeted cells (Supplementary Fig. S3h). Taken together, the data suggest that, when Notch receptors are activated, the resulting NICD/RBPJk complex bind to the Notch1 gene and enhances its transcription, hence producing more Notch1 receptors and forming a positive feedback in stem cells.

Positive feedback is critical to self-renewal, niche homeostasis and recovery

To our knowledge, this positive feedback (PF) mechanism via direct NICD activation of Notch1 has never been reported in other systems, despite extensive studies of Notch signaling. This raises the question as to its role in the stem cell niche and intestinal homeostasis. CRISPR mutation of the binding motif (PF KO) reduced colony-forming efficiency and growth rate of

intestinal organoids markedly (Fig. 3c, 3d). Furthermore, the mutation significantly reduced the ratio of CBC to Paneth cells in the niche (Fig. 3c, 3e, Supplementary Fig. S3i).

Next, to understand how this positive feedback influences Notch signaling and cell fate, we transfected sorted LGR5-EGFP+ CBCs with an RBPJk-dsRED reporter as an indicator of Notch activity and grew them into organoids, followed by FACS analysis and time-lapse microscopy. Notch activation by JAG1 treatment hardly increased the $Notch^{high}/LGR5^{high}$ ($dsRed^{high}/GFP^{high}$) CBC population in PF KO organoids in contrast to the empty vector control. On the other hand, Notch inhibition by DAPT depleted $Notch^{high}/LGR5^{high}$ CBCs more thoroughly in PF KO organoids than the empty vector control (Fig. 3f, Supplementary Fig. S4a). Therefore, the positive feedback amplifies the effect of Notch activation for stem cell renewal, and helps prolong stem cell fate when Notch signaling is disrupted.

We next investigated the role of the Notch1 positive feedback in maintaining the integrity of the CBC/Paneth cell niche in organoids using single-cell laser ablation. LGR5+ cells located in the budding arms of wild-type or PF KO organoids were selected for laser ablation. After ablation, we observed reorganization and recovery of the mosaic CBC pattern within 4 hours, and the pattern was still sustained after 10 hours in wild-type organoids (Fig. 3g, Supplementary Fig. S4b; Supplementary Movie 1). In contrast, PF KO organoids started with much fewer LGR5-GFP CBCs, and was unable to recover from ablation of a single LGR5-EGFP CBC; strikingly, surrounding cells lost cell-cell attachments and the targeted budding arm eventually collapsed (Fig. 3g, Supplementary Fig. S4b; Supplementary Movie 2). These data demonstrate that direct Notch1 PF promotes stem cell self-renewal, maintains the mosaic niche configuration, and regulates its recovery.

The Notch1 PF motif is conserved in human colon organoids

Like their mouse counterparts, human intestinal and colon epithelia also contain LGR5+

CBCs and are highly regenerative. A similar computational analysis of the human genome identified an analogous NICD/RBPJk binding region (TTCCCACG, Chr9: 139,425,108-139,425,115) located on the 2nd intron of the human Notch1 sequence (Fig. 4a), which also showed high enrichment of H3K4me1 and H3K27ac enhancer chromatin marks in several human cell lines (Supplementary Fig. S5a). We then derived human colon organoids using normal colon tissue in surgically resected specimens from colorectal cancer (CRC) patients[32]. ChIP-PCR validated NICD binding on the predicted sequence (Fig. 4b) in human colon stem cells marked by EPHB2^{high}OLFM4^{high} expression[33]. Consistent with mouse CBCs, NICD binding to the motif was suppressed by DAPT and enhanced by JAG1 treatment. We then designed CRISPR-Cas9 vectors to mutate the NICD/RBPJk binding motif in human colon stem cells (Supplementary Fig. S5b, S5c). ChIP-qPCR validated that the CRISPR/Cas9-mediated mutation reduced NICD binding to the motif in all three conditions (DMSO, JAG1, and DAPT), and prevented JAG1 treatment from increasing NICD binding (Supplementary Fig. S5d). Suppression of the Notch1 PF by the mutations (PF KO) significantly reduced organoid-forming efficiency, size of organoids, and the percentage of EPHB2^{high}OLFM4^{high} colon stem cells compared to empty vector control (Fig. 4c, 4d, 4e, Supplementary Fig. S5e). The epithelial cell identity of the EPHB2^{high}OLFM4^{high} cells was validated by their EpCAM expression (Supplementary Fig. S5e). Without the signal-amplifying Notch1 PF, colon stem cells had lower Notch1 transcript levels (Fig. 4f). Mutated colon stem cells also had lower expression levels of NICD, other Notch signaling components, and human colon stem cell markers (LGR5 and OLFM4) (Fig. 4g, 4h). In summary, the Notch1 PF promotes both mouse intestinal and human colon stem cells by amplifying and sustaining receptor activation.

Notch1 PF enhances robustness of dynamic stem cell niche

However, it is not clear how Notch1 positive feedback (PF) fits into the 'big picture' in

terms of spatiotemporal regulation of the mosaic CBC/Paneth cell pattern in the niche. It seems that lateral inhibition (LI) alone should be sufficient for generating such patterns as it did for other developmental patterning[22]. To understand the underlying control principle of Notch signaling in the intestinal niche, we constructed single-, pair-, and multi-cell mathematical models to analyze LI with and without PF (Supplementary Information).

We first analyzed Notch response to external ligands in a single cell as an input-output function. In LI, external ligands activate receptors and Notch signaling, which in turn, suppresses internal ligand expression. Hence, increasing levels of external ligands leads to a monotonic decrease of internal ligands (Fig. 5a, Supplementary Fig. S6a). The addition of the Notch positive feedback to LI (PFLI) causes bifurcation and generates a more switch-like response with hysteresis (Fig. 5a, Supplementary Fig. S6b).

Pair-cell analysis suggests that both LI and PFLI could achieve intercellular bistability, with two neighboring cells settling in opposite ($Notch^{high}$ vs. $Notch^{low}$) states. Nevertheless, PFLI is much more robust in generating bistability than LI alone, and is less dependent on cooperativity (hill coefficient) of the reactions (Fig. 5b, Supplementary Fig. S6c, S6d).

Next, we used the Maximum Lyapunov Exponent (MLE) to analyze the stability of patterning in multicellular systems[34]. PFLI is able to maintain stable patterns over a much wider parameter range than LI, especially when cooperativity of reaction is low, suggesting that PFLI is a more robust patterning mechanism (Fig. 5c). We then scaled up the pair-cell model to a multicellular model with stationary cells surrounding each other to explore Notch patterning dynamics. In steady state analysis, both LI and PFLI can generate stable mosaic patterns with varying levels of Notch signaling and ligands (Supplementary Fig. S7a). However, dynamic simulations from an initial homogeneous state suggest that PFLI reaches the steady-state pattern much faster than LI by speeding up divergence of individual cell signaling states (Fig. 5d).

Taken together, the analyses suggest that PFLI increases robustness, stability, and speed of Notch-mediated patterning.

These properties are not necessarily critical to largely stationary patterns with low cellular turnovers. However, they could be important for the intestinal stem cell niche, which is very dynamic with rapid cell division and migration that regenerate the entire epithelium every 3~5 days. We therefore constructed a multiscale, agent-based stochastic model using CompuCell3D[35]. The model takes into consideration the three-dimensional structure of the crypt, cell growth, division, migration, and cell-cell physical contact (Fig. 5e). Notch signaling is only modeled in the niche at the base of the crypt, while cells above the niche are simply pushed upwards with no specific assumptions made about their properties. This model does not attempt to capture every aspect of the crypt, which involves many signaling pathways and cell types. Rather, it is solely designed to test how cell division and migration in the niche would affect PFLI- vs. LI-mediated Notch patterning.

As expected, PFLI generates bimodality in niche cells with regard to Notch signaling (NICD) levels (Supplementary Fig. S7b). When the strength of the PF is reduced, the ratio of $NICD^{high}$ to $NICD^{low}$ cells as well as NICD levels in $NICD^{high}$ cells decrease (Supplementary Fig. S7b), consistent with our observation that CRISPR/Cas9-mutated PF KO organoids have lower CBC/Paneth cell ratio, and those CBCs have weaker signals (Fig. 3c, 3e-3g, Supplementary Fig. 3f-3i).

However, can the Notch signaling pattern be maintained by LI alone if we simply change its parameters to increase Notch signaling levels? In other words, is the PF's role limited to enhancing Notch signaling levels, or is PFLI an inherently different control scheme from LI? To address this, we readjusted the maximum Notch transcription rate in the LI model, so that LI and PFLI have equivalent Notch signaling levels. Indeed, both LI and PFLI can generate mosaic

Notch signaling patterns when cell proliferation rate is slow (Fig. 5e). We then gradually increased the proliferation rate inside the niche, which led to increased rates of cell division, migration, and anoikis (Supplementary Fig. S7c). PFLI is still able to maintain bimodality and binary patterns with higher turnover rate in the niche, whereas LI starts to show less bimodality and more blurred pattern (Fig. 5e). Therefore, PFLI is a more robust control motif than LI when the pattern is highly dynamic with a lot of cell turnover. The discovery of the direct Notch1 PF in the intestinal niche is probably not a coincidence; rather, it may be an evolutionary response to the unique regulatory challenges of the highly regenerative intestinal epithelium.

DISCUSSION

By designing and surgically implanting a 3D-printed intestinal scaffold and an openable abdominal window, coupled with a low-repetition-rate, high-pulse-energy femtosecond (fs) laser, we studied how the intestinal stem cell niche recovers from cell ablation *in vivo*. Instead of having a fixed "floor plan", the mosaic CBC/Paneth cell pattern in the niche is rather fluidic and can spatially rearrange upon damage. We then characterized Notch signaling in the niche, and discovered a direct positive feedback, in which NICD cleaved from activated receptors directly activates Notch1 receptor expression. This positive feedback is active in mouse intestinal and colon epithelial cells, and its silencing by CRISPR/Cas9 mutation reduced CBC/Paneth cell ratio, limited self-renewal, and deprived organoids of the ability to recover from cell ablation. Dynamical systems analysis and multiscale stochastic simulation further revealed that, compared to LI, PFLI enhances robustness of the spatiotemporal Notch signaling pattern, especially in the presence of perturbation and turnover.

The stem cell niche is a dynamic environment that controls regeneration and homeostasis of the tissue. However, it is notoriously difficult to study spatiotemporal regulation of biological systems involving intercellular communication and feedback. Here, we demonstrate that

integration of *in vivo*, *in vitro*, and *in silico* models coupled with precise methods of physical and genomic perturbation (laser ablation, CRISPR) provides a way to unravel some of the "design principles" underlying such systems.

Biological systems such as the stem cell niche are known to be robust. They work most of the time, capable of accommodating different conditions and recovering from mistakes and damages. Control theory would predict that they rely on additional mechanisms such as feedback to enhance their regulation. However, conventional assays seldom reveal such intricacies. The importance of these "safeguard" mechanisms is often revealed only when systems are perturbed. Here, precise laser ablation highlights the flexibility of the niche regulation. Further investigation shows that control motifs like PFLI and LI can appear similar in steady-state conditions, but display different dynamic properties that can have important implications to a rapidly regenerative tissue like the intestinal epithelium.

The direct Notch1 PF seems to be an evolutionary response to the challenges of regulating intestinal and colon epithelium, since it has not been reported in other tissues or model systems such as *Drosophila* and *C. elegans* despite extensive study of Notch. Nonetheless, it is also likely that the direct PF is a widely conserved mechanism that simply awaits discovery in other systems. In that case, it will be interesting to see whether the existence of PF is associated with the rate of tissue regeneration.

Notch signaling is certainly not the only mechanism responsible for niche pattern. Other signaling pathways like developmental (Wnt, BMP, EGFR, Hedgehog), chemokine, and mechanotransduction pathways likely reinforce or crosstalk with Notch to regulate the niche collectively[12,36,37]. Hopefully, our integrated approach will help unravel this intricate control scheme step by step.

METHODS

Antibodies

Primary Antibody	Supplier	Catalog Number	Dilution*
anti-ATOH1	Abcam	ab137534	1:1000 (WB)
anti-β-ACTIN	Abcam	ab6276	1:4000 (WB)
Anti-CD24 (APC)	Abcam	ab51535	1:500 (FC)
Anti-DLL1	Abcam	ab85346	1:500 (WB)
Anti-DLL4	Abcam	ab7280	1:1000 (WB)
Anti-EPHB2	R&D Systems	AF467	1:1000 (FC)
Anti-EpCAM (FITC)	Abcam	ab8666	1:500 (FC)
Anti-GFP	Abcam	ab5450	1:200 (IF)
Anti-HES1	Abcam	ab108937	1:1000 (WB)
Anti-HES5	Santa Cruz Biotechnology	sc-25395	1:500 (WB)
Anti-JAG1	Santa Cruz Biotechnology	sc-6011	1:500 (WB)
Anti-LYSOZYME	Abcam	ab108508	1:100 (IF)
Anti-(human)NICD	R&D Systems	AF3647	1:200 (ChIP)
Anti-(mouse)NICD	Cell Signaling	4147	1:200 (ChIP)
Anti-NOTCH1	Santa Cruz Biotechnology	sc-9170	1:1000 (WB)
Anti-NOTCH2	Santa Cruz Biotechnology	sc-32346	1:1000 (WB)
Anti-OLFM4	Sino Biological Inc.	11639-MM12-50	1:1000 (FC)

***Application: IF: (Immunofluorescence); WB: (Western Blotting); FC: (Flow Cytometry)**

Mouse strains

LGR5-EGFP mice on a mixed 129/C57BL/6 background and Rosa26-CAG-LSL-tdTomato-WPRE mice on a mixed 129/C57BL/6 background were purchased from The Jackson laboratory. Notch1-CreERT2 knock-in (KI) mice, Notch2-CreERT2 KI mice, and Rosa26-NICD-IRES-YFP KI mice were a generous give from Dr. **Spyros Artavanis-Tsakona**'s laboratory at Harvard University. Subsequently, we generated an inducible Notch1 reporter mouse strain (Notch1-CreERT2 KI x Rosa26-CAG-LSL-tdTomato-WPRE) and an inducible Notch2 reporter mouse strain (Notch2-CreERT2 KI x Rosa26-CAG-LSL-tdTomato-WPRE). We also generated a LGR5-EGFP-CreERT2 x Rosa26-NICD-IRES-YFP KI mouse strain for inducible NICD overexpression (NICD-OE). Genotyping was performed using the following PCR primer pairs for Notch1 (Forward: ATAGGAACTTCAAAATGTCGCG; Reverse: CACACTTCCAGCGTCTTTGG), Notch2: (Forward: ATAGGAACTTCAAAATGTCGCG;

Reverse: CCCAACGGTGCCAAAAGAGC), and NICD: (Forward: CTTCACACCCCTCATG ATTGC; Reverse: GCAATCGGTCCATGTGATCC). The thermocyling profile used for PCR amplification is described as follows: 95°C (5 min)/[95°C (30 sec), 60°C (30 sec), 72°C (60 sec)] for 35 cycles/72°C (10 min). Notch1 and Notch2 reporter mice were induced with 75 mg/kg Tamoxifen by i.p. injection. The LGR5-EGFP-CreERT2 x Rosa26-NICD-IRES-YFP KI mouse strain was treated daily with 75 mg/kg Tamoxifen (i.p. injection) for 8 consecutive days to induce Cre enzyme activity and NICD-OE phenotype.

Abdominal window

Abdominal window were surgically implanted on LGR5-EGFP mice for imaging and laser ablation studies. At the beginning of surgery, animals received an anticholinergic (atropine) to assist in keeping the airways clear of fluid build-up. Body temperature was kept at 37°C using a heating blanket controlled by a rectal thermometer (50-7053; Harvard Apparatus, Holliston, MA, USA). All areas to be incised were cleaned and shaved with #40 clippers, sterilized with 70% ethanol, swabbed with betadine, and were numbed with a subcutaneous injection of bupivacaine (0.125%). Dexamethasone (0.1mg/ml) and Ketopropane (2.0 mg/ml) were administered i.p. to help recovery after surgery. Eyes were covered with veterinary eye ointment to prevent drying. The animals were hydrated with subcutaneous injections of 5% glucose in saline for isotonic fluid replacement. Abdominal skin was removed in circular shape to implant commercially available window frame (12 mm in inner diameter, APJ trading, CA). Outer edge of the window was covered by skin with tissue glue (Loctite 406, Henkel). Muscular layer of inner circle was incised by scissor to expose small intestine directly. 3D printed insert (RPL lab, Cornell University) was sutured to the skin to be placed under the small intestine loop and a portion of small intestine was position on top of the insert. Window was secured by 12 mm cover glass with a retaining ring to keep physiological environment intact. All experiments were

performed in accordance with the ethical and care guidelines established by the Research Animal Resource Center and Institutional Animal Care and Use Committee of Cornell University.

***In vivo* Two Photon Excited Fluorescent Microscopy**

Animals with abdominal window were imaged using a custom-built two-photon excited fluorescent (2PEF) microscope with four simultaneous fluorescent detection channels. All animals were anesthetized with isoflurane during the imaging time and monitored by physiological condition. Texas-red dextran (Molecular Weight: 70,000; Thermo Fisher Scientific. NY) was administered through retro-orbital injection to visualize vasculature. Images were acquired using a Ti:Sapphire laser (Chameleon; Coherent, Santa Clara, CA), a central wavelength at 880 nm. A X20 1.0 numerical aperture (NA) water-immersion microscope objective and X4 0.28 NA objective lens (Zeiss, Thornwood, NY) were used for all imaging. A 494-nm bandpass filter with 41-nm bandwidth and a 641-nm bandpass filter with a 75-nm bandwidth were used for detecting green fluorescent protein (GFP) and Texas-red dextran dye, respectively. Image series were acquired before and after laser ablation, and three dimensional (3D) image stacks with 1 um spacing in the axial direction were acquired through the entire imaging session. All images were processed using ImageJ. The raw stack was separated into four channels, and each channel was color-coded accordingly. The image frames containing abrupt movement from respiration or peristalsis were deleted and the stack has re-aligned by using Stackreg[38]. Z-projection was used for final image presentation to incorporate the 3D structure. The average z-axis in each image is 5-10 um.

Femtosecond Laser Photodisruption

Selective disruption of cellular contact was performed using a low-repetition-rate, high-pulse-energy Ti:Sapphire regenerative amplifier with 100-fs pulse duration, 1-kHz repetition rate, and 800-nm central wavelength (Legend-USP; Coherent, Santa Clara, CA). A polarizing

beamsplitter cube was used to introduce this beam into the 2PEF microscope so that the pulses were focused at the center of the imaging field and in the 2PEF imaging plane, enabling real-time monitoring of recovery process. Laser energy incident on the cells was controlled by neutral density filters, and a fast mechanical shutter limited the number of pulses incident on each cell. Laser energy to remove a single cell did not exceed 100 nJ.

***In vivo* Notch Signaling Inhibition**

DBZ (Syncom, Netherlands), a small molecule gamma-secretase inhibitor, was locally injected into the submucosal layer of the small intestine through the implanted abdominal window on mice. Each animal was anesthetized with isoflurorane to inject DBZ. DBZ was dissolved in DMSO at final concentration of 30 uM. Animals were pre-treated with DBZ (15 umol/kg) for 2 hours before ablation to inhibit Notch signaling.

Murine Intestinal Crypt Isolation and Organoid Culture

8-week-old LGR5-EGFP or LGR5-EGFP/NICE-OE mice were sacrificed to establish intestinal organoid culture. Briefly, small intestines were harvested, flushed with $Ca2^{+/}Mg^{2+}$-free PBS to remove debris, and opened up longitudinally to expose luminal surface. A glass coverslip was then gently applied to scrape off villi, and the tissue was cut into 2-3 mm fragments. Intestinal tissues were then washed again with cold PBS and incubated with 2.0mM EDTA for 45 minutes on a rocking platform at 4°C. EDTA solution was then decanted without disturbing settled intestinal fragments and replaced with cold PBS. In order to release intestinal crypts in solution, a 10 mL pipette was used to vigorously agitate tissues. The supernatant was collected and this process was repeated several times to harvest multiple fractions. The crypt fractions were then centrifuged at 6,000 RPM for 5 minutes. Based on microscopic examination, the appropriate enriched crypt fractions were pooled and centrifuged again to obtain a crypt-containing pellet. Advanced DMEM/F12 (Life Technologies) containing Glutamax (Life

Technologies) was used to resuspend the cell pellet and subsequently a 40um filter was used to purify crypts. Next, single cell dissociation was achieved by incubating purified crypt solution at 37°C with 0.8 KU/ml DNase (Sigma), 10 uM ROCK pathway inhibitor, Y-27632 (Sigma), and 1 mg/mL Trypsin-EDTA (Invitrogen) for 30 minutes. Single cells were then passed again though a 40um filter and resuspended in cold PBS with 0.5% BSA for FACS analysis to collect LGR5-EGFP+ intestinal stem cells (ISCs), which are also called crypt base columnar (CBC) cells.

Single LGR5-EGFP+ CBCs were suspended in Matrigel (BD Biosciences) at a concentration of 1000 cells or crypts/mL and 50ul Matrigel drops were seeded per well on pre-warmed 24-well plates. Matrigel polymerization occurred at 37°C for 10 minutes, and was followed by the addition of complete media to each well. ISC media included the following: Advanced DMEM/F12 supplemented with Glutamax, 10mM HEPES (Life Technologies), N2 (Life Technologies), B27 without vitamin A (Life Technologies), and 1 uM N-acetylcysteine (Sigma). Growth factors were freshly prepared each passage in an ISC media solution containing 50ng/mL EGF (Life Technologies), 100ng/mL Noggin (Peprotech), and 10% R-SPONDIN1 conditioned media (generated in house). The addition of growth factors occurred every 2 days and the media was fully replaced every 4 days. Organoids were passaged once per week at a ratio of 1:4 by removing organoids from Matrigel with ice-cold PBS. Next, organoids were incubated on ice for 10 minutes followed by mechanical disruption, centrifugation, and resuspension in fresh Matrigel.

For *in vitro* studies, organoids derived from single LGR5-EGFP ISCs were treated with one of the following: DMSO or 10uM DAPT (EMD Millipore) added to the media for 48 hours [39], or 1uM JAG-1 (AnaSpec) embedded in Matrigel for 48 hours [40]. EDTA was added to ISC media (for a final concentration of 0.5mM EDTA) to treat organoids for 4 hours. Subsequently, organoids were harvested and analyzed by FACS to isolate LGR5-EGFP cells and Paneth cells

for RT-PCR or protein analysis. FACS was conducted using a Beckman Coulter flow cytometer with a 40um filter. Data analysis was performed using FlowJo software to gate populations according to 7-AAD viability, and forward and side scattering. Cutoff thresholds were provided by unstained ISCs and single stained ISCs when using multiple fluorochromes in order to achieve appropriate compensation.

CRISPR/Cas9 genomic editing

The procedure for CRISPR/Cas9-mediated transfection in mouse ISC organoids has been previously described [41]. Briefly, guide RNA (gRNA) sequences were designed by Optimized CRISPR Design tool (http://crispr.mit.edu), and CRISPR/Cas9 plasmids including gRNA sequences were purchased from GenScript. For murine experiments gRNAs targeting the NICD binding motif on Notch1 included the following: gRNA1: (TACATGCATGGAAGGTGCGT) or gRNA2: (GTACATGCATGGAAGGTGCG) and were cloned into a pGS-gRNA-Cas9-Puro vector backbone. A pGS-CAS9-PURO only vector (no gRNA) was used as a control. Single sorted LGR5-EGFP+ ISCs were transfected using Lipofectamine-2000 (Life Technologies) according to the manufacturer's instructions. Briefly, 4uL Lipofectamine-2000 (diluted in 50uL Opti-MEM) and 2ug of CRISPR/Cas9 plasmids (diluted in 50uL Opti-MEM) were mixed 1:1: and incubated for 5 minutes at room temperature. Lipofectamine/DNA complexes were then added to single LGR5-EGFP+ ISCs (50uL/well) in a 24-well plate, which was subsequently centrifuged for 1 hour and incubated at 37C for 4 hours. ISCs were then resuspended in Matrigel and overlaid with ISC media (as prepared above) and supplemented with Y-27632 for 48 hours. Next, transfected ISCs were selected in media (without R-SPONDIN) containing 300ng/uL Puromycin for 72 hours. Selection media was then replaced with ISC media and organoids were monitored for 15 days followed by FACS analysis or co-immunofluorescence. Individual CRISPR/Cas9-mutated organoid clones were also harvested and lysed for DNA extraction using

a QIAmp DNA Mini kit (Qiagen: 51304) according to the manufacturer's instructions. Subsequently, the NICD binding site on mouse Notch1 was amplified by PCR using the following primers (Forward: AGAAGAGAAGACAGGAGAAGGA and Reverse: GAAGCCACTGACTTTCCTAGAG) and analyzed by Sanger sequencing to visualize mutations. CRISPR/Cas9-mutated organoids derived from single transfected LGR5-EGFP ISCs were also treated for 48 hours with DAPT or JAG-1 (as described earlier) before harvesting cells for FACS to isolate LGR5-EGFP+ cells for RT-PCR analysis.

In order to study Notch signaling dynamics, a RBPJk-dsRed reporter on a pGA981-6 vector backbone (Addgene #47683) was transfected into single wild-type or CRISPR/Cas9-mutated sorted LGR5-EGFP ISCs using Lipofectamine-2000 according to the protocol described above. ISCs were then treated for 48 hours with 10uM DAPT or 1uM JAG-1 and analyzed by microscopy and flow cytometry for LGR5-EGFP and RBPJk-dsRed expression.

Mouse organoids derived from single wild-type or CRISPR/Cas9-mutated ISCs were also subjected to single cell multi-photon laser ablation. Single cells in wild-type organoids were targeted based on LGR5-EGFP expression. CRISPR/Cas9-mutated organoids were incubated with Hoechst-33342 dye (Life Technologies) to target single cells. The organoid imaging and laser ablation were performed using ZEISS Inverted LSM880 (i880) laser scanning confocal microscope with full confocal and multiphoton capability. The i880 system is integrated with a heated chamber with CO_2 and humidity regulation. The temperature was controlled at 37°C, and concentration of CO_2 was kept at 5% through the imaging periods. A X10 0.3 NA objective lens was used for imaging, and 780nm 2-photon laser was used for targeting single-cell ablation. Time-lapse imaging series was used to analyze organoid dynamics pre- and post-ablation.

Isolation of Single Cells from Human Colonic Tissue

Approval for this research protocol was obtained from IRB committees at Weill Cornell

Medical College and NY Presbyterian Hospital. Patients undergoing colorectal surgery provided written informed consent for use of human tissues. Material was derived from proximal colonic tissue during surgical biopsies. The procedure for isolation of colonic stem cells and organoid culture are previously described [33]. Briefly, colonic specimens were collected and incubated in Advanced DMEM/F12 supplemented with gentamycin (Life Technologies) and fungizone (Life Technologies). Extraneous muscular and sub-mucosal layers were removed from colonic mucosa. The tissue was cut into 1 cm fragments and incubated with 8mM EDTA for 1 hour on a rocking platform at 37°C followed by a 45 minute incubation at 4°C. The supernatant was replaced with Advanced DMEM/F12 supplemented with Glutamax, HEPES, and 5% FBS. Vigorous shaking released crypts, which were collected in several fractions. Crypt fractions were then centrifuged (400 RPM, 5 minutes) and visualized by microscopy to determine which enriched fractions to combine. Subsequently, pooled crypt fractions were centrifuged and resuspended in Advanced DMEM/F12 supplemented with Glutamax, HEPES, N-2, B-27 without vitamin A, 1 mM N-Acetyl-L-cysteine, Nicotinamide (Sigma), 10 **μ**M Y-27632, 2.5 **μ**M PGE2 (Sigma), 0.5 mg/ml Dispase (BD Biosciences), and 0.8 KU/ml DNAse I. Cells were then incubated for 15 min at 37°C followed by mechanical disruption and passage of cell solution through 40um filter to obtain a single cell suspension.

Human Colon Organoid Culture

Single human colon cells were stained with EPHB2 (conjugated to PE), OLFM4 (conjugated to APC), EpCAM-FITC and 7-AAD according to standard protocols and were suspended in cold PBS with 0.5% BSA for FACS analysis. FlowJo software was used to gate populations according to 7-AAD viability, and forward and side scattering. Cutoff thresholds were provided by unstained ISCs and single stained ISCs when using multiple fluorochromes in order to achieve appropriate compensation. $EPHB2^{high}OLFM4^{high}$ colon stem cells were

harvested, and subjected to lipotransfection of CRISPR/Cas9 plasmids using lipofectamine-2000 in a similar method as described earlier for mouse ISCs. CRISPR/Cas9 gRNAs targeting the NICD binding motif of human Notch1 (cloned into a pGS-gRNA-Cas9-Puro vector backbone) were designed and ordered from Genscript with the following inserted gRNA sequences: (gRNA1: TGCTTTTGGGGGATCCGCGT, gRNA2: CACTGCGGGAATTTCCCACG). A pGS-CAS9-PURO only vector (no gRNA) was used as a control. Transfected human colon stem cells were selected in medium lacking WNT-3A, and R-SPONDIN1 and containing Y-27632 and 300 ng/ul puromycin for 48 hours.

Subsequently, transfected cells were suspended in Matrigel, and overlaid with human colon stem cell medium containing Advanced DMEM/F12 supplemented with Glutamax, HEPES, N-2, B-27 without vitamin A, 1 mM N-Acetyl-L-cysteine, Nicotinamide, PGE2, Y-27632, human Noggin (Peprotech), human EGF (Life Technologies), Gastrin (Sigma), TGF-ß type I Receptor inhibitor A83-01 (Tocris), P38 inhibitor SB202190 (Sigma-Aldrich), WNT3A-conditioned media (generated in house) and R-SPONDIN1 conditioned medium (generated in house) [33]. For organoid culture, full medium was replaced every 2 days. Transfected organoids were monitored for 14 days and then harvested and analyzed by FACS to isolate $EPHB2^{high}OLFM4^{high}$ colon stem cells for RT-PCR and protein analysis. Individual CRISPR/Cas9-mutated organoid clones were also harvested and lysed for DNA extraction using a QIAmp DNA Mini kit (Qiagen: 51304) according to the manufacturer's instructions. Subsequently, the NICD binding site on human Notch1 was amplified by PCR and analyzed by Sanger sequencing to visualize mutations.

Quantitative RT-PCR and Protein Analysis

Total RNA from mouse ISCs or human colon stem cells was extracted using a Qiagen RNeasy Plus kit. Subsequently, isolated RNA was reverse transcribed to cDNA using ABI

Taqman Reverse Transcription kit (Applied Biosystems). ABI Taqman Master mix and ABI Prism HT7900 were used to run quantitative real-time PCR. Taqman primers (ABI) purchased from Life Technologies were used for the following mouse genes: Notch1 (Product ID: Mm00627185_m1), Notch2 (Product ID: Mm00803077_m1), Hes1 (Product ID: Mm01342805_m1), Hes5 (Product ID: Mm00439311_g1), Dll1 (Product ID: Mm01279269_m1), Dll4 (Product ID: Mm00444619_m1), Jag1 (Product ID: Mm00496902_m1), Atoh1 (Product ID: Mm00476035_s1), Lgr5 (Product ID: Mm00438890_m1). Human Taqman primers purchased from Life Technologies include: Notch1 (Product ID: Hs01062014_m1), Notch2 (Product ID: Hs01050702_m1), Hes1 (Product ID: Hs00172878_m1), Hes5 (Product ID: Hs01387463_g1), Lgr5 (Product ID: Hs00969422_m1), and Olfm4 (Product ID: Hs00197437_m1). RT-PCR analysis represents the average of three independent experiments normalized to GAPDH expression. Error bars designate S.E.M. Protein extraction from mouse ISCs or human colon stem cells and western blotting were performed as previously described. β-actin was used as a control for normalization [42].

ChIP-PCR

Mouse intestinal and human colonic organoids were harvested and ChIP-PCR was performed according to manufacturer's instructions (EMD Millipore: 17-408). Briefly, normal rabbit IgG was used as a negative control while rabbit anti-Acetyl Histone H3 was used as a positive control for immunoprecipitation (IP). Subsequently, primer pairs specific for human or mouse GAPDH sequences were for positive PCR controls. Following IP using anti-mouse NICD, PCR primers (Forward: AGATGAAGGTGGAGCATGTG, Reverse: TTTTCCCACGGCCTAGAAG) were used for amplification of Notch1. Similarly, for ChIP assays involving anti-human NICD, PCR primers (Forward: ACTAGGTGTCACCAAAGTGC, Reverse: CATGACCATCTTGGCCTCTC) were used to amplify Notch1. Sanger sequencing

was used to validate NICD binding motif on Notch1 for PCR products. Subsequently, ChIP-qPCR analyses were performed according to the manufacturer's instructions (ActiveMotif: 53029).

Immunofluorescence

Intestinal tissues from Tamoxifen-induced Notch1- and Notch2- (tdTomato) reporter mice were harvested at various time points, fixed with 4% PFA, snap-frozen in O.C.T, cryo-sectioned and visualized on a Zeiss LSM 510 laser scanning confocal microscope. DAPI was used as a nuclear counterstain. For *in vitro* imaging, wild-type or CRISPR/Cas9-mutated intestinal organoids derived from LGR5-EGFP mice were embedded in Matrigel on glass chamber slides. Cells were fixed for 15 minutes at room temperature using 4% PFA and rinsed three times with PBS. 0.2% Triton X-100 was used for permeabilization of cell membranes. Next, cells were incubated in a serum-free blocking solution (Dako) for 30 minutes. For co-immunofluorescence staining, an antibody diluent solution (Dako) was used to prepare primary and secondary antibodies. Primary antibodies were added overnight at room temperature followed by application of Alexa-flour 488/555 secondary antibodies for 1 hour. Organoids were visualized using Lysosyme (LYZ) and LGR5 (detected by GFP) expression. DAPI (Life Technologies) was as a nuclear counterstain on a Zeiss LSM 510 laser scanning confocal microscope using an Apo 40Å~ 1.40 oil objective.

Statistical Analysis

The data is displayed as mean ± S.E.M. Statistical comparisons between two groups was made using Student t-test. $P < 0.05$ was used to establish statistical significance.

Computational Modeling

The deterministic model is constructed and simulated in Matlab, and the systems dynamics analysis is also solved by numerical optimization in Matlab. The 3D stochastic crypt

model is designed and simulated based on the Glazier-Graner-Hogeweg (GGH) computational model using Compucell3D[35]. Initially, a supporting layer covered by a single-cell layer of epithelial cells was designed to mimic the finger-like shape of intestine crypts. All of the designed epithelial cells inherit an effective energy programmed in the CGH's cell-lattice configuration to have the desired cell prosperities, behaviors, and interactions. The epithelial cells are programmed to possess the essential cellular prosperities: 1. cell growth, 2. cell divisions, 3. cell-cell adhesion, 4. anoikis when epithelial cells detach from supporting layers. In addition, a module of SBML (Systems Biology Markup Language) solver is applied to integrate the Notch signaling models (LI, PFLI) programmed in SBML[43] format to every epithelial cell at the bottom of the crypt. Simultaneously, the Notch signaling simulation is performed with the stochastic cellular dynamics. Combining the Notch signaling and programmed cellular properties, a Notch signaling threshold is assigned to determine the $Notch^{high}$ stem cells and $Notch^{low}$ Paneth cells at the crypt bottom. In these cells, $Notch^{high}$ stem cells are actively growing and dividing when the volumes of the cells reach division threshold, while $Notch^{low}$ Paneth cells are programmed as terminally differentiated without cellular division to recapitulate the nature of Paneth cells. These cells naturally migrate upward to leave the bottom of the crypt with the force generated by these growing cells and newly generated cells after divisions at crypt base, which shows similar migration dynamics to real crypts. R is used to analyze and plot the statistical results.

ODEs Models of Notch signaling circuits

S1.1: MATHEMATICAL MODEL

In the mathematical model of Notch signaling circuit of the intestinal cells, we include 3 types of regulations: 1. Trans-Activation (TA), 2. Lateral Inhibition (LI), and 3. Notch Positive

Feedback (PF) to investigate how these distinct regulations maintain homeostasis of intestinal stem cells and Paneth cells.

In the model, an increasing hill function $\sigma(x,k,p)=\frac{x^p}{k^p+x^p}$ is used for transcriptional activation and a decreasing hill function $\delta(x,k,h)=\frac{k^h}{k^h+x^h}$ is used for transcriptional suppression, where x refers to the regulator, k refers to saturation coefficient, and h is the hill coefficient. The complete kinetic ODEs are designed as:

$$\dot{Notch}_{mRNA_i}=\beta_{n0}+\beta_n\cdot\sigma\left(k_t\cdot NOTCH_i\langle DLL_j\rangle,k_p,p\right)-\alpha_n\cdot Notch_{mRNA_i}$$

$$\dot{NOTCH}_i=\beta_N\cdot Notch_{mRNA_i}-\alpha_N\cdot NOTCH_i-k_t\cdot NOTCH_i\langle DLL_j\rangle$$

$$\dot{Dll}_{mRNA_i}=\beta_{d0}+\beta_d\cdot\delta\left(k_t\cdot NOTCH_i\langle DLL_j\rangle,k_d,h\right)-\alpha_d\cdot Dll_{mRNA_i}$$

$$\dot{DLL}_i=\beta_D\cdot Dll_{mRNA_i}-\alpha_D DLL_i-k_t\cdot\langle NOTCH_j\rangle DLL_i$$

$$\dot{R}_i=k_t NOTCH_i\langle DLL_j\rangle-\alpha_R R_i$$

where $Notch_{mRNA}$, $NOTCH$, Dll_{mRNA}, DLL, *and* R refer to the expression level of Notch mRNA, NOTCH receptor, Dll mRNA, DLL ligand, and cleaved NICD (activated Notch signaling), respectively. The annotation i and j refer to cell j adjacent to cell i. β_s are the synthesis rates (transcription rates for mRNAs and translation rates for protein), while α_s are the degradation rates. $\langle X_j\rangle_i$ is the average expression of X from the neighboring j cells of cell i. k_t is the reaction rate of trans-activation. We consider the leakiness of the LI and PF, and β_{1_0} and β_{3_0} are the basal transcriptional rates of $Notch_{mRNA}$ and Dll_{mRNA} without any regulation respectively. By changing the ratios of $\beta_n/(\beta_{n0}+\beta_n)$ and $\beta_d/(\beta_{d0}+\beta_d)$, we adjust the strength of the regulations of LI and PF.

S1.2: Dimensionless Analysis

For simplicity, we transform the equations into dimensionless equations with dimensionless parameters: $\tau \equiv t_0 t, Nm \equiv \frac{Notch_{mRNA}}{Nm_0}, N \equiv \frac{NOTCH}{N_0}, Dm \equiv \frac{Dll_{mRNA}}{Dm_0}, D \equiv \frac{DLL}{D_0}, R \equiv \frac{R}{R_0}, N_0 = D_0 = R_0 \equiv \frac{t_0}{k_t}$.

Model 1:

$$\dot{Nm_i} = \beta_{n0} + \beta_n \cdot \sigma\left(NOTCH_i\langle DLL_j\rangle, k_p, p\right) - \alpha_n \cdot Nm_i$$

$$\dot{N_i} = \beta_N \cdot Nm_i - \alpha_N \cdot N_i - N_i\langle D_j\rangle$$

$$\dot{Dm_i} = \beta_{d0} + \beta_d \cdot \delta\left(NOTCH_i\langle DLL_j\rangle, k_d, h\right) - \alpha_d \cdot Dm_i$$

$$\dot{D_i} = \beta_D \cdot Dm_i - \alpha_D \cdot D_i - \langle N_j\rangle D_i$$

$$\dot{R_i} = NOTCH_i\langle DLL_j\rangle - \alpha_R R_i$$

Where$\beta_{n0} \equiv \frac{\beta_{n0}}{t_0 \cdot Nm_0}, \beta_n \equiv \frac{\beta_n}{t_0 \cdot Nm_0}, \beta_N \equiv \frac{\beta_N \cdot Nm_0}{t_0 \cdot N_0}, \beta_{d0} \equiv \frac{\beta_{d0}}{t_0 \cdot Dm_0}, \beta_d \equiv \frac{\beta_d}{t_0 \cdot Dm_0}, \beta_D \equiv \frac{\beta_D \cdot Dm_0}{t_0 \cdot D_0}, \alpha_n \equiv \frac{\alpha_n}{t_0}, \alpha_N \equiv \frac{\alpha_N}{t_0}, \alpha_d \equiv \frac{\alpha_d}{t_0}, \alpha_D \equiv \frac{\alpha_D}{t_0}, \alpha_R \equiv \frac{\alpha_R}{t_0}, k_p \equiv \frac{k_p}{k_t \cdot N_0 \cdot D_0}, k_d \equiv \frac{k_d}{k_t \cdot N_0 \cdot D_0}$.

To modulate the relative strength of the transcriptional regulations (LI, PF), we rescaled the ratios of basal transcriptional rates and regulated transcriptional rates as: $S_{PF} \equiv \frac{\beta_n}{\beta_{n0}+\beta_n}, S_{LI} \equiv \frac{\beta_d}{\beta_{d0}+\beta_d}$, and maximum transcriptional rate as: $\beta_{nm} = (\beta_{n0} + \beta_n), \beta_{dm} = (\beta_{d0} + \beta_d)$, where $0 \leq S_{PF}, S_{LI} \leq 1$. A new set of equations can be shown as:

Model 2:

$$\dot{Nm_i} = \beta_{nm}\left[(1 - S_{PF}) + S_{PF} \cdot \sigma\left(NOTCH_i\langle DLL_j\rangle, k_p, p\right)\right] - \alpha_n \cdot Nm_i$$

$$\dot{N_i} = \beta_N \cdot Nm_i - \alpha_N \cdot N_i - N_i\langle D_j\rangle$$

$$\dot{Dm_i} = \beta_{dm}\left[(1 - S_{LI}) + S_{LI} \cdot \delta\left(NOTCH_i\langle DLL_j\rangle, k_d, h\right)\right] - \alpha_d \cdot Dm_i$$

$$\dot{D}_i = \beta_D \cdot Dm_i - \alpha_D \cdot D_i - \langle N_j \rangle D_i$$

$$\dot{R}_i = N_i \langle D_j \rangle - \alpha_R R_i$$

S1.3: Dimension Reduction

First, we assume the time scale for mRNA is much faster than proteins, so quasi-steady state method is applied to reduce the mRNA species in the equations:

Set $\dot{Nm}_i = 0,\ \dot{Dm}_i = 0$

$$Nm_i^* = \frac{\beta_{nm}}{\alpha_n}\left[(1 - S_{PF}) + S_{PF} \cdot \sigma\left(NOTCH_i\langle DLL_j\rangle, k_p, p\right)\right],$$

$$Dm_i^* = \frac{\beta_{dm}}{\alpha_d}\left[(1 - S_{LI}) + S_{LI} \cdot \delta\left(NOTCH_i\langle DLL_j\rangle, k_d, h\right)\right]$$

replace $[Nm_i, Dm_i]$ with $[Nm_i^*, Dm_i^*]$ in $\dot{N}_i$ and $\dot{D}_i$ respectively, and set $\beta_N = \beta_N \frac{\beta_{nm}}{\alpha_n}$, $\beta_D = \beta_D \frac{\beta_{dm}}{\alpha_d}$. A simple protein model can be shown as:

Model 3:

$$\dot{N}_i = \beta_N \cdot \left[(1 - S_{PF}) + S_{PF} \cdot \sigma\left(NOTCH_i\langle DLL_j\rangle, k_p, p\right)\right] - \alpha_N \cdot N_i - N_i\langle D_j\rangle$$

$$\dot{D}_i = \beta_D \cdot \left[(1 - S_{LI}) + S_{LI} \cdot \delta\left(NOTCH_i\langle DLL_j\rangle, k_d, h\right)\right] - \alpha_D \cdot D_i - \langle N_j\rangle D_i$$

$$\dot{R}_i = N_i\langle D_j\rangle - \alpha_R R_i$$

S2.0: Parameter Table

Figure	Model	Parameters
Figure 5a (LI)	Model 1	β_{n0}= 1, β_{d0}= 0.01, β_n= 0, β_d= 1, β_N= 1, β_D= 1,α_n= 1, α_d= 1, α_N= 1, α_D= 1, k_d= 0.1, h= 1
Figure 5a (PFLI)	Model 1	β_{n0}= 0.04, β_{d0}= 0.01, β_n= 1, β_d= 1, β_N= 1, β_D= 1,α_n= 1, α_d= 1, α_N= 1, α_D= 1 , k_p= 0.01, k_d= 0.1, h= 1, p= 3
Figure 5b (LI)	Model 1	β_{n0}= 1, β_{d0}= 0.01, β_n= 0, β_d= 1, β_N= 1, β_D= 1, α_n= 1, α_d= 1, α_N= 1, α_D= 1, k_d= 0.1, h= [1-2]
Figure 5b (PFLI)	Model 1	β_{n0}= 0.1, β_{d0}= 0.01, β_n= 1, β_d= 1, β_N= 1, β_D= 1,α_n= 1, α_d= 1, α_N= 1, α_D= 1 , k_p= 0.0774, k_d= 0.0167, h= [1-2], p= 1
Figure 5c (LI)	Model 1	β_{n0}= 10^{-2}-10^{2}, β_{d0}=10^{-5}, β_n=0, β_d= 10^{-2}-10^{2}, β_N= 1, β_D= 1,α_n= 1, α_d= 1, α_N= 1, α_D= 1, k_d= 0.1778, h= [1-3]
Figure 5c (PFLI)	Model 1	β_{n0}= 10^{-5}, β_{d0}=10^{-5}, β_n= 10^{-2}-10^{2}, β_d= 10^{-2}-10^{2}, β_N= 1, β_D= 1,α_n= 1, α_d= 1, α_N= 1, α_D= 1, k_p= 0.0774, k_d= 0.0167, h= [1-3], p= 1
Figure 5d	Model 1	β_{nm}=10, S_{PF}=0-1, β_{dm} =100, S_{LI}=1, β_N= 1, β_D= 1, α_n= 1, α_d= 1, α_N= 1, α_D= 1 , k_p= various, k_d= various, h= 3, p= 3
Figure 5e (LI)	Model 3	β_N= 10, S_{PF}=0, β_D=100, S_{LI}= 1,α_n= 1, α_d= 1, α_N= 1, α_D= 1, α_R = 1, k_d= 0.1778, h= 3
Figure 5e (PFLI)	Model 3	β_N= 10, S_{PF}=1, β_{D0}= 0, β_D= 100,α_n= 1, α_d= 1, α_N= 1, α_D= 1, α_R = 1, k_n=0.0042, k_d= 0.015, h= 3, p=3
Figure S5-1a (LI)	Model 1	β_{n0}= 1, β_{d0}= 0.0100, β_n= 0, β_d= 1, β_N= 1, β_D= 1,α_n= 1, α_d= 1, α_N= 1, α_D= 1,k_d= 0.1,h= [1-3]
Figure S5-1b (PFLI)	Model 1	β_{n0}= 0.04, β_{d0}= 0.01, β_n= 1, β_d= 1, β_N= 1, β_D= 1,α_n= 1, α_d= 1, α_N= 1, α_D= 1 , k_p= 0.01, k_d= 0.1,h= [1-3],p= [1-3]
Figure S5-1c (LI)	Model 1	β_{n0}= 1, β_{d0}= 0.0100, β_n= 0, β_d= 1, β_N= 1, β_D= 1,α_n= 1, α_d= 1, α_N= 1, α_D= 1,k_d= 0.1,h= [1-3]
Figure S5-1d (PFLI)	Model 1	β_{n0}= 0.1, β_{d0}= 0.01, β_n= 1, β_d= 1, β_N= 1, β_D= 1,α_n= 1, α_d= 1, α_N= 1, α_D= 1 , k_p= 0.0774, k_d= 0.0167, h= [1-3], p= [1-3]
Figure S5-2a (LI)	Model 1	β_{n0}= 5, β_{d0}= 10^{-5}, β_n= 0, β_d= 5, β_N= 1, β_D= 1,α_n= 1, α_d= 1, α_N= 1, α_D= 1,k_d= 0.1778,h= 3
Figure S5-2a (PFLI)	Model 3	β_{n0}= 10^{-5}, β_{d0}= 10^{-5}, β_n= 5, β_d= 5, β_N= 1, β_D= 1,α_n= 1, α_d= 1, α_N= 1, α_D= 1 ,k_p= 0.0115, k_d= 0.015,h= 3,p= 1
Figure S5-2b	Model 3	β_{N0}= 0.1, $\beta_{N'}$=[0.1,1,5,10], β_{D0}= 0, $\beta_{D'}$= 100,α_n= 1, α_d= 1, α_N= 1, α_D= 1, α_R = 1, k_n=0.0042, k_d= 0.015, h= 3, p=3, β_{N0}= β_N(1- S_{PF}), $\beta_{N'}$= β_N(S_{PF}), β_{D0}= β_D(1- S_{LI}), $\beta_{D'}$= β_D(S_{LI})

Figure 1. Imaging and laser ablation of the intestinal stem cell niche.

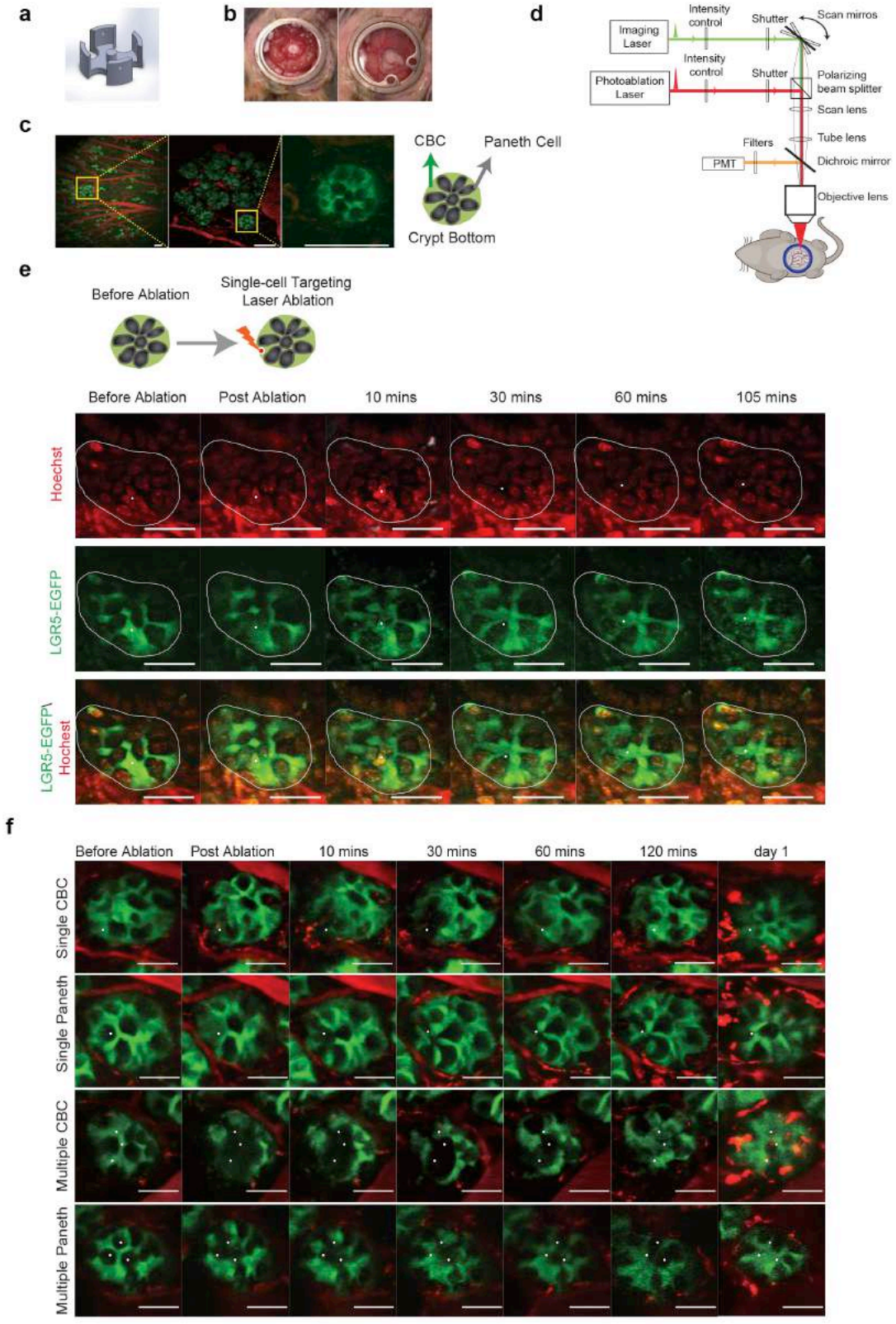

(a) Design of the 3-D printed intestinal scaffold. **(b)** Images of an open (left) and a closed (right) abdominal window. **(c)** Representative images of crypts and vasculature at low (left), intermediate (middle) and high (right) magnification. Green, CBCs in LGR5-EGFP mice. Red, vasculature labeled by Texas-red dextran. Yellow, field of view magnified in each subsequent panel. Also shown is a cartoon of a crypt bottom. (Scale bar: left: 150 μm, middle, right: 50 μm). **(d)** Schematic illustrating the *in vivo* multiphoton imaging and laser ablation setup. **(e)** Time-lapse images following laser ablation. Nuclei were stained by Hoechst dye. GFP signal in the ablated cell dissipated right away, and the nucleus of the ablated cell disappeared between 10 and 30 minutes. White dot marks the target position of laser focus. Scale bar: 30 μm. **(f)** Time-lapse series following laser ablation of single or multiple CBCs or Paneth cells. Post ablation, crypts were continuously monitored for 2 hours (120 minutes), and imaged again after approximately 24 hours. Green, GFP signaling from LGR5+ CBCs. Red, vasculature labeled by Texas-red dextran. White dots mark the target positions of laser focus. Scale bar: 30 μm.

Figure 2. Notch signaling in niche cells.

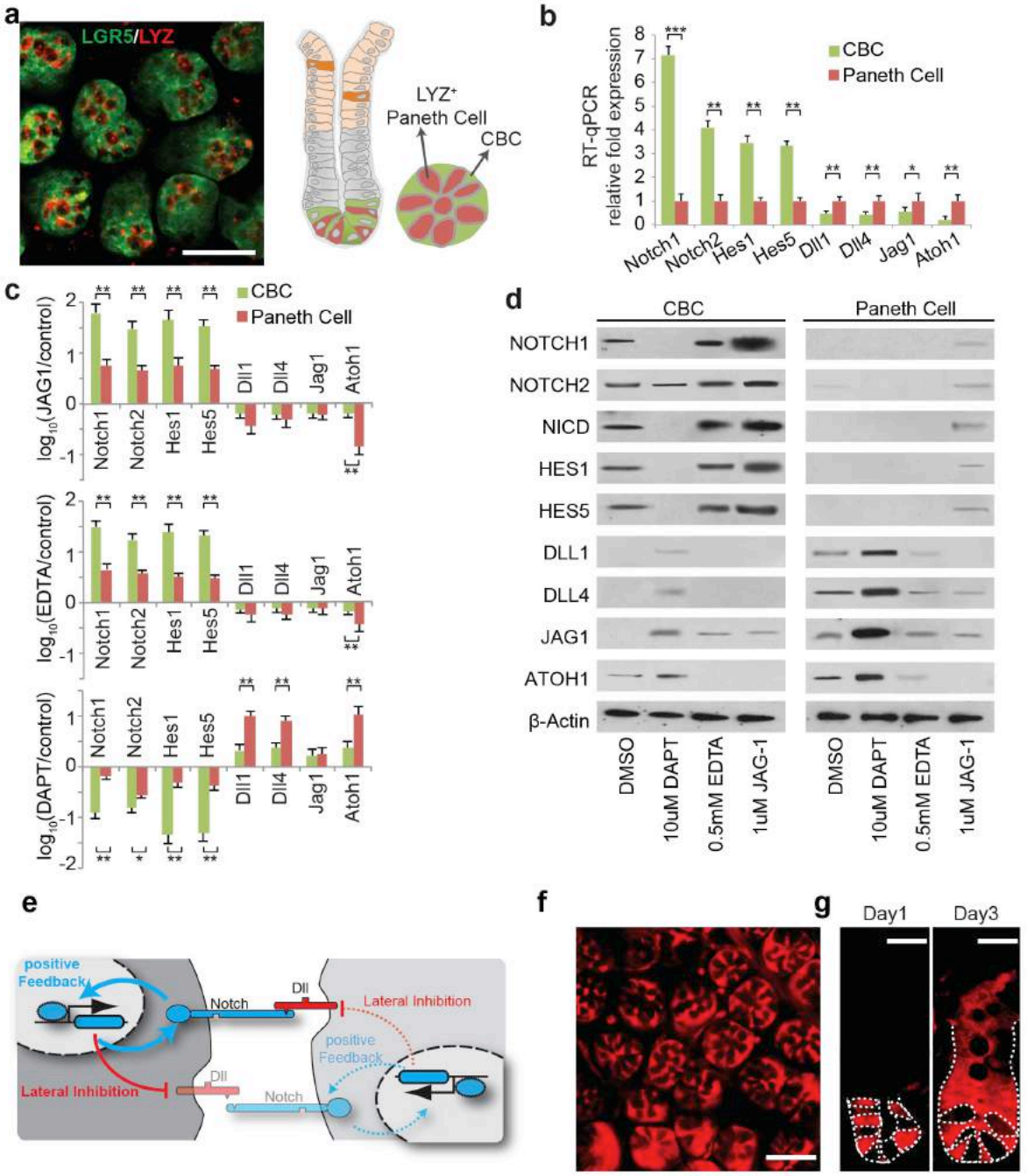

(a) Left: Cross-sectional view of murine intestinal crypt bottoms with co-immunofluorescence (co-IF) showing intermingled LGR5-EGFP+ (green) CBCs and lysozyme+ (LYZ, red) Paneth cells. Scale bar: 50 μm. Right: schematic illustration of a niche pattern in both longitudinal and cross sectional views of a crypt. **(b)** RT-qPCR quantification of Notch signaling components in

CBC and Paneth cell populations. The experiment was performed in triplicate and presented mean ± S.E.M. (***, p=0.001, **, p = 0.01, *, p=0.05; Student t-test). **(c)** RT-qPCR quantification of Notch signaling components in CBCs and Paneth cell populations after organoids were treated with JAG1 (top), EDTA (middle) or DAPT (bottom). The experiments were performed in triplicate and presented mean ± S.E.M. (**, p = 0.01, *, p=0.05; Student t-test). **(d)** Western blot analysis of Notch signaling components from *in vitro* conditions described in (c). Actin was used as a loading control. **(e)** Schematic illustration of lateral inhibition and positive feedback between neighboring cells. **(f)** Representative IF image indicating Notch1 expression (red) in intestinal crypt bottoms of Tamoxifen-induced $Notch1^{CreER}$ x $Rosa26^{tdTomato}$ mice. Scale bar: 50 μm. **(g)** Representative IF images of intestinal crypts showing progeny of Notch1+ cells 1 day (left) and 3 days (right) after Tamoxifen induction in $Notch1^{CreER}$ x $Rosa26^{tdTomato}$ mice. Scale bar: 20 μm.

Figure 3. Notch1 positive feedback.

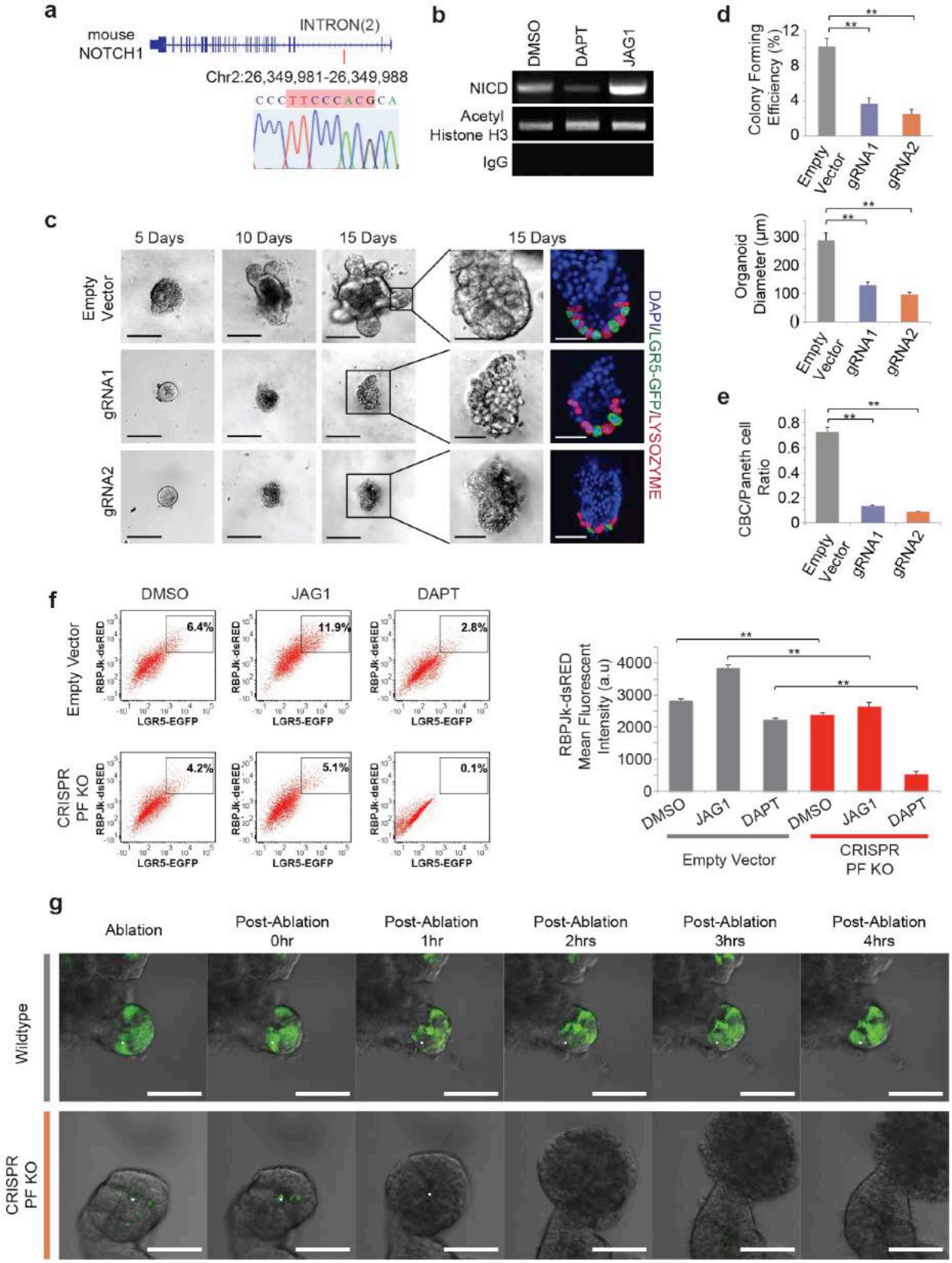

(a) Top: Predicted sequence and location of putative NICD/RBPJk binding motif on Notch1. Bottom: Sequence and chromatogram of NICD binding motif in mouse Notch1 following ChIP-PCR from LGR5-EGFP+ CBCs. **(b)** Agarose gel analysis of ChIP-PCR products from LGR5-EGFP+ CBCs validating NICD binding to motif in Notch1 sequence. LGR5-EGFP+ CBCs were sorted from organoids treated with DMSO, DAPT or JAG1. **(c)** Single LGR5-EGFP+ CBCs were transfected with either an empty vector (control) or CRISPR/Cas9 gRNAs. Shown are representative brightfield images over 15 days and co-IF images indicating LGR5-EGFP (green) and LYZ (red) expression with DAPI nuclear staining. Scale bar represents 100 μm in low magnification and 25 μm in high magnification images, respectively. **(d)** Single LGR5-EGFP CBCs were transfected with either an empty vector (control) or CRISPR/Cas9 gRNAs. Top: Colony forming efficiency measured after 5 days. Quantitative analysis calculated from 1000 cells/replicated. The experiment was performed in triplicate and presented mean ± S.E.M. (**, p = 0.01; Student t-test). Bottom: Quantitative comparison of organoid diameters after 15 days. The experiment was performed in triplicate and presented mean ± S.E.M. (**, p = 0.01; Student t-test). **(e)** Single LGR5-EGFP ISCs were transfected with either an empty vector (control) or CRISPR/Cas9 gRNAs. Ratio of LGR5-EGFP+ CBCs/LYZ+ Paneth cells as determined by FACS analysis after 15 days. The experiment was performed in triplicate and presented mean ± S.E.M. (**, p = 0.01; Student t-test). **(f)** Single empty vector control or CRISPR/Cas9-postive feedback knockout (PF KO) LGR5-EGFP+ CBCs were transfected with an RBPJk-dsRed reporter construct and grown into organoids, which were subsequently treated with DMSO, DAPT or JAG1 for 48 hours. Left: Representative FACS plots for RBPJk-dsRED and LGR5-EGFP expression indicating a gated double positive fraction for each condition. Right: Mean fluorescence intensity (MFI) of RBPJk-dsRed expression. The experiment was performed in triplicate and presented mean ± S.E.M. (**, p = 0.01; Student t-test). **(g)** Wild-type or

CRISPR/Cas9 PF KO CBCs propagated as organoids were subjected to single cell laser ablation. Shown are representative images pre- and post-ablation for 4 hours. White dots mark the target position of laser focus. Green: LGR5-EGFP. Scale bar: 50 μm.

Figure 4. Notch1 positive feedback is conserved in human colon organoids.

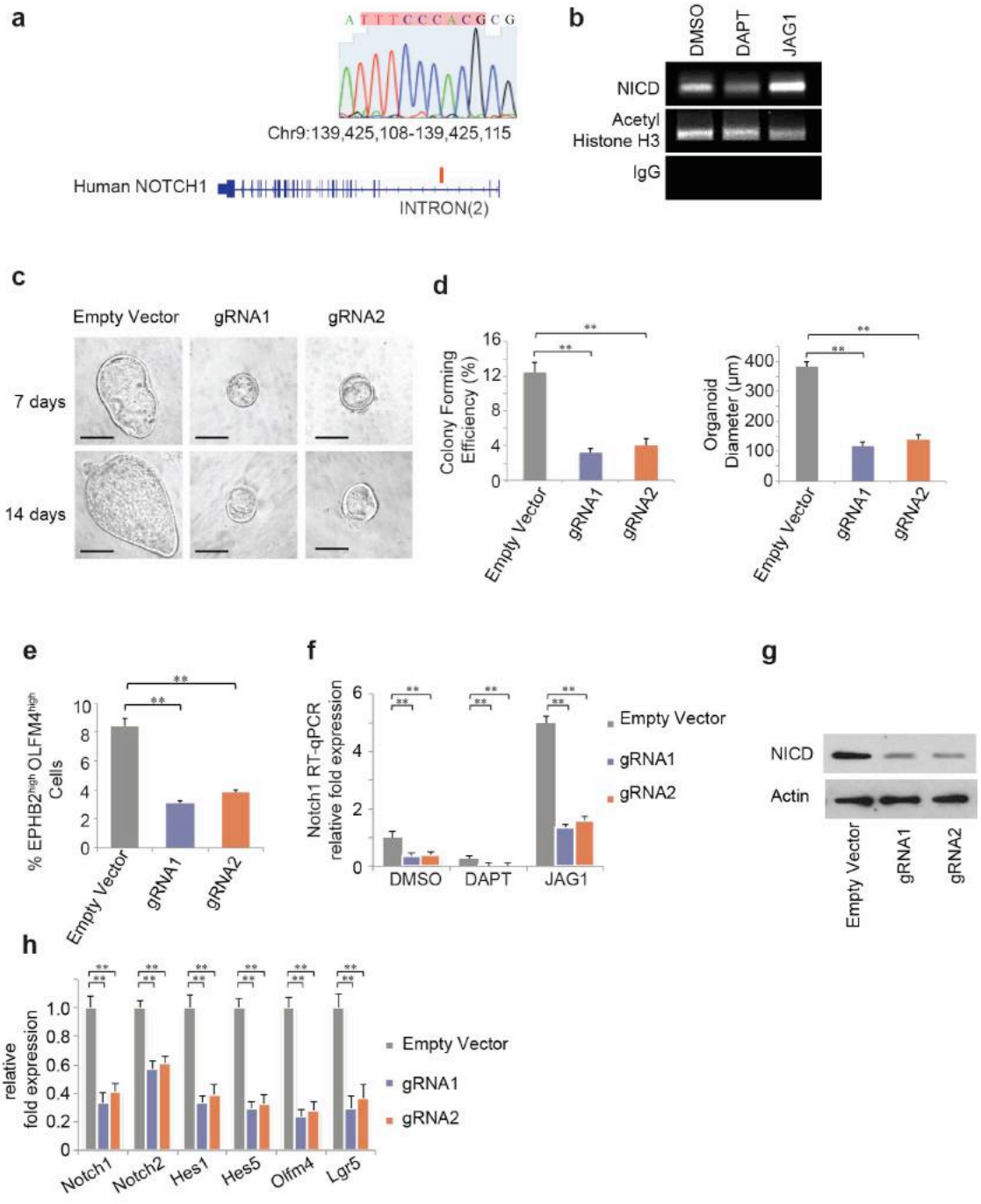

(a) Top: Sequence and chromatogram of NICD binding motif to human Notch1 following ChIP-PCR from EPHB2^{high}OLFM4^{high} colon stem cells. Bottom: Predicted sequence and location of putative NICD binding motif on human Notch1. **(b)** Agarose gel analysis of ChIP-PCR products

indicating active binding of NICD to motif in Notch1 sequence in EPHB2^{high}OLFM4^{high} colon stem cells treated with DMSO, DAPT, or JAG1. **(c)** Representative brightfield images of organoids derived from single EPHB2^{high}OLFM4^{high} colon stem cells transfected with either an empty vector control or CRISPR/Cas9 gRNAs after 7 days (top panel) and 14 days (bottom panel). Scale bar represents 50 μm. **(d)** Single EPHB2^{high}OLFM4^{high} colon stem cells were transfected with either an empty vector control or CRISPR/Cas9 gRNAs. Left: Colony forming efficiency measured after 7 days. Quantitative analysis calculated from 1000 cells/replicated. The experiment was performed in triplicate and presented mean ± S.E.M. (**, p = 0.01; Student t-test). Right: Quantitative comparison of organoid diameters after 14 days for each condition. The experiment was performed in triplicate and presented mean ± S.E.M. (**, p = 0.01; Student t-test). **(e)** Percentage of EPHB2^{high}OLFM4^{high} stem cells based on FACS analysis for each condition described in (d) after 14 days. The experiment was performed in triplicate and presented mean ± S.E.M. (**, p = 0.01; Student t-test). **(f)** RT-PCR measurements indicating NOTCH1 expression in EPHB2^{high}OLFM4^{high} colon stem cells transfected with either an empty vector control or CRISPR/Cas9 gRNAs and subsequently treated with DMSO, DAPT or JAG1. The experiment was performed in triplicate and presented mean ± S.E.M. (**, p = 0.01; Student t-test). **(g)** Single EPHB2^{high}OLFM4^{high} colon stem cells were transfected with either an empty vector control or CRISPR/Cas9 gRNAs. Shown is Western blot analysis for NICD expression in sorted EPHB2^{high}OLFM4^{high} colon stem cells from each condition. Actin was used as a loading control. **(h)** RT-PCR measurements indicating Notch1/2, Hes1/5, Olfm4, and Lgr5 expression in EPHB2^{high}OLFM4^{high} colon stem cells for each condition described in (g). The experiment was performed in triplicate and presented mean ± S.E.M. (**, p = 0.01; Student t-test).

Figure 5. Computational modeling analysis of Notch1 positive feedback.

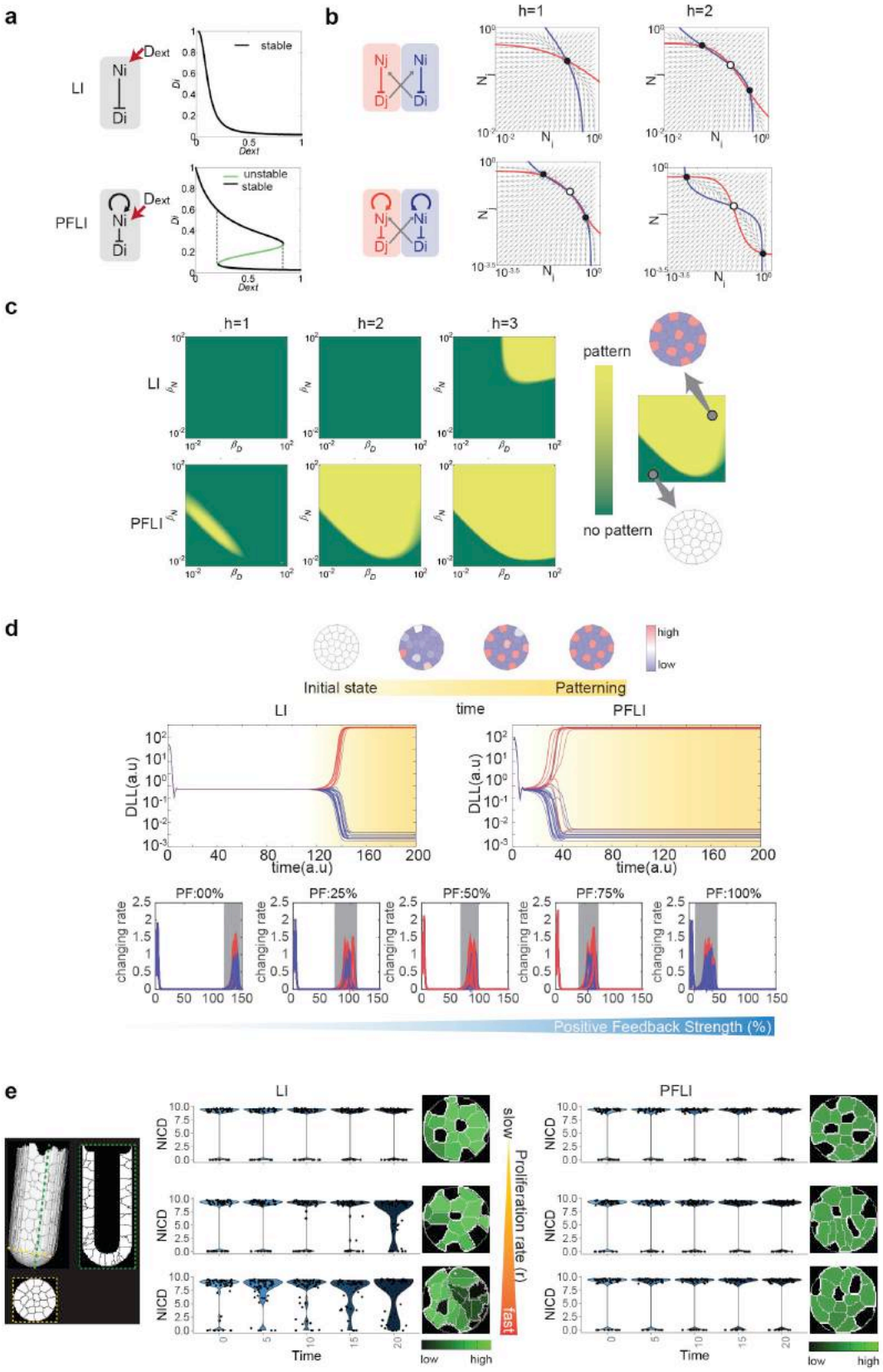

(a) Dynamic analysis of the single-cell Notch signaling model. Internal Dll (D_i) vs. external Dll (D_{ext}) protein levels are plotted. Lateral inhibition (LI) exhibits monostable behavior (top panel) while Notch positive feedback + LI (PFLI) exhibits bifurcation (bottom panel) in response to external Notch activation. **(b)** Phase portraits of the pair-cell Notch signaling model. LI (top panel) requires higher cooperativity (Hill coefficient, h) than PFLI (bottom panel) to generate bistability. Lines: nullclines; solid dots: stable steady states; hollow dots: unstable steady states. **(c)** Multi-cell analysis by Maximum Lyapunov Exponents (MLE) in Notch LI-only (top) or PFLI (bottom) circuits spanning parameters of production rates of Notch and Dll with varying degrees of cooperativity (h). Yellow regions (positive MLE values) represent the patterning state and green regions (negative MLE values) represent the state without patterning. PFLI generates patterns over a broader parameter range than LI. **(d)** Multi-cellular simulation of Notch signaling models showing DLL levels from initially homogeneous unstable steady states to heterogeneous stable steady states (top panel). Middle-left panel: representative simulation of LI. Middle-right panel: representative simulation of PFLI. Bottom panel shows the change rates of DLLs levels during patterning with varying relative strength of positive feedback. Red: signaling dynamics of cells reaching high steady states. Blue: signaling dynamics of cells reaching low steady states. Grey: patterning transition period from homogeneous steady states to heterogeneous steady state. **(e)** Analysis of a stochastic 3D crypt model integrated with Notch signaling simulation. Left: Structure of the 3D crypt model. Right: representative violin plots indicating NICD level dynamics in the 3D crypt base model with varying turnover rates. Shown also are corresponding representative simulated patterns of NICD levels in crypt bottoms. PFLI shows stronger NICD bimodality and binary patterns than LI when turnover rates become higher.

Supplementary Figure S1. *In vivo* imaging and laser ablation.

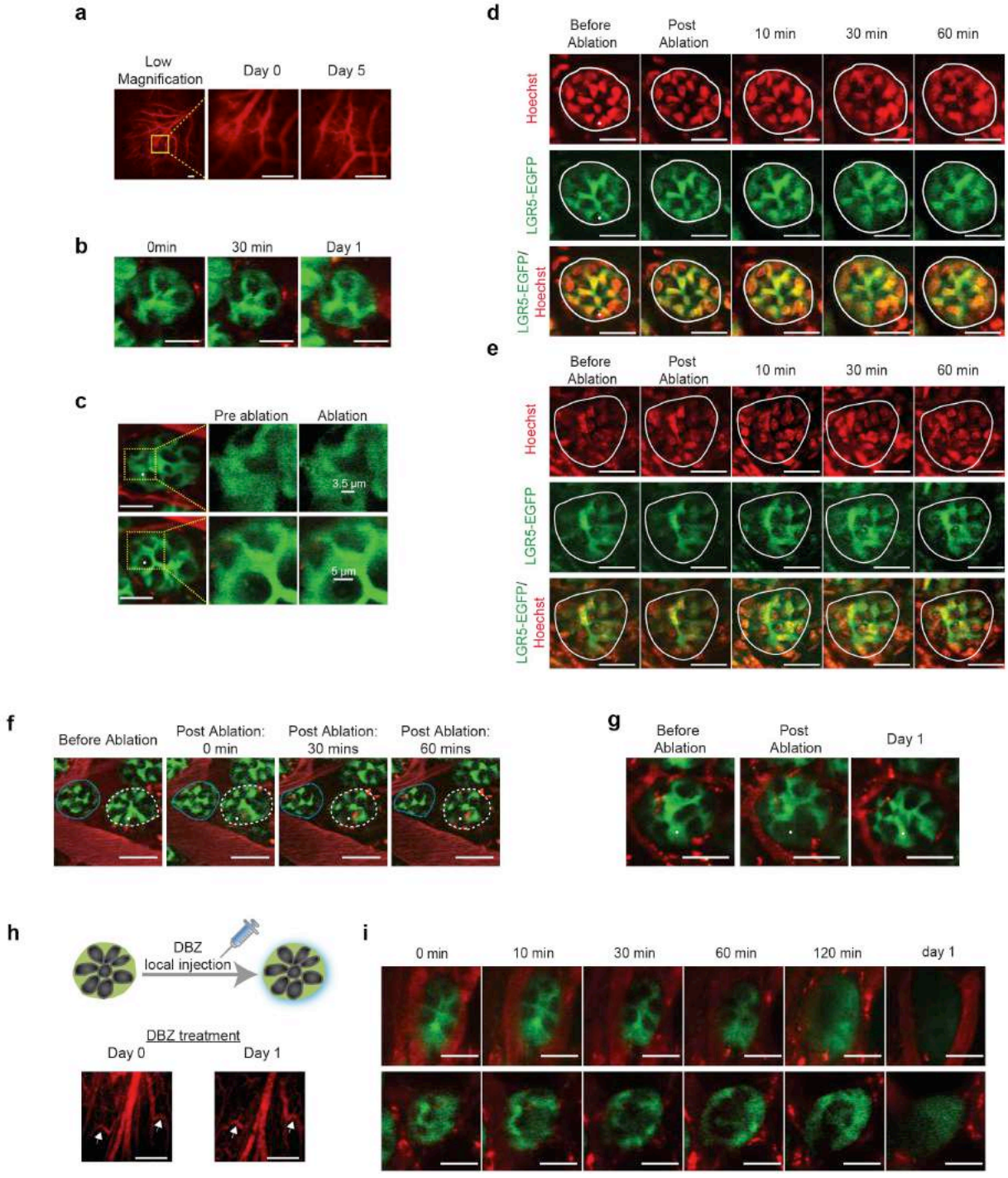

(a) Intestinal vasculature imaged through abdominal window. The vasculature remains largely unchanged after 5 days. Scale bar: 150 µm. (b) Time-lapse images showing the LGR5+ CBC/Paneth pattern remains the same for one day. Scale bar: 30 µm. (c) Top: ablation on a LGR5+ CBC. Bottom: ablation on a Paneth cell. Laser ablation created focal damage on the

targeted cells. The bars in the high magnification images show the diameter of the focal damage generated by ablation. White dot marks the position of laser focus. Scale bar: 30 μm in low magnification images. (d) Time-lapse images following laser ablation on a Paneth cell. The nucleus of the ablated Paneth cell disappeared between 30 and 60 minutes. Nuclei were stained by Hoechst dye. White dot marks the target position of laser focus. Scale bar: 30 μm. (e) Time-lapse images of a control crypt without ablation. The CBCs and Paneth cells remain unchanged up to one hour during the imaging period. Nuclei were stained by Hoechst dye. White dot marks the target position of laser focus. Scale bar: 30 μm (f) Time-lapse images following laser ablation showing targeted niche undergoing rearrangement while adjacent untargeted niche remains the same. White dot marks the position of laser focus. Scale bar: 40 μm. (g) Representative time-lapse series following laser ablation of LGR5-EGFP+ CBC showing crypt base pattern the next day. White dot marks the target position of laser focus. Scale bar: 20 μm. (h) Vasculature labeled by Texas-red dextran (red) remained largely unchanged after DBZ treatment. Scale bar: 150 μm. (i) Time-series images starting at 2 hours after local injection of Notch inhibitor DBZ via the openable abdominal window. Two independent series are presented in top and bottom panels, respectively. Green, LGR5-GFP; Red,Texas-red dextran labeled vasculature. Scale bar: 30 μm.

Supplementary Figure S2. Notch levels in niche cells.

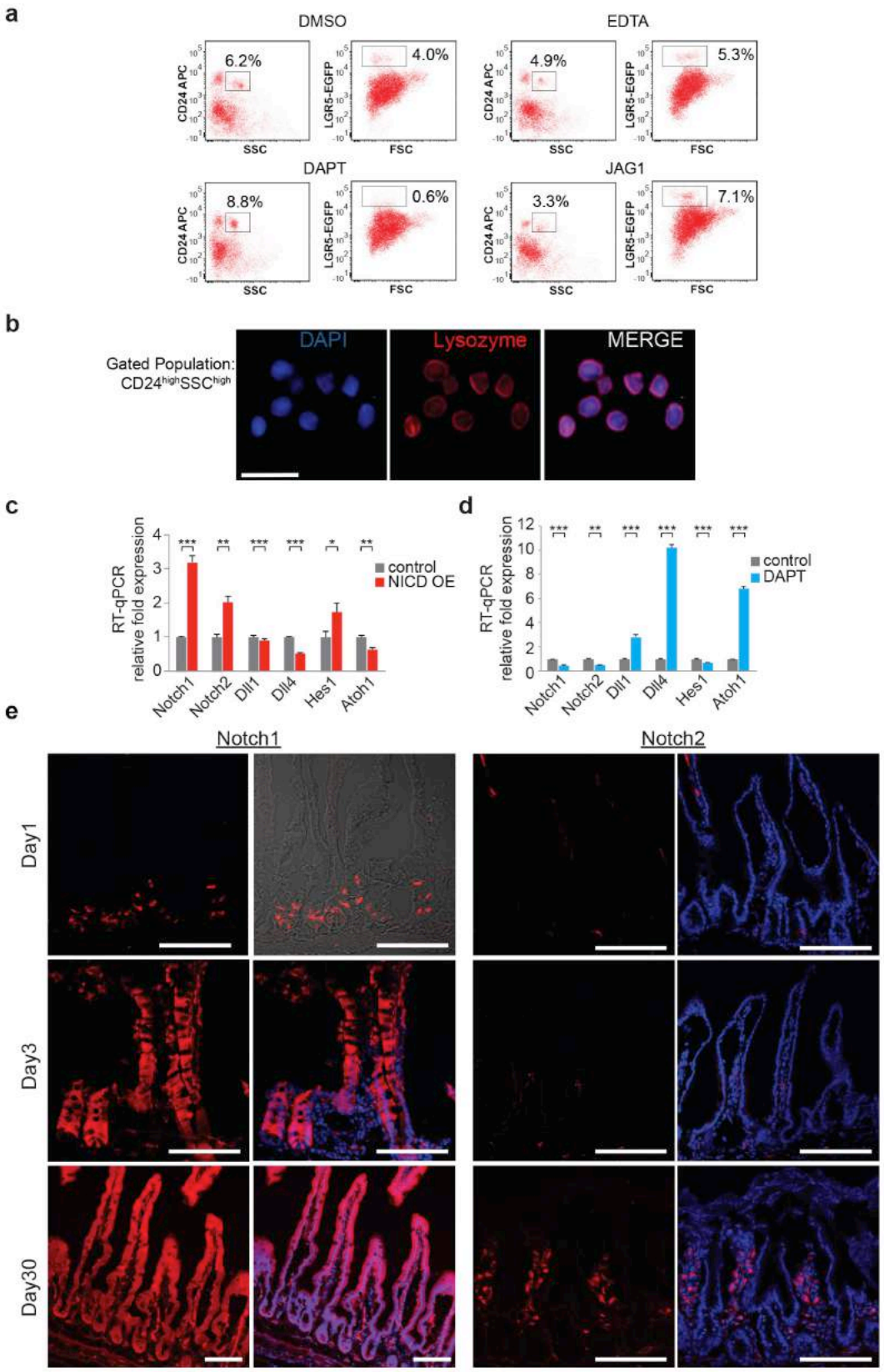

(a) Representative FACS plots of organoids treated with DMSO, JAG1, EDTA or DAPT for 48 hours, including gated analysis to isolate $CD24^{high}/SSC^{high}$ Paneth cells and LGR5-EGFP+ CBCs according to an established protocol[3]. **(b)** Immunofluorescent (IF) image of sorted $CD24^{high}/SSC^{high}$ cells showing expression of Paneth cell-specific marker Lysozyme (red). DAPI labels nuclei and scale bar represents 50 μm. **(c)** Organoids extracted from LGR5-EGFP x CreERT2/Rosa26-YFP-NICD mice were treated with Tamoxifen to induce NICD overexpression (NICD-OE). Shown is RT-qPCR quantification of Notch levels. The experiment was performed in triplicate and presented mean ± S.E.M. (*, p=0.05; **, p = 0.01; ***, p=0.001, Student t-test). **(d)** RT-qPCR measurements of Notch levels with DMSO or DAPT treatment. The experiment was performed in triplicate and presented mean ± S.E.M. (**, p = 0.01; ***, p=0.001, Student t-test). **(e)** Representative IF images of intestinal tissue derived from Tamoxifen-induced Notch1-CreERT2 KI x Rosa26-tdTomato-WPRE mice (left) and Notch2-CreERT2 KI x Rosa26-tdTomato-WPRE) mice (right). Shown are images from 1 day, 3 days, and 30 days post-Tamoxifen induction. Notch1/2 IF (red). DAPI labels nuclei and scale bar represents 100 μm.

Supplementary Figure S3. Notch 1 positive feedback in mouse intestine.

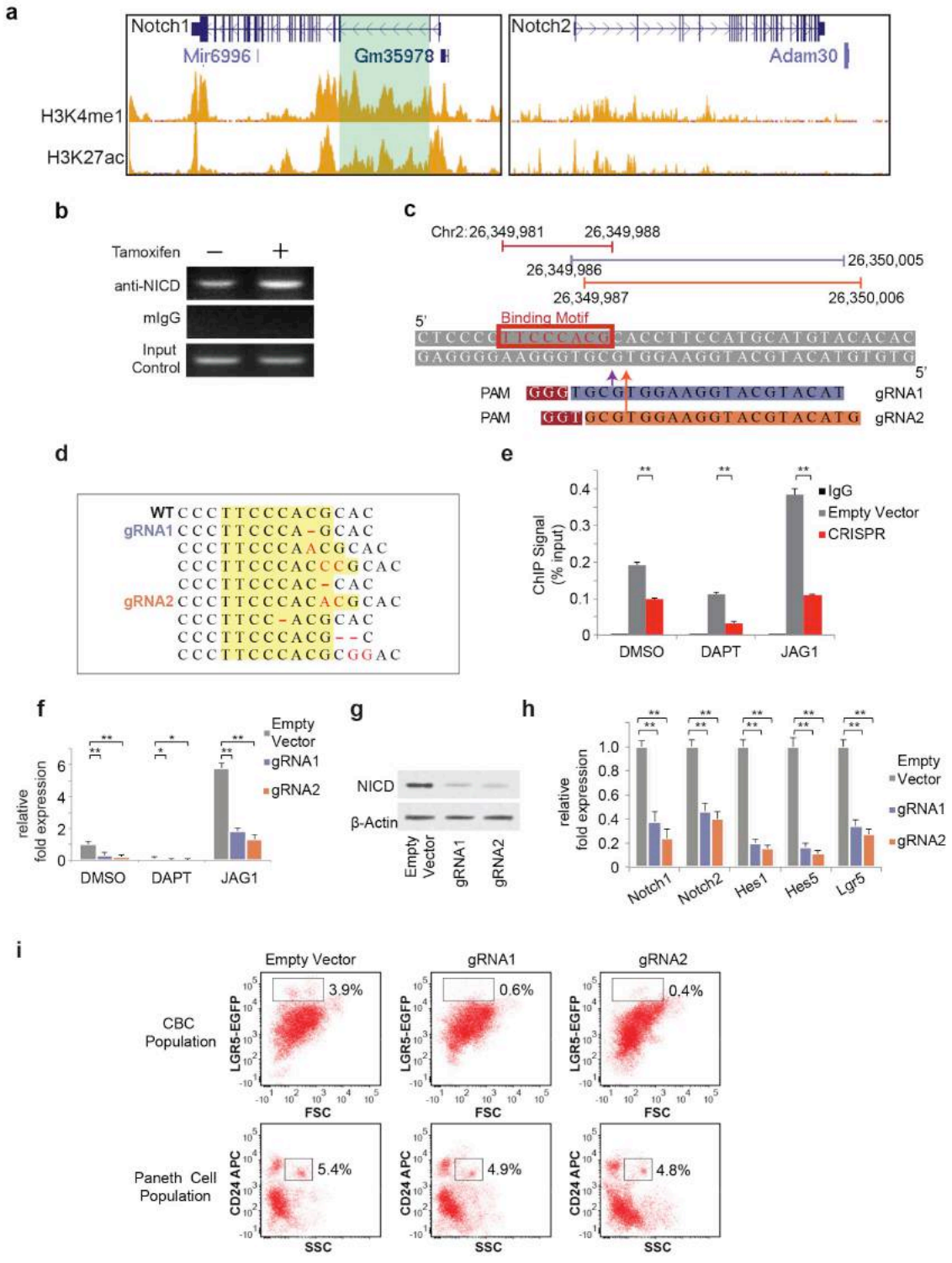

(a) ChIP-Seq signal of LICR Histone tracks (H3K4me1 and H3K27ac) on mouse small intestine cells from ENCODE at UCSC Genome Browser. Left: H3K4me1 (top) and H3K27ac (bottom)

occupancy related to Notch1. Right: H3K4me1 (top) and H3K27ac (bottom) occupancy related to Notch2. **(b)** Organoids extracted from LGR5-EGFP x CreERT2/Rosa26-YFP-NICD mice were treated with Tamoxifen to induce NICD overexpression (NICD-OE). Shown is agarose gel analysis of ChIP-PCR products to validate active NICD binding on Notch1. **(c)** Design of gRNAs for CRISPR/Cas9 mutagenesis to target the putative NICD/RBPJk binding motif on mouse Notch1 sequence. **(d)** Representative sequences from selected organoid clones transfected with CRISPR/Cas9 gRNAs showing indel mutations in the targeted region of the mouse NICD binding motif. **(e)** LGR5-EGFP+ CBCs were transfected with either an empty vector control or CRISPR/Cas9 gRNA and subsequently treated with DMSO, DAPT or JAG1. Shown is ChIP-qPCR analysis of Notch1, indicating enrichment with NICD antibody compared with IgG control. The experiment was performed in triplicate and presented mean ± S.E.M. (**, p = 0.01; Student t-test). **(f)** RT-PCR measurements indicating Notch1 expression in LGR5-EGFP+ CBCs transfected with either an empty vector control or CRISPR/Cas9 gRNAs and subsequently treated with DMSO, DAPT or JAG1. The experiment was performed in triplicate and presented mean ± S.E.M. (*, p=0.05, **, p = 0.01; Student t-test). **(g)** Single LGR5-EGFP+ CBCs were transfected with either an empty vector control or CRISPR/Cas9 gRNAs and propagated as organoids. Shown is Western blot analysis for NICD expression in sorted LGR5-EGFP+ CBCs from each condition. Actin was used as a loading control. **(h)** RT-PCR measurements indicating Notch1/2, Hes1/5, and Lgr5 expression in LGR5-EGFP+ ISCs for each condition described in (f). The experiment was performed in triplicate and presented mean ± S.E.M. (**, p = 0.01; Student t-test). **(i)** Single LGR5-EGFP+ CBCs were transfected with either an empty vector control or CRISPR/Cas9 gRNAs and propagated as organoids for 15 days. Shown are representative FACS plots for each condition including gated analysis to isolate $CD24^{high}/SSC^{high}$ Paneth cells and LGR5-EGFP+ ISCs.

Supplementary Figure S4. Disruption of Notch1 positive feedback.

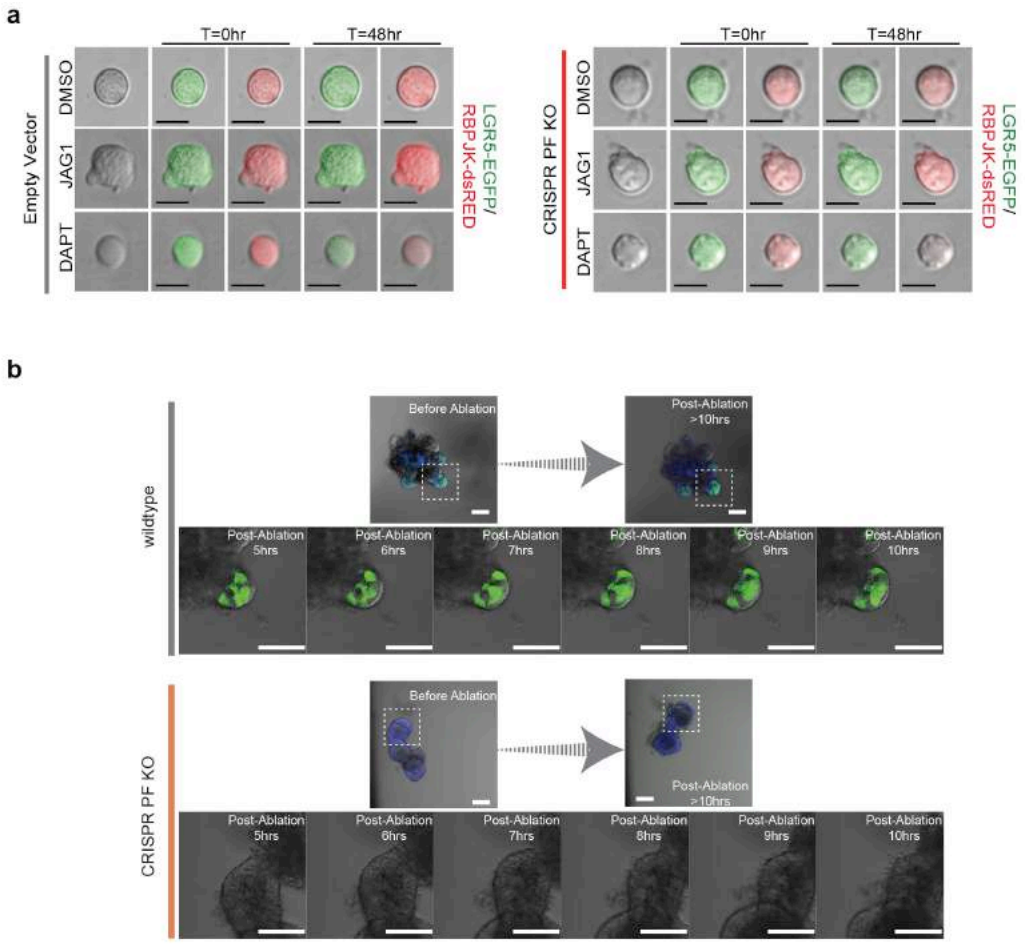

(a) Single empty vector (control) containing cells or CRISPR/Cas9-mutated LGR5-EGFP+ CBCs were transfected with a RBPJk-dsRed reporter construct and subsequently treated with DMSO, DAPT or JAG1 for 48 hours. Shown are representative images indicating LGR5-EGFP (green) and RBPJk-dsRed (red) expression for each condition. **(b)** Wild-type (top) or CRISPR/Cas9 gRNA-transfected (bottom) CBCs propagated as organoids were subjected to single cell laser ablation. Shown are representative images of whole organoids pre-ablation and 10 hours post-ablation, and magnified time-lapse images of the targeted budding region from 5 hours to 10 hours post-ablation. LGR5-EGFP (green). Hoescht dye (blue) labels nuclei and scale bar represents 50 μm.

Supplementary Figure S5. Notch 1 positive feedback in human colon stem cells.

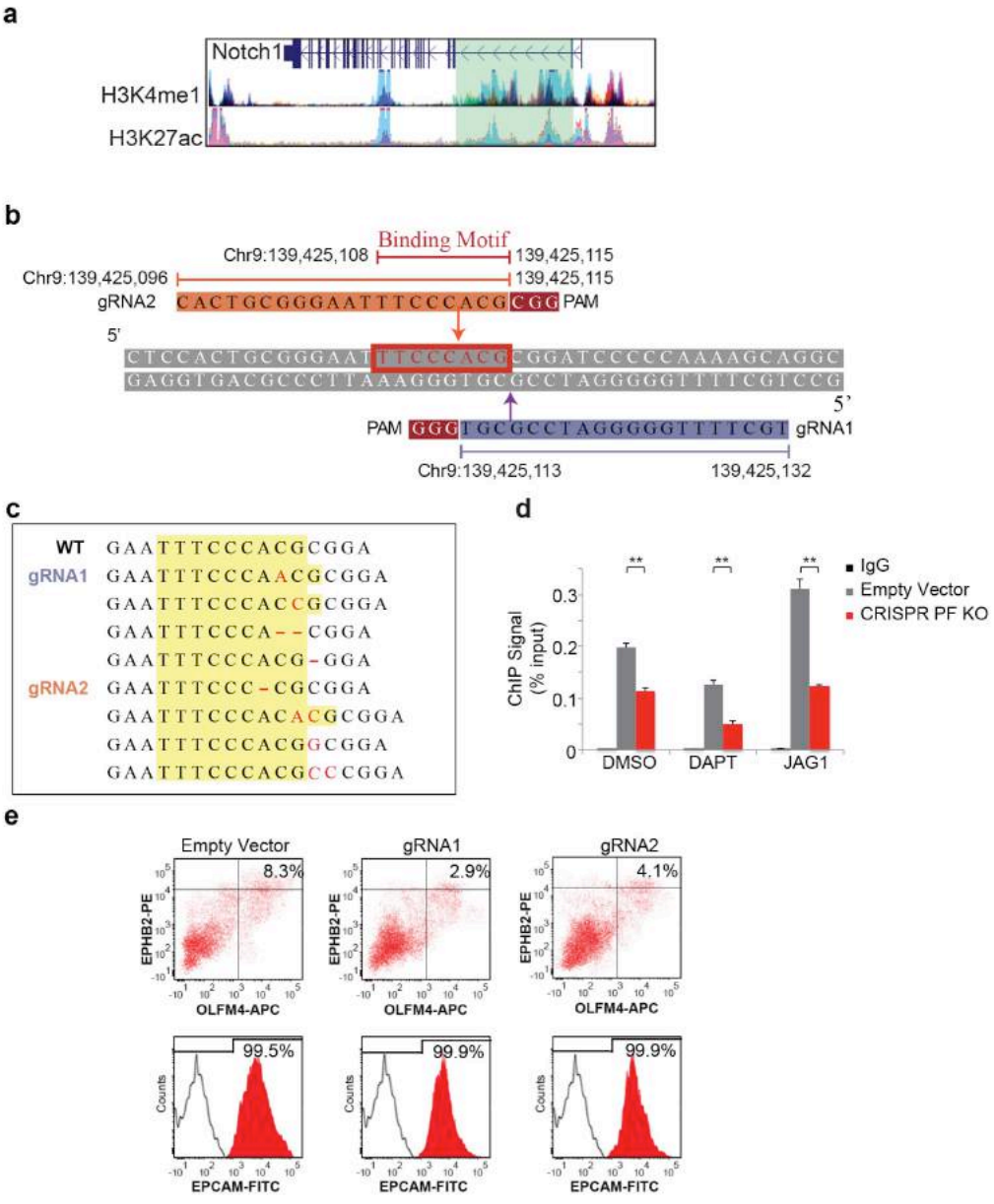

(a) ChIP-Seq signal of H3K4me1 (top) and H3K27ac (bottom) occupancy related to human Notch1 on 7 human cell lines from ENCODE at UCSC Genome Browser. **(b)** Design of gRNAs for CRISPR/Cas9 mutagenesis to target the putative NICD/RBPJk binding motif on human Notch1. **(c)** Single EPHB2^{high}OLFM4^{high} colon stem cells were transfected with either an empty vector control or CRISPR/Cas9 gRNAs. Shown are representative sequences from selected

clones with indel mutations in the targeted region of the human NICD binding motif. **(d)** EPHB2^{high}OLFM4^{high} colon stem cells were transfected with either an empty vector control or CRISPR/Cas9 gRNA and subsequently treated with DMSO, DAPT or JAG1. Shown is ChIP-qPCR analysis of Notch1, indicating enrichment with NICD antibody compared with IgG control. The experiment was performed in triplicate and presented mean ± S.E.M. (**, p = 0.01; Student t-test). **(e)** Single EPHB2^{high}OLFM4^{high} colon stem cells were transfected with either an empty vector control or CRISPR/Cas9 gRNAs and cultured as organoids for 14 days. Top: Representative FACS plots for EPHB2 and OLFM4 expression and the percentage of EPHB2^{high}OLFM4^{high} stem cells for each condition. Bottom: FACS histograms indicating expression for the epithelial-specific cell marker EpCAM in the EPHB2^{high}OLFM4^{high} subset of cells for each condition.

Supplementary Figure S6. Bistability of LI vs. PFLI.

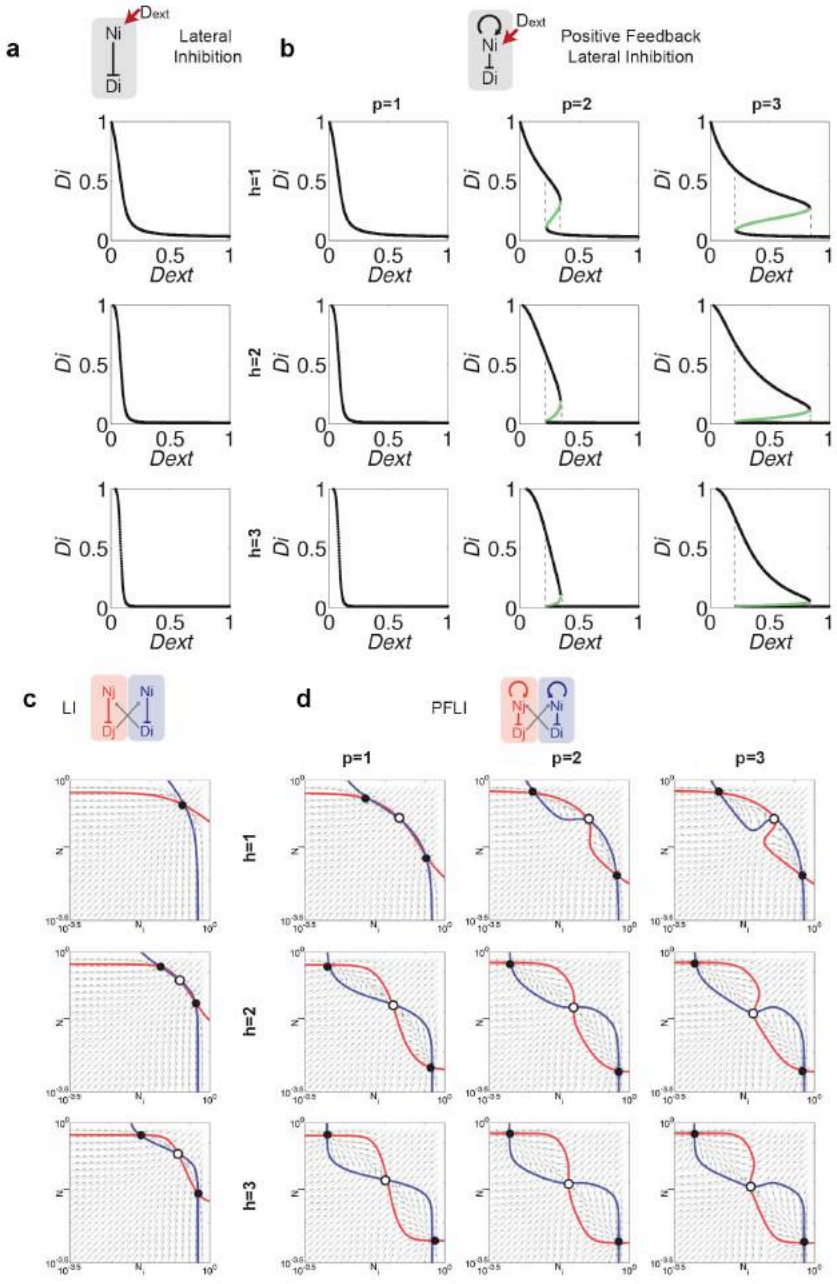

(a) Dynamic analysis of the single-cell LI model. Internal Dll (D_i) vs. external Dll (D_{ext}) protein levels are plotted. **(b)** Dynamic analysis of the single-cell PFLI model. Internal Dll (D_i) vs. external Dll (D_{ext}) protein levels are plotted. **(c)** Phase portraits of the pair-cell LI model. h, Hill coefficient representing cooperativity of LI reaction. **(d)** Phase portraits of the pair-cell PFLI

model. h, Hill coefficient representing cooperativity of LI reaction. p, Hill coefficient representing cooperativity of the Notch positive feedback.

Supplementary Figure S7. Multicellular patterning simulation.

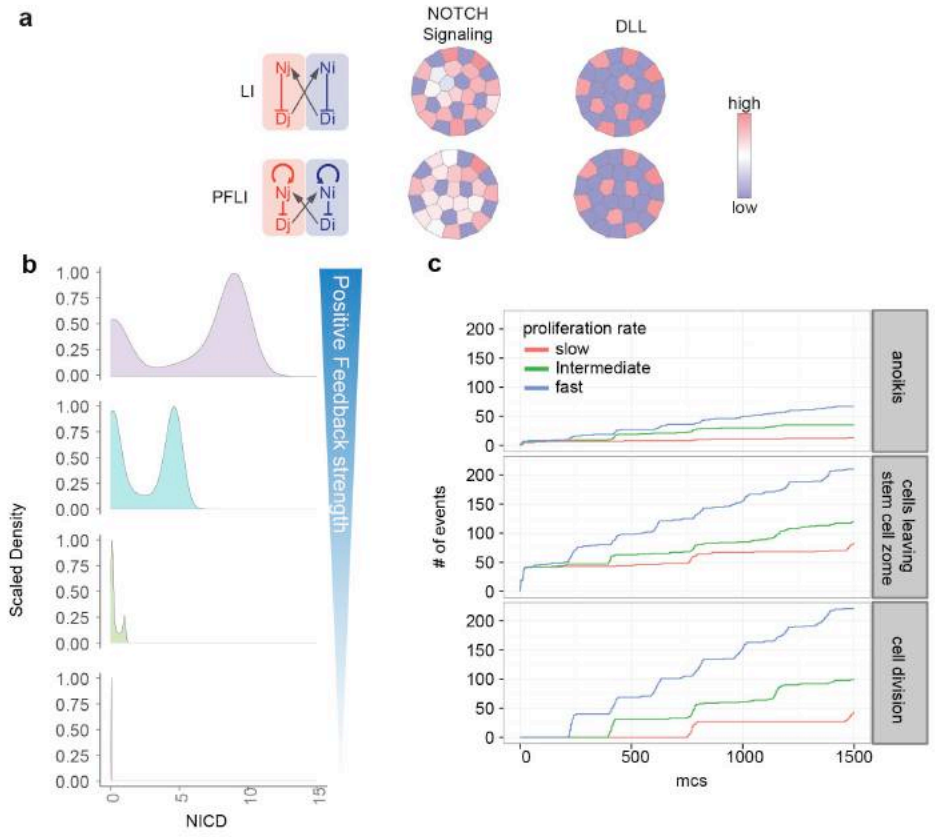

(a) Deterministic multi-cellular simulation of Notch expression patterns with LI and PFLI circuitry. **(b)** Representative density plots of NICD distribution in the multiscale, stochastic model with gradual suppression of Notch positive feedback. **(c)** Simulated stochastic cellular events (anoikis, cells leaving stem cell zone, and cell division) with increasing cell proliferation rates.

REFERENCES

1 Lander, A. D. *et al*. What does the concept of the stem cell niche really mean today? *BMC Biol* **10**, 19, doi:10.1186/1741-7007-10-19 (2012).

2 Barker, N. *et al*. Identification of stem cells in small intestine and colon by marker gene Lgr5. *Nature* **449**, 1003-1007, doi:10.1038/nature06196 (2007).

3 Sato, T. *et al*. Paneth cells constitute the niche for Lgr5 stem cells in intestinal crypts. *Nature*, doi:nature09637 [pii]10.1038/nature09637 (2010).

4 Snippert, H. J. *et al*. Intestinal crypt homeostasis results from neutral competition between symmetrically dividing Lgr5 stem cells. *Cell* **143**, 134-144, doi:S0092-8674(10)01064-0 [pii] 10.1016/j.cell.2010.09.016 (2010).

5 Lopez-Garcia, C., Klein, A. M., Simons, B. D. & Winton, D. J. Intestinal stem cell replacement follows a pattern of neutral drift. *Science* **330**, 822-825, doi:science.1196236 [pii]10.1126/science.1196236 (2010).

6 Metcalfe, C., Kljavin, N. M., Ybarra, R. & de Sauvage, F. J. Lgr5+ stem cells are indispensable for radiation-induced intestinal regeneration. *Cell stem cell* **14**, 149-159, doi:10.1016/j.stem.2013.11.008 (2014).

7 Buczacki, S. J. *et al*. Intestinal label-retaining cells are secretory precursors expressing Lgr5. *Nature* **495**, 65-69, doi:10.1038/nature11965 (2013).

8 Ritsma, L. *et al*. Intestinal crypt homeostasis revealed at single-stem-cell level by in vivo live imaging. *Nature* **507**, 362-365, doi:10.1038/nature12972 (2014).

9 Ritsma, L. *et al*. Intravital microscopy through an abdominal imaging window reveals a pre-micrometastasis stage during liver metastasis. *Science translational medicine* **4**, 158ra145, doi:10.1126/scitranslmed.3004394 (2012).

10 Schaffer, C. B., Nishimura, N., Glezer, E. N., Kim, A. M. T. & Mazur, E. Dynamics of femtosecond laser-induced breakdown in water from femtoseconds to microseconds. *Optics Express* **10**, 196-203 (2002).

11 Nishimura, N. *et al*. Targeted insult to subsurface cortical blood vessels using ultrashort laser pulses: three models of stroke. *Nature methods* **3**, 99-108 (2006).

12 Barker, N. Adult intestinal stem cells: critical drivers of epithelial homeostasis and regeneration. *Nat Rev Mol Cell Biol* **15**, 19-33, doi:10.1038/nrm3721 (2014).

13 Artavanis-Tsakonas, S., Rand, M. D. & Lake, R. J. Notch signaling: cell fate control and signal integration in development. *Science* **284**, 770-776 (1999).

14 Kopan, R. & Ilagan, M. X. The canonical Notch signaling pathway: unfolding the activation mechanism. *Cell* **137**, 216-233, doi:10.1016/j.cell.2009.03.045 (2009).

15 Fre, S. *et al*. Notch signals control the fate of immature progenitor cells in the intestine. *Nature* **435**, 964-968, doi:10.1038/nature03589 (2005).

16 van der Flier, L. G. & Clevers, H. Stem cells, self-renewal, and differentiation in the intestinal epithelium. *Annu Rev Physiol* **71**, 241-260, doi:10.1146/annurev.physiol.010908.163145 (2009).

17 Riccio, O. *et al*. Loss of intestinal crypt progenitor cells owing to inactivation of both Notch1 and Notch2 is accompanied by derepression of CDK inhibitors p27Kip1 and p57Kip2. *EMBO Rep* **9**, 377-383, doi:10.1038/embor.2008.7 (2008).

18 Wu, Y. *et al*. Therapeutic antibody targeting of individual Notch receptors. *Nature* **464**, 1052-1057, doi:10.1038/nature08878 (2010).

19 Fre, S. *et al*. Notch lineages and activity in intestinal stem cells determined by a new set of knock-in mice. *PLoS One* **6**, e25785, doi:10.1371/journal.pone.0025785 (2011).

20 Pellegrinet, L. *et al*. Dll1- and dll4-mediated notch signaling are required for homeostasis of intestinal stem cells. *Gastroenterology* **140**, 1230-1240 e1231-1237, doi:10.1053/j.gastro.2011.01.005 (2011).

21 Yang, Q., Bermingham, N. A., Finegold, M. J. & Zoghbi, H. Y. Requirement of Math1 for Secretory Cell Lineage Commitment in the Mouse Intestine. *Science* **294**, 2155-2158, doi:10.1126/science.1065718 (2001).

22 Collier, J. R., Monk, N. A., Maini, P. K. & Lewis, J. H. Pattern formation by lateral inhibition with feedback: a mathematical model of delta-notch intercellular signalling. *J Theor Biol* **183**, 429-446, doi:10.1006/jtbi.1996.0233 (1996).

23 Yamamura, H. *et al*. Activation of Notch signaling by short-term treatment with Jagged-1 enhances store-operated Ca(2+) entry in human pulmonary arterial smooth muscle cells. *American journal of physiology. Cell physiology* **306**, C871-878, doi:10.1152/ajpcell.00221.2013 (2014).

24 Rand, M. D. *et al*. Calcium depletion dissociates and activates heterodimeric notch receptors. *Mol Cell Biol* **20**, 1825-1835 (2000).

25 Wu, C., Cain-Hom*, L, Hagenbeek T. et al & Siebel, C. Therapeutic antibody targeting of individual Notch receptors. *Nature* **464**, doi:10.1038 (2010).

26 Oh, P. *et al*. In vivo mapping of notch pathway activity in normal and stress hematopoiesis. *Cell stem cell* **13**, 190-204, doi:10.1016/j.stem.2013.05.015 (2013).

27 Consortium, E. P. An integrated encyclopedia of DNA elements in the human genome. *Nature* **489**, 57-74, doi:10.1038/nature11247 (2012).

28 Bonn, S. *et al*. Tissue-specific analysis of chromatin state identifies temporal signatures of enhancer activity during embryonic development. *Nature genetics* **44**, 148-156, doi:10.1038/ng.1064 (2012).

29 Shlyueva, D., Stampfel, G. & Stark, A. Transcriptional enhancers: from properties to genome-wide predictions. *Nat Rev Genet* **15**, 272-286, doi:10.1038/nrg3682 (2014).

30 Hon, G. C., Hawkins, R. D. & Ren, B. Predictive chromatin signatures in the mammalian genome. *Hum Mol Genet* **18**, R195-201, doi:10.1093/hmg/ddp409 (2009).

31 Wang, H. *et al*. NOTCH1-RBPJ complexes drive target gene expression through dynamic interactions with superenhancers. *Proc Natl Acad Sci U S A* **111**, 705-710, doi:10.1073/pnas.1315023111 (2014).

32 Sato, T. *et al*. Long-term expansion of epithelial organoids from human colon, adenoma, adenocarcinoma, and Barrett's epithelium. *Gastroenterology* **141**, 1762-1772, doi:10.1053/j.gastro.2011.07.050 (2011).

33 Jung, P. *et al*. Isolation and in vitro expansion of human colonic stem cells. *Nature medicine* **17**, 1225-1227, doi:10.1038/nm.2470 (2011).

34 Sprinzak, D., Lakhanpal, A., Lebon, L., Garcia-Ojalvo, J. & Elowitz, M. B. Mutual inactivation of notch receptors and ligands facilitates developmental patterning. *PLoS computational biology* **7**, e1002069-e1002069, doi:10.1371/journal.pcbi.1002069 (2011).

35 Swat, M. H. *et al*. Multi-scale modeling of tissues using CompuCell3D. *Methods in cell biology* **110**, 325-366, doi:10.1016/B978-0-12-388403-9.00013-8 (2012).

36 Madison, B. B. *et al*. Epithelial hedgehog signals pattern the intestinal crypt-villus axis. *Development (Cambridge, England)* **132**, 279-289, doi:10.1242/dev.01576 (2005).

37 Crosnier, C., Stamataki, D. & Lewis, J. Organizing cell renewal in the intestine: stem cells, signals and combinatorial control. *Nat Rev Genet* **7**, 349-359, doi:nrg1840 [pii] 10.1038/nrg1840 (2006).

38 Thevenaz, P., Ruttimann, U. E. & Unser, M. A pyramid approach to subpixel registration based on intensity. *IEEE Trans Image Process* **7**, 27-41, doi:10.1109/83.650848 (1998).

39 Sikandar, S. S. *et al*. NOTCH signaling is required for formation and self-renewal of tumor-initiating cells and for repression of secretory cell differentiation in colon cancer. *Cancer research* **70**, 1469-1478, doi:10.1158/0008-5472.CAN-09-2557 (2010).

40 Takeda, N. *et al*. Interconversion between intestinal stem cell populations in distinct niches. *Science* **334**, 1420-1424, doi:10.1126/science.1213214 (2011).

41 Schwank, G. *et al*. Functional repair of CFTR by CRISPR/Cas9 in intestinal stem cell organoids of cystic fibrosis patients. *Cell stem cell* **13**, 653-658, doi:10.1016/j.stem.2013.11.002 (2013).

42 Pan, Z. *et al*. Impaired placental trophoblast lineage differentiation in Alkbh1(-/-) mice. *Developmental dynamics : an official publication of the American Association of Anatomists* **237**, 316-327, doi:10.1002/dvdy.21418 (2008).

43 Hucka, M. *et al*. The systems biology markup language (SBML): a medium for representation and exchange of biochemical network models. *Bioinformatics* **19**, 524-531 (2003).

CHAPTER 4

FRINGE-dependent modification of NOTCH ligands in the intestine

Contributing Authors:

Preetish KL Murthy[*]*, Tara Srinivasan*[*]*, Skye Bochter, Pengcheng Bu, Anastasia Kristine Varanko, Sandy Nandagopal, Michael Elowitz, Susan Cole, and Xiling Shen*

***** These authors contributed equally to the manuscript.

PREFACE

Notch signaling is an essential pathway in maintaining intestinal homeostasis. Mammalian Fringe proteins (Lunatic (LFNG), Manic (MFng), or Radical (RFng)) comprise a class of *O*-fucose-β1,3-*N*-acetylglucosaminyltransferases responsible for modulating Notch signaling through post-translational modifications of Delta/Serrate/Lag2 (DSL) ligands and Notch receptors. Although Fringe has been extensively studied in developmental processes, the precise details of Fringe-mediated Notch ligand-receptor interactions in adult tissues remains to be fully characterized. We report that in murine intestinal tissues RFNG is expressed by Paneth cells at the base of crypts and contributes to LGR5+ intestinal stem cell (ISC) self-renewal. LFNG and, to a lesser degree MFNG, were detected in Goblet cells in the small intestine and colon. Genetic ablation of RFNG reduced the relative number of ISCs while LFNG deletion resulted in Goblet cell hyperplasia. RFNG and LFNG activity improved DSL binding to Notch1 receptor, promoting a role for sugar modifications *in vivo*. In contrast, we did not identify a functional role for MFNG and extracellular secreted LFNG. Overall, these findings suggest Fringe members are differentially expressed in adult intestinal tissues and modify DSL ligands to support cell-cell contact-mediated Notch signaling.

BACKGROUND

Notch is a widely expressed and evolutionarily conserved signaling pathway necessary for intestinal stem cell (ISC) self-renewal and overall epithelial homeostasis [1, 2]. The epithelium is quickly recycled and is maintained by LGR5+ ISCs present at the bottom of the crypts [3]. Paneth cells, also present in the crypt base, provide direct intercellular contact and niche cues for their ISC neighbors [4]. Additionally, differentiated lineages, including enterocytes, enteroendocrine cells and goblet cells populate the epithelium in the upper compartments of crypts and villi [5]. Among the Notch receptors, Notch1 is highly expressed in

LGR5+ ISCs [4]. In contrast, Notch ligands, DLL1, DLL4 and JAG1 are expressed by Paneth and Goblet cells [6]. Notch1, upon its activation by the ligand from a neighboring cell, is cleaved and its intracellular domain (NICD) translocates to the nucleus, leading to the transcription of multiple genes such as HES and HEY families [7, 8]. The extracellular domain of the Notch1 receptor and ligands contain EGF-like repeats which serve as substrates for O-fucosylation by POFUT1 [9, 10]. The fucosylated product may be further intracellularly modified within the Golgi network by a class of β1-3-N-acetylglucosaminyltransferases called Fringe [11]. Three types of Fringes, Lunatic (LFNG), Manic (MFNG) and Radical (RFNG), are found in mammalian cells [1, 10]. However, the precise role for Fringe-mediated sugar modifications in regulating Notch receptor-ligand interaction remains to be fully characterized [12].

The Fringe family has been extensively studied in the developmental context. In particular, cyclic LFNG activity has been shown to modify Notch signaling to regulate vertebrate segmentation and somitogenesis [13-16]. Endocardial expression of MFNG temporally affects DLL4-Notch1 interaction during ventricular chamber development [17]. Additionally, RFNG contributes to the formation of the apical ectodermal ridge of the vertebrate limb bud [18]. Furthermore, each of the Fringes has also been reported to play a role in T and B cell development [19].

Previous studies on the interaction between mammalian Fringes and Notch ligands and receptors have resulted in varied and potentially contradictory findings, suggesting that Fringe activity is both nuanced and highly context dependent. In particular, glycosylation of Notch1 by LFNG and MFNG increases its activation by DLL1 and decreases its activity by JAG1 [10, 20, 21]. LFNG also increases *cis*-inhibition of Notch1 by DLL1 and decreases this effect by JAG1 [22]. In contrast, glycosylation by RFNG increases the activation of Notch1 by both DLL1 and JAG1 [10]. RFNG also increases *cis*-inhibition of Notch1 by both DLL1 and JAG1 ligands [22].

Interestingly, glycosylation of the ligands by Fringe was found not to perturb Notch signaling *in vitro*. Previous reports have shown that LFNG and MFNG can be secreted from the cells in their functional form. However, an *in vitro* study found that extracellular LFNG did not affect Notch signaling [20]. Various investigations since then have been mainly restricted to the glycosylation of Notch receptors in Golgi bodies [17]. Here we show the differential expression pattern of each of the Fringe members in adult intestinal and colonic tissue and examine their functional role in the modification of Notch ligands.

RESULTS

RFNG supports LGR5+ stem cell self-renewal

Fringe RNA transcripts have been detected in small intestine by *in-situ* hybridization (ISH) [23]. In order to further investigate their exact localization and their influence on gut homeostasis, we first performed immunofluorescence (IF) microscopy to identify the expression pattern of RFNG in intestinal and colonic tissues of LGR5-EGFP mice. RFNG, a Golgi resident protein [24], was detected in Paneth cells interspersed between LGR5+ stem cells at the base of crypts in the small intestine (Figure 1a; Supplementary Fig. 1A) and could not be detected in the colon (data not shown). Harvested LGR5-EGFP+ ISCs and Paneth cells were analyzed by RT-qPCR, which confirmed RFNG-expressing Paneth cells (Fig. 1b).

To understand the role of RFNG, a knockdown model was established using *in vitro* organoid cultures of epithelial cells obtained from LGR5-EGFP mice, which express EGFP driven by an LGR5 promoter. Single LGR5-EGFP+ ISCs were transduced with scrambled (Sc.) shRNA (control) or RFNG shRNA and propagated as organoids. Quantitative RT-PCR measurements validated RFNG knockdown in sorted Paneth cells (Fig. 1c). Next, the colony forming efficiency of RFNG shRNA-expressing ISCs was reduced to 7.2% compared to 12.3% in the scrambled control (Fig. 1d), consistent with Paneth cells providing niche cues for ISCs

(p=0.01; Student t-test). Co-IF staining in organoids based on EGFP (labels LGR5+ ISCs) and Lysozyme (Paneth cell marker) expression revealed a diminished number of stem cells in RFNG knockdown organoids (Fig. 1e). We quantified this observation using flow cytometry, which indicated that the ratio of the number of LGR5+ ISCs/Paneth cells decreased significantly in RFNG-/- organoids compared to the control (Fig. 1f). The levels of Notch ligands (DLL1, DLL4, and JAG1) and effectors (HES1, HEY1) were analyzed by Western blotting in LGR5+ ISCs and Paneth cell populations to observe the effect of RNFG knockdown (Fig. 1g). Consistent with the post-translational modifying role of Fringe, Notch ligand expression in the Paneth cells was not significantly altered in RFNG shRNA-expressing organoids. In contrast, Notch downstream effector genes, HES1 and HEY1, were downregulated in LGR5+ ISCs, suggesting that RFNG in Paneth cells has a role in maintaining the stem cell niche. To further understand how RFNG influences Notch signaling, we transfected sorted LGR5 EGFP+ ISCs with an RBPJk-dsRED reporter as an indicator of Notch activity and grew them into two-cell (ISC/Paneth) cell organoids, followed by FACS analysis and time-lapse microscopy (Fig. 1h; Supplementary Fig. 1B). RFNG shRNA decreased the $Notch^{high}$/$LGR5^{high}$ (dsRedhigh/GFPhigh) ISC population and the mean RBPJk-dsRed fluorescent intensity compared to the scrambled shRNA-expressing control, indicating RFNG knockdown reduced overall Notch signaling in ISCs.

To validate *in vitro* studies, intestinal tissues were analyzed from a RFNG null ($RFNG^{-/-}$) mouse strain maintained on a mixed 129/Ola x C57Bl6/J background [25] with targeted deletion of the RFNG locus (Supplementary Fig. 1C). IF microscopy showed diminished ASCL2 (ISC marker) in intestinal crypts of RFNG-/- compared to wild-type (RFNG+/+) mice (Fig. 1i). Quantification in intestinal crypts based on IF expression indicated that the ratio of ISC/Paneth cells was significantly reduced from 0.94 in RFNG+/+ mice to 0.39 in RFNG-/- mice (p=0.008; Student t-test). Taken together, these data suggest RFNG activity promotes Notch signaling to

contribute to stem cell renewal.

LFNG is expressed by Goblet cells

We then determined the expression pattern of LFNG by IF microscopy. LFNG was found in MUC2+ Goblet cells of the mouse small intestine and colon (Fig. 2a; Supplementary Fig. 2A). RT-qPCR measurements in isolated LGR5+ and Goblet cellss from harvested intestinal and colonic tissue of LGR5-EGFP mice confirmed elevated LFNG expression in Goblet cells (Fig. 2b). We then studied the functional significance of LFNG by knocking down its expression using LFNG shRNA in organoid cultures from LGR5-EGFP mice and validating this model by RT-qPCR and Western blotting (Fig. 2c; Supplementary Figure 2B). Analysis of protein levels showed that the expression of Notch ligands, DLL1 and DLL4, in Goblet cell was consistent between LFNG knockdown and the scrambled control. Additionally, the expression of Notch effectors, HES1 and HEY1, in LGR5+ ISCs remained unaltered, suggesting that LFNG does not affect Notch signaling in ISCs (Supplementary Fig. 2B). We then observed a only a slight decrease in colony forming efficiency with LFNG knockdown compared to scrambled shRNA-expressing organoids (Fig. 2d). Additionally, the number of Goblet cells (detected by MUC2 expression) was shown to increase while the number of LGR5+ ISCs was similar in LFNG shRNA-transduced organoids compared to the scrambled control (Fig. 2e). We quantified this observation by FACS analysis, which indicated the LGR5-EGFP+ stem cell population remained consistent between LFNG shRNA-expressing organoids (3.9% of the total cell population) and the scrambled control (4.2%). Importantly, the number of Goblet cells (UEA-1+/CD24-) [26] was increased in LFNG-/- organoids (5.5% of the total population) when compared to the scrambled control (1.9%) (Fig. 2f). Accordingly, the ratio of the number of Goblet cells/LGR5+ ISCs increased approximately three times in LFNG shRNA-expressing organoids compared to the control (Fig. 2f), suggesting that LFNG balances Goblet cell numbers.

To characterize the function of LFNG *in vivo*, we examined intestinal tissues from LFNG null (LFNG-/-) mice generated as previously described [25] (Supplementary Fig. 2C). Goblet cells were quantified in villus crypt units (VCU) of the small intestine or crypt units (CU) of the colon [27]. IF analysis based on MUC2 expression in small intestinal tissues from LFNG-/- mice showed Goblet cell hyperplasia in VCUs compared to wild-type (LFNG+/+) mice (Fig. 2g). Similarly, LFNG null mice also had elevated numbers of Goblet cells in the colon (Supplementary Fig. 2D). Finally, using flow cytometry we quantified Goblet cells numbers: 14.1% of small intestinal cells (Supplementary Fig. 2E) and 12.6% of colonic cells (Supplementary Fig. 2F), which confirmed a significant increase in both tissues of LFNG-/- mice compared to wild-type mice which showed 7.9% and 9.8% Goblet cells in the small intestine and colon, respectively. Overall, these findings imply a role for LFNG in maintaining the number of Goblet cells, contributing to tissue homeostasis.

Goblet cells express MFNG

IF microscopy was used to identify the expression pattern of MFNG in intestinal and colonic tissues of LGR5-EGFP mice. Low MFNG signal was detected in Goblet cells at the top of crypts and throughout villi (Fig. 3a). Harvested LGR5-EGFP+ ISCs and Goblet cells were analyzed by RT-qPCR, which showed low levels of expression of MFNG in Goblet cells (Fig. 3b). Next, we established a MFNG knockdown model using *in vitro* organoid cultures derived from LGR5-EGFP mice to observe associated phenotypic changes. Single LGR5-EGFP+ ISCs were transduced with scrambled (Sc.) shRNA (control) or MFNG shRNA and propagated as organoids. Western blotting and RT-qPCR analysis validated RFNG knockdown (Fig. 3c, Fig. 3d). Gene expression levels of LGR5 and Notch components were comparable between Sc. control-and MFNG shRNA-expressing organoids (Fig. 3d). Additionally, the colony forming efficiency (Fig. 3e) and the expression pattern of LGR5 and MUC2 (Fig. 3f) of MFNG shRNA-

expressing ISCs was similar to the scrambled control. We quantified this observation using flow cytometry, which confirmed a consistent number of LGR5+ ISCs and Goblet cells (Fig. 3g, Fig. 3h). Finally, the percentage of differentiated cytokeratin 20+ (KRT20+) cells was not significantly altered between Sc. control- and MFNG shRNA-expressing organoids (Fig. 3i). The lack of a phenotype associated with MFNG knockdown *in vitro* suggests that MFNG expression is not essential for LGR5+ ISC or Goblet cell function. To validate *in vitro* studies, we analyzed intestinal and colonic tissues from MFNG null ($MFNG^{-/-}$) mice maintained on a mixed 129/Ola x C57Bl6/J background [25] (Supplementary Fig. 3A). IF microscopy showed similar MUC2 staining in intestinal villus crypt units (VCU) and colonic crypt units (CU) of MFNG-/- compared to wild-type (MFNG+/+) mice (Supplementary Fig. 3B, 3C). Quantification in intestinal and colonic tissues based on IF expression indicated that the number of Goblet cells was not significantly altered in MFNG+/+ mice compared to MFNG-/- mice. Finally, we examined the total number of KRT20+ in intestinal VCU and colonic CU, which was similar in wild-type and MFNG null mice (Supplementary Fig. 3D). Overall, these data suggest MFNG does not play a critical role in intestinal and colonic tissues.

Non-functional role of secreted LFNG

Previous reports have indicated that LFNG may be secreted into the extracellular space [28, 29], yet a functional role in adult intestinal tissues has not been studied. We first examined the medium from intestinal organoid cultures derived from LGR5-EGFP mice using solid-phase ELISA. Secreted LFNG was detected at a concentration of approximately 315-325 ng/mL using two independent LFNG primary antibodies (Fig. 4a; Supplementary Fig. 4A). In contrast, RFNG (Supplementary Fig. 4B) and MFNG (Supplementary Fig. 4C) could not detected in culture medium, consistent with their intracellular expression. In order to understand the functional role of secreted LFNG, we employed the LFNG knockdown model established earlier. Single LGR5-

EGFP+ ISCs were transduced with LFNG shRNA and propagated as organoids followed by incubation with conditioned medium harvested from wild-type organoids that contained soluble form of secreted LFNG (sLFNG). After 24 hours, organoid cultures were analyzed using FACS, which showed that the percentage of Goblet cells (5.8%) was similar to the LFNG shRNA condition alone (5.5%) and increased significantly compared to scrambled shRNA-expressing organoids (1.9%) (Fig. 4b). Quantitative RT-PCR revealed that the expression levels of Notch ligands DLL1 and DLL4 were consistent between LFNG knockdown with and without soluble LFNG (Supplementary Fig. 4D), indicating secreted LFNG does not affect transcriptional regulation of DLLs.

To characterize the function of secreted LFNG *in vivo*, we examined intestinal tissues from mutant LFNG (RLFNG) mice in which the N-terminal sequence of LFNG, which normally allows for protein processing and secretion, is replaced with the N-terminus of Radical fringe (a Golgi resident protein) [29] (Supplementary Fig. 4E). IF analysis based on MUC2 expression in small intestinal tissues from RLFNG mice showed similar Goblet cell numbers in villus crypt units (VCU) compared to wild-type (LFNG+/+) mice (Fig. 4c). Similarly, RLFNG and wild-type mice also had consistent numbers of Goblet cells in the colon (Fig. 4d). Taken together, our findings suggest that secretion of LFNG is not essential to maintain Goblet cell numbers and intestinal homeostasis.

Fringe affects Notch ligand-receptor affinity

In order to determine a functional role for Fringe-dependent sugar modifications in Notch signaling, we examined ligand availability and ligand concentration on the cell surface according to a previously established method [22] using flow cytometry, a technique which has been used to study binding affinity of Notch components [11, 30]. Using the model we described earlier, single LGR5-EGFP+ ISCs transduced with Sc. shRNA (control) or RFNG shRNA were

propagated as organoids for 7 days. Following dissociation, single unpermeabilized cells were labeled with CD24 to mark Paneth cells and 0.5 ug/mL Notch1-Fc to quantify ligand binding to Notch1 (Fig. 5a). Using mean fluorescent intensity (MFI), reduced Notch1 binding was observed in Paneth cells with RFNG knockdown compared to the scrambled control, suggesting that RFNG-mediated glycosylation improves Notch ligand-receptor binding. DLLs and JAG1 were also labeled using specific antibodies to determine ligand concentration expressed on the surface of Paneth cells (Fig. 5b). FACS analysis indicated that RFNG activity significantly enhanced DLL1 and DLL4 ligand expression on Paneth cells, suggesting that RFNG-dependent glycosylation improves Notch ligand maturation and localization to the plasma membrane.

Next, LGR5-EGFP+ ISCs transduced with Sc. shRNA (control), LFNG shRNA, or MFNG shRNA were propagated as organoids. Following dissociation, unpermeabilized Goblet cells were labeled with antibodies against Notch1-Fc, DLL1 and DLL4 (Fig. 5c, Fig. 5d). We observed that LFNG deletion in Goblet cells resulted in diminished MFI measurements and Notch1 binding compared to the scrambled control, suggesting that LFNG activity enhances Notch ligand-receptor binding (Fig. 5c). Additionally, LFNG significantly increased the surface expression of DLL1 and DLL4 on Goblet cells (Fig. 5d), promoting a role for LFNG glycosylation in trafficking mature ligands from the Golgi network to the plasma membrane. Consistent with our earlier results, MFNG knockdown did not result in significant changes in Notch1 binding or ligand concentration (Supplementary Fig. 5A-5D). Taken together, our findings suggest that Fringe-mediated Notch ligand glycosylation improves their expression on the plasma membrane and their binding affinity to Notch1 receptor in intestinal cells.

DISCUSSION

We have shown that mammalian Golgi-resident Fringe proteins are expressed in specific Notch ligand-expressing lineages in adult intestinal and colonic tissues. In particular, RFNG was

found to localize in DLL1+/DLL4+/JAG1+ Paneth cells, modulating Notch signaling through direct cell-cell interaction to promote intestinal stem cell renewal. LFNG and MFNG were expressed at abundant or low levels, respectively, in MUC2+ Goblet cells in the differentiated compartment of intestinal crypts and villi. Genetic ablation of RFNG diminished intestinal stem cell numbers while LFNG deletion increased differentiation of progenitors into Goblet cells, resulting in overall Goblet cell hyperplasia. While secreted LFNG was detected, a functional role in Notch signaling was not identified in the extracellular space *in vitro* or *in vivo*, suggesting that intracellular glycosylation within the Golgi network is the catalytic site of activity. Fringe-dependent addition of *O*-fucose glycans to DLLs enhanced ligand-Notch1 receptor binding and increased ligand expression on the plasma membrane. Together with previous studies, our results indicate that Fringe-mediated glycosltransferase activity has a dual role in trafficking mature ligands to the cell surface and supporting ligand-induced Notch signaling.

Previous reports in various artificial cell systems have indicated that Fringe glycosylation of EGF repeats of Notch1 differentially modulates the strength of receptor-ligand interactions depending on the ligand [10, 20-22]. Indeed a role for Fringe-mediated Notch1 proteolysis following ligand binding to activate downstream signaling has also been reported [30]. In dorsal cells of the *Drosophila melanogaster* wing, Fringe enhances Notch signaling through Delta ligands and suppresses Notch activation through Serrate [10]. Here we demonstrate a physiological role for the activity of Fringe members in adding sugar modifications to Notch ligands, increasing their affinity for Notch1 and downstream signaling. Overall, findings from this study add more nuances to our understanding of the Fringe repertoire and its regulation of Notch receptor-ligand interaction in adult tissues.

METHODS

Antibodies

Primary Antibody	Supplier	Catalog Number	Dilution*
anti-ATOH1	Abcam	ab137534	1:1000 (WB)
anti-β-ACTIN	Abcam	ab6276	1:4000 (WB)
Anti-CD24 (APC)	Abcam	ab51535	1:500 (FC)
Anti-DLL1	Abcam	ab85346	1:500 (WB)
Anti-DLL4	Abcam	ab7280	1:1000 (WB)
Anti-GFP	Abcam	ab5450	1:200 (IF) (IF-p)
Anti-HES1	Abcam	ab108937	1:1000 (WB)
Anti-HES5	Santa Cruz Biotechnology	sc-25395	1:500 (WB)
Anti-HEY1	Abcam	ab154077	1:1000 (WB)
Anti-JAG1	Santa Cruz Biotechnology	sc-6011	1:500 (WB)
Anti-KRT20	Origene	TA300936	1:1000 (FC)
Anti-LFNG	Santa Cruz Biotechnology	sc-324092	1:1000 (WB) 1:500 (ELISA)
Anti-LFNG	LSBio	LS-B9718	1:200 (IF-p)
Anti-LYSOZYME	Abcam	ab108508	1:100 (IF)
Anti-MFNG	Santa Cruz Biotechnology	sc-292668	1:1000 (WB) 1:500 (ELISA)
Anti-MUC2	Abcam	ab76774	1:100 (IF)
Anti-MUC2	Santa Cruz Biotechnology	sc-15334	1:200 (IF-p)
Anti-RFNG	Santa Cruz Biotechnology	sc-8240	1:1000 (WB) 1:500 (ELISA)
Anti-RFNG	Abcam	ab42429	1:300 (IF-p)
Anti-UEA-1 (PE)	Abcam	ab50683	1:500 (FC)

***Application: IF: (Immunofluorescence); WB: (Western Blotting); FC: (Flow Cytometry); IF-p: (IF on paraffin embedded sections)**

The corresponding Alexa Fluor® -488 or Alexa Fluor® -555 conjugated secondary antibodies were purchased from Life Technologies.

Mouse strains

LGR5-EGFP mice on a mixed 129/C57BL/6 background were purchased from The Jackson laboratory. LFNG null ($Lfng^{tm1Rjo}$), MFNG null ($Mfng^{tm1Seco}$), and RFNG null ($Rfng^{tm1Tfv}$) mouse strains were a generous gift from Dr. **Susan Cole's** laboratory [25]. LFNG and RFNG mutant mouse strains were originally maintained on a mixed 129/Ola x C57Bl6/J background. Since LFNG null mice were not viable postnatally on this background, the strains were outcrossed onto FVB/NJ for one generation, and then intercrossed to produce animals of desired genotypes. MFNG null mice were maintained on a mixed 129/Ola x C57Bl6/J background.

Littermates are used as controls. Genotyping was performed using the following PCR primer pairs for LFNG: (FNG325: 5'- AGA GTT CCT GAA GCG AGA G, FNG322: 5'- GAG CAC CAG GAG ACA AGC C, FNG326: 5'- CTT GTG TAG CGC CAA GTG C). FNG322 and FNG325 amplify a 170 base pair (bp) wild-type (wt) band while FNG322 and FNG326 amplify a 200 bp mutant band. The following PCR primer pairs were used for MFNG genotyping: (SC-209: 5'-GAG ACC CAG CTT CCT CCT TT, SC-210: 5'-CCT GTA TCA TCC TCT GGG ACA, SC-211: 5'-TGT GTG CAC AAG TGC ATG AG). SC209 and SC210 amplify a 253 bp wt band; SC209 and SC211 amplify a 400 bp mutant band. Genotyping was performed using the following PCR primer pairs for RFNG: (FNG237: 5'-CGA CAT TTT GCA GCA CAG, FNG239: 5'-TTC ACC GAT GGA GAC GAC, FNG240: 5'- CAT GGC TGA ATA TCG ACG). FNG237 and FNG239 amplify a 472 bp wt band, FNG237 and FNG240 amplify a 575 bp mutant band. The thermocyling profile used for PCR amplification is described as follows: 95°C (5 min)/[95°C (30 sec), 55°C (30 sec), 72°C (60 sec)] for 35 cycles/72°C (10 min).

Murine Intestinal Crypt Isolation and Organoid Culture

8-week-old LGR5-EGFP mice were sacrificed to establish intestinal organoid culture. Briefly, small intestines were harvested, flushed with $Ca2^{+/}Mg^{2+}$-free PBS to remove debris, and opened up longitudinally to expose luminal surface. A glass coverslip was then gently applied to scrape off villi, and the tissue was cut into 2-3 mm fragments. Intestinal tissues were then washed again with cold PBS and incubated with 2.0mM EDTA for 45 minutes on a rocking platform at 4°C. EDTA solution was then decanted without disturbing settled intestinal fragments and replaced with cold PBS. In order to release intestinal crypts in solution, a 10 mL pipette was used to vigorously agitate tissues. The supernatant was collected and this process was repeated several times to harvest multiple fractions. The crypt fractions were then centrifuged at 6,000 RPM for 5 minutes. Based on microscopic examination, the appropriate

enriched crypt fractions were pooled and centrifuged again to obtain a crypt-containing pellet. Advanced DMEM/F12 (Life Technologies) containing Glutamax (Life Technologies) was used to resuspend the cell pellet and subsequently a 40um filter was used to purify crypts. Next, single cell dissociation was achieved by incubating purified crypt solution at 37°C with 0.8 KU/ml DNase (Sigma), 10 uM ROCK pathway inhibitor, Y-27632 (Sigma), and 1 mg/mL Trypsin-EDTA (Invitrogen) for 30 minutes. Single cells were then passed again though a 40um filter and resuspended in cold PBS with 0.5% BSA for FACS analysis to collect LGR5-EGFP+ intestinal stem cells (ISCs).

Single LGR5-EGFP+ ISCs were suspended in Matrigel (BD Biosciences) at a concentration of 1000 cells or crypts/mL and 50ul Matrigel drops were seeded per well on pre-warmed 24-well plates. Matrigel polymerization occurred at 37°C for 10 minutes, and was followed by the addition of complete media to each well. ISC media included the following: Advanced DMEM/F12 supplemented with Glutamax, 10mM HEPES (Life Technologies), N2 (Life Technologies), B27 without vitamin A (Life Technologies), and 1 uM N-acetylcysteine (Sigma). Growth factors were freshly prepared each passage in an ISC media solution containing 50ng/mL EGF (Life Technologies), 100ng/mL Noggin (Peprotech), and 10% R-SPONDIN1 conditioned media (generated in house). The addition of growth factors occurred every 2 days and the media was fully replaced every 4 days. Organoids were passaged once per week at a ratio of 1:4 by removing organoids from Matrigel with ice-cold PBS. Next, organoids were incubated on ice for 10 minutes followed by mechanical disruption, centrifugation, and resuspension in fresh Matrigel.

Lentiviral constructs containing LFNG shRNA (Cat. no: sc-39491-SH), MFNG shRNA (Cat. no. sc-39493-SH), RFNG shRNA (Cat. no. sc-39495-SH), or scrambled shRNA (control) (Cat. no. sc-108060) were purchased from Santa Cruz Biotechnology. Lentiviral packaging

particles **(SHP001)** were ordered from Sigma Aldrich. Subsequently, empty vector (EV), LFNG shRNA, MFNG shRNA, or RFNG shRNA -expressing lentivirus was generated when HEK293T cells were co-transfected with the viral vectors and associated packaging plasmids. After 48 hours, the supernatant (NUMB-shRNA, JAG-1 shRNA, NICD-OE, NUMB-SYM) was collected and used to infect ISCs with puromycin selection in accordance with a previously described method [31] with minor modifications. Briefly, organoids derived from single LGR5-EGFP ISCs were suspended in 250ul transduction medium containing 10 μM Y-27632 (Sigma), polybene (Sigma; 8μg/mL) and concentrated EV, LFNG, MFNG, or RFNG shRNA lentivirus. ISCs then were centrifuged for 60 minutes at 250×g and incubated for 12 hours before applying selection medium. Transduced organoids were selected using 10 μg/mL puromycin (Sigma) dissolved in complete ISC medium (described earlier) for 3 days. Subsequently, organoids were propagated in normal complete ISC culture medium for 7 days. In an additional experiment, LFNG shRNA-infected organoids were then incubated in conditioned medium (harvested earlier from wild-type organoids) containing soluble LFNG for 24 hours before FACS analysis.

Organoids were harvested and analyzed by FACS to isolate LGR5-EGFP^{high} cells, CD24^{high}/SSC^{low} (Paneth) cells or UEA-1^{+}/CD24^{-} (Goblet) cells for RT-PCR or protein analysis. M-FNG shRNA-expressing cells were labeled with cytokeratin 20 (KRT20) to isolate and quantify differentiate cells. FACS was conducted using a Beckman Coulter flow cytometer with a 40um filter. Data analysis was performed using FlowJo software to gate populations according to 7-AAD viability, and forward and side scattering. Cutoff thresholds were provided by unstained ISCs and single stained ISCs when using multiple fluorochromes in order to achieve appropriate compensation.

In order to study Notch signaling, a RBPJk-dsRed reporter on a pGA981-6 vector backbone (Addgene #47683) was transfected into single Sc. shRNA-expressing or LFNG

shRNA-expressing sorted LGR5-EGFP ISCs using Lipofectamine-2000 (Life Technologies) according to the manufacturer's protocol. Briefly, 4uL Lipofectamine-2000 (diluted in 50uL Opti-MEM) and 2ug of RBPJk-dsRED reporter plasmid (diluted in 50uL Opti-MEM) were mixed 1:1: and incubated for 5 minutes at room temperature. Lipofectamine/DNA complexes were then added to single LGR5-EGFP+ ISCs (50uL/well) in a 24-well plate, which was subsequently centrifuged for 1 hour and incubated at 37C for 4 hours. ISCs were then resuspended in Matrigel overlaid with ISC media (as prepared above) supplemented with Y-27632 for 24 hours, and analyzed by microscopy and flow cytometry for LGR5-EGFP and RBPJk-dsRed expression.

Intestinal and colonic tissues from LGR5-EGFP mice and LFNG+/+ and LFNG-/- were also harvested and subjected to crypt isolation and single cell dissociation as described earlier. Subsequently, FACS analysis was used to isolate LGR5-EGFP ISCs, Paneth cells or Goblet cells. Data analysis was performed using FlowJo software to gate populations according to 7-AAD viability, and forward and side scattering. Cutoff threshold were used as described above.

Quantitative RT-PCR and Protein Analysis

A Qiagen RNeasy Plus kit was used to extract total RNA from mouse ISCs followed by reverse transcription to cDNA using ABI Taqman Reverse Transcription kit (Applied Biosystems). Quantitative RT-PCR was performed using ABI Taqman Master mix and ABI Prism HT7900. RT-PCR primers from Genecopoeia were used for the following genes: LFNG (Cat # MQP027549), MFNG (Cat # MQP027643), and RFNG (Cat # MQP028076). Taqman primers (ABI) purchased from Life Technologies were used for the following mouse genes: LGR5 (Product ID: Mm00438890_m1), NOTCH1 (Product ID: Mm00627185_m1), HES1 (Product ID: Mm01342805_m1), HES5 (Product ID: Mm00439311_g1), DLL1 (Product ID: Mm01279269_m1), DLL4 (Product ID: Mm00444619_m1), and JAG1 (Product ID:

Mm00496902_m1). RT-PCR data is presented as the mean of three independent experiments normalized to GAPDH expression. Error bars represent S.E.M. Protein isolation and western blotting were performed as previously described. β-actin was used for normalization [32].

ELISA

Solid phase ELISA kits for LNFG (Cat. no. MBS7236431), RFNG (Cat no. MBS7221374), and MFNG (Cat. no. MBS7219833) were purchased from MyBioSource and assays were performed according to the manufacturer's instructions similar to the following protocol. Solid-phase ELISA assays were independently conducted using LFNG, RFNG, and MFNG antibodies purchased from Santa Cruz Biotechnology for verification of results obtained from the corresponding kits. Briefly, microtiter plates were coated with anti-mouse LFNG, RFNG, or MFNG antibodies diluted 1:500 in PBS overnight at 4°C. Subsequently, plates were washed three times and incubated for 1 hour at room temperature with blocking buffer containing PBS and 1% BSA. Plates were washed another three times and incubated for 2 hours at room temperature with protein standards and sample (organoid culture medium). Next, plates were washed three times followed by the addition of HRP-conjugated secondary antibody (Abcam) (goat anti-mouse for LFNG and RFNG; rabbit anti-mouse for MFNG. Plates were incubated for 2 hours at room temperature and washed four times. TMB substrate solution (Abcam) was added to plates followed by the addition of equal volume stop solution for TMB substrate (Abcam). A plate reader was used to collect absorbance data.

Ligand Availability

Ligand availability were performed as previously described [22]. Briefly, blocking buffer (PBS, 2% FBS, 100µg/mL CaCl2) and binding Buffer (PBS, 2% BSA, 100µg/mL CaCl2) were prepared. Subsequently, cells were incubated in blocking buffer for 30 minutes at 37°C followed by incubation with 1 µg/mL Notch1-Fc (R&D, cat. no 5267-TK) diluted in binding

buffer for 1 hour at 4°C. Cells were then washed three times in blocking buffer and incubated in secondary antibody diluted in binding buffer for 40 minutes at room temperature. Finally, cells were washed again three times in blocking buffer before FACS analysis.

Immunofluorescence

Intestinal and colonic tissues from 8 week old LFNG-/-, MFNG-/-, and RFNG-/- mice were harvested, embedded in OCT, and snap-frozen in liquid nitrogen or fixed in formalin and embedded in paraffin. Murine intestinal sections were stained with Hematoxylin and Eosin (H&E) according to standard methods.

Intestinal and colonic tissues from LGR5-EGFP and wild type C57BL/6 mice were harvested, fixed in 4% PFA for 4 hours at 4^0C, washed in 70% ethanol and embedded in paraffin. Additionally, formalin fixed and paraffin embedded sections from intestinal and colonic tissues of chimeric RFNG/LFNG (RLFNG) mice [29] which lack LFNG secretion were a generous gift from Dr. Susan Cole's laboratory. Sections of these tissues were deparafinnised using Xylene and rehydrated. Antigen retrieval was performed as mentioned below.

Antigen	Retrieval method
RFNG	Proteinase K (Dako) for 6 min at RT
LFNG	Slides were heated in Tris buffer (10mM Tris base, 0.05% Tween20 at pH10) in a microwave oven until the solution was brought to its boiling point and it was let to cool for 15 min. Repeat twice.
MFNG	Proteinase K (Dako) for 6 min at RT
MUC2	Slides were heated in Tris buffer (10mM Tris base, 0.05% Tween20 at pH10) in a microwave oven until the solution was brought to its boiling point and it was let to cool for 15 min. Repeat twice.

The sections were incubated in Protein Block (Dako, Cat. No. X0909) for 10 min at RT. Primary antibodies diluted in Antibody Diluent (Dako, Cat. No. S0809) were added and incubated overnight at 4^0C. Slides were then washed three times in PBS for 5 min each. They were incubated in secondary antibodies diluted in Antibody Diluent for 1hr at RT and washed in PBS. The slides were then mounted using Vectashield mounting medium containing DAPI

(Vector Labs, Cat. No. H-1500).

In case of co-staining RFNG with Lysozyme and LFNG with MUC2, the protocol was slightly modified. As all the primary antibodies are made in Rabbit, standard co-IF protocol cannot be used. After incubating the slide in Protein Block, one of the primary antibodies (say LFNG) was added and incubated overnight at 4°C. The slide was then washed as described above and the secondary antibody was added. The slide was washed again and incubated in Protein block for 10 min at RT. The section was incubated in the second primary antibody (MUC2) for 1hr at RT, washed and incubated in the second secondary antibody similarly. The experiment was repeated by reversing the order of primary antibody incubation (MUC2 and then LFNG). DAPI (Invitrogen) was used as a counterstain for IF on an inverted fluorescent microscope.

For quantification based on IF, RFNG+/+, RFNG-/-, LFNG+/+, LFNG-/-, RLFNG sections from intestinal and colonic tissues were examined. ASCL2 (ISC marker), LYZ (Paneth cell marker), and MUC2 (Goblet cell marker) expression was quantified in 500 villus-crypt units (VCU) of the small intestine or 500 crypt units (CU) of the colon per mouse. The data represents n=4 mice/condition.

Intestinal organoids embedded in Matrigel were fixed with 3% PFA for 15 minutes at room temperature for co-IF according to the protocol described above. Co-IF staining included LYZ, MUC2 and LGR5 (detected by GFP) expression. ToPro-3 was used as a nuclear counterstain. A Zeiss LSM 510 laser scanning confocal microscope with an Apo 40 × 1.40 oil objective was used to visualize organoids.

Statistical Analysis

The data is represented as mean ± S.E.M. A Student t-test was applied to compare two groups using $P < 0.05$ to establish statistical significance.

Fig. 1. RFNG Characterization.

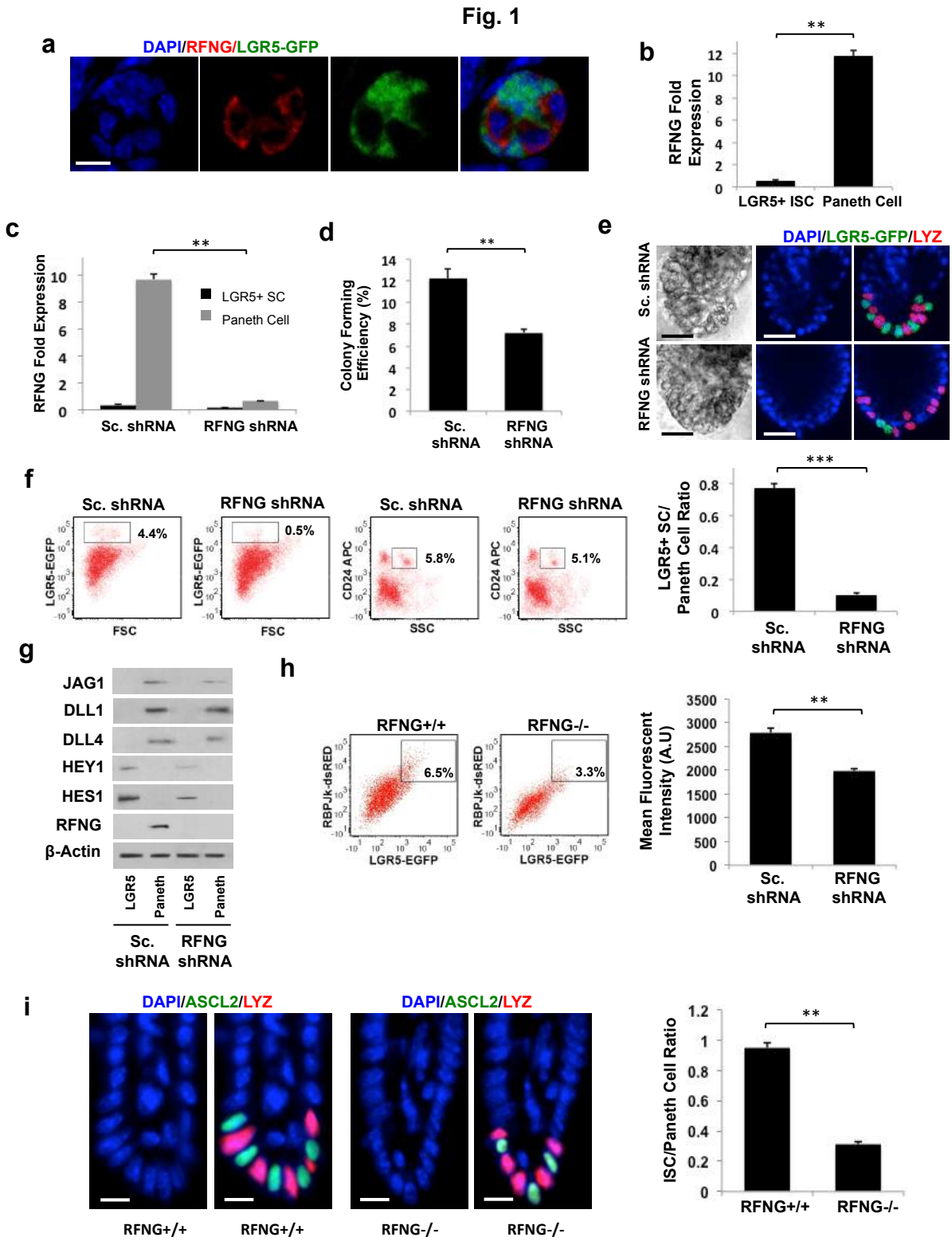

(a) Representative co-immunoflourescent (co-IF) panel showing the localization of RFNG (red)

in the Paneth/LGR5 ISC crypt base of the small intestine of LGR5-EGFP mice. DAPI (blue) labels nuclei and scale bar represents 50 μm.

(b) RT-qPCR quantification of RFNG in LGR5+ ISC and Paneth cell populations from LGR5-EGFP murine intestinal tissue. The experiment was performed in triplicate and presented mean ± S.E.M. (**, p = 0.01; Student t-test).

(c) RT-qPCR quantification of RFNG in LGR5+ ISC and Paneth cell populations after organoids were infected with Scrambled shRNA (Sc. shRNA) or RFNG shRNA. The experiment was performed in triplicate and presented mean ± S.E.M. (**, p = 0.01; Student t-test).

(d) Single LGR5-EGFP ISCs were transduced with either Sc. shRNA or RFNG shRNA. Shown is colony forming efficiency measured after 7 days. Quantitative analysis calculated from 1000 cells/replicate. The experiment was performed in triplicate and presented mean ± S.E.M. (**, p = 0.01; Student t-test).

(e) Single LGR5-EGFP ISCs were transduced with either Sc. shRNA or RFNG shRNA and propagated as organoids for 7 days. Shown are representative brightfield and co-IF images indicating LGR5-EGFP (green) expression. LYZ (red) marks Paneth cells. DAPI (blue) labels nuclei and scale bar represents 25 μm.

(f) Left: Representative FACS plots indicating gated percentage of LGR5+ (GFP^{high}) and Paneth cells ($CD24^{high}/SSC^{low}$) from assay in (e). Right: Ratio of LGR5-EGFP+ ISCs/Paneth cells as determined by FACS analysis . The experiment was performed in triplicate and presented mean ± S.E.M. (***, p = 0.001; Student t-test).

(g) Western blot analysis of Notch signaling components from conditions described in (e). Actin was used as a loading control.

(h) Single scrambled shRNA (control)- or RFNG shRNA-expressing LGR5-EGFP+ ISCs were transfected with an RBPJk-dsRed reporter construct and grown into organoids, which were

subsequently analyzed after 16 hours. Left: Representative FACS plots for RBPJk-dsRED and LGR5-EGFP expression indicating a gated double positive fraction for each condition. Right: Mean fluorescence intensity (MFI) of RBPJk-dsRed expression. The experiment was performed in triplicate and presented mean ± S.E.M. (**, p = 0.01; Student t-test).

(i) Left: Representative co-IF images of crypts from the small intestine of RFNG+/+ and RFNG-/- mouse strains. ASCL2 (green) marks ISCs. LYZ (red) marks Paneth cells. DAPI (blue) labels nuclei and scale bar represents 50 μm. Right: Quantification of the ratio of ISCs/Paneth cells of n=4 mice/condition. Data represents mean ± S.E.M of n=500 crypts per mouse. (**, p = 0.008; Student t-test).

Fig. 2. LFNG Characterization.

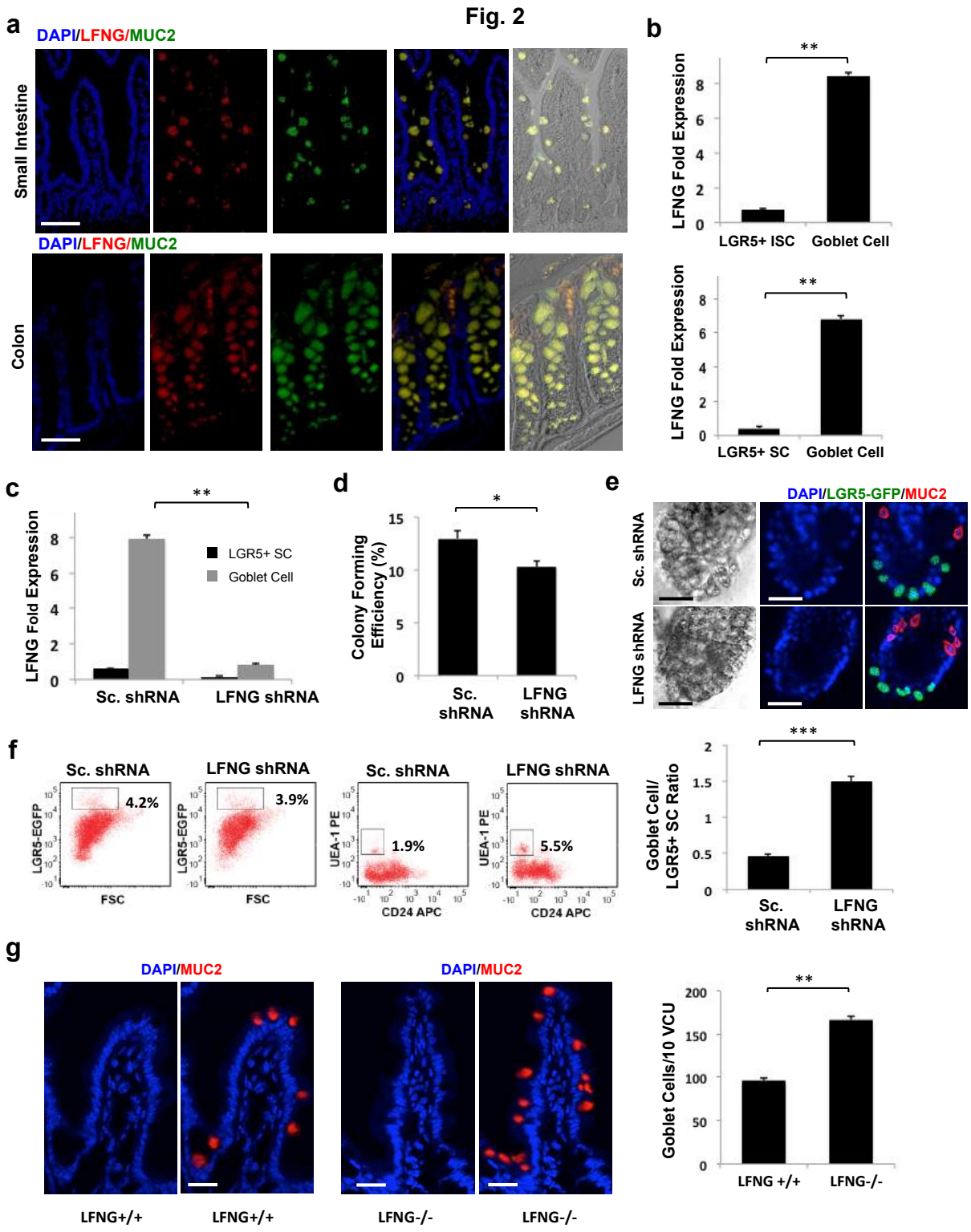

(**a**) Representative IF images indicating localization of LFNG (red) in the mouse small intestine

(top panel) and distal colon (bottom panel). MUC2 (green) labels Goblet cells. DAPI (blue) labels nuclei and scale bar represents 50 μm.

(b) Top: RT-qPCR quantification of LFNG in LGR5+ ISC and Goblet cell populations from small intestinal tissue of LGR5-EGFP mice. The experiment was performed in triplicate and presented mean ± S.E.M. (**, p = 0.01; Student t-test). Bottom: RT-PCR measurements of LFNG in LGR5+ stem cells and Goblet cells from colonic tissue of LGR5-EGFP mice. The experiment was performed in triplicate and presented mean ± S.E.M. (**, p = 0.01; Student t-test).

(c) RT-qPCR quantification of LFNG in LGR5+ ISC and Goblet cell populations after organoids were infected with Scrambled shRNA (Sc. shRNA) or LFNG shRNA. The experiment was performed in triplicate and presented mean ± S.E.M. (**, p = 0.01; Student t-test).

(d) Single LGR5-EGFP ISCs were transduced with either Sc. shRNA or LFNG shRNA. Shown is colony forming efficiency measured after 7 days. Quantitative analysis calculated from 1000 cells/replicate. The experiment was performed in triplicate and presented mean ± S.E.M. (*, p = 0.03; Student t-test).

(e) Single LGR5-EGFP ISCs were transduced with either Sc. shRNA or LFNG shRNA and propagated as organoids for 7 days. Shown are representative brightfield and co-IF images indicating LGR5-EGFP (green) expression. MUC2 (red) marks Goblet cells. DAPI (blue) labels nuclei and scale bar represents 25μm.

(f) Left: Representative FACS plots indicating gated percentage of LGR5+ (GFP^{high}) and Goblet cells ($UEA\text{-}1^{+}/CD24^{-}$) from assay in (e). Right: Ratio of Goblet cells/LGR5-EGFP+ ISCs as determined by FACS analysis. The experiment was performed in triplicate and presented mean ± S.E.M. (***, p = 0.001; Student t-test).

(g) Left: Representative IF images of villus-crypt units (VCU) from the small intestine and crypt

units (CU) from the colon of LFNG+/+ and LFNG-/- mouse strains. MUC2 (green) marks Goblet cells. DAPI (blue) labels nuclei and scale bar represents 50 μm. Right: Quantification of the number of Goblet cells of n=4 mice/condition. Data represents mean ± S.E.M of n=500 VCU or CU per mouse. (**, p = 0.01; *, p=0.03; Student t-test).

Fig. 3. MFNG Characterization.

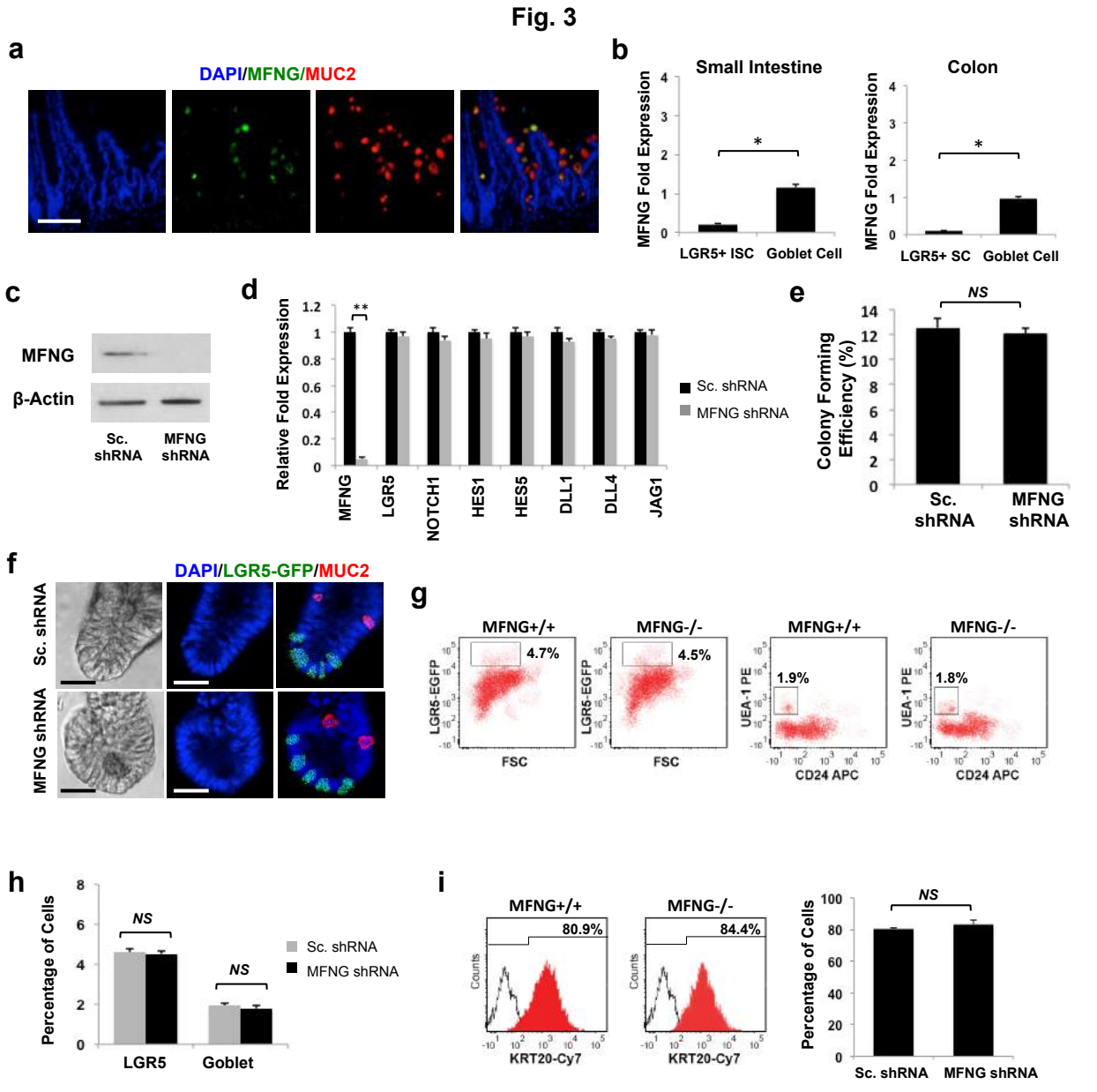

(**a**) Representative IF images indicating localization of MFNG (green) in the mouse intestinal tissue. MUC2 (red) labels Goblet cells. DAPI (blue) labels nuclei and scale bar represents 50 μm.

(b) Left: RT-qPCR quantification of MFNG in LGR5+ ISC and Goblet cell populations from small intestinal tissue of LGR5-EGFP mice. The experiment was performed in triplicate and presented mean ± S.E.M. (*, p = 0.02; Student t-test). Right: RT-PCR measurements of MFNG in LGR5+ stem cells and Goblet cells from colonic tissue of LGR5-EGFP mice. The experiment was performed in triplicate and presented mean ± S.E.M. (*, p = 0.03; Student t-test).

(c) Single LGR5-EGFP ISCs were transduced with either Sc. shRNA or MFNG shRNA and cultured as organoids for 7 days. Shown is Western blot analysis for MFNG expression. Actin was used as a loading control.

(d) RT-qPCR quantification of MFNG and Notch components in organoids that were infected with Scrambled shRNA (Sc. shRNA) or MFNG shRNA. The experiment was performed in triplicate and presented mean ± S.E.M. (**, p = 0.01; Student t-test).

(e) Single LGR5-EGFP ISCs were transduced with either Sc. shRNA or MFNG shRNA. Shown is colony forming efficiency measured after 7 days. Quantitative analysis calculated from 1000 cells/replicate. The experiment was performed in triplicate and presented mean ± S.E.M. (***NS***; Student t-test).

(f) Single LGR5-EGFP ISCs were transduced with either Sc. shRNA or MFNG shRNA and propagated as organoids for 7 days. Shown are representative brightfield and co-IF images indicating LGR5-EGFP (green) expression. MUC2 (red) marks Goblet cells. DAPI (blue) labels nuclei and scale bar represents 25μm.

(g) Single LGR5-EGFP ISCs were transduced with either Sc. shRNA or MFNG shRNA and propagated as organoids for 7 days. Shown are representative FACS plots indicating gated percentage of LGR5+ (GFP^{high}) and Goblet cells ($UEA\text{-}1^{+}/CD24^{-}$).

(h) Percentage of LGR5+ ISCs and Goblet cells as determined by FACS analysis from assay in (g). The experiment was performed in triplicate and presented mean ± S.E.M. (***NS***; Student t-

test).

(i) Single LGR5-EGFP ISCs were transduced with either Sc. shRNA or MFNG shRNA and propagated as organoids for 7 days. Left: Representative FACS histograms indicating differentiated KRT20+ cells. Right: Percentage of KRT20+ cells as determined by FACS analysis. The experiment was performed in triplicate and presented mean ± S.E.M. (***NS***; Student t-test).

Fig. 4. Secretion of LFNG.

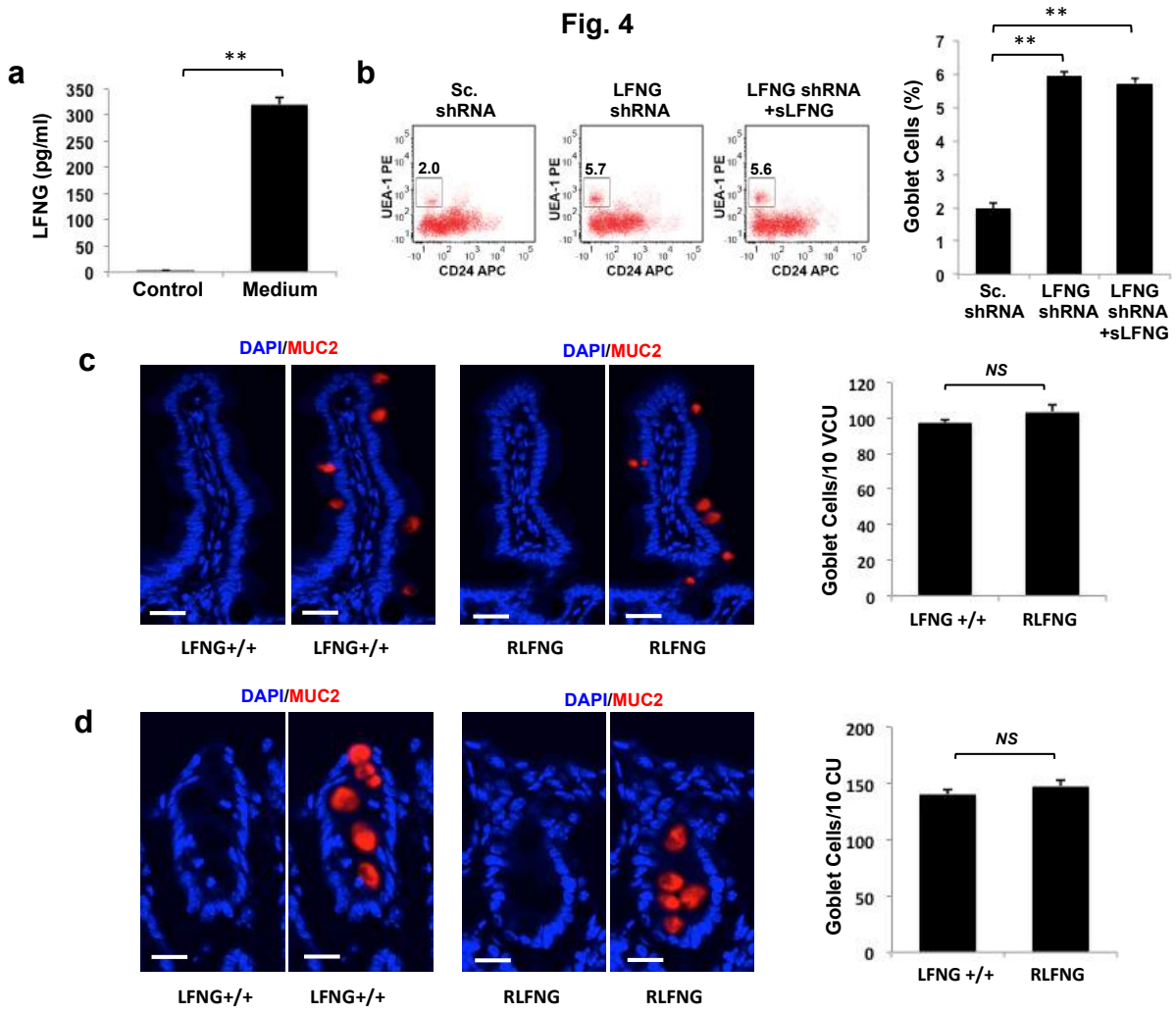

(a) ELISA of the secretion of LFNG in culture medium from murine LGR5-EGFP ISCs propagated as organoids for 7 days using an additional primary LFNG antibody (LFNG-2). Culture medium (T = 0 days) was used as a control. The experiment was performed in triplicate

and presented mean ± S.E.M. (**, p = 0.01; Student t-test).

(b) Single LGR5-EGFP ISCs were transduced with either Sc. shRNA or LFNG shRNA and propagated as organoids for 7 days. LFNG shRNA-expressing ISC organoids were subsequently incubated in conditioned medium containing soluble LFNG (sLFNG) for 24 hours. Left: Representative FACS plots indicating gated percentage of Goblet cells (UEA-1^{+}/$CD24^{-}$) in each condition. Right: Percentage of Goblet cells in each condition as determined by FACS analysis. The experiment was performed in triplicate and presented mean ± S.E.M. (**, p = 0.01; Student t-test).

(c) Left: Representative IF images of villus-crypt units (VCU) from the small intestine of LFNG+/+ and RLFNG mouse strains. MUC2 (green) marks Goblet cells. DAPI (blue) labels nuclei and scale bar represents 50 μm. Right: Quantification of the number of Goblet cells of n=4 mice/condition. Data represents mean ± S.E.M of n=500 VCU/mouse. (***NS***; Student t-test).

(d) Left: Representative IF images of crypt units (CU) from the colon of LFNG+/+ and RLFNG mouse strains. MUC2 (green) marks Goblet cells. DAPI (blue) labels nuclei and scale bar represents 50 μm. Right: Quantification of the number of Goblet cells of n=4 mice/condition. Data represents mean ± S.E.M of n=500 CU/mouse. (***NS***; Student t-test).

Fig. 5. RFNG and LFNG modulation of Notch ligands.

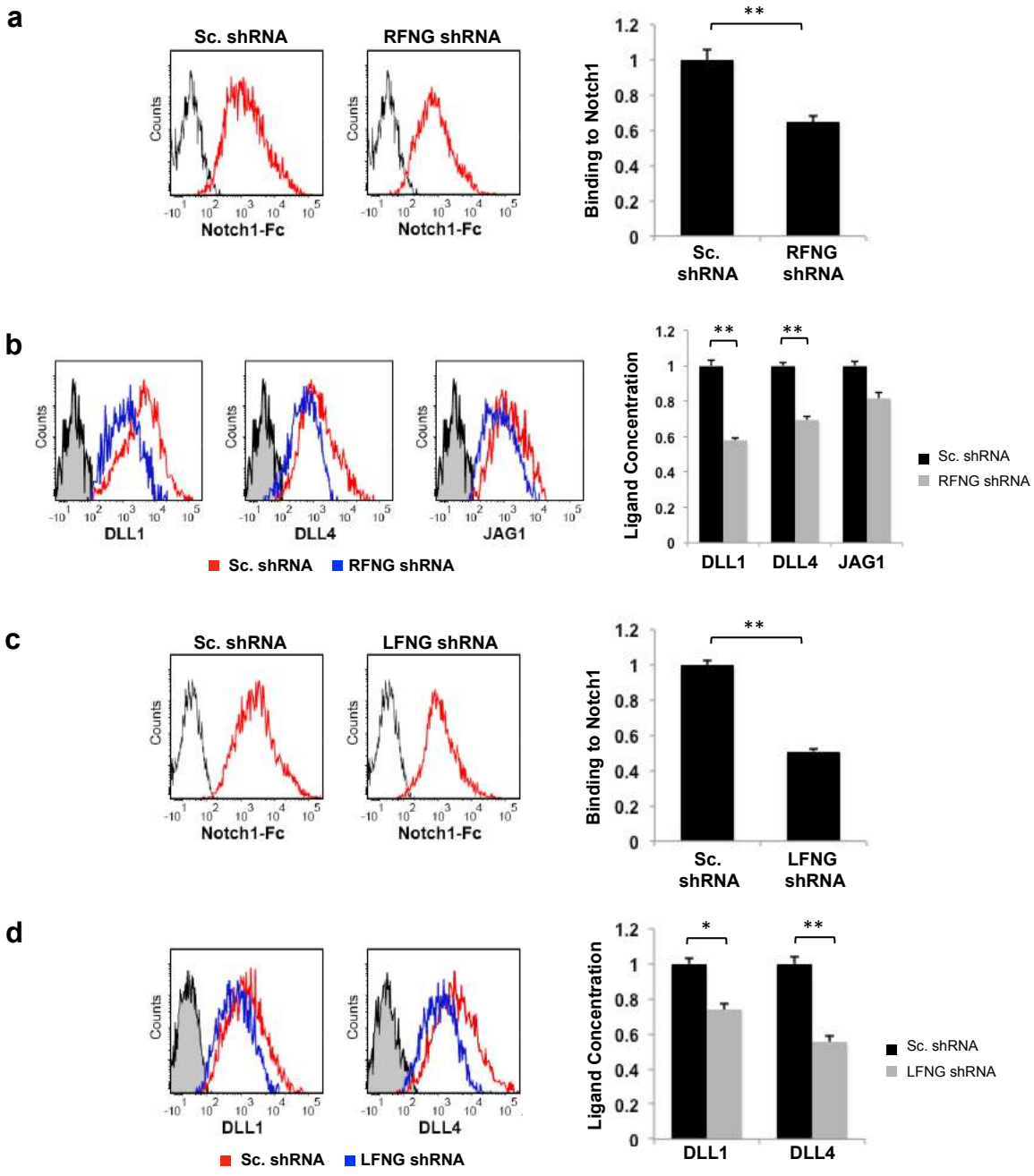

(a) Single LGR5-EGFP ISCs were transduced with either Sc. shRNA or RFNG shRNA and propagated as organoids for 7 days. Isolated Paneth cells were incubated with 0.5 µg/ml Notch1-Fc. Left: Representative traces showing ligand binding to Notch1 measured by flow cytometry in Paneth cells. Unstained Paneth cells were used as a negative control. Right: Ligand binding data

to Notch1 in RFNG shRNA-expressing Paneth cells normalized to Sc. shRNA-transfected Paneth cells using FACS mean fluorescent intensity (MFI) measurements. The experiment was performed in triplicate and presented mean ± S.E.M. (**, p = 0.01; Student t-test).

(b) Single LGR5-EGFP ISCs were transduced with either Sc. shRNA or RFNG shRNA and propagated as organoids for 7 days. Isolated Paneth cells were incubated with antibodies directed against DLL1, DLL4, and JAG1 ligands. Left: Representative traces showing surface ligand concentration measured by flow cytometry on Paneth cells. Unstained Paneth cells were used as a negative control. Right: Surface ligand concentration on RFNG shRNA-expressing Paneth cells normalized to Sc. shRNA-transfected Paneth cells using FACS mean fluorescent intensity (MFI) measurements. The experiment was performed in triplicate and presented mean ± S.E.M. (**, p = 0.01; Student t-test).

(c) Single LGR5-EGFP ISCs were transduced with either Sc. shRNA or LFNG shRNA and propagated as organoids for 7 days. Isolated Goblet cells were incubated with 0.5 μg/ml Notch1-Fc. Left: Representative traces showing ligand binding to Notch1 measured by flow cytometry in Goblet cells. Unstained Goblet cells were used as a negative control. Right: Ligand binding data to Notch1 in LFNG shRNA-expressing Goblet cells normalized to Sc. shRNA-transfected Goblet cells using FACS mean fluorescent intensity (MFI) measurements. The experiment was performed in triplicate and presented mean ± S.E.M. (**, p = 0.01; Student t-test).

(d) Single LGR5-EGFP ISCs were transduced with either Sc. shRNA or LFNG shRNA and propagated as organoids for 7 days. Isolated Goblet cells were incubated with antibodies directed against DLL1 and DLL4 ligands. Left: Representative traces showing surface ligand concentration measured by flow cytometry on Goblet cells. Unstained Goblet cells were used as a negative control. Right: Surface DLL1 and DLL4 ligand concentration on LFNG shRNA-expressing Goblet cells normalized to Sc. shRNA-transfected Goblet cells using FACS mean

fluorescent intensity (MFI) measurements. The experiment was performed in triplicate and presented mean ± S.E.M. (**, p = 0.01; *, p = 0.03; Student t-test).

Supplementary Fig. 1. RFNG characterization.

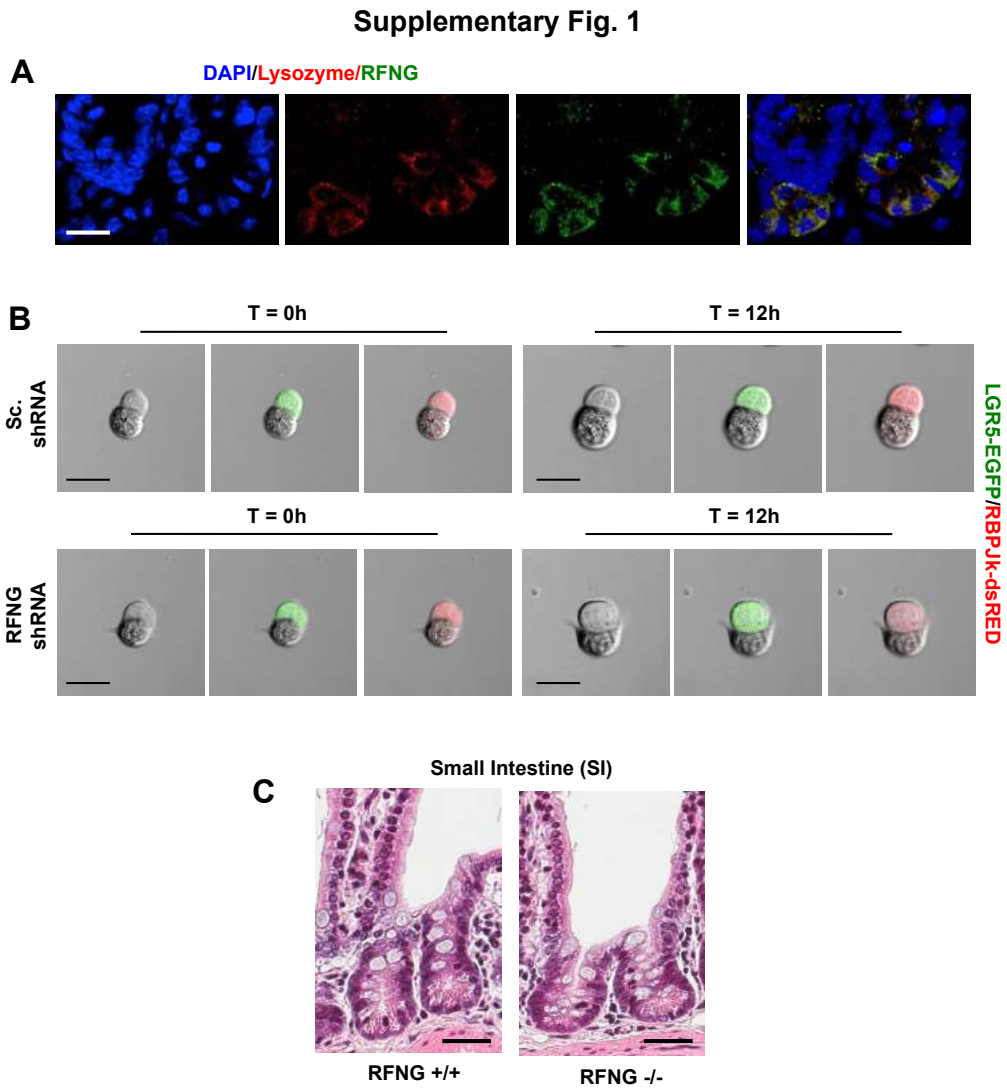

(**A**) Representative co-IF panel showing the localization of RFNG (green) in the crypt base of the mouse small intestine. LYZ (red) labels Paneth cells. DAPI (blue) labels nuclei and scale bar represents 50 μm.

(B) Single scrambled shRNA (control)- or RFNG shRNA-expressing LGR5-EGFP+ ISCs were

transfected with an RBPJk-dsRed reporter construct and grown into organoids, which were subsequently analyzed after 16 hours. Shown are representative images indicating LGR5-EGFP (green) and RBPJk-dsRed (red) expression for each condition. Scale bar represents 20 μm.

(C) Representative H&E images from the small intestine of RFNG+/+ and RFNG-/- mouse strains. Scale bar represents 50μm.

Supplementary Fig. 2. Deletion of LFNG.

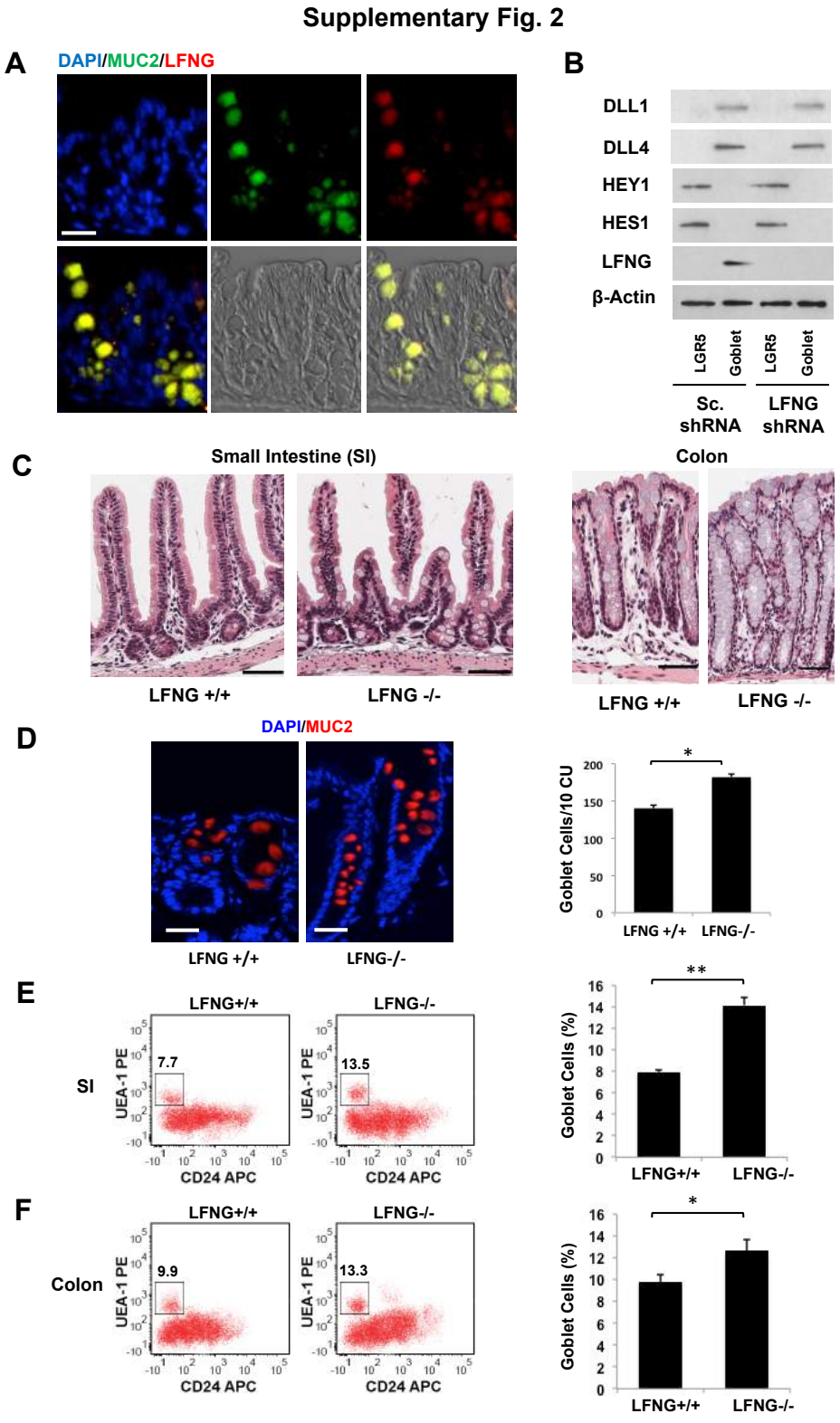

(**A**) Representative co-IF images indicating localization of LFNG (red) in the mouse proximal

colon. MUC2 (green) labels Goblet cells. DAPI (blue) labels nuclei and scale bar represents 50μm.

(B) Single LGR5-EGFP ISCs were transduced with either Sc. shRNA or LFNG shRNA and propagated as organoids for 7 days. Shown is Western blot analysis for LFNG and Notch signaling components. Actin was used as a loading control.

(C) Representative H&E sections from the small intestine (left) and colon (right) of LFNG+/+ and LFNG-/- mice. Scale bar represents 50μm.

(D) Left: Representative IF images of crypt units (CU) from the colon of LFNG+/+ and LFNG-/- mouse strains. MUC2 (green) marks Goblet cells. DAPI (blue) labels nuclei and scale bar represents 50 μm. Right: Quantification of the number of Goblet cells of n=4 mice/condition. Data represents mean ± S.E.M of n=500 CU per mouse. (**, p = 0.01; *, p=0.03; Student t-test).

(E) Left: Representative FACS plots indicating gated percentage of Goblet cells (UEA-1^{+}/$CD24^{-}$) from small intestinal tissue derived from LFNG+/+ or LFNG-/- mice. Right: Percentage of Goblet cells in small intestinal tissue as determined by FACS analysis. The data represent n=3 mice/condition and is presented mean ± S.E.M. (**, p = 0.01; Student t-test).

(F) Left: Representative FACS plots indicating gated percentage of Goblet cells (UEA-1^{+}/$CD24^{-}$) from colonic tissue derived from LFNG+/+ or LFNG-/- mice. Right: Percentage of Goblet cells in colonic tissue as determined by FACS analysis. The data represent n=3 mice/condition and is presented mean ± S.E.M. (**, p = 0.01; *, p = 0.03; Student t-test).

Supplementary Fig. 3. MFNG characterization *in vivo*.

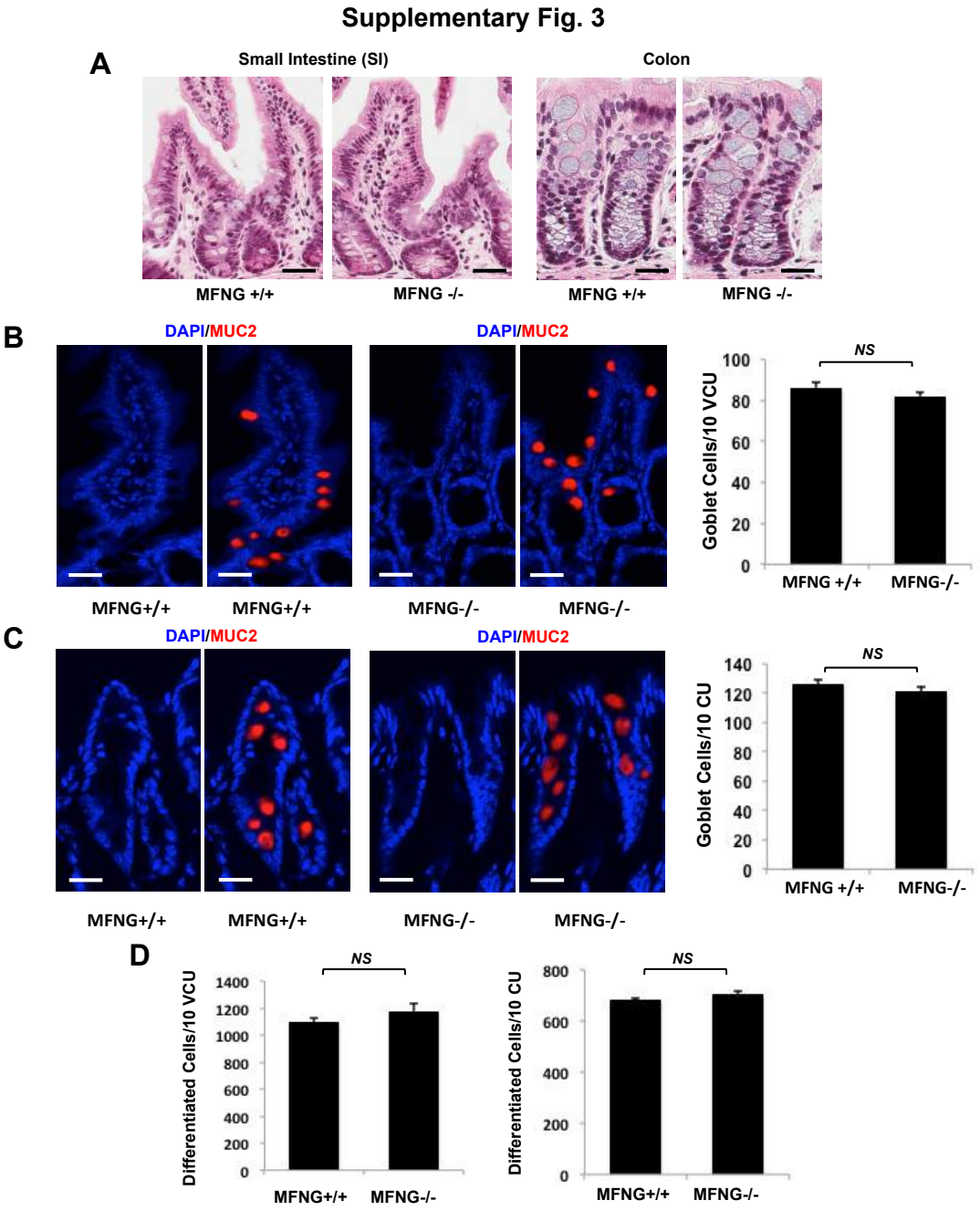

(**A**) Representative H&E sections from the small intestine (left) and colon (right) of MFNG+/+ and MFNG-/- mice. Scale bar represents 50μm.

(B) Left: Representative IF images of villus-crypt units (VCU) from the small intestine of MFNG+/+ and MFNG-/- mouse strains. MUC2 (green) marks Goblet cells. DAPI (blue) labels

nuclei and scale bar represents 50 μm. Right: Quantification of the number of Goblet cells of n=4 mice/condition. Data represents mean ± S.E.M of n=500 VCU per mouse. (***NS*** (not significant); Student t-test).

(C) Left: Representative IF images of crypt units (CU) from the colon of MFNG+/+ and MFNG-/- mouse strains. MUC2 (green) marks Goblet cells. DAPI (blue) labels nuclei and scale bar represents 50 μm. Right: Quantification of the number of Goblet cells of n=4 mice/condition. Data represents mean ± S.E.M of n=500 CU per mouse. (***NS*** (not significant); Student t-test).

(D) Quantification of KRT20+ differentiated cells in villus crypt units (VCU) of the small intestine (top) or in crypt units (CU) of the colon (bottom) of MFNG+/+ and MFNG-/- mice based on IF. The data represents 500 VCU/mouse of n=4 mice/condition and is presented as mean ± S.E.M. (***NS*** (not significant); Student t-test).

Supplementary Fig. 4. Secretion of LFNG.

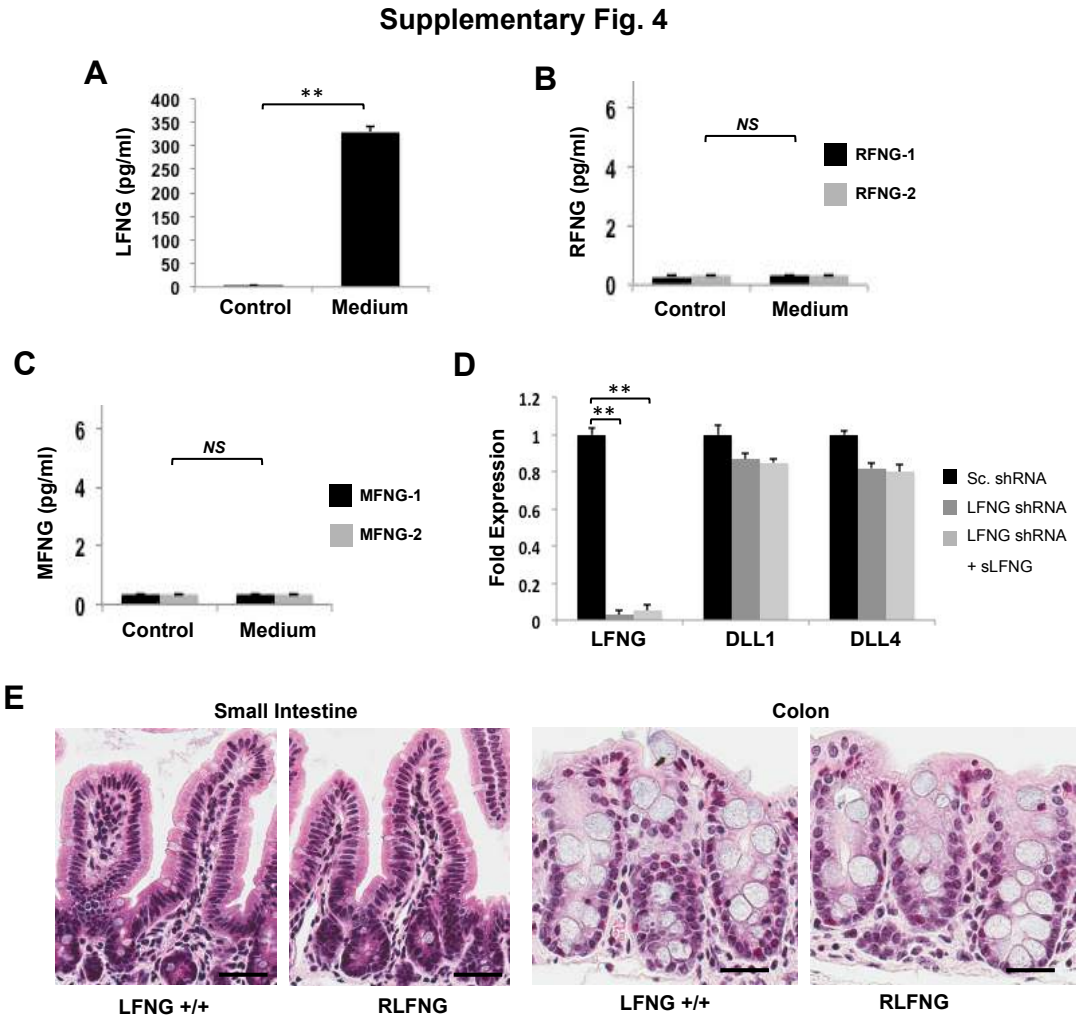

(A) ELISA of the secretion of LFNG in culture medium from murine LGR5-EGFP ISCs propagated as organoids for 7 days using an additional primary LFNG antibody (LFNG-2). Culture medium (T = 0 days) was used as a control. The experiment was performed in triplicate and presented mean ± S.E.M. (**, p = 0.01; Student t-test).

(B) ELISA of the secretion of RFNG in culture medium from murine LGR5-EGFP ISCs propagated as organoids for 7 days using two separate primary RFNG antibodies (RFNG-1, RFNG-2). Culture medium (T = 0 days) was used as a control. The experiment was performed in triplicate and presented mean ± S.E.M. (**, p = 0.01; Student t-test).

(C) ELISA of the secretion of MFNG in culture medium from murine LGR5-EGFP ISCs propagated as organoids for 7 days using two separate primary MFNG antibodies (MFNG-1, MFNG-2). Culture medium (T = 0 days) was used as a control. The experiment was performed in triplicate and presented mean ± S.E.M. (NS; Student t-test).

(D) RT-PCR quantification of LFNG and Notch ligands (DLL1 and DLL4) in LGR5-EGFP organoids that were infected with Scrambled shRNA (Sc. shRNA) or LFNG shRNA. LFNG shRNA-expressing ISC organoids were subsequently incubated in conditioned medium containing soluble LFNG (sLFNG) for 24 hours. The experiment was performed in triplicate and presented mean ± S.E.M. (**, p = 0.01; Student t-test).

(E) Representative H&E sections from the small intestine (left) and colon (right) of LFNG+/+ and RLFNG mice. Scale bar represents 50μm.

Supplementary Fig. 5. MFNG modification of DLL ligands.

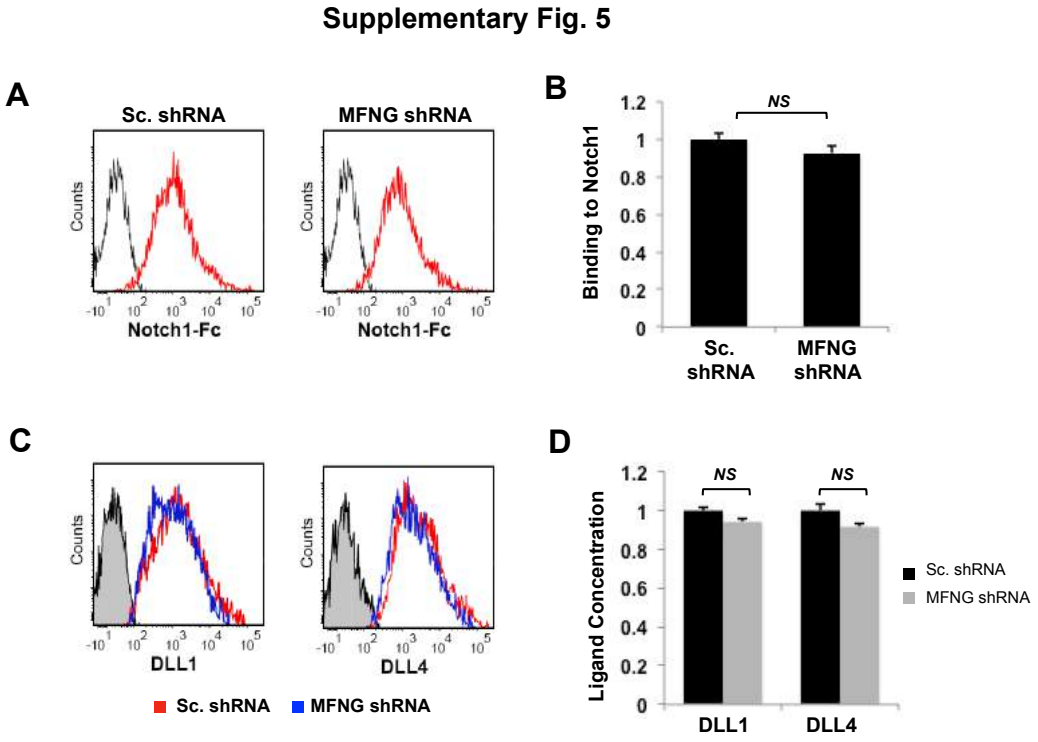

(A) Single LGR5-EGFP ISCs were transduced with either Sc. shRNA or MFNG shRNA and propagated as organoids for 7 days. Isolated Goblet cells were incubated with 0.5 μg/ml Notch1-Fc. Shown are representative traces indicating ligand binding to Notch1 measured by flow cytometry in Goblet cells. Unstained Goblet cells were used as a negative control.

(B) Ligand binding data to Notch1 in MFNG shRNA-expressing Goblet cells normalized to Sc. shRNA-transfected Goblet cells using FACS mean fluorescent intensity (MFI) measurements. The experiment was performed in triplicate and presented mean ± S.E.M. (***NS***; Student t-test).

(C) Single LGR5-EGFP ISCs were transduced with either Sc. shRNA or MFNG shRNA and propagated as organoids for 7 days. Isolated Goblet cells were incubated with antibodies directed against DLL1 and DLL4 ligands. Shown are representative traces showing surface ligand concentration measured by flow cytometry on Goblet cells. Unstained Goblet cells were used as a negative control.

(D) Surface DLL1 and DLL4 ligand concentration on MFNG shRNA-expressing Goblet cells normalized to Sc. shRNA-transfected Goblet cells using FACS mean fluorescent intensity (MFI) measurements. The experiment was performed in triplicate and presented mean ± S.E.M. (***NS***; Student t-test).

REFERENCES

1. Bray, S.J., *Notch signalling: a simple pathway becomes complex*. Nat Rev Mol Cell Biol, 2006. **7**(9): p. 678-89.
2. Pellegrinet, L., et al., *Dll1- and dll4-mediated notch signaling are required for homeostasis of intestinal stem cells*. Gastroenterology, 2011. **140**(4): p. 1230-1240 e1-7.
3. Barker, N., et al., *Identification of stem cells in small intestine and colon by marker gene Lgr5*. Nature, 2007. **449**(7165): p. 1003-7.
4. Sato, T., et al., *Long-term expansion of epithelial organoids from human colon, adenoma, adenocarcinoma, and Barrett's epithelium*. Gastroenterology, 2011. **141**(5): p. 1762-72.
5. Radtke, F. and H. Clevers, *Self-renewal and cancer of the gut: two sides of a coin*. Science, 2005. **307**(5717): p. 1904-9.
6. Shimizu, H., et al., *Distinct expression patterns of Notch ligands, Dll1 and Dll4, in normal and inflamed mice intestine*. PeerJ, 2014. **2**: p. e370.

7. Kopan, R., *Notch: a membrane-bound transcription factor*. J Cell Sci, 2002. **115**(Pt 6): p. 1095-7.
8. Iso, T., L. Kedes, and Y. Hamamori, *HES and HERP families: multiple effectors of the Notch signaling pathway*. J Cell Physiol, 2003. **194**(3): p. 237-55.
9. Moloney, D.J., et al., *Fringe is a glycosyltransferase that modifies Notch*. Nature, 2000. **406**(6794): p. 369-75.
10. Haines, N. and K.D. Irvine, *Glycosylation regulates Notch signalling*. Nat Rev Mol Cell Biol, 2003. **4**(10): p. 786-97.
11. Taylor, P., et al., *Fringe-mediated extension of O-linked fucose in the ligand-binding region of Notch1 increases binding to mammalian Notch ligands*. Proc Natl Acad Sci U S A, 2014. **111**(20): p. 7290-5.
12. Stanley, P., *Regulation of Notch signaling by glycosylation*. Curr Opin Struct Biol, 2007. **17**(5): p. 530-5.
13. Evrard, Y.A., et al., *lunatic fringe is an essential mediator of somite segmentation and patterning*. Nature, 1998. **394**(6691): p. 377-81.
14. Dale, J.K., et al., *Periodic notch inhibition by lunatic fringe underlies the chick segmentation clock*. Nature, 2003. **421**(6920): p. 275-8.
15. Morales, A.V., Y. Yasuda, and D. Ish-Horowicz, *Periodic Lunatic fringe expression is controlled during segmentation by a cyclic transcriptional enhancer responsive to notch signaling*. Dev Cell, 2002. **3**(1): p. 63-74.
16. Cole, S.E., et al., *Clock regulatory elements control cyclic expression of Lunatic fringe during somitogenesis*. Dev Cell, 2002. **3**(1): p. 75-84.
17. D'Amato, G., et al., *Sequential Notch activation regulates ventricular chamber development*. Nat Cell Biol, 2016. **18**(1): p. 7-20.
18. Laufer, E., et al., *Expression of Radical fringe in limb-bud ectoderm regulates apical ectodermal ridge formation*. Nature, 1997. **386**(6623): p. 366-73.
19. Song, Y., et al., *Lunatic, Manic, and Radical Fringe Each Promote T and B Cell Development*. J Immunol, 2016. **196**(1): p. 232-43.
20. Hicks, C., et al., *Fringe differentially modulates Jagged1 and Delta1 signalling through Notch1 and Notch2*. Nat Cell Biol, 2000. **2**(8): p. 515-20.
21. Panin, V.M., et al., *Fringe modulates Notch-ligand interactions*. Nature, 1997. **387**(6636): p. 908-12.
22. LeBon, L., et al., *Fringe proteins modulate Notch-ligand cis and trans interactions to specify signaling states*. Elife, 2014. **3**: p. e02950.
23. Schroder, N. and A. Gossler, *Expression of Notch pathway components in fetal and adult mouse small intestine*. Gene Expr Patterns, 2002. **2**(3-4): p. 247-50.
24. Johnston, S.H., et al., *A family of mammalian Fringe genes implicated in boundary determination and the Notch pathway*. Development, 1997. **124**(11): p. 2245-54.
25. Moran, J.L., et al., *Manic fringe is not required for embryonic development, and fringe family members do not exhibit redundant functions in the axial skeleton, limb, or hindbrain*. Dev Dyn, 2009. **238**(7): p. 1803-12.
26. Wong, V.W., et al., *Lrig1 controls intestinal stem-cell homeostasis by negative regulation of ErbB signalling*. Nat Cell Biol, 2012. **14**(4): p. 401-8.
27. Ishikawa, N., D. Wakelin, and Y.R. Mahida, *Role of T helper 2 cells in intestinal goblet cell hyperplasia in mice infected with Trichinella spiralis*. Gastroenterology, 1997. **113**(2): p. 542-9.

28. Shifley, E.T. and S.E. Cole, *Lunatic fringe protein processing by proprotein convertases may contribute to the short protein half-life in the segmentation clock*. Biochim Biophys Acta, 2008. **1783**(12): p. 2384-90.
29. Williams, D.R., et al., *A novel targeted Lunatic fringe allele predicted to reduce protein secretion is dominant and disrupts somitogenesis*. Development, 2016.
30. Yang, L.T., et al., *Fringe glycosyltransferases differentially modulate Notch1 proteolysis induced by Delta1 and Jagged1*. Mol Biol Cell, 2005. **16**(2): p. 927-42.
31. Koo, B.K., et al., *Controlled gene expression in primary Lgr5 organoid cultures*. Nat Methods, 2012. **9**(1): p. 81-3.
32. Pan, Z., et al., *Impaired placental trophoblast lineage differentiation in Alkbh1(-/-) mice*. Dev Dyn, 2008. **237**(2): p. 316-27.

CHAPTER 5

CONCLUSION

Preface

The research investigations presented in this dissertation examine compelling phenomena such as asymmetric division, stem cell patterning, mechanisms of cell-cell signaling, and differential gene expression in intestinal tissues. We engineered an inter-disciplinary model system to study the process of intestinal niche recovery following acute injury via two-photon laser ablation in the gastrointestinal tract. We also combined *in vitro*, *in vivo* and computational approaches to gain insight into mechanisms contributing to crypt homeostasis. Furthermore, we extended our findings in clinical research of human colorectal cancer to understand colon cancer stem cell renewal, interconversion, and tumorigenesis. Accordingly, Chapter 5 provides concluding remarks of the significance of our findings within the context of the scientific community and presents future directions of exploratory study to advance the field of clinical colorectal cancer research.

1. Mechanistic Insight

1.1. Plasticity of epithelium

We showed that BMI1+/LGR5+ divisions, regulated by NOTCH signaling levels, exist in mouse intestinal organoids and in the intestinal mucosa. In the mouse intestine, LGR5+ CBCs are fast-cycling and proliferate largely through symmetric division [1, 2], while BMI1+/HOPX+ cells are mostly quiescent. However, single-molecule RNA FISH suggests that the mRNA levels of these markers do not as clearly distinguish the fast and slow cycling populations, raising the possibility of plasticity and interconversion among these populations [3, 4]. Targeted ablation of LGR5+ intestinal stem cells (ISCs) in transgenic mice with diphtheria toxin revealed that intestinal crypt homeostasis could be rescued by rare, normally quiescent ISCs [5]. Remarkably, the two populations can be replenished when each is depleted [6]. Potential plasticity between LGR5+ ISCs and other quiescent cell types in response to tissue injury has also been suggested [7]. In addition, lineage tracing studies show that LGR5+ ISCs may be replaced by short-lived enterocyte precursors following targeted ablation, adding more nuances to our understanding of epithelial plasticity in the gastrointestinal tract [8].

Our data suggest potential roles for the NOTCH pathway to regulate the balance between fast- and slow-cycling populations. Additionally, asymmetric BMI1+/LGR5+ division can potentially be activated to aid direct interconversion when the balance is disrupted and needs to be restored. While LGR5+ ISCs predominantly divide symmetrically in a neutral drift process, this does not exclude the possibility of asymmetric division, which may be triggered under conditions of physiological stress. Previous reports did observe asymmetric cell division in the intestinal crypt, including events at the +4 position where the BMI1+ ISC resides [9]. Importantly, the frequency of such BMI1+/LGR5 division does not need to be high, given that the normally quiescent ISCs are relatively rare and long-lasting. However, the low frequency of

quiescent cells may still serve an important role as reserve stem cells, establishing an important link to repopulation and maintenance of homeostasis.

1.2. Cell-cell signaling in the ISC niche

In Chapter 3 we described spatiotemporal regulation of NOTCH intercellular signaling in the intestinal stem cell niche. Using a combinatorial approach of *in vitro*, *in vivo* and *in silico* models, we discovered a novel NOTCH1 positive feedback mechanism that critically maintains the robust ISC/Paneth cell formation in crypts. This mechanism relies on cleaved NICD binding to the second intron of NOTCH1, elevating its expression to promote ISC renewal and crypt homeostasis. Interestingly, NOTCH1 positive feedback is conserved and activated in human colon stem cells, contributing to self-renewal capacity. This specific NOTCH1 intronic locus contains several histone marks, indicative of elevated enhancer activity. As super enhancers have been shown to role in stem cell fate determination and plasticity [10], further research would be valuable in determining whether this NOTCH1 intron plays a role as a super enhancer in ISCs to promote crosstalk between NOTCH signaling and other transcription factors.

Dynamic computational and multiscale stochastic analyses indicated that NOTCH1 positive feedback significantly enhances the robustness, speed, and stability of patterning in the niche compared to lateral inhibition alone, especially under conditions of physiological perturbation and rapid cell turnover. A murine surgical implant comprised of a 3D-printed intestinal scaffold and an openable abdominal window was then subjected to a femtosecond photodisruption laser with single cell precision. We observed that the niche ISC/Paneth cell pattern is robust, capable of rapid recovery and dynamic rearrangement. The application of DBZ, a NOTCH signaling inhibitor, suppressed recovery of ISC/Paneth cell patterning *in vivo*, indicating NOTCH activity is essential for the stability of the niche configuration.

Overall, controlled regulation through feedback and crosstalk mechanisms in the stem

cell niche is responsible for regeneration and homeostasis of intestinal tissue. We have described a novel NOTCH1 genetic motif and positive feedback that contributes robust maintenance of the niche pattern, ensuring signaling states and cell fates remain consistent. Future incorporation of transcriptomics, proteomics, or ChIP-seq will identify other feedback and crosstalk to fully elucidate the complex control scheme within the intestinal stem cell niche.

1.3. NOTCH Signaling

NOTCH is a critical signal transduction pathway to regulate intestinal homeostasis, relying on direct cell-cell contact between its family of ligands and receptors. Despite the abundance of research efforts dedicated to this signaling pathway, the design principles underlying the elegant NOTCH system have not yet been fully characterized. Importantly, FRINGE glycosyltransferases modulate the interaction between NOTCH ligands and receptors, potentially biasing receptor affinity towards DSL ligands. However, due to the repertoire of multiple NOTCH receptors, DSL ligands and FRINGE enzymes, the precise configurations and glycosylation events to enable or inhibit NOTCH signaling have not yet been elucidated. Furthermore, the functional role of sugar modification on DSL ligands remains unclear. Our findings in Chapter 4 indicate a role for the members of the FRINGE family in adult intestinal tissues. We show functional R-FRINGE activity in Paneth cells and L-FRINGE activity in Goblet cells. Using transgenic knockout mouse models, we observed R-FRINGE deletion affects LGR5+ ISC numbers and self-renewal while L-FRINGE ablation resulted in hyperplasia of mucus-secreting Goblet cells. Interestingly, DLL1 ligands were shown to be modified by L-FRINGE, and this glycosylation event may contribute to expression of functional DLL1 on the cell surface. Since the discovery of NOTCH O-glycosylation in 2000, the functional significance of FRINGE continues to expand. In particular, defects in NOTCH glycosylation are linked to several human genetic diseases, including developmental disorders and cancers [11]. Therefore,

future studies are required to enhance the characterization and our understanding of molecular mechanisms governing FRINGE modulation of NOTCH activity to maintain tissue homeostasis.

2. Clinical Implications

The cancer stem cell hypothesis has been central to our understanding of hierarchical organization of tumors, which are composed of rapidly proliferating cells, differentiated post-mitotic cells, and cancer stem cells. In the context of colorectal cancer (CRC), surface markers, including CD24, CD44, CD133, CD166, have been used to identify colon cancer initiating cells (CCICs) that are capable of self-renewal, drive tumor growth, and promote cancer progression. CCICs have been consistently treated as a homogenous population; however, our findings from Chapter 1 indicate the co-existence of distinct subpopulations of CCICs. We identified fast-proliferating LGR5+ and slow-cycling BMI1+ CCIC fractions that are balanced within a tumor and are capable of NOTCH-dependent asymmetric division as a means of interconversion. Fast-cycling CCICs express markers such as LGR5 and CD133, and depend on MYC for their proliferation, whereas slow-cycling CCICs express markers such as BMI1 and hTERT, and are independent of MYC. The ability of both BMI1+ and LGR5+ CCICs to undergo asymmetric division in order to generate each other highlights the plasticity within the CCIC population.

Despite their relatively low frequency, slow-cycling cells may still serve an important role as reserve stem cells. In the context of CRC, BMI1+ CCICs may provide a slow-cycling, long-lasting, more chemo-resistant reserve population, establishing an important link to tumor growth and repopulation. Promotion of slow-cycling BMI1+ CCICs by NOTCH signaling is consistent with its role in supporting chemoresistance [12]. The direct interconversion process between LGR5+ and BMI1+ CCIC may provide CRCs with a growth and survival strategy to promote self-renewal, tumorigenicity, and chemoresistance. It is important to note that chemotherapies that focus on targeting fast-proliferating cells and shrinking tumor volume may

inadvertently enrich the slow-cycling CCIC population, giving rise to recurrence and chemoresistance.

The characterization of specific CCIC subtypes is important in evaluating the efficacy of current treatment strategies and in the development of new rational therapies. In particular, isolation of BMI1+ and LGR5+ CCIC may be useful in the discovery of new biomarkers and drug targets specific to slow- and fast-cycling CCIC. Gene expression signatures from both populations will aid in identifying pharmacological sensitivity, EMT phenotype, and metastatic potential. Furthermore, as NOTCH signaling modulation is known to be a critical strategy in chemotherapy, γ-secretase inhibitors (GSIs) may be administered in a combination therapy or as a single agent to treat CRC by suppression of NOTCH activity. However, GSI-induced toxicity, side effects and chemoresistance have been reported in clinical studies [12]. Therefore, it is necessary to characterize drug resistance mechanisms, including up-regulation of anti-apoptosis and autophagy genes in both slow-cycling and fast-cycling CCICs for appropriate combination therapies to enhance CRC tumor eradication. The numerous off-target side effects of GSIs suggests that monoclonal antibodies directed against NOTCH components may be promising. Indeed, there is ongoing pre-clinical and clinical research in evaluating antibody-based targeting against NOTCH receptors and ligands in cancer treatment [12, 13]. We have shown asymmetric pairs composed of BMI1+ ($NOTCH^{high}$) and LGR5+ ($NOTCH^{low}$) CCIC daughters, suggesting that anti-NOTCH therapies should be developed and evaluated in specific CCIC fractions. The identification of CCIC heterogeneity is essential in informing clinical treatment strategies to more effectively eliminate CRC tumor cells and prevent recurrence.

In addition to therapies directed at cell surface markers and signaling cascades, our data suggest that the process of interconversion also provides a novel pharmacological target. Suppression of asymmetric division to prevent regeneration of fast- and slow-cycling CCICs

may be useful in developing combination therapies where the frequency of CRC recurrence will be reduced. Furthermore, it is worth reexamining previous therapeutic strategies and biomarker studies that have relied on CCICs being a homogenous population. Overall, our findings provide insight in the context of CRC diagnosis, prognosis, and therapeutic development.

3. Impact of technological advances

3.1. Single cell analysis

Innovative and sensitive sequencing methods are being rapidly developed for high-throughput analysis, revolutionizing our ability to characterize cell populations on a multi-scale level. Importantly, single cell RNA-seq provides whole transcriptome amplification with single cell resolution using a microfluidics platform (Figure 1), differing significantly compared to traditional RNA-seq of cell populations. Single-cell approaches offer valuable quantitative and qualitative information in studying CRC and may be used to enhance our understanding of CCICs [14]. Our research investigations previously relied on selection based on specific cell surface markers to identify CCIC subpopulations. However, parallel single-cell RNA sequencing of thousands of dissociated cells from a primary patient CRC tumor or CCIC lines does not require predetermined selection markers. In fact, unsupervised hierarchical clustering analysis will reflect global heterogeneity and reveal subpopulations, yielding novel classifications. Furthermore, due to the inherent quantitative sensitivity of this technology, it is possible to reveal rare populations of cells that may be important in regulating tumorigenesis, CRC progression and metastasis. Importantly, unsupervised clustering analysis of CCIC is a valuable tool to identify new and robust biomarkers with diagnostic and prognostic value. Functional analysis of such rare subtypes may also provide a link to address chemoresistance and develop new pharmacological agents. Overall, technological innovation to advance single cell analysis will have a significant impact in revealing the complexity of hierarchical dynamics in CCICs.

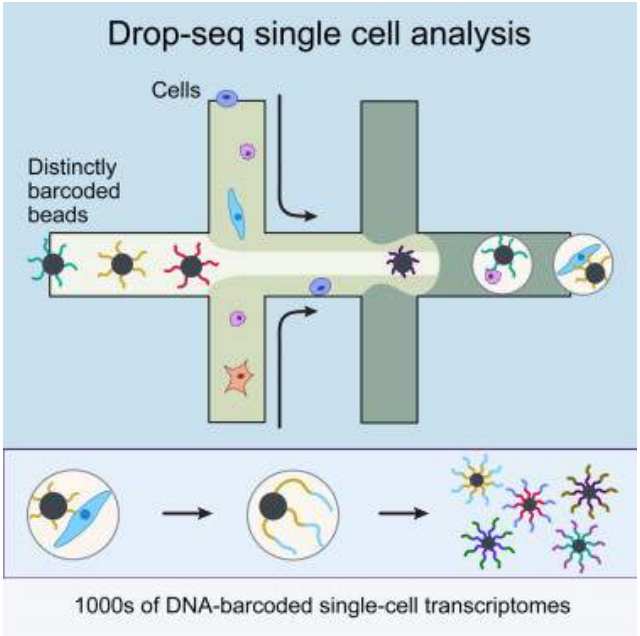

Figure 1. Single Cell RNA sequencing schematic based on Drop-Seq microfluidic platform. Single cells from a heterogeneous mixture are separated into aqueous droplets and the RNA content from each cell is assigned a distinct barcode. Subsequently, thousands of mRNA transcriptomes are simultaneously sequenced.

3.2. Epigenetic regulation

ChIP-Seq, a methodology that combines chromatin immunoprecipitation (ChIP) with genomic sequencing, is a powerful tool to identify global epigenetic chromatin modifications. We examined ChIP-Seq datasets in both murine and human intestinal tissue and identified a significant number of histone marks (H3K4m1, H3K4m3, H3K27ac, H3K27m3, and H3K36m3), indicative of elevated enhancer activity on the second and fourth introns of NOTCH1. This analysis led to the discovery of the conserved NOTCH1 positive feedback mechanism and binding motif active in intestinal and colonic stem cells. Importantly, the utility of ChIP-Seq is also invaluable in conducting further analysis on NOTCH1 to discover super enhancer elements that are the sites of numerous transcription factor recruitments and signaling pathway crosstalk. Super enhancers are associated with stem cell fate decisions [10], but have

not yet been identified in intestinal stem cells, indicating that ChIP-Seq technology will be useful in resolving their presence and functional role. Additionally, other genes involved in NOTCH and WNT signaling that regulate intestinal stem cell renewal, including DLL1, DLL4, HES1, HES5, β-CATENIN, show an abundance of histone marks for enhancer elements (Figure 2). Therefore, ChIP-Seq offers powerful insight into the identification of novel super enhancers, transcriptional regulation, and complex genetic networks that contribute to intestinal stem cell self-renewal and differentiation.

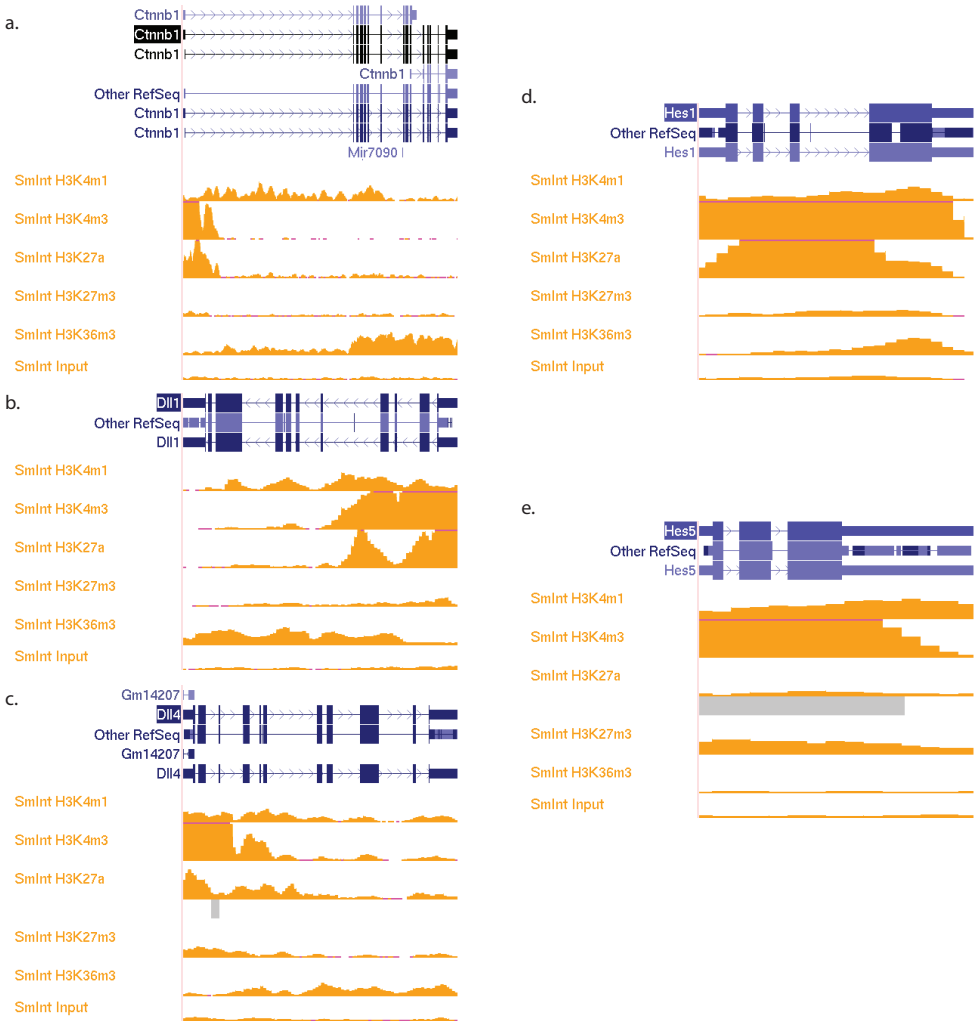

Figure 2. ChIP-Seq of histone marks H3K4m1, H3K4m3, H3K27ac, H3K27m3, and H3K36m3 in intestinal tissue. Histone mark data at the following loci in the mouse genome

(blue) of small intestinal tissue: a) β-CATENIN, b) DLL1, c) DLL4, d) HES1, and e) HES5. Different marks are associated with promoters, transcribed regions and enhancers. Clustered peaks of histone marks are shown in yellow.

3.3. Combinatorial approaches

Dynamic processes, such as intercellular communication and feedback, are difficult to study with high resolution and sensitivity using traditional methods. Therefore, innovative and combinatorial strategies are required to study biological systems in real time. We integrated *in vivo*, *in vitro*, and *in silico* models coupled with precise methods of physical disruption through laser ablation and genomic perturbation through CRISPR editing as a strategy to probe underlying control principles within the ISC niche. We also designed and surgically implanted a 3D-printed intestinal scaffold and an openable abdominal window on mice, which could be targeted by a femtosecond photodisruption laser with high spatial resolution (Figure 3). Using the abdominal window and imaging techniques, we were able to track cell nuclei in real time to understand migration within the niche. Flexible photoablation of single or multiple cells provided insight into niche regulation *in vitro* and *in vivo*, revealing that the niche is capable of dynamic rearrangement to compensate for immediate cell loss. Rather than relying on fixed ISC patterning or delaying until cell division, the niche is fluidic and able to quickly and robustly recover its ISC/Paneth cell configuration.

Computational analysis and *in silico* modeling allowed us to identify and understand the contribution of specific mechanisms in crypt homeostasis. In particular, we discovered that NOTCH1 positive feedback is essential to maintain the ISC/Paneth cell ratio and patterning in the niche; loss of this feedback suppresses recovery capability, causing the niche to collapse after single-cell ablation. Future combinations of the abdominal window, scaffold, laser ablation, and lineage tracing in transgenic mice along with *in vitro* and *in silico* techniques may provide

scientists with advanced technology to study control schemes of the intestinal niche in real-time. Our combinatorial strategy may also inspire the development of new technologies to dynamically study other biological tissues.

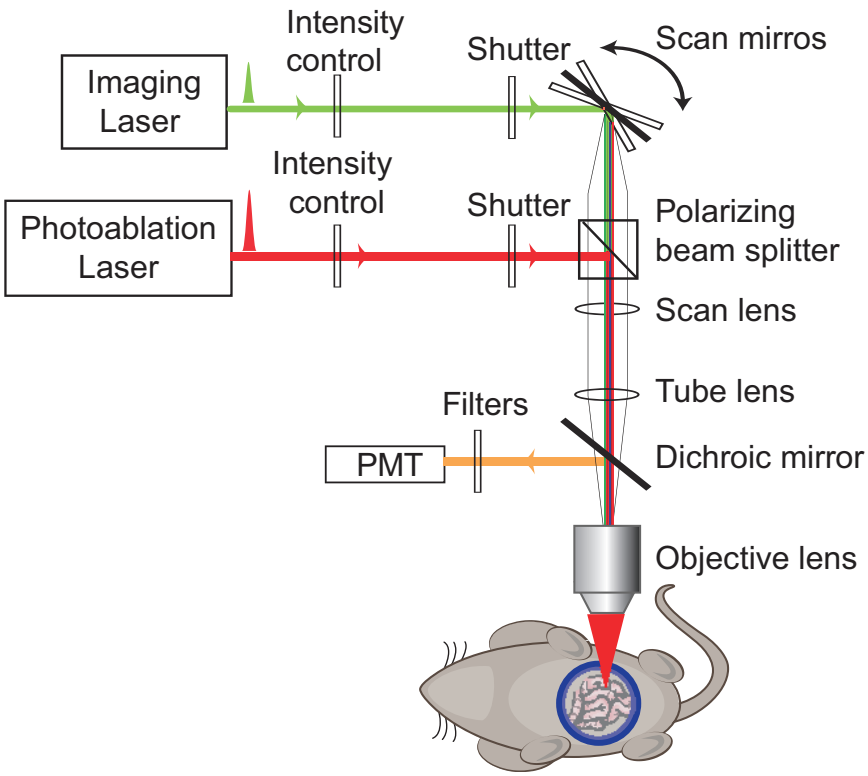

Figure 3. *In vivo* multi-photon imaging and laser ablation schematic.

4. Future Directions

4.1. Applications of an engineered *ex vivo* Colon Model

Based on the joint expertise from the collaboration between the Shen and Lipkin laboratories, several exploratory studies can be used to extend the findings developed in this thesis. These projects will expand the existing foundation of CCIC and ISC biology from our previous studies. Furthermore, we have recently developed an *ex vivo* human colon model using native colon extracellular matrix (ECM) recellularized with epithelial, fibroblast and endothelial cell populations [15]. This versatile system offers significant utility to study unique aspects of crypt dynamics under physiological and pathological conditions that complements *in vitro*

organoid models and *in vivo* mouse modes (Figure 4, Figure 5, Figure 6). This is due to the biomimetic properties of the ECM that more closely recapitulates the native colon and the ability to execute high-resolution time-lapse microscopy. Ultimately, this newly established colon model can be engineered and characterized for specific applications, offering broad potential to enhance our understanding of stem cell behavior and cancer biology.

The engineered *ex vivo* colon offers advantages to study the repopulation of individual crypts from a single stem cell with high resolution time lapse imaging. Physiological crypt turnover involves NOTCH, WNT, BMP and HEDGEHOG pathways; although the precise programming of a signaling hierarchy over time has not been fully characterized. We propose to seed single LGR5+ stem cell into the mucosal layer of this decellularized system while fibroblasts and endothelial cells are used to recellularize the muscularis and submucosal layers, respectively. Using reporter constructs, we can focus on how NOTCH and WNT signaling evolves from a single LGR5+ to repopulation of the crypt base to the generation of progenitors in the TA zone. This developmental model can be compared with reestablishment of crypt base, progenitors and differentiated progeny from a single BMI1+ stem cell. In order to study the evolution of NOTCH and WNT signaling, the recellularized model may be fixed at different stages and visualized at single cell resolution by immunofluorescence. Additionally, where necessary, gene expression analyses may be incorporated to support signaling pathway activity.

Another application of the engineered *ex vivo* colon is to analyze plasticity of the crypt stem cell populations. Specifically, this involves studying symmetric and asymmetric division of LGR5+ and BMI1+ stem cells, as well as their process of interconversion, during repopulation of individual crypts. Laser ablation to selectively knockout single stem cell populations would also provide insight into crypt regeneration and mechanisms used to promote such plasticity. We previously noted that the occurrence of BMI1+/LGR5+ asymmetric cell pairs *in vivo* is an

extremely rare event, but is detected in mouse $APC^{-/-}$ tissue as well as under inflammatory conditions with greater frequency, suggesting that these pairs may be associated with oncogenic transformation. Additionally, using transposon-mediated mutagenesis, Chen, J., *et al.* have identified several genes that cooperate with mutant APC to drive invasive neoplasia using the recellularized colon model. In this study, we may further analyze how such mutations introduced into recellularized epithelial cells may be associated with division symmetry of stem cells during CRC progression.

Finally, the recellularization of the mucosal layer can be modified to co-culture normal stem cells and CCIC, which may provide insight into competition dynamics, tumor initiation and invasion. Specifically, the spatial arrangement of the ECM architecture, and signaling cues from supporting fibroblasts and endothelial cells highlights the utility of an engineered *ex vivo* colon model to recapitulate the microenvironment and to be analyzed temporally with high resolution. This is particularly useful to study invasive CRC where current mouse models have limited extrapolation to human disease [16]. We aim to observe the effect of recellularization with CCIC on a potential competition advantage, displacement and transformation of normal LGR5+ and BMI1+ stem cells. Furthermore, it is possible to characterize specific mechanisms used by CCIC to promote a tumorigenic niche, including excessive proliferation, dedifferentiation, and altering the balance of symmetric and asymmetric divisions. Using CCIC to generate a tumorigenic epithelium, we may further analyze properties related to their invasive potential. Chen, J., *et al.* have previously established that invading tumor cells may be isolated from the recellularized colon model using laser-capture microdissection and studied based on their gene expression. Therefore, such analysis may provide insight into the composition and behavior of invading tumors that contain CCIC and non-CCIC phenotypes.

Overall, these projects may be investigated to employ a physiologically relevant human colon model, providing an enhanced temporal context to study stem cell behavior and CRC progression.

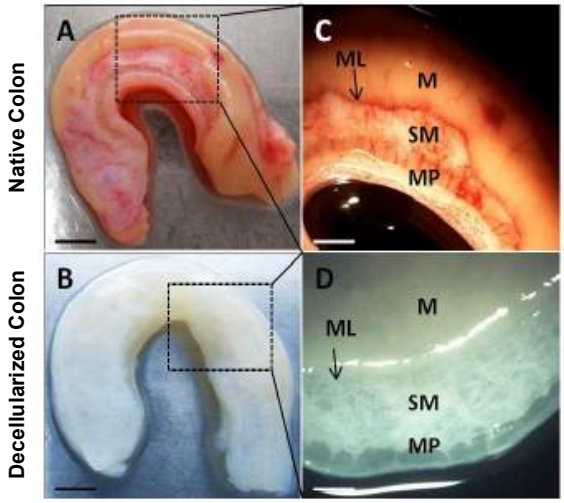

Figure 4. Decellularized *ex vivo* human colon. A: Representative image of normal human colonic tissue. Scale bar represents 0.5 cm. B: Intact colonic extracellular matrix following decellularization of tissue shown in panel A. Scale bar represents 0.5 cm. (C, D): Shown are the various layers comprising the native and decellularized colon tissue: (**ML**, muscularis layer; **M**, mucosa layer; **SM**, submucosal area; **MP**, muscularis propria). Scale bar represents 0.1 cm. Adapted from [15].

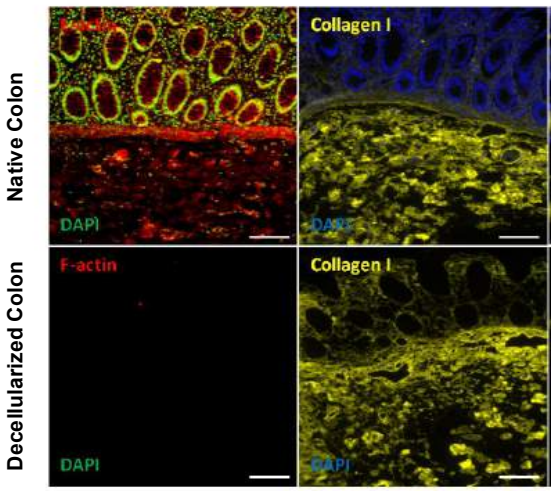

Figure 5. Characterization of decellularized *ex vivo* human colon. Representative immunofluorescent images of native (top panels) and decellularized colon (bottom panels), indicating expression of F-actin (cytoskeleton), DAPI (cell nuclei), and collagen-I (ECM: extracellular matrix). Scale bars represent 100 μm. Adapted from [15].

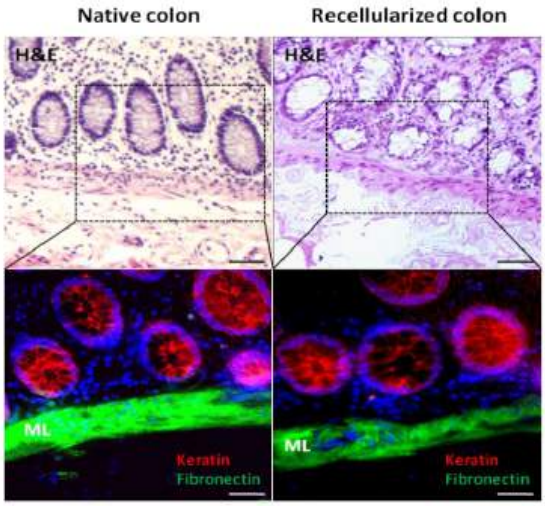

Figure 6. Recellularized *ex vivo* human colon. Representative H&E and co-immunofluorescent (co-IF) images of native colon (left panels) and colon recellularlized with epithelial cells, fibroblasts, and endothelial cells. **ML:** muscularis layer. Co-IF staining: cytokeratin (red); fibronectin (green); DAPI (blue). Scale bar represent 50 μm. Adapted from [15].

4.2. Systems Biology

Systems biology analysis is a powerful and sensitive methodology that has already made significant contributions to the field of cancer research in the identification of novel biomarkers, drug targets, and treatment strategies. Importantly, systems biology and computational approaches can be integrated to extend the findings from our research and advance our understanding of CCIC subpopulations, CRC chemoresistance, and metastasis. The use of a fluorescent reporter with the BMI1 promoter driving mCherry expression (BMI1-mCherry) may be lentivirally transduced into CCIC. This marker in addition to antibody labeling of LGR5 enables FACS analysis and isolation of BMI1+ and LGR5+ CCIC populations to study in downstream applications that may collectively enhance our understanding of fast vs. slow-cycling CCIC and their role in CRC.

One area of great interest is establishing metabolic profiles and bioenergetic analyses of BMI1+ and LGR5+ CCICs. Our laboratory has already established that CCICs show global metabolic reprogramming compared to non-CCICs by integrating transcriptomic and metabolomic data from various CRC cell lines and CCIC lines [17]. Furthermore, pathway analysis indicated substantial alterations in glycolysis and citric acid (TCA) in CCICs, suggesting that metabolic reprogramming may contribute to the proliferative, tumorigenic, and self-renewal capacity of CCICs. Since LGR5+ CCICs are highly proliferative while BMI1+ CCICs are more quiescent, it will be promising to examine their relative bioenergetics through metabolomics and elucidate greater complexity. Preliminary investigations have demonstrated that the number of mitochondria are increased in LGR5+ CCICs compared to BMI1+ CCICs, which is consistent with the metabolic states of active vs. slow cycling CCICs.

Next, ribosome profiling (Ribo-Seq) may be explored to understand the global active translation status of BMI1 vs. LGR5 CCICs. Beyond traditional RNA-Seq, which includes

sequencing data for all mRNAs and provides information about overall gene expression, Ribo-Seq detects only mRNAs being actively translated at a given time. This analysis provides an interesting link between gene expression and metabolic profiling, enabling insight into the major cellular processing dominating active vs. slow-cycling CCICs. Additionally, post-translational modifications, including phosphorylation, acetylation, and oxidation, of LGR5+ and BMI1+ CCICs may be characterized through proteomics and mass spectrometry. Differentially modified proteins between these two populations may be identified to enhance our knowledge of regulatory mechanisms.

Additionally, the epigenetic states of LGR5+ and BMI1+ CCICs may be analyzed through bisulfite sequencing and ChIP-seq, which will provide information about DNA methylation and chromatin modifications, respectively. In particular, identification of epigenetically modified gene promoters in each population may be validated by functional assays to understand their significance. ChIP-seq is also a powerful tool to identify novel super enhancer regions composed of putative enhancer elements located in close genomic proximity with high Mediator and transcription factor recruitment. Super enhancers may reveal in-depth information concerning gene regulation, CCIC behavior and CRC progression.

The regulatory network involved in BMI1+ and LGR5+ CCICs may also be characterized by total transcrptomic (total RNA-seq) analysis and microRNA microarray to identify long non-coding RNAs (lncRNAs) and microRNAs (miRNAs). Our lab has previously shown that miR-34a plays a critical role in regulating NOTCH1 levels in a bimodal manner in CCICs, determining self-renewal vs. differentiation [18]. Therefore, differentially regulated lncRNAs and miRNAs in BMI1+ or LGR5+ CCICs may provide insight into complex signaling networks and feedback loops that regulate cell fate decisions and tumorigenic potential specific to each population.

A final area of interest is to examine the chemoresistant properties of BMI1+ CCICs. A systematic study involving treating both LGR5+ and BMI1+ CCICs with a panel of chemotherapy agents, including 5-FU and Oxaliplatin, following by RNA-seq will be useful in understanding global alteration of gene expression that confer chemoresistant properties. Again, candidate genes may be validated *in vitro* and *in vivo* to establish functional significance and provide novel targets for drug development.

In conclusion, each of these approaches is intricately connected to provide a more complete understanding of cellular pathways and CCIC subpopulations. In particular, metabolism affects translation and epigenetics, while non-coding RNA regulation of CRC metabolism has also been established [19]. Furthermore, there has been evidence that 5-FU and Oxaliplatin serve as chemotherapy agents by interfering with translation through ribosomal RNA synthesis [20] and metabolism through the one-carbon cycle [21]. Therefore, systems biology-based analyses will be promising methods to better characterize proliferative and slow-cycling subpopulations of CCICs and inspire new rational therapies for colorectal cancer.

REFERENCES

1. Snippert, H.J., et al., *Intestinal crypt homeostasis results from neutral competition between symmetrically dividing Lgr5 stem cells.* Cell, 2010. **143**(1): p. 134-44.
2. Lopez-Garcia, C., et al., *Intestinal stem cell replacement follows a pattern of neutral drift.* Science, 2010. **330**(6005): p. 822-5.
3. Munoz, J., et al., *The Lgr5 intestinal stem cell signature: robust expression of proposed quiescent '+4' cell markers.* EMBO J, 2012.
4. Itzkovitz, S., et al., *Single-molecule transcript counting of stem-cell markers in the mouse intestine.* Nat Cell Biol, 2012. **14**(1): p. 106-14.
5. Tian, H., et al., *A reserve stem cell population in small intestine renders Lgr5-positive cells dispensable.* Nature, 2011. **478**(7368): p. 255-9.
6. Takeda, N., et al., *Interconversion between intestinal stem cell populations in distinct niches.* Science, 2011. **334**(6061): p. 1420-4.
7. Roth, S., et al., *Paneth cells in intestinal homeostasis and tissue injury.* PLoS One, 2012. **7**(6): p. e38965.
8. Tetteh, P.W., et al., *Replacement of Lost Lgr5-Positive Stem Cells through Plasticity of Their Enterocyte-Lineage Daughters.* Cell Stem Cell, 2016. **18**(2): p. 203-13.

9. Itzkovitz, S., et al., *Optimality in the development of intestinal crypts.* Cell, 2012. **148**(3): p. 608-19.
10. Di Micco, R., et al., *Control of embryonic stem cell identity by BRD4-dependent transcriptional elongation of super-enhancer-associated pluripotency genes.* Cell Rep, 2014. **9**(1): p. 234-47.
11. Rampal, R., K.B. Luther, and R.S. Haltiwanger, *Notch signaling in normal and disease States: possible therapies related to glycosylation.* Curr Mol Med, 2007. **7**(4): p. 427-45.
12. Capaccione, K.M. and S.R. Pine, *The Notch signaling pathway as a mediator of tumor survival.* Carcinogenesis, 2013. **34**(7): p. 1420-30.
13. Jenkins, D.W., et al., *MEDI0639: a novel therapeutic antibody targeting Dll4 modulates endothelial cell function and angiogenesis in vivo.* Mol Cancer Ther, 2012. **11**(8): p. 1650-60.
14. Saliba, A.E., et al., *Single-cell RNA-seq: advances and future challenges.* Nucleic Acids Res, 2014. **42**(14): p. 8845-60.
15. Chen, H., et. al, *A Forward Genetic Screen Identifies Genes Driving Invasive Neoplasia in Engineered Organotypic Recellularized Human Colon.* Nature Biotechnology, 2015. **in review**.
16. Vermeulen, L. and H.J. Snippert, *Stem cell dynamics in homeostasis and cancer of the intestine.* Nat Rev Cancer, 2014. **14**(7): p. 468-80.
17. Chen, K.Y., et al., *A metabolic signature of colon cancer initiating cells.* Conf Proc IEEE Eng Med Biol Soc, 2014. **2014**: p. 4759-62.
18. Bu, P., et al., *A microRNA miR-34a-regulated bimodal switch targets Notch in colon cancer stem cells.* Cell Stem Cell, 2013. **12**(5): p. 602-15.
19. Redis, R.S., et al., *Allele-Specific Reprogramming of Cancer Metabolism by the Long Non-coding RNA CCAT2.* Mol Cell, 2016.
20. Longley, D.B., D.P. Harkin, and P.G. Johnston, *5-fluorouracil: mechanisms of action and clinical strategies.* Nat Rev Cancer, 2003. **3**(5): p. 330-8.
21. Locasale, J.W., *Serine, glycine and one-carbon units: cancer metabolism in full circle.* Nat Rev Cancer, 2013. **13**(8): p. 572-83.

APPENDIX

Clinical Application of Single Cell RNA Sequencing in Colorectal Cancer

Contributing Authors:

(Tara Srinivasan, Kai-Yuan Chen*, Asaf Poran, Omar Aly, Jeff Milsom, Olivier Elemento, Steven M. Lipkin, and Xiling Shen)*

* These authors contributed equally to the study.

PREFACE

Transcriptional profiling with single cell resolution is a powerful methodology in clinical research to characterize cellular heterogeneity, identify rare, yet critical populations, and predict drug resistance. Here we implement DROP-SEQ, a high-throughout technique to sequence mRNA transcripts from individual cells derived from primary colorectal cancer (CRC) tumors in nanoliter-sized aqueous droplets. Xenograft and *in vitro* organoid models derived from early stage CRC were evaluated following treatment with traditional chemotherapy agents, 5-Fluorouracil and Oxaliplatin. Transcriptomes from over 5000 cells were sequenced and we identified differential responsiveness to 5-Fluorouracil in xenograft tumors, suggesting intratumoral heterogeneity. As proof-of-concept using the DROP-SEQ platform, parallel analysis of mRNA expression in various CRC models is useful for in-depth characterization of cell populations and their response to chemotherapy.

BACKGROUND

High-throughput gene expression analysis of bulk tissues, termed RNA-seq, has been a revolutionary tool in clinical research, enhancing the scope and depth of the transcriptome on a population level. However, there is a growing need to conduct transcriptional profiling with increased sensitivity and single cell resolution where they may be an insufficient amount of primary tissue for conventional RNA-seq and more importantly, to characterize cellular heterogeneity in various solid cancers [1, 2]. Several single-cell approaches to RNA sequencing have been explored with varying degrees of signal-to-noise ratios and overall utility in producing robust quantitative measurements that can reflect full transcriptome complexity. In particular, a combination of flow cytometry to isolate single cells with a specific phenotype and multiplex PCR has been used to revealed transcriptional diversity in colorectal cancer (CRC) tissues compared to the normal colonic mucosa [3]. A more recent methodology, termed DROP-SEQ,

utilizes a microfluidic platform to run nanoliter-sized aqueous droplets that capture mRNAs from single cells. DROP-SEQ has been reported to identify transcriptional variation in individual cells and offers a significant improvement in time and cost relative to other methods [4]. We implemented single cell RNA profiling using DROP-SEQ as a proof-of-concept to study heterogeneity in CRC as a result of chemotherapy.

In the context of traditional CRC drug treatment regimens, 5-Fluorouracil (5-FU), a member of pyrimidine class of compounds, is a thymidylate synthase inhibitor and among the most commonly used anti-tumor agents. Additionally, Oxaliplatin, a Platinum derivative, is a principal chemotherapy agent that induces single- and double-strand breaks in DNA through collapse of the replication fork [5]. While combination regimens involving both 5-FU and Oxaliplatin are often used to treat advanced stages of CRC, recurrence and drug resistance remain critical challenges [5, 6]. Consequently, global approaches, such as single cell RNA sequencing, offer significant value in identifying gene expression patterns that correlate with drug response in specific intra-tumoral populations [2]. Such technology has the potential to inform the development of novel therapeutics and combination treatments to improve patient survival. Here we show the utility of single cell RNA sequencing using the microfluidic DROP-SEQ platform in clinical models of colorectal cancer.

PRELIMINARY RESULTS

As proof of concept for the application of DROP-SEQ, we performed a pilot study analyzing a single early stage CRC tumor directly and following propagation both in xenograft and *in vitro* organoid models. The number of cells captured and detected by DROP-SEQ varied between 500 and 1900 depending on the precise treatment condition (Fig. 1). Unsupervised clustering revealed specific subgroups based on gene expression from fresh isolated CRC tissue, indicating a high degree of sensitivity in this methodology (Fig 2). However, the number of total

transcript reads in single cells was unexpectedly low, especially following treatment with chemotherapy agents, 5-FU and Oxaliplatin (Fig. 3). The data was then processed with normalization to run principle component analysis as a measure of variation between single cells (Fig. 4a-4c). Single cells isolated from fresh CRC tissue, xenograft tumors, and organoid cultures were similar in gene expression. Interestingly, single cells derived from organoids displayed some variation, suggesting an *in vitro* specific gene signature (Fig. 4a). With 5-FU administration, the xenograft model indicated two clear subgroups: non-responsive and responsive (Fig. 4b). This finding suggests that differential response to chemotherapy agents may be due to intra-tumoral heterogeneity. In contrast, treatment with 5-FU and Oxaliplatin in organoids did not display as much variation as shown in xenograft tumors (Fig 4c). This may be explained by technical factors, including low drug concentration, low efficiency of drug administration to cells or due to biological limitations of *in vitro* assays. Future experimentation will involve specific titration of 5-FU and Oxaliplatin in organoid cultures to resolve this discrepancy. Whole transcriptome features displayed in a dendrogram indicated that fresh CRC tissue, xenograft, and organoid clustered together closely on neighboring branches or were intermingled (Fig. 5). Additionally, the color spectrum revealed that transcriptomes from treated single cells were distinct from the untreated (control) cells, suggesting that DROP-SEQ is capable of identifying novel subgroups based on global transcriptional activity. Future computational analysis will be required to resolve specific gene expression signatures within each subgroup.

DISCUSSION

In the study of solid tumors, traditional techniques, such as flow cytometry and immunohistochemistry, are limited in their efficacy due to their dependence on robust antibody markers and the number of parallel assays that can be performed together. By comparison, high-

throughput assays offer significant insight about global gene expression, representing an intra-tumoral population average. The ability to analyze transcriptomes with single cell resolution is, therefore, a unique and powerful strategy to reveal minority subpopulations, inform novel therapeutic development, and predict cancer relapse or drug resistance. Previous reports using single-cell PCR gene expression analysis have investigated transcriptional diversity in primary human normal colon and colon cancer epithelia [3]. Here we implemented a specific protocol for single cell transcriptional profiling using the microfluidic DROP-SEQ platform as a proof-of-principle in the study of clinical CRC models. We examined primary CRC cells propagated as xenograft tumors and *in vitro* organoids and analyzed the resulting cellular heterogeneity when treated with traditional chemotherapy agents, including 5-FU and Oxaliplatin. Unsupervised clustering analysis revealed differential sensitivity to 5-FU in xenograft tumors, suggesting intratumoral heterogeneity.

Microfluidic automation of single cell mRNA amplification has enabled broad and in-depth insight into diverse biological processes with high sensitivity [2, 4]. Since RNA is diversely involved in coding functions as mRNA, housekeeping roles, and regulatory processes as non-coding RNAs, future applications will broaden RNA profiling for a more complete single cell transcriptome. Such information will be critical in revealing subcellular complexity that contributes to tumor development or chemoresitance. Ultimately, innovation in high-throughout single cell RNA sequencing has the potential to enhance our multi-dimensional understanding of normal and neoplastic tissue heterogeneity and identify novel targets for chemotherapy.

METHODS

Isolation of primary CRC cells

Early stage (Stage I) primary human CRC tumors (previously untreated with chemotherapy agents) surgically resected during biopsies were used for this study and informed consent was obtained from each patient. Approval for this research protocol was obtained from

IRB committees at Weill Cornell Medical College and NY Presbyterian Hospital. The procedure for isolation of cancer cells and organoid culture are previously described [7, 8]. Briefly, colonic tumors were collected and incubated in Advanced DMEM/F12 supplemented with gentamycin (Life Technologies) and fungizone (Life Technologies). Extraneous muscular and sub-mucosal layers were removed from tumor specimens. Solid tissue was cut into 1 cm fragments and enzymatically digested with 200 units/ml Collagenase Type III (Worthington) and 100 units/ml DNase-I (Worthington) on a rocking platform for 2 hours at 37°C. Vigorous shaking released cells, which were collected in several fractions. Fractions were then centrifuged (400 RPM, 5 minutes) and visualized by microscopy to determine which enriched fractions to combine. This was followed by mechanical disruption and passage of cell solution through 40um filter to obtain a single cell suspension. Single cells were stained with EpCAM-FITC (Abcam, ab8666) and 7-AAD according to standard protocols and were suspended in cold PBS with 0.5% BSA for FACS analysis to isolate epithelial cells. FlowJo software was used to gate populations according to 7-AAD viability, and forward and side scattering. Cutoff thresholds were provided by unstained ISCs.

Culture of primary CRC cells

For xenograft assays, 8-week-old NOD/SCID mice were injected subcutaneously (s.c) into the upper back with cells derived from primary patient tumors. Injections contained 100,000 EpCAM+ cells suspended in 200ul of 1:1 culture medium: Matrigel mixture. Tumors were propagated for 8 weeks; Oxaliplatin (Tocris) and 5-fluorouracil (Tocris) were dissolved at a final concentration of 100 μg/ml [6] and directly injected into tumors during the last 48 hours. Following euthanasia, tumors were harvested and prepared for single cell RNA sequencing.

For *in vitro* organoid culture, EpCAM+ cells were suspended in Matrigel, and overlaid with human colon stem cell medium containing Advanced DMEM/F12 supplemented with

Glutamax, HEPES, N-2, B-27 without vitamin A, 1 mM N-Acetyl-L-cysteine, Y-27632, Gastrin (Sigma), TGF-ß type I Receptor inhibitor A83-01 (Tocris), and P38 inhibitor SB202190 (Sigma-Aldrich) [7]. Specific concentrations for each reagent are listed in Table 1. During organoid culture, full medium was replaced every 2 days. For drug treatments, oxaliplatin (Tocris) and 5-fluorouracil (Tocris) were dissolved at a final concentration of 100 µg/ml in culture medium for 48 hours [5, 6].

Table 1. Culture medium for primary human colon cancer cells propagated as organoids.

Reagent name	Supplier Cat No	Solvent Stock	solution final conc
Advanced DMEM/F12	Invitrogen	N/A	500 ml
HEPES	Invitrogen 15630-056	100x	10mM
GlutaMAX-I	Invitrogen 35050-079	200 mM	2 mM
Penicillin/Streptomycin	Invitrogen 15140-122	10000/10000 U/ml	100/100 U/ml
N2 supplement	Invitrogen 17502-048	100x	1x
B27 supplement	Invitrogen 17504-044	50x	1x
N-Acetylcysteine	Sigma A9165-5G	DW 500 mM	1 mM
[Leu15]-Gastrin I	Sigma-Aldrich G9145	PBS/BSA 100 µM	10 nM
A-83-01	Tocris 2939	DMSO 500 µM	500 nM
SB202190	Sigma-Aldrich S7067	DMSO 30 mM	10 µM
Y-27632	Sigma-Aldrich Y0503	PBS 10 mM=	10 µM

Adapted from [8].

Sample Preparation for DROP-SEQ

Xenograft tumors were harvested and enzymatically digested according to the protocol described earlier. *In vitro* cultures were harvested and digested with TrypLE (Life Technologies) for 20 minutes at 37°C. Cell suspensions were then centrifuged (600 RPM, 5 minutes), resuspended in RNase-free PBS containing 0.01% BSA, and passed through a 40um filter to obtain a single cell suspension. Single cells were counted using a hemocytometer to adjust to a concentration of 130,000 cells/ml in PBS containing 0.01% BSA before running on the DROP-SEQ microfluidic platform.

Figure 1.

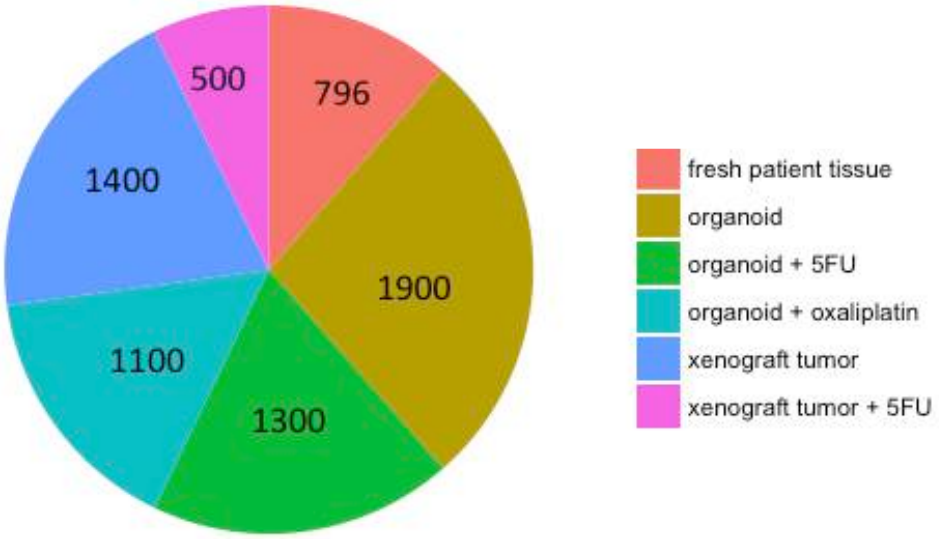

Figure 1. Number of cells captured and detected by DROP-SEQ.

Figure 2.

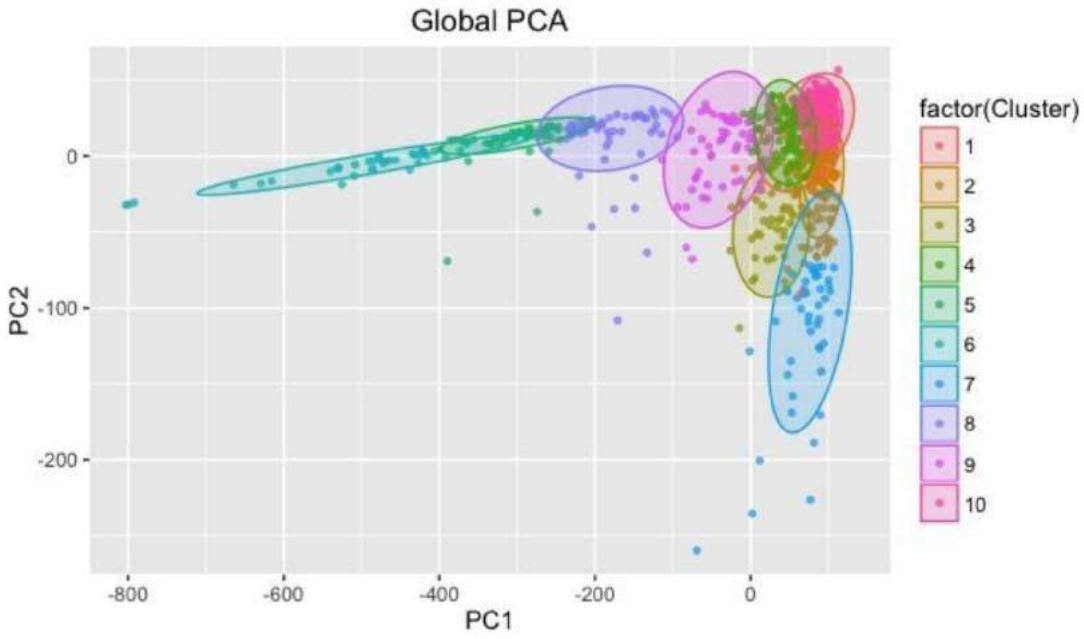

Figure 2. Principal Component Analysis (PCA) showing variation of single cells and unsupervised clustering on the basis of gene expression in fresh CRC tissue.

Figure 3.

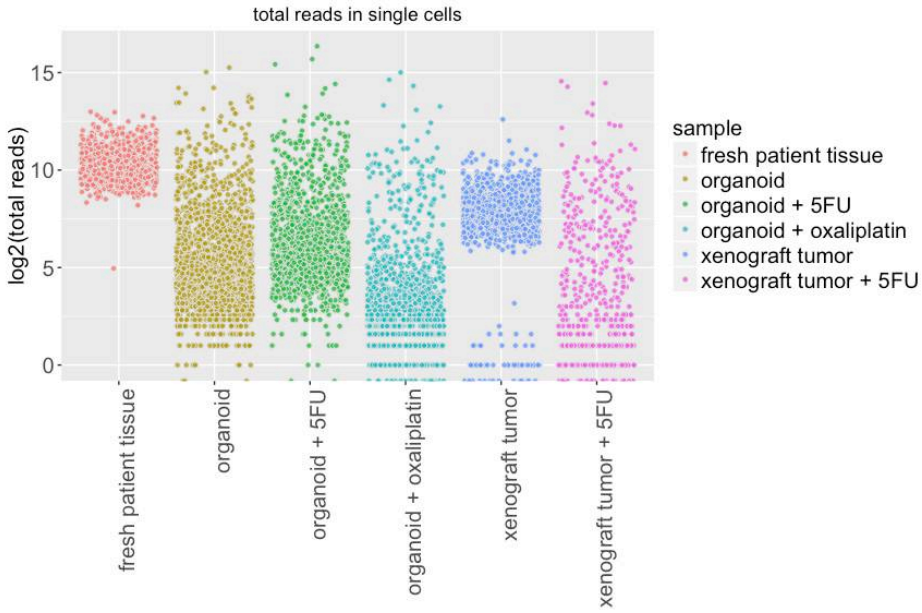

Figure 3. Total number of transcript reads detected per single cell.

Figure 4.

a

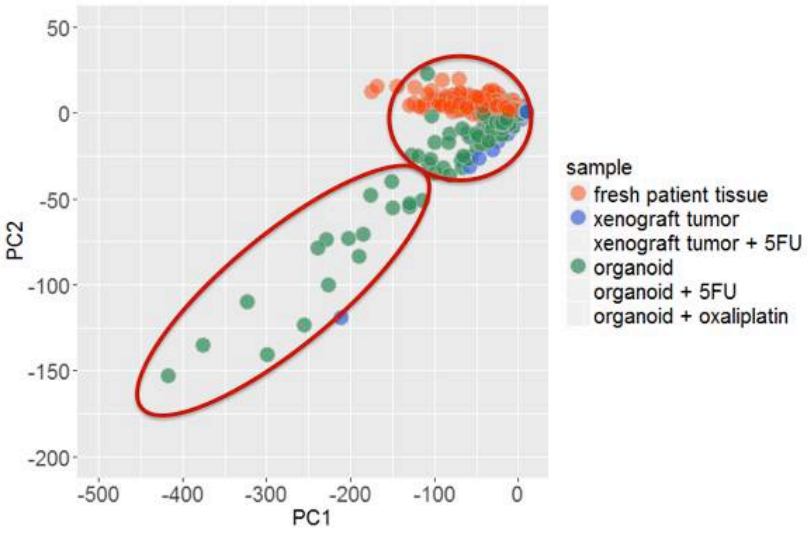

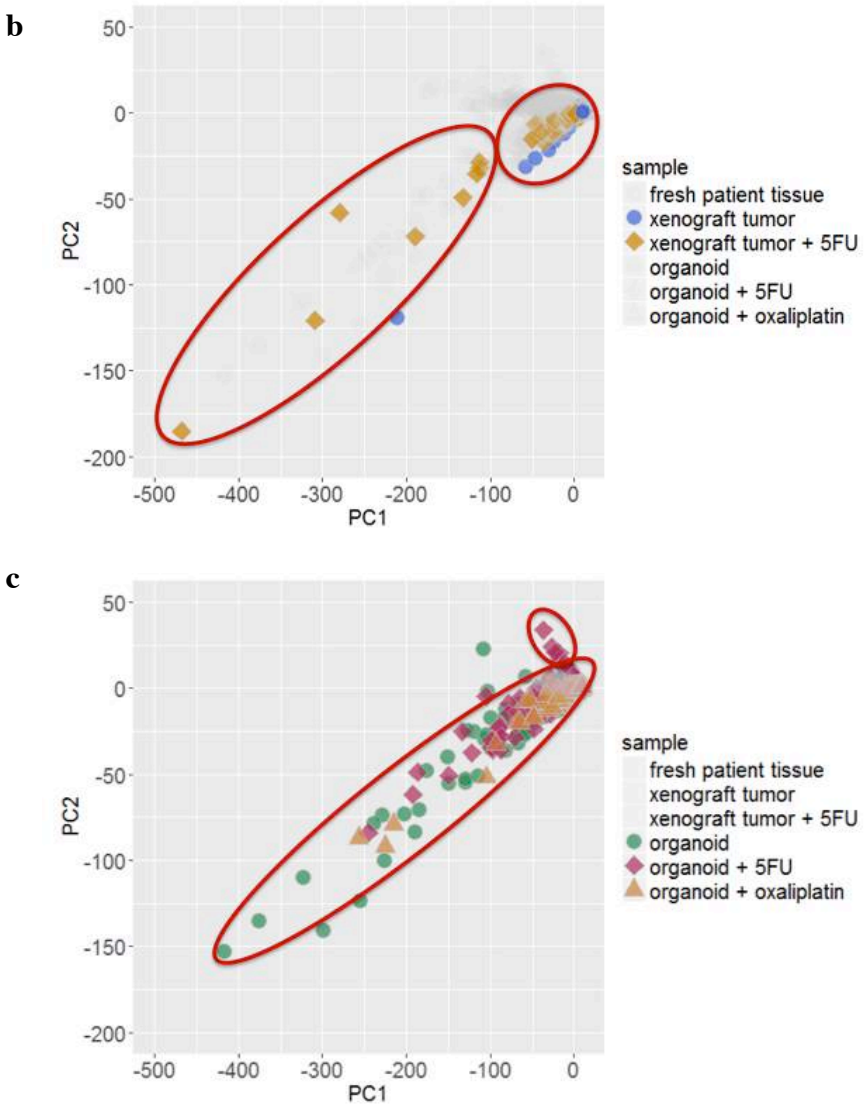

Figure 4. Principal Component Analysis (PCA) showing variation of single cells on the basis of gene expression. **(a)** Variation of single cells derived from fresh CRC tissue, untreated xenograft tumors and untreated organods. Large oval gates an *in vitro*-specific subgroup based on gene expression. **(b)** Variation of single cells derived from xenograft tumors that were untreated (control) or injected with 5-FU. Large oval gates a 'responsive' population. **(c)** Variation of single cells derived from CRC organoids treated with DMSO (control), 5-FU, or Oxaliplatin. Small oval gates a 'responsive' population.

Figure 5.

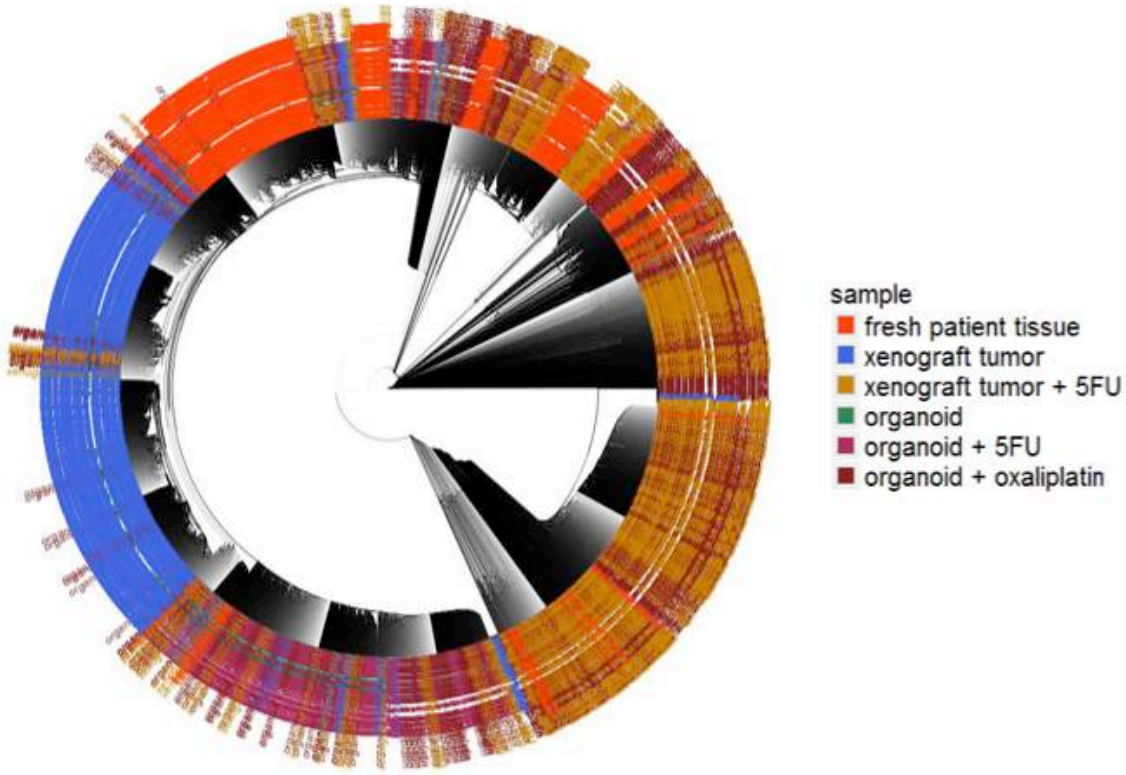

Figure 5. Circular dendrogram indicating distinct transcriptome features among different experimental models and treatment conditions.

COMPETING FINANCIAL INTERESTS

The authors declare no competing financial interests.

REFERENCES

1. Wu, A.R., et al., *Quantitative assessment of single-cell RNA-sequencing methods.* Nat Methods, 2014. **11**(1): p. 41-6.
2. Saliba, A.E., et al., *Single-cell RNA-seq: advances and future challenges.* Nucleic Acids Res, 2014. **42**(14): p. 8845-60.
3. Dalerba, P., et al., *Single-cell dissection of transcriptional heterogeneity in human colon tumors.* Nat Biotechnol, 2011. **29**(12): p. 1120-7.
4. Macosko, E.Z., et al., *Highly Parallel Genome-wide Expression Profiling of Individual Cells Using Nanoliter Droplets.* Cell, 2015. **161**(5): p. 1202-14.
5. Pires, I.M., T.H. Ward, and C. Dive, *Oxaliplatin responses in colorectal cancer cells are modulated by CHK2 kinase inhibitors.* Br J Pharmacol, 2010. **159**(6): p. 1326-38.
6. Nannizzi, S., et al., *Cellular and molecular mechanisms for the synergistic cytotoxicity elicited by oxaliplatin and pemetrexed in colon cancer cell lines.* Cancer Chemother Pharmacol, 2010. **66**(3): p. 547-58.

7. Jung, P., et al., *Isolation and in vitro expansion of human colonic stem cells.* Nat Med, 2011. **17**(10): p. 1225-7.
8. Sato, T., et al., *Long-term expansion of epithelial organoids from human colon, adenoma, adenocarcinoma, and Barrett's epithelium.* Gastroenterology, 2011. **141**(5): p. 1762-72.